Estimation of load sharing among muscles acting on the same joint and Applications of surface electromyography

Babak Afsharipour

Department of Electronics and Telecommunications

Politecnico di Torino

A thesis submitted for the degree of

PhilosophiæDoctor (PhD)

2014 Feb.

The Board

1. Prof. Marco Knaflitz

2. Prof. Tommaso D'Alessio

3. Prof. Giovanni Vozzi

Day of the defense: February 27$^{\text{th}}$, 2014

Supervisor: Prof. Roberto Merletti

Laboratory for Engineering of the Neuromuscular System (www.lisin.polito.it)
Department of Electronics and Telecommunications, Politecnico di Torino

Acknowledgements

Acronyms

AGA	Analytical Graphical Approach
AP	Action Potential
ARV	Average Rectified Value
BB	Biceps Brachii muscle
BR	Brachioradialis muscle
DD	Double Differential
eMVC	Maximum Voluntary Contraction in elbow extension
eq.	equation
EC	Evolutionary Computations
Eval.	Evaluation
fMVC	Maximum Voluntary Contraction in elbow flexsion
FT	Fourier Transform
IZ	Innervation Zone
IED	Inter Electrode Distance
MDF	Median Frequency
MN	Monopolar
MNF	Mean Frequency
MVC	Maximum Voluntary Contraction
MU	Motor Unit
NA	Numerical Approach
PSO	Particle Swarm Optimization
RMS	Root Mean Square
SD	Single Differential
sEMG	surface ElectroMyoGram
TBL	Lateral head of Triceps Brachii
TBM	Medial head of Triceps Brachii

Summary

Despite many years of research, the issue of load sharing among muscles acting on the same joint is still unresolved and very controversial. There is a monotonic relationship between the EMG amplitude of a specific muscle and its force. Such relationship depends on the specific anatomical (subcutaneous thickness, fiber orientation, etc.) and detection conditions (electrode location, inter-electrode distance) and recruitment modality of motor units (random, superficial to deep, deep to superficial). The force produced by a specific muscle cannot be measured and what is measured is the total force provided by all the active muscles acting on a joint, including agonists and antagonists The first part of this work (ch 3) addresses the issue of load sharing by proposing two possible approaches and testing them. The second part (ch. 4 and 5) addresses two applications of surface EMG focusing on the study of a) muscle relaxation associated to Yoga sessions and b) the activation of muscle of the back and shoulder of musicians playing string instruments (violin, viola and cello).

In both parts the element of innovation is the use of two dimensional electrode arrays and of techniques based on EMG Imaging. The objectives of this work are presented and explained in chapter 1 while the basic concepts of surface EMG are summarized in chapter 2. Different EMG-based muscle force models found in the literature are explained and discussed.

Two renowned amplitude indicators in surface EMG (sEMG) studies are the average rectified value (ARV) and the root mean square (RMS). These two amplitude indicators are computed over a defined time window of the recorded signals to represent the muscle activity. In the second chapter, ARV and RMS are defined in both time (1D) and space (2D). The advantages and disadvantages of RMS and ARV are compared and discussed for a simple sinusoid as well as for more complex signals (simulated motor unit

action potential detected by high density electrode grid). The results show that RMS is more robust to the sampling frequency than ARV. For a simple sinusoid (i.e. $x(t) = A\sin(2\pi f_t + \varphi)$) is shown that, even if the signal is sampled below the Nyquist frequency, the RMS is fixed and is equal to the expected value ($\frac{A}{\sqrt{2}}$). It is shown that the ARV of a sampled signal will not be equal to the correct value even if the sampling theorem (i.e. $F_{samp.} >$ Nyquist Frequency) is observed.

New technologies based on high density sEMG (HDsEMG) recording provide more muscle information decoded from the sEMG maps. In such maps, the resolution, which is defined by the inter-electrode distance (IED), is important. In this thesis, starting from the simulation of a single fiber and of a group of fibers (motor unit), it is shown that IED$>$10 mm causes aliasing. Aliasing is a source of error in sEMG map interpretation or decisions that are made by automatic algorithms such as those providing image segmentation for the identifications of regions of interest.

Image segmentation is a technique for partitioning an image (data set) into regions of interest and is used in many different fields. Different segmentation techniques can be found in the literature. K-means, watershed, and h-dome are used to extract the active portion of the muscle(s) covered by the detection system. Chapter 2 discusses these three segmentation algorithms and compares them in order to find the most suitable method. Since the watershed method had been validated for ARV sEMG map segmentation in the literature, it was used in these investigations, although the RMS indicator is shown to be more robust with respect to ARV. The comparison of the algorithms was therefore done on ARV maps. Results reveal that among K-means, watershed, and h-dome segmentation algorithms, watershed provides most accurate segmentation for the ARV maps. The spatial average of ARV, within each region of interest and for each epoch, was then used to define the muscle activation level for that epoch.

Chapter 3 presents a mathematical model that is associated to the monotonic Force–EMG relation. A possible non-linear relationship between the

EMG and force or torque is

$$F_{tot.} = \sum_{m \in muscles}^{N} F_m = \sum_{m \in muscles}^{N} x_m \times sEMG_m^{y_m}$$

, where $F_{tot.}$ represents the total force or torque (produced by "N" muscles acting on a joint and measurable by load cell or a torque meter), "$muscles$" indicates the group of muscles contributing to produce the total force, F_m is the force produced by the individual muscle "m", $sEMG_m$ is the surface EMG amplitude (defined above) of muscle "m", x_m and y_m are suitable coefficients to be identified.

A system of "M" equations is obtained by performing "M" measurements at "M" different force levels in isometric conditions. The solutions of such system of equations are the "x" and "y" values for each muscles (i.e. x_m and y_m). The force or torque contributions of the individual muscles can then be found from the muscle model. Two different approaches were investigated for finding the solutions of the system, which are:

- Analytical-Graphical Approach (AGA)

- Numerical Approach(NA) consisting of error minimization (between the total estimated and measured force) applying optimization algorithms

The AGA was used to find the model parameters of each muscle (i.e. "x_m" and "y_m") contributing to the force production on a joint by finding the intersection of those surfaces that can be obtained from sequential substitutions of the model parameters in the equations corresponding to each contraction level. Sequential substitutions help us to find the exponential parameter of one muscle (ex.: y_m) versus its corresponding parameter associated to the other muscles. Since, it is not possible to graph more than three dimensions (see chapter 3), the AGA was investigated for the theoretical case of two muscles acting on the same joint (simulation study). In real cases, there are at least four muscles (two agonists + two antagonists) acting on the same joint, therefore, the AGA can not be easily applied to the load sharing problems. However such approach is useful to find the

number of possible solutions and to test other algorithms in simple cases (two muscles).

In simulation studies, the AGA graphically shows that there is more than one solution to the load sharing problem even for the simplest theoretical case(i.e. a joint spanned by only two muscles). The second approach, based on minimization of the mean square error between the measured and the total estimated force or torque (with "N" muscles involved) provides an estimate of the model parameters "x_m" and "y_m" that in turn provides the force contributions of the individual muscles. The optimization algorithms can find the solutions of our system made of non-linear equations (see chapter 3). Starting from different point (initial conditions), different solutions can be found, as predicted by the AGA approach for the two-muscle case. The main conclusion of this study is that the load sharing strategy is not unique. Physiologically, for each muscle, different model parameters "x_m" and "y_m" provide the same total force. Additional minimization criteria (e.g. minimizing the energy consumption to carryout a certain task, or other quantities) are probably implemented. This can be investigated in future studies.

Chapter 4 discusses the application of surface electromyography to a single case study of Yoga relaxation to show the feasibility of measurements. The effect of yoga relaxation on muscle activity (sEMG amplitude), as well as on mean and median frequencies and muscle fiber's conduction Velocity, is discussed in this chapter. No changes in the sEMG activity pattern distribution were found for the same task performed before and after applying yoga relaxation technique. However, myoelectric manifestations of fatigue were smaller after relaxation and returned to the normal pattern after the recovery phase from relaxation. Further studies are justified.

Chapter 5 describes results obtained in collaboration with Massimo Testone and discusses the spatial distribution of muscle activity over the Trapezius and Erector Spinae muscles of musicians playing string instruments. Musicians and populations whose job requires daily intensive repetitive tasks often suffer from musculoskeletal disorders after some years. Musicians are an important group of individuals who start their work and their training

at early ages. Becoming a professional player can be considered as a goal which motivates this population to work as hard as possible in a repetitive task that leads to playing-related musculoskeletal disorders (PRMDs) with a prevalence of 80% among professionals.

In chapter 5, the effect of backrest support in sitting position during playing cello, viola, and violin on the muscle activity index of upper and lower Trapezius muscle of the bowing arm, upper Trapezius muscle of non-bowing arm, left and right Erector Spinae muscles is investigated. Two professional players (one cello and one viola) and five student players (one cello, three violin and one viola) participated in this study. The muscle activity index (MAI) was defined as the spatial average of RMS values of the muscle active region detected by watershed segmentation for Trapezius muscles (left and right), and thresholding technique (70% of the maximum value) for left and right Erector Spinae muscles. It was found that the MAI is string (note) dependent. Considering the string # 1 as the most medial string and string # 4 as the most lateral string (with respect to the subject's sagittal plane) and regardless of the bowing type - i.e. slow (1 bow/s) but large (entire bow) and fast (6 bows/s) but short (3cm of the head or tail of the bow)- and backrest support (with/without), the highest value of the sEMG activity index in the Trapezius was obtained during playing string # 4 with a decreasing trend toward string # 1. Statistical difference ($p < 0.05$) between the MAIs of left Erector Spinae muscle during playing with and without backrest support was observed in four (out of five) student players. No statistical differences were observed on the muscle activity of Trapezius (bowing and no-bowing arms) during playing with and without backrest support in different types of bowing for all musicians.

In conclusion, this work addresses a) the issue of spatial sampling and segmentation of sEMG using 2D electrode arrays, b) two possible approaches to the load-sharing issue, c) a single-case study of Yoga relaxation and d) the distribution of muscle activity above the Trapezius and Erector Spinae muscles of musicians playing string instruments. Previously unavailable knowledge has been achieved in all these four studies.

To my love Sayeh

Contents

List of Figures

List of Tables

1

Introduction and Objectives of the work

1.1 Position of the problem:
From surface electromyography to muscle force

Measuring the forces applied to a joint and estimating how these forces are partitioned among surrounding muscles, ligaments, and articular surfaces is fundamental to understanding joint function, injury, and disease. This knowledge would be also useful in many situations related to ergonomics, sports and rehabilitation. The only information we can obtain in non-invasive manner concerns the total torque or force F^M at the joint and the surface EMG of the muscles (see figure 1.1).

Load sharing describes the distribution of observable total force/torque which comes from different muscles acting on a joint among them. No human joint is spanned by a single muscle, since synergy is always present (1). Let's consider the position of holding a weight in hand. The analysis of load sharing answers to questions such as (as an example) how is the force produced for holding the load shared by active muscles acting on the elbow. We know that the two heads of Biceps Brachii, Brachialis, and Brachioradialis muscles are responsible for elbow flexion and Anconeus with the three heads of Triceps Brachii are in charge for elbow extension. The activity of muscles can be represented by the electrical activity recorded from the surface of a muscle. So, the main idea is finding the relation between the EMG, as representative of muscle activity, and the force produced by the muscle. In other words, what model can estimate force

(as the output) based on the input which is EMG activity (figure 1.2).
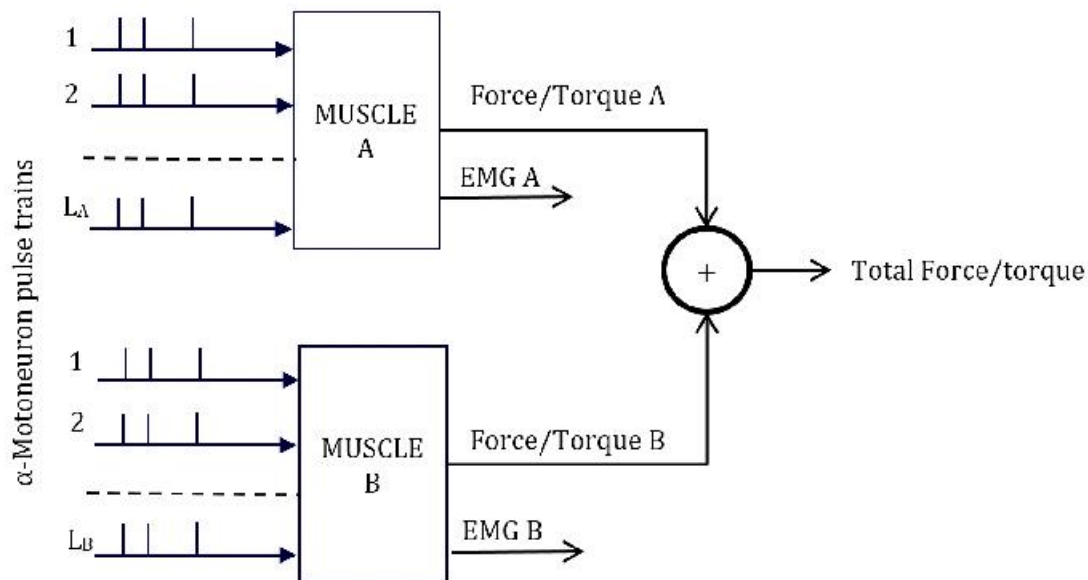
Figure 1.1: Model of simple joint with two muscles in isometric conditions. The observable quantities are EMG A, EMG B and the total force/torque. EMG A and EMG B can be recorded by placing electrodes (arrays or matrices) on the muscle (non-invasive, surface EMG) or using electrode needles (invasive method, intramuscular EMG). The total force/torque is measured with an isometric brace or a load cell and is the sum of the contributions from many muscles (two muscles in the example).

Concerning the EMG based force estimation, several questions come to mind that must be answered to step forward. Some of these questions are as follows:

1. How should the muscle activity (in space and time) be defined?

2. What models or tools should be used to associate EMG to force?

3. Are these models useful for force estimation?

Muscle activity can be represented by EMG amplitude. Average rectified value (ARV) and root means square (RMS) are the two most common EMG amplitude estimators used by researchers. Choosing the proper muscle activity indicator is the first step toward the study of the muscle force estimation and load sharing issue. EMG amplitude is highly dependent on the electrode location and its geometry over the muscle. Recent technologies allow the researchers to use two-dimensional (2-D) high density (HD)
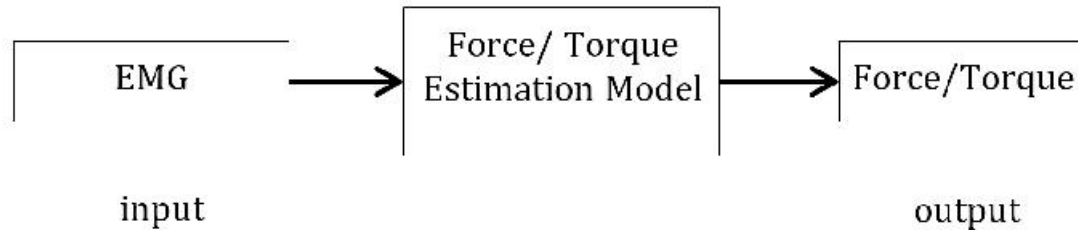
Figure 1.2: Mapping the EMG to the Force through a model (single input single output) is a basic issue of this study. By a suitable model and recording the muscles activity, the force produced by each muscle can be estimated.

electrode arrays. In HDsEMG, the continuous surface potential distribution is sampled by a grid of NxM electrodes equally spaced along x and y. An image of NxM pixels (i.e. spatial samples of the instantaneous potential distribution) provides more information about muscle activity with respect to the conventional bipolar recording. In spatial sampling, spatial aliasing due to the too large inter electrode distances (IEDs) along x and y can occur. The maximum IED to avoid spatial aliasing and analyzing ARV and RMS from aliasing point of view to select the proper amplitude indicator in force estimation and load sharing issue can be considered as the first steps in addressing the complexity of the load sharing issue. There is a monotonic non-linear relationship between the EMG amplitude of a specific muscle and its force. Such relationship depends on the specific anatomical (subcutaneous thickness) and detection condition (electrode location, inter electrode distance) and MU recruitment modality (random, superficial to deep, deep to superficial). Needless to say that, taking into account each of these parameters increases the complexity of the study. This chapter covers the anatomy of muscles and their architecture, the mechanism of EMG generation, muscle force generation and the relation between EMG and muscle force.

1.1.1 Anatomy of muscles

The term of muscle is derived from the Latin musculus meaning "little mouse" perhaps because of the shape of certain muscles or because contracting muscles under the skin look like mice moving under a rug[1].

---

[1] www.anatomyalamanac.blogspot.it/2008/01/from-archive-muscle-comes-from-latin.html

1. INTRODUCTION AND OBJECTIVES OF THE WORK

Muscle is a kind of soft tissue of animals. Three types of muscle tissue are recognized in vertebrates[1]:

- Skeletal muscle or "voluntary muscle" is anchored by tendons (or by aponeurosis) to bone.

- Smooth muscle or "involuntary muscle" is found within the walls of organs and structures such as stomach, esophagus, and bronchi.

- Cardiac muscle is also an "involuntary muscle" but is more akin in structure to skeletal muscle, and is found only in the heart.

Skeletal muscles are sheathed by a tough layer of connective tissue called the epimysium. The epimysium anchors muscle tissue to tendons at each end, where the epimysium becomes thicker and collagenous. It also protects muscles from friction against other muscles and bones. Within the epimysium are multiple bundles called fascicles, each of which contains 10 to 100 or more muscle fibers collectively sheathed by a perimysium. Besides surrounding each fascicle, the perimysium is a pathway for nerves and the flow of blood within the muscle. The threadlike muscle fibers are the individual muscle cells (myocytes), and each cell is encased within its own endomysium of collagen fibers. Thus, the overall muscle consists of fibers (cells) that are bundled into fascicles, which are themselves grouped together to form muscles. At each level of bundling, a collagenous membrane surrounds the bundle, and these membranes support muscle function both by resisting passive stretching of the tissue and by distributing forces applied to the muscle. Scattered throughout the muscles are muscle spindles that provide sensory feedback information to the central nervous system.

---

[1]www.en.wikipedia.org/wiki/Muscle#cite_note-1
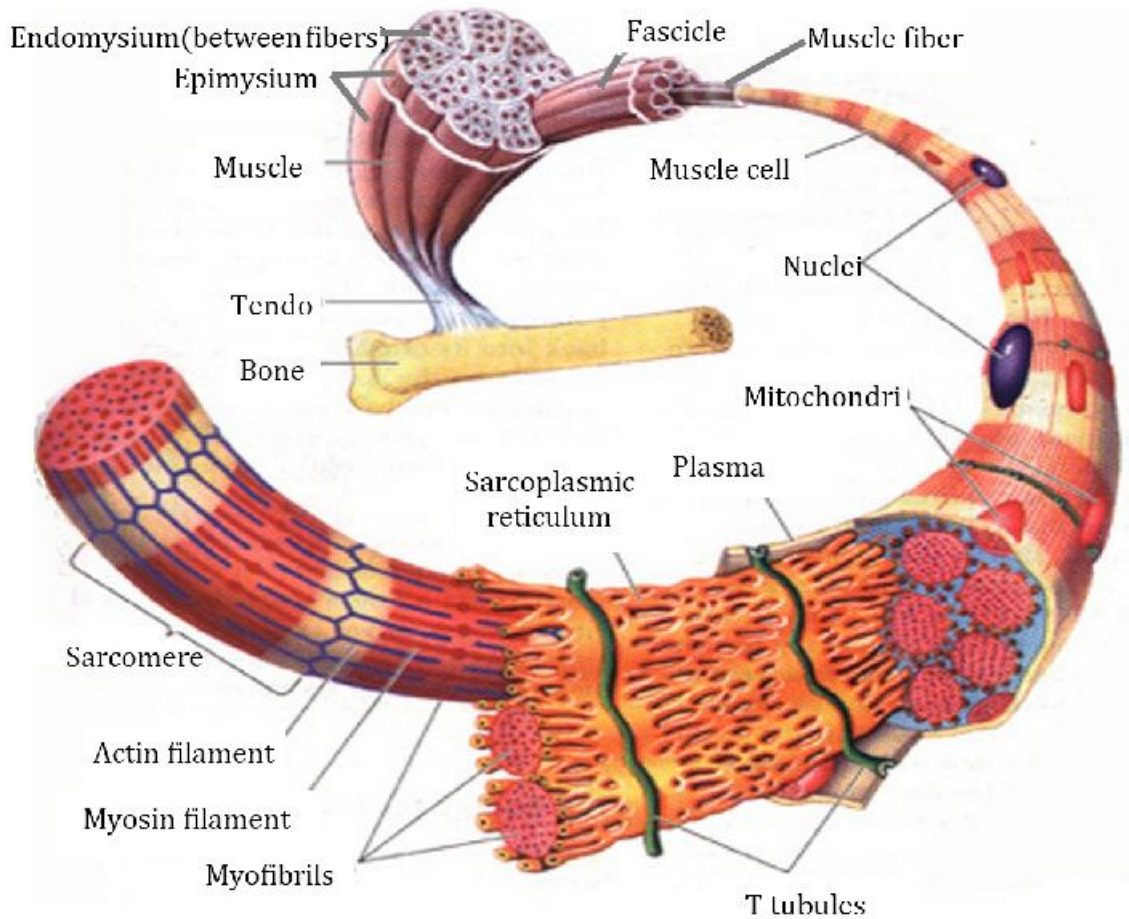
Figure 1.3: Microanatomy of a muscle (http://media.tumblr.com/tumblr_lh1ym goLFY1qd1wp5.jpg). Skeletal muscle cells are elongated or tubular. They have multiple nuclei and these nuclei are located on the periphery of the cell. Skeletal muscle is striated. The muscle is made up of smaller bundles known as fascicles. Fascicles are actually bundles of individual muscle cells (myofibers). Each fascicle is made up of several muscle cells known as myocytes. They may also be called myofibers or muscle fibers. Each muscle cell is surrounded by a connective tissue sheath known as the endomysium. This sheath is very important in the physiology of muscle contraction because it electrically insulates the individual muscle cells from each other(http://faculty.etsu.edu/forsman/histologyofmuscleforweb.htm).

1.1.2   Architecture of muscles

Muscle can be considered to be a collection of equally long fibers in parallel, where all fibers are oriented either in the direction of the tendon (a fusiform muscle) or at an

acute angle ($\varphi > 0$) to the tendon (i.e., a pinnate muscle). The fibers of a pinnated muscle are connected to the aponeurosis of the muscle which is also called the internal portion of the tendon because its properties appear identical to the properties of the external portion of the tendon ((2)).
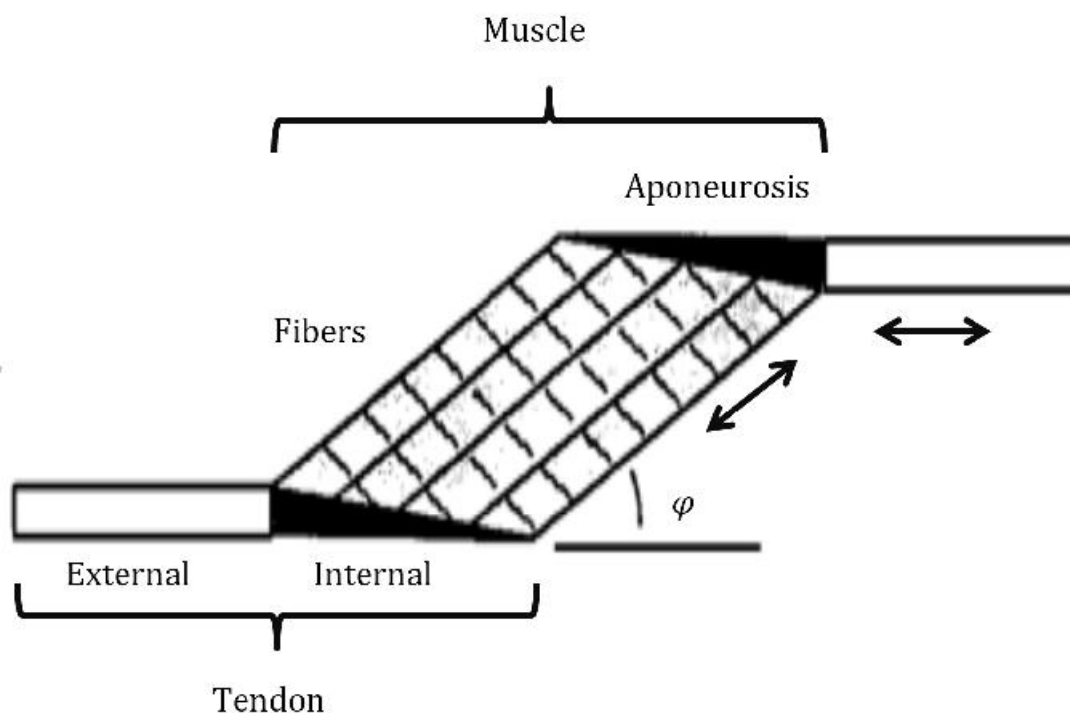
Figure 1.4: Muscle fibers (lightly shaded region) lie in parallel (same length) oriented in some angle (φ) to the tendon axis. Tendon can be considered to consist of an internal portion (i.e. the aponeurosis of muscle origin and insertion, shaded region) and an external portion. Arrows show that the tendons move along their axis and muscle shortens along its fibers ((2)).

1.1.3 Mechanisms of EMG generation

Electrical signals (e.g. action potential) within biological organisms are driven by ions. Sodium (Na $^+$), potassium (K^+) and chloride (Cl^-) are the main ions responsible for the EMG generation (3). EMG is the summation of the motor unit action potential trains (MUAPT) produced by the active motor units (MU) of a muscle. A motor unit consists of a α-motoneuron in the spinal cord and the muscle fibers it innervates (1.5). The α-motoneuron is the final point of summation for all the descending and

reflex input. The net membrane current induced in this motoneuron by the various synaptic innervation sites determines the discharge (firing) pattern of the motor unit and thus the activity of the MU. The number of MUs per muscle in humans may range from about 10–20 in the eye muscles, 100 for a small hand muscle, 200–300 in the Biceps Brachii, to 1000 (or more) for large limb and back muscles. It has also been shown that different MUs vary greatly in force generating capacity, with a 100-fold (or more) difference in twitch force (3). Recruitment order was firstly investigated by Henneman et al. and is well-known as size principle (4). Size principle implies that in a progressive isometric muscle contraction there is a specific sequence of recruitment in order of increasing motoneuron and motor unit (MU) size.
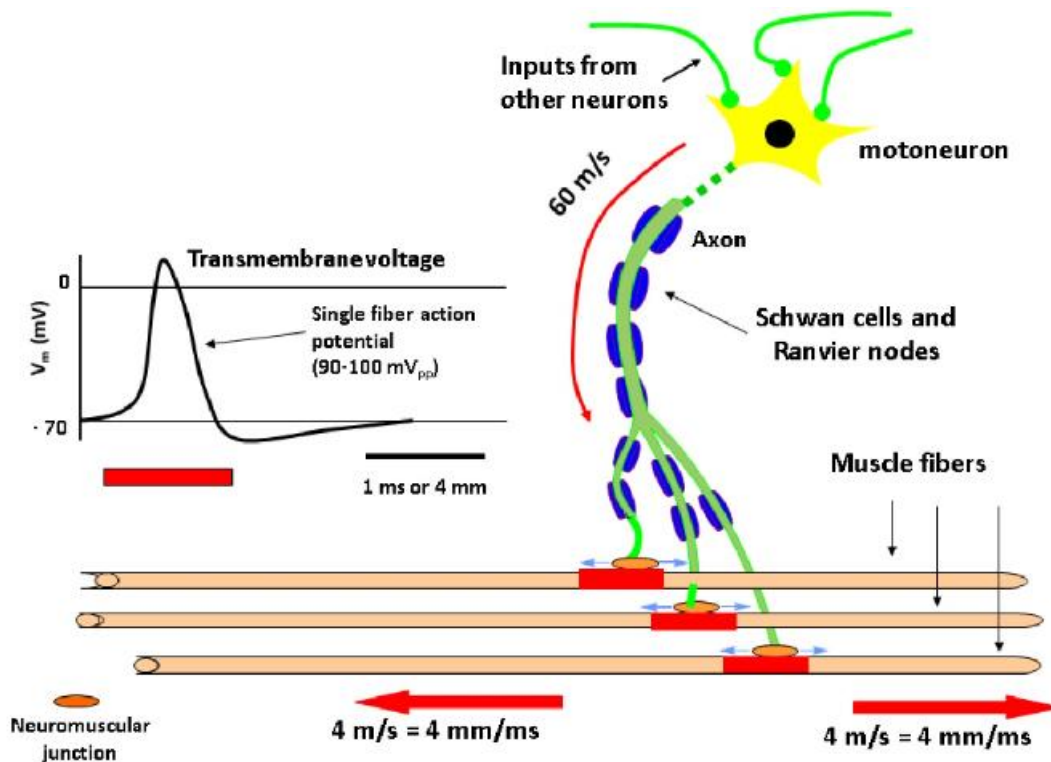
Figure 1.5: Muscle fibers that are innervated by a motoneuron form a motor unit. Action potentials propagate from the neuromuscular junction towards tendons (end of fibers) with approximately 4m/s. Three fibers are shown while a motor unit consists of 50-1000 fibers of the same type (I or II) (courtesy of Prof. Roberto Merletti).

The surface EMG at the detection point is the summation of the contributions

of the individual motor units. Figure 1.6 shows surface EMG generation during a voluntary contraction. The contributions of the individual motor unit action potentials (MUAPs) are added asynchronously and generate a random signal (EMG). EMG signal can be detected intramuscularly, inside the muscle, by needle electrodes or from the skin above the muscle (sEMG) by surface electrode arrays. Both signals contain (in different degrees) information concerning the motor control drive (from the spinal cord and the brain) and the motor performance (muscle structure, anatomy and physiology, fatigue, fiber constituency, etc).
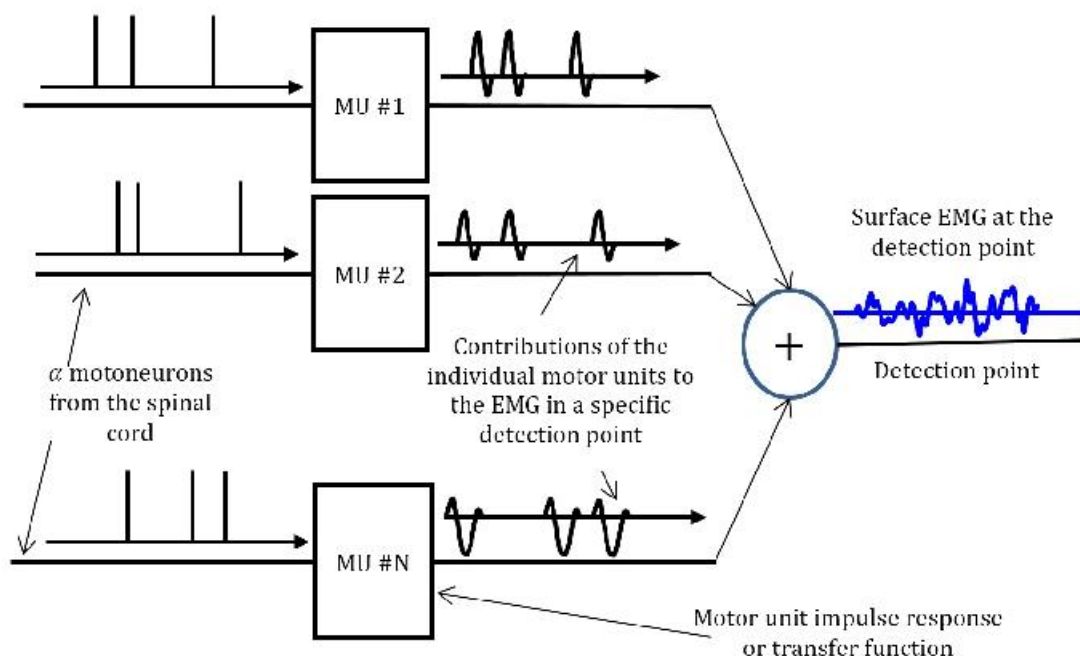
Figure 1.6: Surface EMG generation during a voluntary contraction (The contributions of the individual motor units (MUAPs) are added asynchronously and generate a random signal. Courtesy of Prof. Roberto Merletti).

1.1.4   Information contained in the EMG

Anatomical information such as innervation zone location (5, 6, 7, 8), shift of innervation zone (9), force (2, 10, 11), fatigue (12, 13, 14, 15), and distribution of muscle activity over the skin can be investigated through recording EMG and analyzing it. Anatomical comparison of the innervation zone location between men and women (Biceps Brachii muscle) and its correlation with anthropometric measurements were investigated by

DeFreitas and Costa et al. (7). The effect of innervation zone on sEMG signals (6)
and its position have also been investigated (16). As an indication of the initiation
of muscle activity, the sEMG can provide the timing sequence of one or more muscles
performing a task, such as during gait or in the maintenance of erect posture.

Understanding the relation between surface EMG to the force produced by a muscle
reveals the force information hidden in the sEMG. The amplitude of the sEMG signal
is qualitatively related to the amount of torque (or force) measured about a joint. The
EMG signal is the result of many physiological, anatomical and technical factors. The
effect of some of these factors may be investigated by proper detection methods but
others are not easily unscrambled with current technology, and their potential effect
on the signal may only be surmised (17). The mentioned studies that are just some
from many, show that EMG contain different kind of information that researchers try
to analyze to understand motor control.

1.1.5 Mechanisms of force generation

Muscle force results from the interaction of the globular heads of myosin-II with actin
filaments (18). Muscle contraction occurs as the result of relative sliding of two (thick
and thin) filament systems composed mainly of two proteins myosin and actin. The
energy for contraction is derived from the small organic molecule ATP (Adenosine
triphosphate). However, the mechanism of the coupling of ATP hydrolysis with force
production is still obscure[1].

In muscle, actin is the major component of thin filaments, which, together with the
motor protein myosin (which forms thick filaments), are arranged into actomyosin my-
ofibrils. These fibrils comprise the mechanism of muscle contraction. Using the hydrol-
ysis of ATP for energy, myosin heads undergo a cycle during which they attach to thin
filaments, exert a tension, and then, depending on the load, perform a power stroke
that causes the thin filaments to slide past, shortening the muscle . Muscle shortening
provides muscle force (see figure 1.7).

In voluntary contractions, force is modulated by a combination of MU recruitment and
changes in MU activation frequency (rate coding). The greater the number of MUs
recruited and their discharge frequency, the greater the force will be. During full MU

---

[1]www.biophys.phys.uri.edu/forceGeneration.html
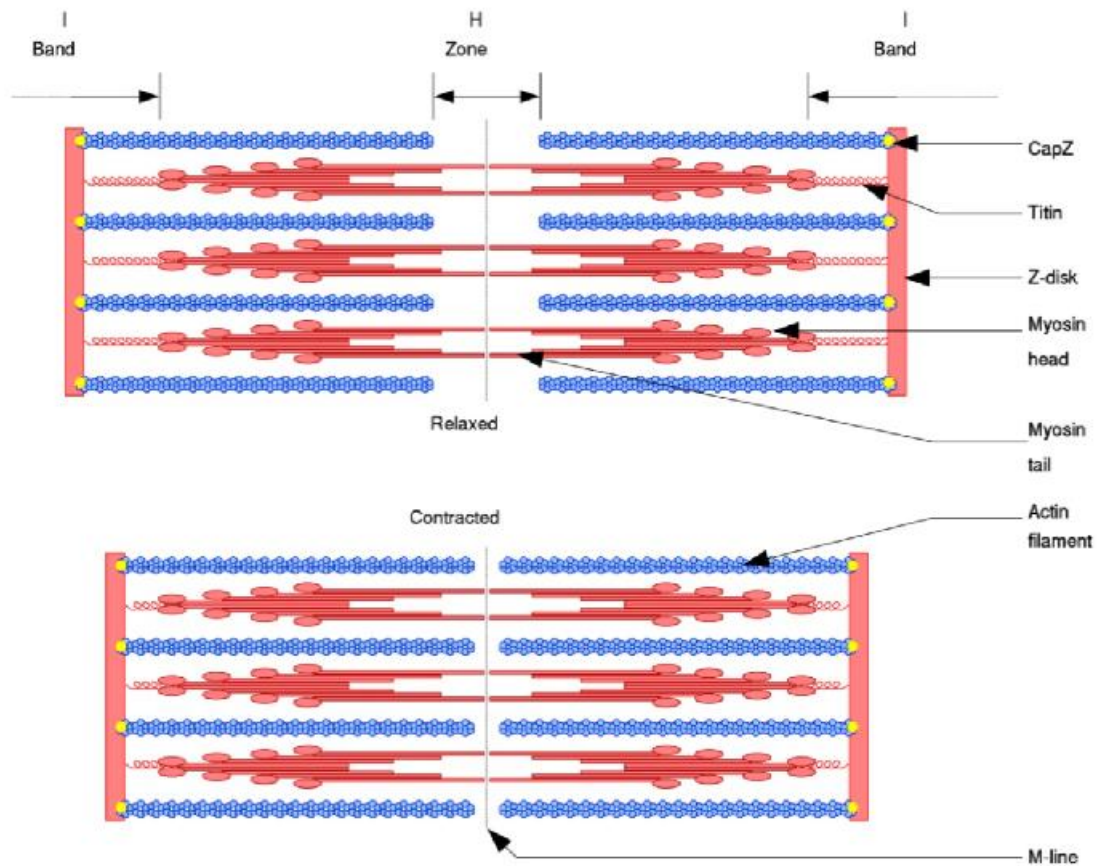
Figure 1.7: the structure of sarcomere, the basic morphological and functional unit of the skeletal muscles that contains actin . Actin and the motor protein myosin are arranged into actomyosin myofibrils. These fibrils comprise the mechanism of muscle contraction and force production.

recruitment the muscle force, when activated at any constant discharge frequency, is approximately 2 to 5kg/cm^2 and in general, this is relatively independent of species, gender, age, and training status (3).

Figure1.8 shows that twitches are added asynchronously in voluntary contraction and produce a relatively smooth torque with small physiological tremor with low discharge rate of the individual MUs. In an electrically elicited contraction (e.g. synchronous
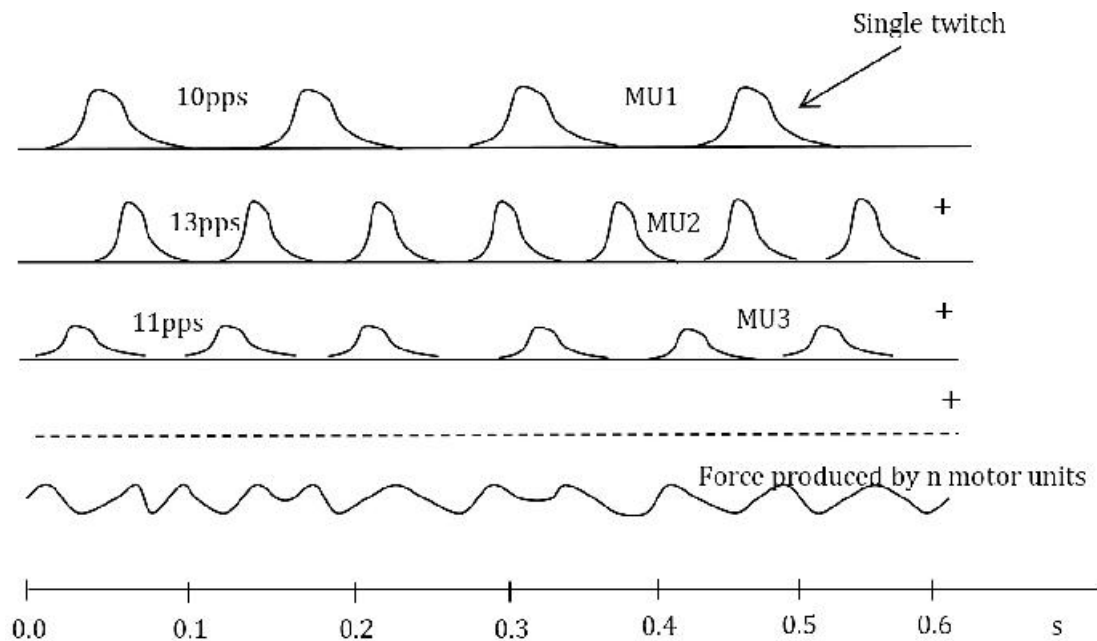
Figure 1.8: Twitches are added asynchronously in voluntary contraction and produce a relatively smooth torque with small physiological tremor with low discharge rate of the individual MUs and limited fatigue (courtesy of Prof. Roberto Merletti).

firing at 10 pps), the resulting force is a sequence of twitches with strong oscillations (see Figure1.8. Figure1.8 indicates that as long as the firing rate is slow (here < 10pps) and the twitches have enough time to return to the rest position before the next fire, the force oscillation is high.

To have a tetanic contraction higher stimulation frequencies (25-30pps) are needed (Figure1.10).
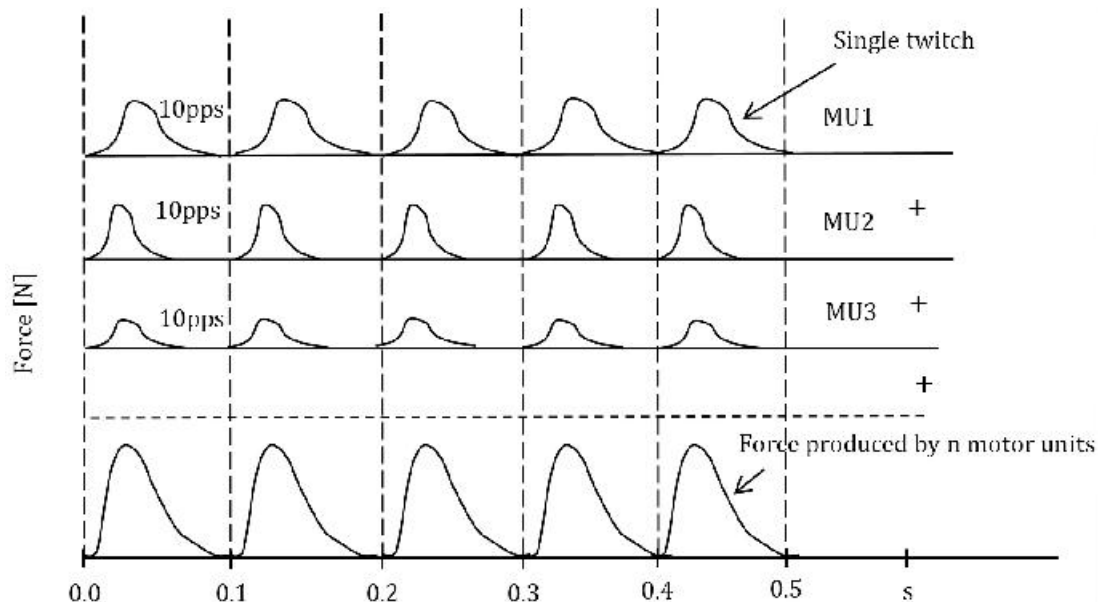
Figure 1.9: Twitches are added synchronously in electrically elicited contraction and produce a sequence of forces (courtesy of Prof. Roberto Merletti).
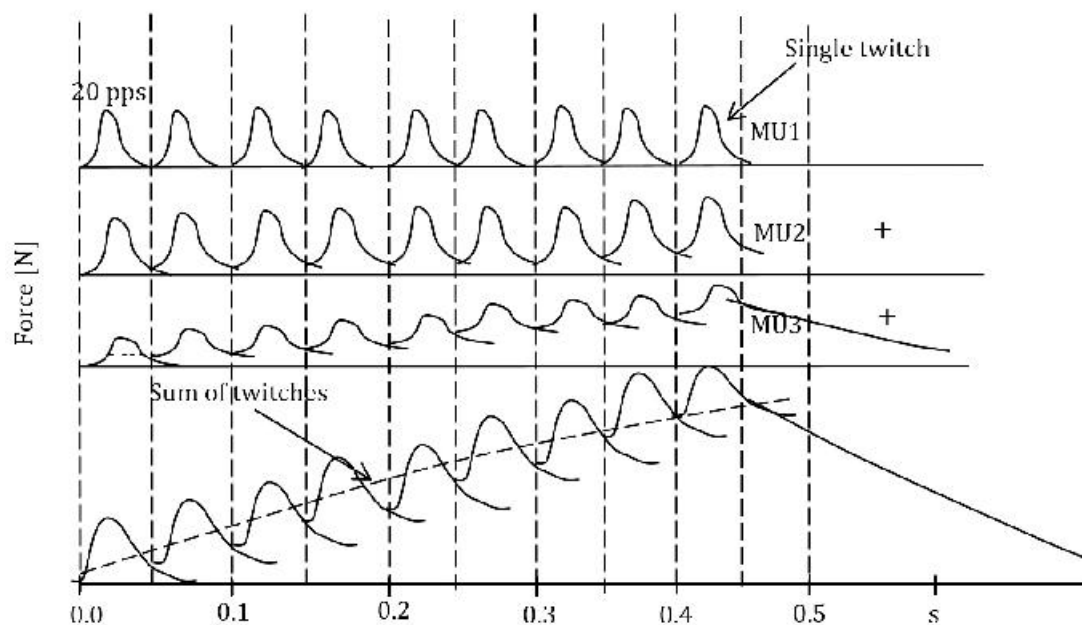
Figure 1.10: Twitches are added synchronously in electrically elicited contraction and produce a sequence of forces. The frequency of stimulation is 20pps (courtesy of Prof. Roberto Merletti).
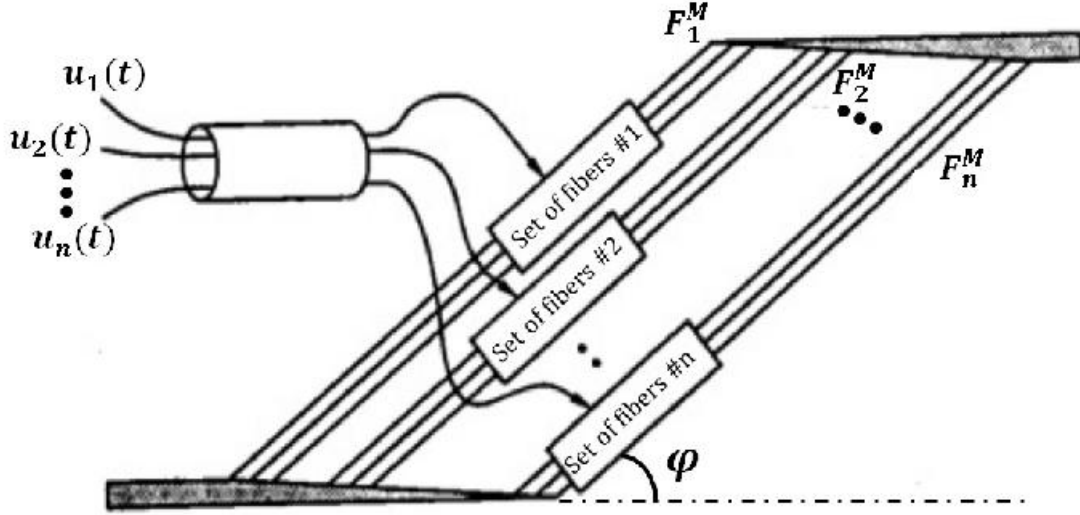
Figure 1.11: A muscle can be considered as a group of motor units controlled by central nervous system. $u_i(t)$ is the control signal of ith motor unit. Set of fibers of the ith motor unit provides force that is called F_i^M. The net force of the muscle is computed as $\sum_{i=1}^{n} F_i^M$ where n is the number of active motor units (2). "φ" is the pinnate angle. For fusiform muscles $\varphi = 0$.

1.2 EMG and muscle force relation and estimation models

Muscles can be considered to be a collection of equally long fibers in parallel. Fibers are innervated by nerve axons originating from the central nervous system. Each axon and its set of fibers organize a motor unit. The muscle fibers of each motor unit (see figure1.11) collectively develop a motor unit force (F_i^M), which is always assumed to sum with the other motor unit forces to produce the net muscle force (F^M).

Usually two steps for mapping EMG to force can be found in EMG-driven models used by researchers (1, 2, 19, 20, 21) as follows: Step1: neural excitation to muscle activation

Step2: muscle activation to muscle force These steps represent the muscle tissue dynamics. In the first step, a procedure that is called activation dynamics, map the input (neural excitation) to muscle activation "$a(t)$" and in the second, through the muscle contraction dynamics procedure the "$a(t)$" transforms into muscle force.

Sequence of motor unit discharges (control signal of motor units) is considered as neural
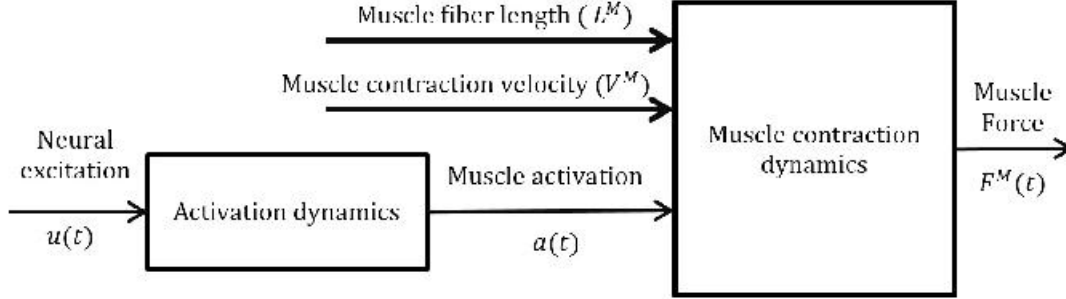
Figure 1.12: Transformation of neural excitation $u(t)$ to Muscle force (F^M) is done through activation dynamics and muscle contraction dynamics (see also figure1.11). The muscle force depends on muscle fiber length (L^M), contraction velocity (V^M) and muscle activation $a(t)$. In basic models (Hill model), Musculotendon actuator dynamics is second order (2), and can be divided into two first order processes (i.e. activation dynamics and muscle contraction dynamics).

excitation ($u(t)$). Association of activation dynamics and the muscle activation ($a(t)$) is done by rectification of raw EMG and low pass filtering of the rectified EMG. Raw EMG activity increases both as the firing rate of individual motor units rises and as inactive motor units become recruited. The envelope of EMG is considered as $a(t)$ in the literature (1, 2).

For the muscle contraction dynamics, Hill-type is usually the first choice model among the researchers. It is simple and sufficiently accurate for many applications (1). In the basic Hill model three elements are considered. A contractile element (CE) models the behavior of actin and myosin cross-bridges at the sarcomere level. This element is responsible for producing the active force. Two non-linear spring elements, one in series (SE) and another in parallel (PE) model the mechanical behavior of tendon and connective tissues respectively (see figure1.13). The PE represents the passive force (when it is stretched) of the connective tissues that surrounds the contractile element. The SE represents the intrinsic elasticity of the myofilaments.

Total force produced by the muscle (F^M) is computed by eq.(1.1)

$$F^M = F^{PE} + F^{SE}, F^{CE} = F^{SE} \tag{1.1}$$

The muscle length (L^M) and the lengths of contractile, series and parallel elements $(L^{CE}, L^{SE}, \text{ and } L^{PE})$ observe the eq.(1.2).

$$L^M = L^{PE}, L^M = L^{CE} + L^{SE} \tag{1.2}$$

During isometric contraction the SE is under tension and therefore is stretched by a small amount. Because the overall length of the muscle is kept approximately constant, the stretching of the series element can only occur if there is an equal shortening of the contractile element itself.
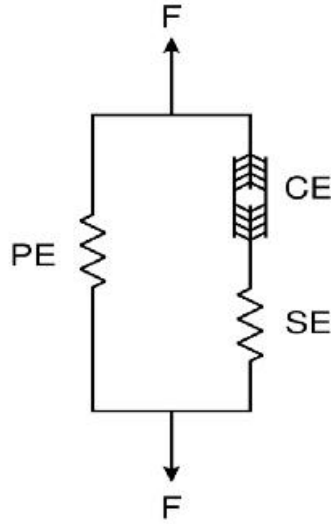
Figure 1.13: Hills elastic muscle model in fusiform muscles. F stands for force, CE is contractile element. SE and PE are series and parallel elements respectively. The PE is for the connective tissues and is responsible for the passive force when it is stretched. The SE represents the tendon.

The muscle-tendon is typically modeled as figure1.14. This model considers the pennation angle which is shown as φ in the figure.

Based on the muscle and tendon properties well documented in the literature (2), a generic muscle model should be scaled by or normalized with respect to some parameters to represent a specific muscle. These parameters for scaling are:

- Peak isometric active force (F_0^M)

- Optimal (in sense of producing maximum force) muscle fiber length (L_0^M)

- Optimal (in sense of producing maximum force) muscle fiber pennation angle (φ_0)
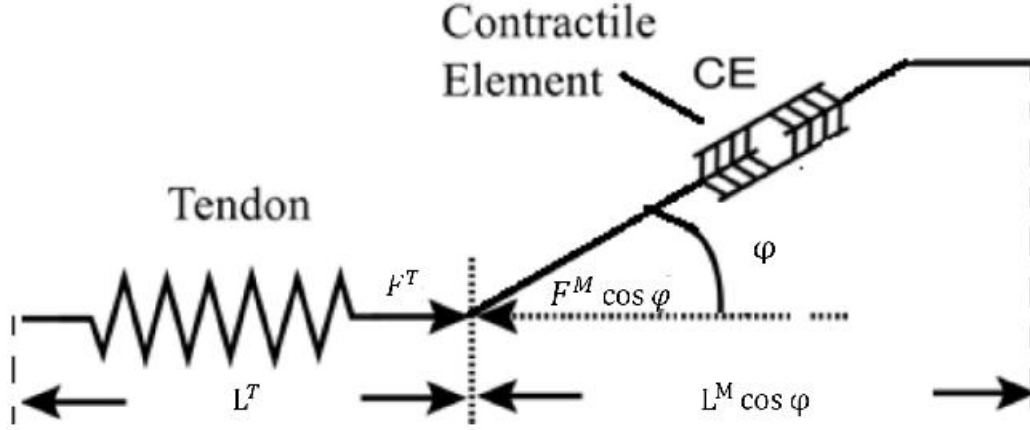
Figure 1.14: typical muscle tendon model (Musculotendon actuator). The force of tendon is F^T and the force contractile element (muscle) is F^M, L^t and L^M are the tendon and contractile lengths respectively. φ is the pennation angle. In fusiform muscles (e.g. Biceps Brachii) $\varphi = 0$.

where φ_0 is the fiber pennation when length of muscle $(L^M) = L_0^M$.

- Activation time (τ_{act}) that is time constant when muscle is fully excited $(u(t) = 1)$.

- Deactivation time (τ_{deact}) that is time constant when muscle is deactivated (No neural excitation, $u(t) = 0$).

- Maximum shortening velocity (V_M).

- Time scaling parameter (τ_c) that is defined as $(\frac{L_0^M}{V_m}$ $(\tau_c = \frac{L_0^M}{V_m})$).

Two important curves that represent the properties of muscle tissue are force-length and force-velocity curves (Figure1.15).

Figure1.15 shows a dimensionless force-length (A) and force-velocity (B) relation of a muscle. The total muscle force is the summation of active and passive forces. Although there are fast and slow motor units, each might have its own force-velocity relation (for fast motor units the force velocity curvature is less with respect to slow motor units (2)), researchers assume identically shaped force-muscle curve for all types of muscles. The scaling parameters should also be applied to the tendon in order to have a general model. Tendon is assumed to be elastic in almost all models and two parameters (stress and strain) are defined to specify its mechanical behavior. Strain (ϵ^T) is defined by the ratio of the amount of tendon stretch $(L^T = L^T - L_s^T)$ to its resting length (L_s^T) where L_s^T is called tendon slack length. Stress of a tendon is defined as the ratio between
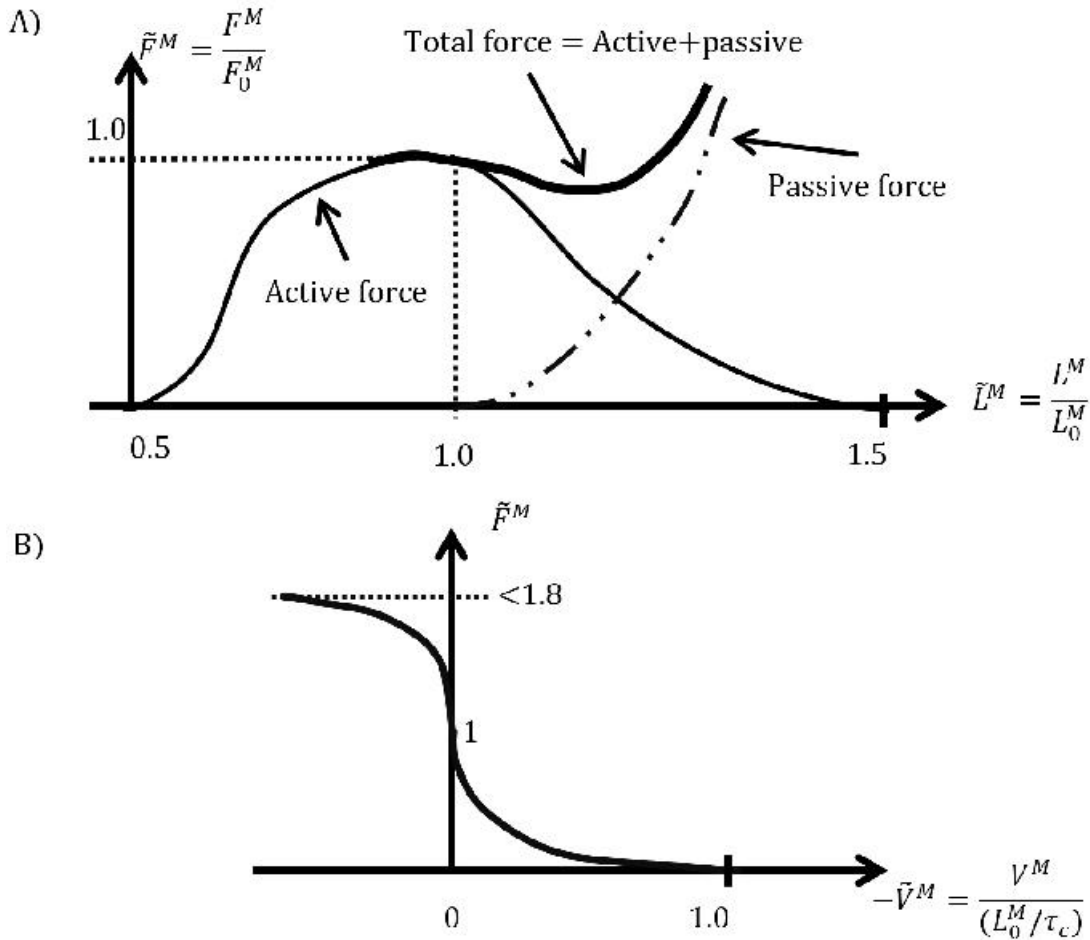
Figure 1.15: Muscle is fully extensible when inactive but capable of shortening when activated. The force-length curve of a general muscle is shown in A). The static properties of passive element (PE in figure1.13) and active element (CE in figure1.13) are given by dimensionless force-length curve. $\tilde{F}^M$ and $\tilde{L}^M$ are force (F^M) and fiber length (L^M) normalized to peak isometric force (F_0^M) and optimal fiber length (L_0^M) respectively. The active force (solid thin line) of contractile element comes from the force generated by the actin and myosin cross-bridges at the sarcomere level. The passive force (dashed line) is due to the tendon. B) force-velocity relation. $\tilde{V}^M$ is shortening velocity (V^M) normalized by the maximum shortening velocity.

the tendon force and the tendon cross sectional area (i.e. $\sigma^T = \frac{F^T}{A^T}$ [Pa]). Figure 1.16 shows a nominal (panel A) and a dimensionless (normalized to $\sigma_0^T = 32$MPa, see panel "B") stress-strain curve of tendon. The strain when tendon force equals peak isometric muscle force (F_0^M) is ϵ_0^T and its corresponding stress is σ_0^T. These two parameters are assumed to be Musculotendon-independent in the Hill model (2). Normalizing the
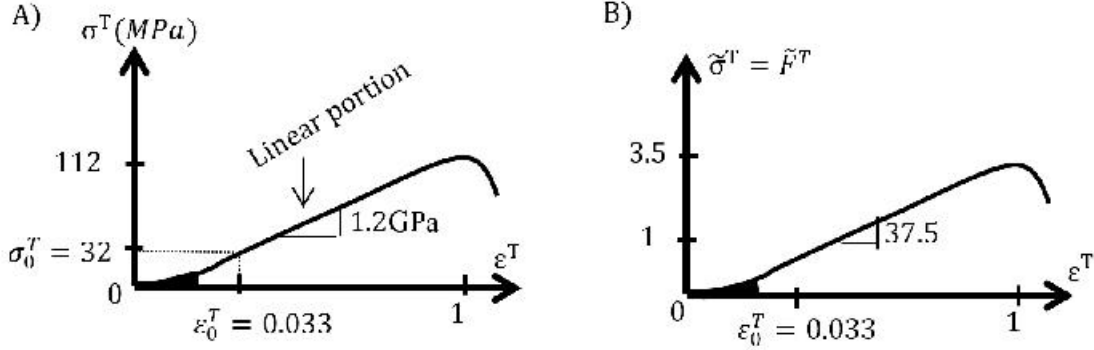
Figure 1.16: A) Nominal stress-strain curve and B) The general strain-stress curve of tendon (the normalized form of "A", the tendon stress is normalized by $\sigma_0^T = 32$MPa). Based on the assumption that the ratio of tendon cross sectional area to the muscle physiological cross sectional area is Musculotendon-independent, the strain when tendon force equals peak isometric muscle force (i.e. ϵ_0^T) and its corresponding value on stress axis (i.e. σ_0^T) is also Musculotendon-independent ($\epsilon_0^T = 0.033, \sigma_0^T = 32$MPa). As the normalized tendon stress ($\tilde{\sigma}^T$)=normalized tendon force ($\tilde{F}^T$), therefore the general strain stress curve (panel "B") is also called tendon force-strain curve (2).

stress axis in figure 1.16-A by the $\boldsymbol{\sigma_0^T}$ provides the general stress-strain plot (Figure 1.16-panel "B") that is also called the dimensionless force-strain curve (see eq. (1.3)).

$$\tilde{\sigma}^T = \frac{\sigma^T}{\sigma_o^T} = \frac{\left(\frac{F^T}{A^T}\right)}{\left(\frac{F_0^M}{A^T}\right)} = \frac{F^T}{F_0^M} = \tilde{F}^T \tag{1.3}$$

Based on the assumption that states the stress-strain property is tendon independent (i.e. the ratio of tendon cross sectional area to the muscle physiological cross sectional area is tendon independent, therefore, the strain when tendon force equals peak isometric muscle force (i.e. ϵ_0^T) and its corresponding value on stress axis (i.e. σ_0^T) are also Musculotendon-independent ($\epsilon_0^T = 0.033, \sigma_0^T = 32$MPa)- see figure 1.16) only one parameter will be specific to each tendon in Hill models. That parameter is the length

on elongation at which it just begins to develop force (i.e. L_s^T). Muscle activation dynamic (see eq. (1.5)) is first order in basic Hill model. Experimental records of EMG can be processed for comparison with muscle input and activation signals. The rectified EMG is compared with $u(t)$ and the low pass filtered form of the rectified EMG is considered as muscle activation $a(t)$ in the Hill type models. Equation (1.4) is the first order dynamics that is used to represent this EMG to activation process(2).

$$\frac{da(t)}{dt} + [\frac{1}{\tau_{act}}(\beta + [1-\beta]u(t))].a(t) = (\frac{1}{\tau_{act}})u(t) \tag{1.4}$$

where β is a constant ranging [0 , 1] and τ_{act} [1/s] is the activation constant (the inverse of time constant to reach the full excitation, i.e. $u(t) = 1$). The rate constant $[\frac{1}{\tau_{act}}(\beta + [1-\beta]u(t))]$ is linear in the amount of excitation $u(t)$, and increases when $u(t) > 0$, since $0 < \beta < 1$, therefore in fully excited muscle (i.e. when $u(t) = 1$), activation dynamics is assumed to be at its fastest rate constant ($\frac{1}{\tau_{act}}$[s]) and at its slowest rate ($\frac{\beta}{\tau_{act}}$[s]) when $u(t) = 0$. The $\frac{\beta}{\tau_{act}}$ is a time constant (relaxation constant) from fully activation to deactivation and is called τ_{deact}. Based on this definition $\beta = \frac{\tau_{act}}{\tau_{deact}}$. Since $0 < \beta < 1$, eq.(1.4) assumes that the time constant for full activation is less than for full relaxation from activation.

Some researchers(19, 22, 23, 24) modeled the activation dynamics as a critically damped linear second order differential system as eq.(1.5).

$$e_i(t) = \alpha_i EMG_i(t-d) - \beta_i e_i(t-1) - \gamma_i e_i(t-2) \tag{1.5}$$

The eq. (1.5) shows the EMG to muscle activation (activation dynamics shown in figure1.12) model for muscle "i", where $e_i(t)$ is the processed EMG related in a recursive manner to the EMG envelope from muscle "i", $EMG_i(t)$ is the normalized to the Maximum Voluntary Contraction (MVC) of sEMG envelope, d is the electromechanical delay (time delay for the muscle activation between the onset of EMG and force generation, typically is considered 40ms (19)), β_i and γ_i are the coefficients that define the second order dynamics. α_i is the gain (scale factor) that accounts for inter subjects differences in muscle parameters. α_i, β_i and γ_i are identified through optimization algorithms when the error function (usually the root mean square error between the measured and estimated force) is minimized.

A linear or non-linear monotonic relationship between the EMG amplitude of a specific muscle and its force is reported by De Luca (17). Increases in muscle force is associated

1. INTRODUCTION AND OBJECTIVES OF THE WORK

with an exponential increase in firing rate (10). To account for linear/non-linear relation between force and EMG, researchers (19, 20, 23, 25) utilized eq.(1.6) to provide muscle activation ($a(t)$) from $e_i(t)$ (see also eq.(1.5)).

$$a(t) = \frac{e^{Ae_i(t)} - 1}{e^A - 1} \qquad (1.6)$$

Where for muscle "i", A is the non-linear shape factor constrained to: $-3 < A < 0$. This shape factor (A) is found through optimization algorithms. As mentioned above (see figure1.15) Total muscle force is the sum of passive force (from passive element) and active force (from contractile element). The active force depends on muscle fiber length, contraction velocity, muscle activation, and pennation angle. A general form of force produced by a contractile element used by Lloyd et.al (19) is presented in eq.(1.7).

$$F_t^M = F^T F_0^M [f(l)f(v)a(t) + f_p(l)]cos(\varphi(t)) \qquad (1.7)$$

Where F_M^T is the muscle tendon unit force, F^T is the tendon force, F_0^M is the maximum isometric muscle force, $f(l)$ and $f(v)$ are muscle force-length and force-velocity relation respectively (see figure1.15 and figure1.16), $a(t)$ is the activation data, $f_p(l)$ is parallel passive elastic force-length, and $\varphi(t)$ is pennation angle. Pennation angle is changed with instantaneous muscle fiber length by assuming that the muscle belly had a constant thickness and volume. This model is a modified hill type. In classical hill model the $f_p(l)$ is neglected.

Although Hill-type models are often used by researcher, the validation of such models is not usually possible in humans since there is no human joint that is spanned by single muscle. However, any inference about muscle functional contribution to the force production should be based on muscle activity analysis, EMG recording of deep synergy muscles is difficult (e.g. Brachialis muscle that is contributing in elbow flexion force). Meanwhile, muscle force measurement in situ is still a highly invasive procedure.

Parameter selection (e.g. tendon slack length) is another critical point in using Hill-type models. These parameters frequently originate from cadavers studies (26) or from promising but sophisticated methods based on medical imaging (27, 28).

Another drawback of the Hill-type model is that it considers only macroscopic physiology. Hayashibe and Guiraud (2009) (24) considered a combination of phenomenological model and Huxley model that reflected more physiological and biophysical details.

Huxley model presents an explanation of the interaction cross-bridge in a sarcomere level. The distinctions between microscopic and macroscopic are not absolute. Thus a sarcomere model can be used to represent a whole muscle which is assumed to be a homogeneous assembly of identical sarcomeres. Although their results show a better estimation of force with respect to classical hill model, the integrated physiological and phenomenological model is complex to be applicable in clinical applications. Furthermore, this model is not validated and is questionable.

It is known that force production in a muscle is regulated by the recruitment of additional motor units (MUs), and the increase of firing rate of the already active MUs (3). These two mechanisms are present in different proportions in different muscles. Therefore, it is expected that muscle force may be estimated from surface EMG analysis for individual muscles. In some muscles, such as those controlling the fingers, the relationship between force and EMG amplitude was found to be linear (29) while in others the relation is non-linear and closer to a parabolic shape (30).

Problems using sEMG to estimate muscle force can occur in both isometric and dynamic situations. In dynamic situation force estimation will be more difficult and prone to have greater estimation error as some of muscle parameters change in a given dynamic task. Change of muscle parameters such as length, innervation zone position, contraction velocity, the rate and type of contraction, joint position, and muscle fatigue, can be considered as sources of the estimation error. However, some problems could be solved taking into account the following suggestions:

- Use of high density sEMG that can increase information obtained from a muscle, minimizing the estimation error between the measured and estimated force (31, 32).

- Formulation of mathematical models which do not rely on geometrical parameters. Note that bad parameters could cause large force prediction errors.

- Calibration of the model parameters for each subject using a model training phase before the estimation of the muscular exerted force can adapt the model to each subject's muscle characteristics.

- Maximization of the considered number of muscles which act on the same joint can minimize the estimation error.

1. INTRODUCTION AND OBJECTIVES OF THE WORK

To go one step forward, some researchers assumed linear relationship between sEMG and muscle. In an isometric fatigue contraction study, Soo et al. proposed a technique base on a limited frequency band of the EMG (15). Based on this hypothesis, Soo et al. attempted to estimate the hand-grip force using the high frequency-band of a sEMG signal (15). Using wavelet transformation and investigation through all possible combinations of frequency ranges, they reported that the frequency range between 242 and 365 Hz (combination of wavelet scale 2 and 3 respectively in their work) improves force estimation in Hand grips task (flexor digitorum superficialis (FDS) and extensor carpi radialis (ECR) muscles of the dominant forearm. The authors mentioned that the frequency range might be different for different muscles. Unfortunately, in this study the cross-talk issue has not been addressed which is important in load sharing problem of a hand grips task. Other drawbacks of this study are 1) considering just a linear relationship between force and sEMG RMS, 2) using just two detection electrodes placed over the belly of the forearm without addressing the innervation zone location, and 3) recording the sEMG and produced force of the given task with unfixed wrist that can affect significantly the reported results.

Rantalainen et al. investigated the effect of innervation zones in EMG based force estimation in isometric contraction of Biceps Brachii muscle (9). For each subject studied by Rantalainen et al., a third order polynomial was fitted to the subject force–EMG relationships (i.e. $Force = aEMG^3 + bEMG^2 + cEMG + d$, where $a, b, c,$ and d are polynomial coefficient). They used 64 electrodes (bi-dimensional, 8mm IED) for their study and they considered EMG as spatial average (global mean) of muscle activities defined as RMS of Monopolar signals, excluding channels over the innervation zone, and also global mean of the whole electrode grid (64 electrodes). The main finding of Rantalainen et al. study is that the force-EMG relationship (3rd order polynomial) is inconsistent (increase of sEMG amplitude accompanied with decrease in recorded force or vice versa) relatively often, at single bipolar channel level especially in case of channels overlaying the innervation zone, even under the highly controlled paradigm of isometric testing. Furthermore, use of multiple sEMG channels and applying segmentation techniques might improve the determination of force-EMG relationship. Consequently, it is argued that the disruption of the physiological single differential RMS map caused by the innervation zone affects the precision of the force-EMG relationship. The main drawback of this study is considering just a 3rd order polynomial relation

between the sEMG and produced force and only one muscle as the force producer in elbow flexion. Biceps Brachii is one muscles contributing in elbow flexion, other muscles such as Brachialis, and Brachioradialis muscles should be considered and were not. Also the possible co-activation of triceps brachii was not addressed.

A possible non-linear relationship between the EMG and force or torque (see also figure 1.1 on page 2) is presented as eq.(1.8) that is reported in the literature (33, 34).

$$F_m = x_m \times sEMG_m^{y_m} \tag{1.8}$$

Where F_m is the force contributed by muscle "m", $sEMG_m$ is the surface EMG amplitude of muscle "m". "x_m" and "y_m" are suitable coefficients to be identified. For "N" muscles that act on a joint the total force ($F_{tot.}$, measurable by load cells) is

$$F_{tot.} = \sum_{m \in muscles}^{N} F_m \tag{1.9}$$

, where "$muscles$" indicates the group of muscles contributing to produce the total force.

Minimization of the mean square error, between the measured and the total estimated force (with "N" muscles involved) provides an estimate of the model parameters "x_m" and "y_m" that in turn provides the force contributions of the individual muscles. The issue of muscle force estimation and approaches (Analytical-Graphical approach and Optimization techniques) for finding solutions of the equation 1.9 (i.e. x_m and y_m of the eq. 1.8) are explained and discussed in the third chapter of this thesis.

1.3 Objectives of the work

The following chapters of this thesis discuss the sEMG–Force model (let's call it exponential sEMG–force model) mentioned in eq.(1.8) In the following chapters I am going to discuss this sEMG–Force model in detail and answer the following questions:

1. since the sEMG in eq.(1.8) is an amplitude value, which value should be considered in the equation? Average rectified value (ARV)? Root mean square (RMS)? Which value is preferable? What parameters must be considered in recording multi-channel sEMG? What is the appropriate inter electrode distance to avoid

spatial aliasing?

When the sEMG amplitude value of each channel in high density sEMG recording (HDsEMG) is obtained and a map of muscle activity is available, what value is the representative value for the detection system? or what value can be considered as the muscle activity index? How should it be calculated? Is it the average of the amplitude of all channels? Should we consider only a portion of the detection system (active portion of muscle) and average over it? How can we detect the active portion automatically? Which method is preferable among the many segmentation/clustering methods?

These kind of questions is going to be answered in chapter 2.

2. In solving eq.(1.9), we know that $F_{tot.}$ is the total force that is known (is measured) and also the sEMG of each muscle is recorded and can be calculated (after answering question 1 and 2). For each muscle, there are two unknown parameters (x_m and y_m). The question is: How can this equation be solved? Is there unique solution for x_m and y_m? Is there only one x_m and y_m that can satisfy sEMG–Force (see eqs. (1.8 and(1.9)) relation? Answer of these questions and discussing about the solutions can be found in chapter 3.

Chapters 4 and 5 concern the sEMG applications. In chapter 4 a single case study of Yoga relaxation is discussed. The purpose of this chapter is only to show the feasibility of measurements. In the chapter 5, which is the last chapter of this thesis, the distribution of sEMG signal over the Trapezius and lumber muscles of musicians is obtained and the effect of posture on the muscle activity index of the musicians is presented and discussed.

References

[1] LUCIANO LUPORINI MENEGALDO AND LILIAM FERNANDES DE OLIVEIRA. **Effect of muscle model parameter scaling for isometric plantar flexion torque prediction.** *Journal of biomechanics*, **42**(15):2597–2601, 2009. 1, 13, 14

[2] F. E. ZAJAC. **Muscle and tendon: properties, models, scaling, and application to biomechanics and motor control.** *Critical reviews in biomedical engineering*, **17**(4):359–411, 1989. viii, ix, x, 6, 8, 13, 14, 15, 16, 18, 19

[3] R. MERLETTI AND P. A. PARKER. *ELECTROMYOGRAPHY Physiology, Engineering, and Noninvasive Applications.* IEEE PRESS, 2004. 6, 7, 11, 21

[4] ELWOOD HENNEMAN, GEORGE SOMJEN, AND DAVID O. CARPENTER. **FUNCTIONAL SIGNIFICANCE OF CELL SIZE IN SPINAL MOTONEURONS.** *Journal of Neurophysiology*, **28**(3):560–580, 1965. 7

[5] TRAVIS W. BECK, TERRY J. HOUSH, JOEL T. CRAMER, JEFFREY R. STOUT, ERIC D. RYAN, TRENT J. HERDA, PABLO B. COSTA, AND JASON M. DEFREITAS. **Electrode placement over the innervation zone affects the low-, not the high-frequency portion of the EMG frequency spectrum.** *Journal of Electromyography and Kinesiology*, **19**(4):660–666, 2009. 8

[6] T. W. BECK, T. J. HOUSH, J. T. CRAMER, AND J. P. WEIR. **The effects of electrode placement and innervation zone location on the electromyographic amplitude and mean power frequency versus isometric torque relationships for the vastus lateralis muscle.** *J Electromyogr Kinesiol*, **18**(2):317–328, 2008. 8, 9

[7] JASON M. DEFREITAS, PABLO B. COSTA, ERIC D. RYAN, TRENT J. HERDA, JOEL T. CRAMER, AND TRAVIS W. BECK. **Innervation zone location of the biceps brachii, a comparison between genders and correlation with anthropometric measurements.** *Journal of Electromyography and Kinesiology*, **20**(1):76–80, 2010. 8, 9

[8] MARCO BARBERO, ROBERTO MERLETTI, AND ALBERTO RAINOLDI. *Atlas of muscle innervation zones.* Springer, New York, 2012. 8

[9] TIMO RANTALAINEN, ADAM KODOWSKI, AND HARRI PIITULAINEN. **Effect of innervation zones in estimating biceps brachii forceEMG relationship during isometric contraction.** *Journal of Electromyography and Kinesiology*, **22**(1):80–87, 2012. 8, 22

[10] A. J. FUGLEVAND, V. G. MACEFIELD, AND B. BIGLAND-RITCHIE. **Force-frequency and fatigue properties of motor units in muscles that control digits of the human hand.** *J Neurophysiol*, **81**(4):1718–1729, 1999. 8, 20

[11] D. STAUDENMANN, A. DAFFERTSHOFER, I. KINGMA, D. F. STEGEMAN, AND J. H. VAN DIEEN. **Independent Component Analysis of High-Density Electromyography in Muscle Force Estimation.** *Biomedical Engineering, IEEE Transactions on*, **54**(4):751–754, 2007. 8

[12] ROBERTO MERLETTI AND LOREDANA R. LO CONTE. **Surface EMG signal processing during isometric contractions.** *Journal of Electromyography and Kinesiology*, **7**(4):241–250, 1997. 8

[13] G. T. ALLISON AND T. FUJIWARA. **The relationship between EMG median frequency and low frequency band amplitude changes at different levels of muscle capacity.** *Clinical biomechanics (Bristol, Avon)*, **17**(6):464–469, 2002. 8

[14] R. MERLETTI, A. RAINOLDI, AND D. FARINA. *Myoelectric Manifestations of Muscle Fatigue*, pages 233–258. John Wiley & Sons, Inc., 2005. 8

[15] YEWGUAN SOO, MASAO SUGI, HIROSHI YOKOI, TAMIO ARAI, MASATAKA NISHINO, RYU KATO, TATSUHIRO NAKAMURA, AND JUN OTA. **Estimation of handgrip force using frequency-band technique during fatiguing muscle contraction.** *Journal of Electromyography and Kinesiology*, **20**(5):888–895, 2010. 8, 22

[16] TADASHI MASUDA, HISAO MIYANO, AND TSUGUTAKE SADOYAMA. **The Position of Innervation Zones in the Biceps Brachii Investigated by Surface Electromyography.** *Biomedical Engineering, IEEE Transactions on*, **BME-32**(1):36–42, 1985. 9

[17] CARLO DE LUCA. **THE USE OF SURFACE ELECTROMYOGRAPHY IN BIOMECHANICS.** *Journal of Applied Biomechanics*, **13**(2):135–163, 1997. 9, 19

[18] M. A. FERENCZI, S. Y. BERSHITSKY, N. KOUBASSOVA, V. SIITHTHANANDAN, W. I. HELSBY, P. PANINE, M. ROESSLE, T. NARAYANAN, AND A. K. TSATURYAN. **The "roll and lock" mechanism of force generation in muscle.** *Structure*, **13**(1):131–141, 2005. 9

[19] DAVID G. LLOYD AND THOR F. BESIER. **An EMG-driven musculoskeletal model to estimate muscle forces and knee joint moments in vivo.** *Journal of biomechanics*, **36**(6):765–776, 2003. 13, 19, 20

[20] MITSUHIRO HAYASHIBE, DAVID GUIRAUD, AND PHILIPPE POIGNET. **EMG-to-force estimation with full-scale physiology based muscle model**, 2009. 13, 20

[21] M. SARTORI, M. REGGIANI, D. FARINA, AND D. G. LLOYD. **EMG-driven forward-dynamic estimation of muscle force and joint moment about multiple degrees of freedom in the human lower extremity.** *PLoS One*, **7**(12):e52618, 2012. 13

[22] D. G. THELEN, A. B. SCHULTZ, S. D. FASSOIS, AND J. A. ASHTON-MILLER. **Identification of dynamic myoelectric signal-to-force models during isometric lumbar muscle contractions.** *J Biomech*, **27**(7):907–919, 1994. 19

REFERENCES

[23] K. Manal, R. V. Gonzalez, D. G. Lloyd, and T. S. Buchanan. **A real-time EMG-driven virtual arm**. *Comput Biol Med*, **32**(1):25–36, 2002. 19, 20

[24] M. Hayashibe, D. Guiraud, and P. Poignet. **EMG-based neuromuscular modeling with full physiological dynamics and its comparison with modified hill model**. In *Engineering in Medicine and Biology Society, 2009. EMBC 2009. Annual International Conference of the IEEE*, pages 6530–6533. 19, 20

[25] J. Potvin, R. Norman, and S. McGill. **Mechanically corrected EMG for the continuous estimation of erector spinae muscle loading during repetitive lifting**. *European Journal of Applied Physiology and Occupational Physiology*, **74**(1):119–132, 1996. 20

[26] R. A. Brand, R. D. Crowninshield, C. E. Wittstock, D. R. Pedersen, C. R. Clark, and F. M. van Krieken. **A model of lower extremity muscular anatomy**. *Journal of Biomechanical Engineering*, **104**(4):304–310, 1982. 20

[27] Allison S. Arnold, Silvia Salinas, Deanna J. Asakawa, and Scott L. Delp. **Accuracy of muscle moment arms estimated from MRI-based musculoskeletal models of the lower extremity**. *Computer Aided Surgery*, **5**(2):108–119, 2000. 20

[28] S. L. Delp, F. C. Anderson, A. S. Arnold, P. Loan, A. Habib, C. T. John, E. Guendelman, and D. G. Thelen. **OpenSim: open-source software to create and analyze dynamic simulations of movement**. *IEEE transactions on bio-medical engineering*, **54**(11):1940–1950, 2007. 20

[29] Brenda Bigland and O. C. J. Lippold. **The relation between force, velocity and integrated electrical activity in human muscles**. *The Journal of Physiology*, **123**(1):214–224, 1954. 21

[30] J. H. Lawrence and C. J. De Luca. **Myoelectric signal versus force relationship in different human muscles**. *Journal of Applied Physiology*, **54**(6), 1983. 21

[31] Didier Staudenmann, Idsart Kingma, Dick F. Stegeman, and Jaap H. van Dien. **Towards optimal multi-channel EMG electrode configurations in muscle force estimation: a high density EMG study**. *Journal of Electromyography and Kinesiology*, **15**(1):1–11, 2005. 21

[32] Dider Staudenmann, Karin Roeleveld, Dick F. Stegeman, and Jaap H. Van Dieen. **Methodological aspects of SEMG recordings for force estimation-A tutorial and review**. *Journal of Electromyography and Kinesiology*, **20**:375–387, 2010. 21

[33] Roberto Merletti and Matteo Aventaggiato. **Emg-Force Relationship: Preliminary Data On Load Sharing**. In *XVIII Congress of the International Society of Electrophysiology and Kinesiology*. 23

[34] A. Botter, H. R. Marateb, B. Afsharipour, and R. Merletti. **Solving EMG-force relationship using Particle Swarm Optimization**. *Conf Proc IEEE Eng Med Biol Soc*, **2011**:3861–3864, 2011. 23

2

EMG amplitude indicators in space and time

2.1 Introduction

This chapter covers the issue of surface electromyography (sEMG) sampling in time (1D) and in space (EMG imaging-2D) from a sinusoid towards more complex signals (simulated motor unit detected by a high resolution detection grid). The preferable sEMG amplitude indicator is discussed by comparing average rectified value (ARV) and root mean square (RMS). These amplitude indicators (ARV and RMS) for continuous and sampled signals in time and space are discussed. Spatial aliasing that comes from sampling the distribution of surface muscle activities below the Nyquist rate in space, is related to the inter electrode distance. Spatial aliasing issue leads us to select the proper inter electrode distance in sEMG-Force studies. This issue is studied in this chapter for a simulated fiber and a motor unit. When we apply a high density sEMG (HDsEMG)detection system (i.e. matrix of electrodes), we will have a map of activity from the recorded sEMG channels. The RMS or ARV of each channel is considered as the map of intensity distribution. Extracting active region of the map (portion of the map with higher intensity values) in an automatic way is covered in the final section of this chapter. Three segmentation approaches (watershed, h-dome, and K-means) were compared and the preferable method was chosen based on a higher rate of correct segmentation of sEMG simulated images.

2.2 EMG in time and in space (EMG imaging)

Since human skeletal muscles show a high diversity and heterogeneity in their fiber architecture, it is not always possible to properly align electrodes to the muscle fiber direction. In the previous chapter (chapter 1), it is discussed that EMG signals constitute a summation of the motor units action potentials, occurring within the detection volume of the electrode system. Since each of the motor unit action potentials is biphasic or triphasic and since they are not synchronized, constructive and destructive superimposition occur, leading to variance in the EMG amplitude that does not represent variance of muscle activation (1) if such variance is defined as the sum of variances of the single MUAPs. Theoretically this problem can be avoided by recording from each motor unit separately. Although this is practically unfeasible, it suggests that the use of multiple, spatially distributed EMG channels, collecting independent information from separate sources, will improve the estimation of muscle force.

Actually, an image showing the distribution of muscle activity over the skin provides more information from the muscle of interest (under the skin) in comparison with information provided by a bipolar electrode. A two dimensional electrode grid including N×M electrodes (equally spaced in "x" and "y" direction), amplifiers and recording tools, make the EMG imaging applicable. High-density sEMG (HDsEMG) grids collect many monopolar EMG signals over a relatively small collection surface of the skin. By HDsEMG recording, each electrode may be conceived as a pixel p with coordinates (x , y) given by the rows and columns in the grid. Muscle activity can be considered as a movie whose frames are generated by the instantaneous amplitude of the individual channels.

In Muscle force estimation, usually the amplitude of sEMG signals is used. The questions are: what amplitude indicator should be considered? Instantaneous amplitude? Average rectified value (ARV)? Root mean square value (RMS)? In case of HDsEMG recording, since we are facing with a spatial distribution, how should the indicator be defined? Should it be as the global spatial mean of the selected amplitude indicator? Should it be the peak?

Through the next sections, two indicators (ARV and RMS) are explained and compared to each other for selecting one as the sEMG amplitude indicator for force estimation applications.

2.3 Study of sEMG amplitude estimation in the continuous and discrete domains

EMG amplitude estimation can be described mathematically as the task of best estimating the standard deviation of a colored random process in additive noise (figure2.1). This estimation problem has been studied for several years. Inman et al. are credited with the first continuous EMG amplitude estimator. They implemented a full wave rectifier followed by a resistor-capacitor low-pass filter (2, 3).

Subsequent early investigators studied the type of nonlinear detector that should be
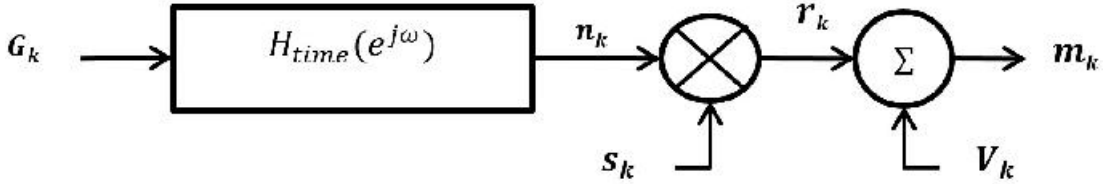
Figure 2.1: Simulation of EMG signals by filtering white Gaussian noise. The output signal is obtained by filtering white Gaussian noise (G_k) with the inverse Fourier transform of the square root of the shaping filter $H_{time}(f)$ and then multiplying it by the EMG amplitude s_k and mixed with additive noise to form the surface EMG waveform (m_k). Shaping filter of power spectrum can be defined by Shwedyks expression ($H_{time}(f) = \frac{K f_h^4 f^2}{(f^2 + f_l^2)(f^2 + f_h^2)^2}$) where f is frequency, f_l and f_h are two frequencies that define the shaping filter (3, 4).

applied to the waveform. This work was primarily empirical, and led to the routine use of analog rectification and low-pass filtering to estimate amplitude. Most modern systems are digital, and use mean absolute value (MAV), also called average rectified value (ARV), and root-mean-square (RMS) indicators.

The aim of this section is to select between ARV and RMS the one which is more appropriate as an EMG amplitude indicator in time or space. In this manner, study of ARV and RMS is carried out from the simplest cases (one dimensional (1D) single sinusoidal signal) toward more complicated signals (1D sum of sinusoids), 2D sinusoids, and simulated action potential (AP) signals in space (1D and 2D).

2.4 Average Rectified Value of a single sinusoid (ARV)

2.4.1 Continuous case

Considering $x(t) = A\sin(2\pi\frac{t}{T} + \varphi)$, $f_0 = \frac{1}{T}$ where $t \in (-\infty, +\infty)$, A is amplitude, T is the period, f_0 is the frequency of signal and φ is the phase.

$$0 \leq \frac{2\pi t}{T} + \varphi < 2\pi$$

$$ARV = \frac{1}{T} \int_{-\frac{\varphi T}{2\pi}}^{T-\frac{\varphi T}{2\pi}} \left| A\sin\left(\frac{2\pi t}{T} + \varphi\right) \right| \, dt \tag{2.1}$$

$$\Rightarrow ARV = \frac{1}{\frac{T}{2}} \int_{-\frac{\varphi T}{2\pi}}^{\frac{T}{2}-\frac{\varphi T}{2\pi}} A\sin\left(\frac{2\pi t}{T} + \varphi\right) \, dt$$

$$\Rightarrow ARV = \frac{2}{T} A \frac{1}{\frac{2\pi}{T}} \left(\cos\left(\frac{2\pi}{T}\left(-\frac{\varphi T}{2\pi}\right) + \varphi\right) - \cos\left(\frac{2\pi}{T}\left(\frac{T}{2} - \frac{\varphi T}{2\pi}\right) + \varphi\right) \right)$$

$$\Rightarrow ARV = \frac{1}{\pi} A \left(\cos(-\varphi + \varphi) - \cos(\pi - \varphi + \varphi) \right) \Rightarrow ARV = \frac{A}{\pi} \left(\cos(0) - \cos(\pi) \right)$$

$$\Rightarrow ARV = \frac{2A}{\pi} \tag{2.2}$$

$$x(t) = A sin(2\pi f_0 t + \varphi)$$
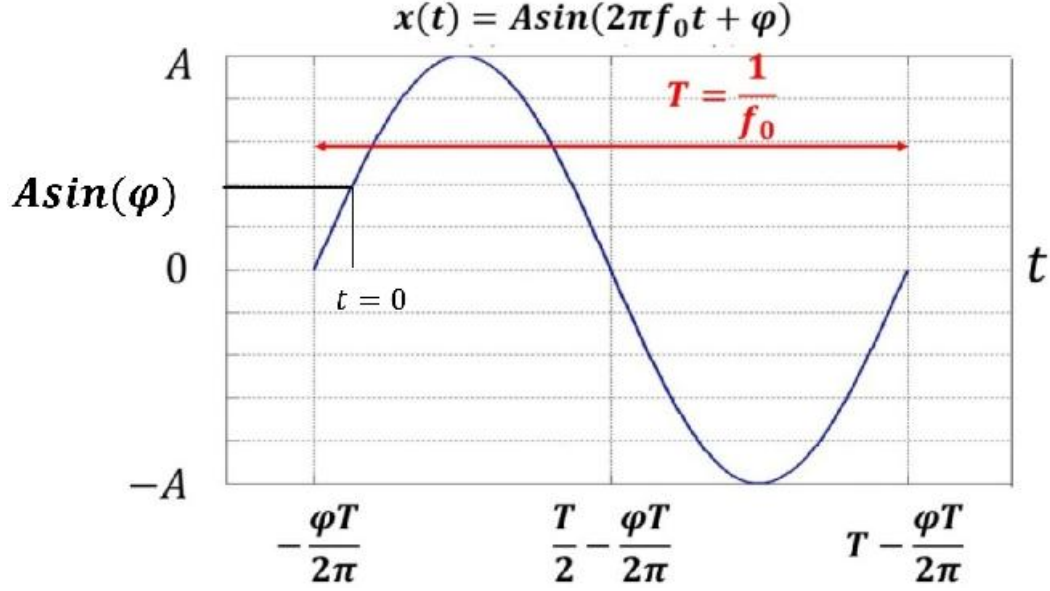
Figure 2.2: One cycle of a single sinusoid with frequency "f_0" with arbitrary amplitude "A" and phase "φ"

2.4.2 Discrete case

In order to discretize the continuous function defined as $x(t) = A\sin(2\pi f_0 t)$, where $t \in (-\infty, +\infty)$, A is amplitude, f_0 is the frequency of signal, the sampling frequency (inverse of time interval between samples $\Delta t = \frac{T}{N}$) is $F_{samp.} = \frac{1}{\Delta t} = \frac{N}{T}$, where T [s] is one period of signal, N is the number of samples per cycle. n is the sample index ranging from 0 to $N - 1$. $n = 0, 1, 2, ..., N - 1$

For one period:

$$ARV = \frac{2}{T} \int\limits_{0}^{\frac{T}{2}} A\sin(2\pi f_0 t)\mathrm{d}t, \quad f_0 = \frac{1}{T} \tag{2.3}$$

By discretizing the eq.(2.3) we will have:

$$ARV = \frac{1}{N} \sum_{n=0}^{\frac{N}{2}-1} A\sin(\frac{2\pi n}{N}) \tag{2.4}$$

2. EMG AMPLITUDE INDICATORS IN SPACE AND TIME

We know that[1]:

$$\sum_{n=0}^{N} \sin(nx) = \frac{\sin(\frac{Nx}{2})\sin\left(\frac{(N+1)x}{2}\right)}{\sin(\frac{x}{2})} \tag{2.5}$$

by changing variable $\frac{2\pi n}{N}$ in eq.(2.4) and applying eq.(2.5) we can have:

$$\sum_{n=0}^{\frac{N}{2}-1} \sin\left(\frac{2\pi n}{N}\right) = \frac{\sin\left(\frac{\left(\frac{N}{2}-1\right)\left(\frac{2\pi}{N}\right)}{2}\right)\sin\left(\frac{\left(\frac{N}{2}\right)\left(\frac{2\pi}{N}\right)}{2}\right)}{\sin\left(\frac{\left(\frac{2\pi}{N}\right)}{2}\right)} \tag{2.6}$$

Applying the trigonometric properties $(\sin(\frac{\pi}{2} - \theta) = \cos(\theta)$ and $\sin(\frac{\pi}{2}) = 1)$ to eq.(2.6) and simplifying it, we can have:

$$\sum_{n=0}^{\frac{N}{2}-1} \sin\left(\frac{2\pi n}{N}\right) = \frac{\cos\left(\frac{\pi}{N}\right)}{\sin\left(\frac{\pi}{N}\right)} \tag{2.7}$$

$$\Rightarrow ARV = \frac{2A}{N} \sum_{n=0}^{\frac{N}{2}-1} \sin\left(\frac{2\pi n}{N}\right) = \frac{2A}{N}\left(\frac{\cos\left(\frac{\pi}{N}\right)}{\sin\left(\frac{\pi}{N}\right)}\right)$$

Now, we are going to find the ARV when $N \to \infty$

$$\lim_{N \to \infty} ARV = \lim_{N \to \infty}\left(\frac{2A}{N}\left(\frac{\cos\left(\frac{\pi}{N}\right)}{\sin\left(\frac{\pi}{N}\right)}\right)\right) = \frac{2A}{\lim\limits_{N \to \infty}\left(N\frac{\sin\left(\frac{\pi}{N}\right)}{\cos\left(\frac{\pi}{N}\right)}\right)} \tag{2.8}$$

with defining $\alpha = \frac{2\pi}{N}$ as the sampling interval in radiant:

$$\lim_{N \to \infty} ARV = \lim_{\alpha \to 0}\left(\frac{2A}{N}\left(\frac{\cos\left(\frac{\alpha}{2}\right)}{\sin\left(\frac{\alpha}{2}\right)}\right)\right) = \frac{2A}{\lim\limits_{\alpha \to 0} N\frac{\sin\left(\frac{\alpha}{2}\right)}{\cos\left(\frac{\alpha}{2}\right)}} = \frac{4A}{N\alpha} = \frac{2A}{\pi} \tag{2.9}$$

The denominator of eq. (2.8) i.e. $f(N) = \left(N\frac{\sin\left(\frac{\pi}{N}\right)}{\cos\left(\frac{\pi}{N}\right)}\right)$ is shown in figure 2.3 panel "A". It can be seen visually (figure 2.3 panel "B") that for $N \geq 25$, $ARV = \frac{2A}{\pi}$.

Although the denominator of ARV ($f(N)$) is monotonically decreasing when N increases, and since, $ARV = \frac{2}{f(N)}$ for a sinusoidal signal, a monotonically increase of ARV might be expected. It is necessary to attend that at low sampling frequencies, ARV depends on the relative phase of the sinusoid with the sampling train. The oscillatory behavior seen in panel "B" of figure 2.3 for sampling frequency < 25 Hz is

---

[1]http://www.wolframalpha.com

due to the phase of $x(t)$ (i.e. $\frac{\pi}{6}$). The highest oscillation (critical deviation from the expected value (i.e. $\frac{2}{\pi}$) for a sinusoidal signal is obtained when the relative phase of the sinusoid with the sampling train is $\frac{\pi}{6}$.

In the following we are going to consider conditions such that the number of samples
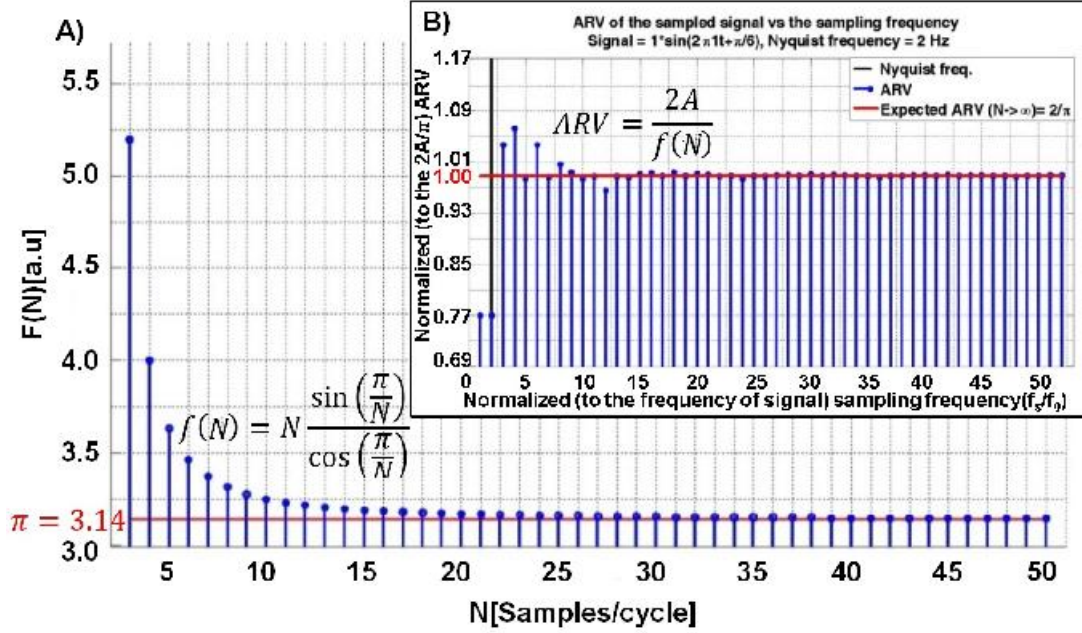
Figure 2.3: A) Plot of $f(N) = \left(N\frac{\sin(\frac{\pi}{N})}{\cos(\frac{\pi}{N})} \right)$ (the denominator of eq.(2.8)) versus N. If $N \to \infty => f(N) \to \pi$. B) Normalized (to the $\frac{2A}{\pi}$) ARV of $x(t) = \sin(2\pi t + \frac{\pi}{6})$ versus normalized (to the frequency of signal i.e. $f_0 = 1$) sampling frequency. Blue lines show the normalized ARV at specified normalized sampling frequency and the red line corresponds to the expected normalized ARV for $A = 1$. For $x(t) = A\sin(2\pi f_0 t)$ if $N \to \infty$ then $\lim_{N\to\infty} ARV = \frac{2}{\pi}$)

in a cycle is not an integer number. We want to study the general case in which N is not necessarily an integer but can be a rational number. In order to do that, we need to consider an integer number of periods K, such that KN is an integer.

K is the number of periods we take into account.

KN is the total number of samples in K periods and therefore, the time interval between samples will be $\Delta t = \frac{KT}{KN}$ and $F_{samp} = \frac{1}{\Delta t}$, n is the sample index $\in [0, KN-1]$ i.e. $n = 0, 1, \ldots, KN - 1$.

We sample our signal at times: $n\Delta t = \frac{nKT}{KN}$
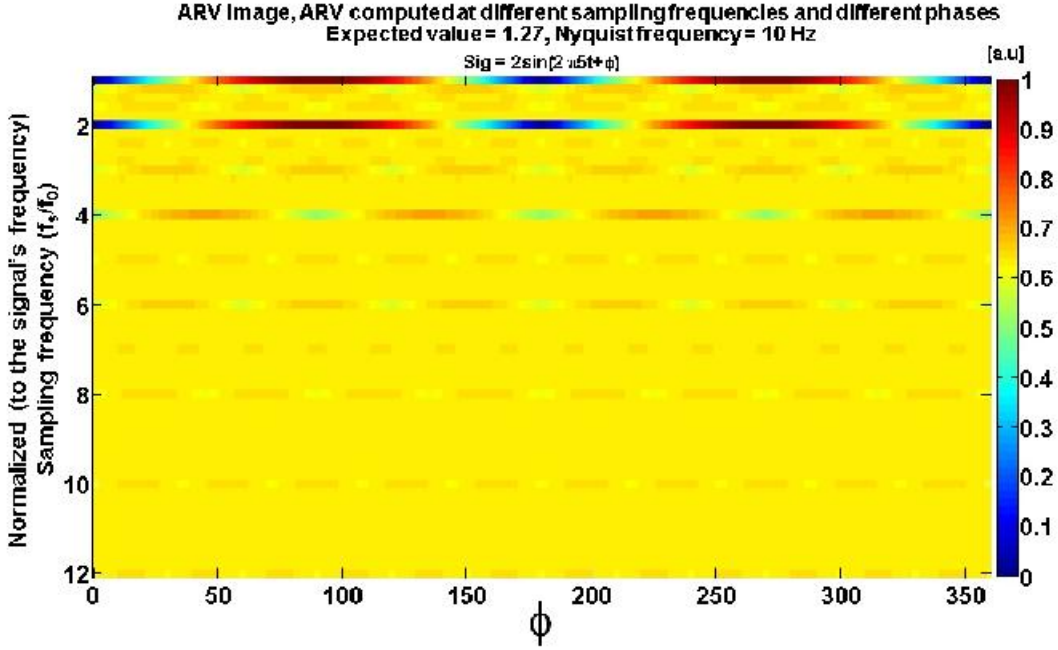
Figure 2.4: *ARV* image of $x(t) = \sin(2\pi 5t + \varphi)$ versus phase (φ in degree) and normalized (to the frequency of signal (f_0)) sampling frequency. The Nyquist frequency =10Hz and the expected *ARV* if the sampling frequency $\rightarrow \infty$ is $\frac{2}{\pi} = 0.64$

by definition of the *ARV* (see eq.(2.3)), for K periods the *ARV* in discrete domain of $x(t) = A\sin(2\pi f_0 t)$ is:

$$ARV = \frac{1}{KN}\left(\sum_{n=0}^{KN-1}\left|A\sin\left(\frac{2\pi n}{N}\right)\right|\right) \tag{2.10}$$

$$\Rightarrow ARV = \frac{1}{KN}\left[\sum_{n=0}^{\frac{KN}{2}-1}A\sin\left(\frac{2\pi n}{N}\right) + \sum_{n=\frac{KN}{2}}^{KN-1}\left(-A\sin\left(\frac{2\pi n}{N}\right)\right)\right] \tag{2.11}$$

by changing the parameter n to $n - \frac{KN}{2}$ in the second part of eq.(2.11) we have:

$$ARV = \frac{1}{KN}\left[\sum_{n=0}^{\frac{KN}{2}-1}A\sin\left(\frac{2\pi n}{N}\right) - \sum_{n=0}^{\frac{KN}{2}-1}\left(A\sin\left(\frac{2\pi}{N}\left(n - \frac{KN}{2}\right)\right)\right)\right] \tag{2.12}$$

knowing trigonometric properties:

$$
\sin\left(\frac{2\pi}{N}\left(n - \frac{KN}{2}\right)\right) = \sin\left(\frac{2\pi n}{N} - K\pi\right) = \begin{cases} \sin\left(\frac{2\pi n}{N}\right) & \text{if } K \text{ is even} \\ -\sin\left(\frac{2\pi n}{N}\right) & \text{if } K \text{ is odd} \end{cases}
$$

therefore, eq.(2.12)can be rewritten as:

for $K = 2L$, $L \in \mathbb{R}$ (i.e. $K = $ even)

$$
ARV = \frac{1}{KN}\left[\sum_{n=0}^{\frac{KN}{2}-1} A\sin\left(\frac{2\pi n}{N}\right) - \sum_{n=0}^{\frac{KN}{2}-1} A\sin\left(\frac{2\pi n}{N}\right)\right] = 0 \qquad (2.13)
$$

and for $K = 2L + 1$, $L \in \mathbb{R}$ (i.e. $K = $ odd)

$$
ARV = \frac{1}{KN}\left[\sum_{n=0}^{\frac{KN}{2}-1} A\sin\left(\frac{2\pi n}{N}\right) + \sum_{n=0}^{\frac{KN}{2}-1} A\sin\left(\frac{2\pi n}{N}\right)\right] = \frac{2K}{KN}\sum_{n=0}^{\frac{KN}{2}-1} A\sin\left(\frac{2\pi n}{N}\right)
$$
$$(2.14)$$

referring to eq.(2.5) i.e. $\left(\sum_{n=0}^{N}\sin(nx) = \frac{\sin\left(\frac{Nx}{2}\right)\sin\left(\frac{(N+1)x}{2}\right)}{\sin\left(\frac{x}{2}\right)}\right)$ and considering $x = \frac{2\pi}{N}$

then:

$$
\sum_{n=0}^{\frac{KN}{2}-1}\sin\left(\frac{2\pi n}{N}\right) = K\sum_{n=0}^{\frac{N}{2}-1}\sin\left(\frac{2\pi n}{N}\right) = K\frac{\sin\left(\left(\frac{N}{2}-1\right)\left(\frac{\pi}{N}\right)\right)\sin\left(\frac{\pi}{2}\right)}{\sin\left(\frac{\pi}{N}\right)} \qquad (2.15)
$$

Therefore, eq.(2.14) can be rewritten as:

$$
ARV = \frac{2A}{N}\left[\frac{\sin\left(\left(\frac{N}{2}-1\right)\left(\frac{\pi}{N}\right)\right)}{\sin\left(\frac{\pi}{N}\right)}\right] \qquad (2.16)
$$

As a conclusion, eq.(2.16) shows that in case of considering rational number of samples in a cycle, the ARV still depends on total number of samples that are taken into account in K periods. The ARV is equal to its expected value in 1D sinusoidal signals (i.e. $\frac{2A}{\pi}$) if a large number of samples ($N > 10$ samples/cycle provides less than 3.5% deviation from the expected value and for $N > 18$ the error$< 1\%$) are available.

2.5 Root Mean Square of a single sinusoid (RMS)

2.5.1 Continuous case

Considering $x(t) = A \sin(2\pi f_0 t + \varphi)$, where $t \in (-\infty, +\infty)$, A is amplitude, f_0 is the frequency of signal, φ is the phase (see figure 2.2) and $0 \leq 2\pi f_0 t + \varphi < 2\pi$ then:

$$RMS^2 = \frac{1}{T} \int_{-\frac{\varphi T}{2\pi}}^{T-\frac{\varphi T}{2\pi}} A^2 \sin^2\left(2\pi f_0 t + \varphi\right) dt \qquad (2.17)$$

$$f_0 = \frac{1}{T}$$

$$RMS^2 = \frac{1}{T} \int_{-\frac{\varphi T}{2\pi}}^{T-\frac{\varphi T}{2\pi}} A^2 \sin^2\left(\frac{2\pi t}{T} + \varphi\right) dt \qquad (2.18)$$

Referring to well-known trigonometric property $\sin^2 \alpha = \frac{1-\cos 2\alpha}{2}$ we can rewrite eq.(2.18) as follows:

$$\Rightarrow RMS^2 = \frac{1}{T} \int_{-\frac{\varphi T}{2\pi}}^{T-\frac{\varphi T}{2\pi}} A^2 dt - \frac{1}{T} \int_{-\frac{\varphi T}{2\pi}}^{T-\frac{\varphi T}{2\pi}} \frac{A^2}{2} \cos\left(\frac{4\pi t}{T} + 2\varphi\right) dt \qquad (2.19)$$

$$\Rightarrow RMS^2 = \frac{A^2}{2} - \frac{A^2}{2T}\frac{T}{4\pi}\left(\sin(4\pi) - \sin(0)\right) \qquad (2.20)$$

Considering the fact that:

$$\sin(4\pi) = \sin(0) = 0 \Rightarrow RMS^2 = \frac{A^2}{2}$$

therefore:

$$RMS = \frac{A}{\sqrt{2}} \qquad (2.21)$$

2.5.2 Discrete case

Let's consider again the continuous function defined as $x(t) = A \sin(2\pi f_0 t + \varphi)$, where $t \in (-\infty, +\infty)$ [s], A is amplitude [a.u], f_0 is the frequency of signal [Hz], φ is the phase [rad] and $0 \leq \varphi < 2\pi$ and discretize it. We have shown that in the continuous case the $RMS = \frac{A}{\sqrt{2}}$ (see eq.(2.21). Now we want to show that this is true even when we sample

our signal provided certain conditions as follows: Let N be the number of samples over a period T. We want to study the general case in which N is not necessarily an integer but can be a rational number. In order to do that, we need to consider an integer number of periods K, such that KN is an integer.

K is the number of periods we take into account.

KN is the total number of samples in K periods and therefore, the time interval between samples will be $\Delta t = \frac{KT}{KN}$ and $F_{samp} = \frac{1}{\Delta t}$, n is the sample index $\in [0, KN - 1]$ i.e. $n = 0, 1, \ldots, KN - 1$.

We sample our signal at times: $n\Delta t = \frac{nKT}{KN}$

by definition of the RMS (see eq.(2.18)), for K periods the RMS in discrete domain of $x(t) = A\sin(2\pi f_0 t)$ is:

$$RMS^2 = \frac{1}{KT} \int_{-\frac{\varphi KT}{2\pi}}^{KT - \frac{\varphi KT}{2\pi}} A^2 \sin^2\left(\frac{2\pi t}{\frac{KT}{K}} + \varphi\right) dt \tag{2.22}$$

by discretizing the eq.(2.22) we will have:

$$RMS^2 = \frac{1}{KN} \sum_{n=0}^{KN-1} A^2 \sin^2\left(\frac{2\pi n KT}{\frac{KN}{K}} + \varphi\right)$$

therefore:

$$RMS^2 = \frac{1}{KN} \sum_{n=0}^{KN-1} A^2 \sin^2\left(\frac{2\pi n}{N} + \varphi\right) \tag{2.23}$$

Applying the trigonometric property ($\sin^2\alpha = \left(\frac{1-\cos 2\alpha}{2}\right)$) to eq.(2.23) provides us:

$$RMS^2 = \frac{1}{KN} \sum_{n=0}^{KN-1} \frac{A^2}{2}\left(1 - \cos 2\left(\frac{2\pi n}{N} + \varphi\right)\right)$$

$$\Rightarrow RMS^2 = \frac{A^2}{2} - \frac{A^2}{2KN} \sum_{n=0}^{KN-1} \cos 2\left(\frac{2\pi n}{N} + \varphi\right) \tag{2.24}$$

by applying $e^{j\theta} = \cos(\theta) + j\sin(\theta)$ to eq.(2.24) we obtain:

$$RMS^2 = \frac{A^2}{2} - \frac{A^2}{2KN} \sum_{n=0}^{KN-1} Real\left[e^{j2\left(\frac{2\pi n}{N} + \varphi\right)}\right] \tag{2.25}$$

in general form:

$$\sum_{n=0}^{KN-1} e^{j2\left(\frac{2\pi n}{N} + \varphi\right)} = e^{j2\varphi} \sum_{n=0}^{KN-1} e^{j\left(\frac{4\pi n}{N}\right)} \tag{2.26}$$

2. EMG AMPLITUDE INDICATORS IN SPACE AND TIME

$\sum_{n=0}^{N-1} r^n$ is the sum of the terms of a geometric series[1] and is defined as:

$$\sum_{n=0}^{N-1} r^n = \frac{\left(1 - r^N\right)}{1 - r} \qquad , r \neq 1 \tag{2.27}$$

Considering

$$\sum_{n=0}^{KN-1} e^{j\left(\frac{4\pi n}{N}\right)} = \sum_{n=0}^{KN-1} e^{j\left(\frac{4\pi}{N}\right)n} = \sum_{n=0}^{KN-1} \left(e^{j\left(\frac{4\pi}{N}\right)}\right)^n \tag{2.28}$$

by applying eq.(2.27) to eq.(2.28) (assuming: $r = e^{j\left(\frac{4\pi}{N}\right)}$)

$$\sum_{n=0}^{KN-1} e^{\left(j\frac{4\pi}{N}\right)n} = \frac{1 - e^{j4K\pi}}{1 - e^{j\frac{4\pi}{N}}} \qquad , 1 - e^{j\frac{4\pi}{N}} \neq 0 \tag{2.29}$$

The numerator of eq.(2.29) is always zero because:

$$e^{j4K\pi} = \cos(4K\pi) + j\sin(4K\pi) = 1$$

$$\sum_{n=0}^{KN-1} e^{\left(j\frac{4\pi}{N}\right)n} = \frac{1 - e^{j4K\pi}}{1 - e^{j\frac{4\pi}{N}}} = \frac{0}{1 - e^{j\frac{4\pi}{N}}} = 0 \qquad , 1 - e^{j\frac{4\pi}{N}} \neq 0 \tag{2.30}$$

$\Rightarrow$ as long as the denominator of eq.(2.30) $\neq 0$ ($1 - e^{j\frac{4\pi}{N}} \neq 0$) then, the eq.(2.25) can be rewritten as:

$$RMS = \sqrt{\frac{A^2}{2} - 0} = \frac{A}{\sqrt{2}} \qquad , 0 \leq \varphi < 2\pi \tag{2.31}$$

The denominator of eq.(2.29) is zero if and only if

$$e^{j\frac{4\pi}{N}} = \cos\left(\frac{4\pi}{N}\right) + j\sin\left(\frac{4\pi}{N}\right) = 1$$

$$\Rightarrow \cos\left(\frac{4\pi}{N}\right) = 1$$

$\cos\left(\frac{4\pi}{N}\right) = 1$ if and only if $\frac{4\pi}{N} = 2l\pi, l \in \mathbb{Z}$

$$\frac{2}{N} = l \quad , l \in \mathbb{Z}$$

$\Rightarrow N$ must be 1 or 2

$$\Rightarrow KN \in \mathbb{Z}$$

---

[1]http://mathworld.wolfram.com/Sine.html

$$\Rightarrow K = 1$$

In K periods we have KN samples and $F_{samp.} = \frac{1}{\Delta t} = \frac{KN}{KT}$, $f_0 = \frac{1}{T}$ therefore,

$$F_{samp.} = N f_0$$

for both conditions($N = 1, 2$):

$N = 1 \Rightarrow F_{samp.} = f_0$

$N = 2 \Rightarrow F_{samp.} = 2 f_0 = $ Nyquist frequency

$\Rightarrow$ eq.(2.23) can be rewritten as:

if $N = 1 \Rightarrow K = 1 \Rightarrow$

$$RMS^2 = \frac{1}{KN} \sum_{n=0}^{KN-1} A^2 \sin^2 \left(\frac{2\pi n}{N} + \varphi \right) = \frac{1}{1*1} \sum_{n=0}^{1*1-1} A^2 \sin^2 \left(\frac{2\pi n}{1} + \varphi \right) = A^2 \sin^2(\varphi)$$

$$\Rightarrow RMS = A \sin(\varphi) \quad , 0 \leq \varphi < 2\pi \tag{2.32}$$

and if $N = 2$

$$RMS^2 = \frac{1}{KN} \sum_{n=0}^{KN-1} A^2 \sin^2 \left(\frac{2\pi n}{N} + \varphi \right) = \frac{1}{1*2} \sum_{n=0}^{1*2-1} A^2 \sin^2 \left(\frac{2\pi n}{2} + \varphi \right) =$$

$$\frac{A^2}{2} \left(\sin^2(0 + \varphi) + \sin^2(\pi + \varphi) \right)$$

Referring to the fact that $\sin^2(\pi + \varphi) = \sin(\pi + \varphi)\sin(\pi + \varphi)$ and $\sin(\pi + \varphi) = -\sin(\varphi)$ we can simplify the eq.(2.23) as:

$$RMS = A \sin(\varphi) \quad , 0 \leq \varphi < 2\pi \tag{2.33}$$

in summary:

In discrete form of $x(t) = A \sin(2\pi f_0 t + \varphi)$ the RMS value can be as follows:

- $RMS = \frac{A}{\sqrt{2}}$ (see eq.(2.31)) for any value of sampling frequency except f_0 and $2f_0$

- $RMS = A \sin(\varphi), 0 \leq \varphi < 2\pi$ (see eq.(2.32 and 2.33)) for two values of sampling frequency, $F_{samp.} = f_0$ or $2f_0$

- No error in computing the RMS provided that we consider a number of periods (K) such that we have an integer number of samples in K periods (see figure 2.6 and figure 2.5).
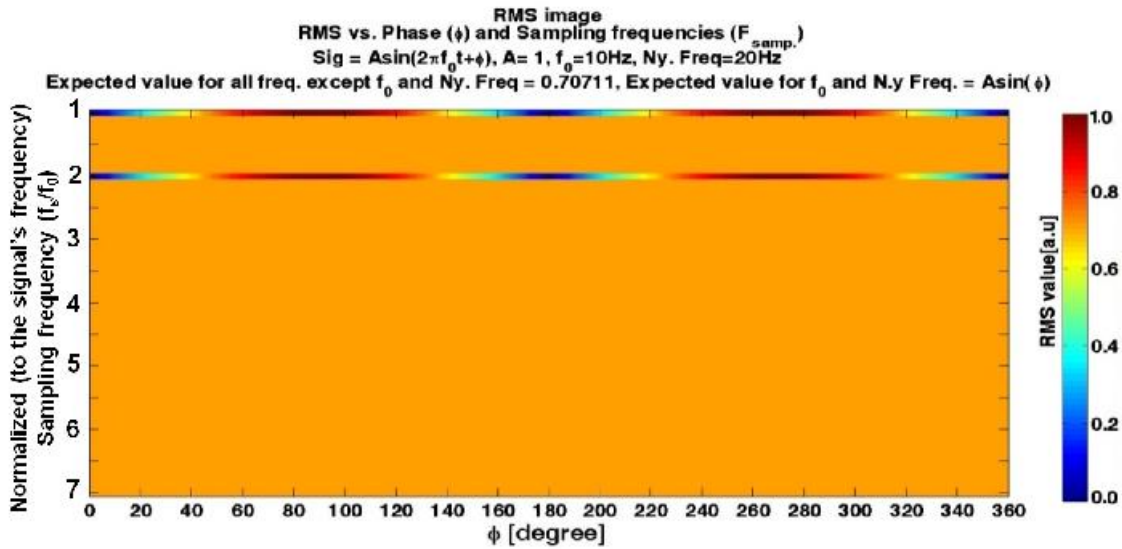
Figure 2.5: RMS image of $x(t) = \sin(2\pi 10t + \varphi)$ versus phase (φ) in degree and normalized (to the frequency of signal, f_0) sampling frequency in Hz. The Nyquist frequency $=20$Hz and the expected RMS for all sampling frequencies except the frequency of signal and the Nyquist frequency (10Hz and 20Hz) is phase independent($RMS = \frac{1}{\sqrt{2}} = 0.707$, represented in orange color) while RMS is phase dependent in 10Hz and 20Hz ($RMS = A\sin(\varphi)$)
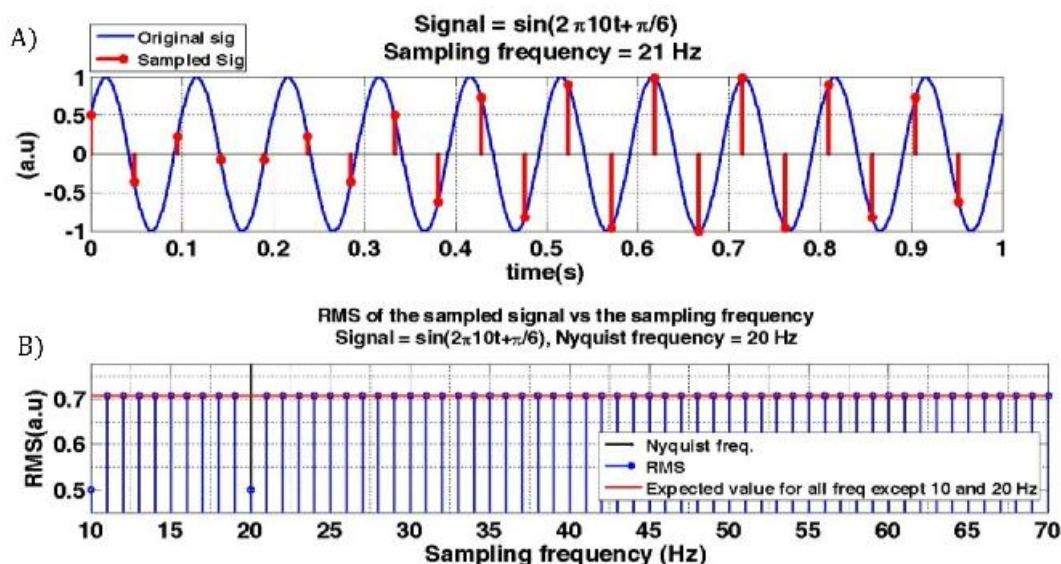
Figure 2.6: a 1s sinusoidal signal (solid blue, $x(t) = \sin(2\pi10t + \frac{\pi}{6})$) and samples (red bars) when the sampling frequency is just a little above the Nyquist rate (2.1 samples/period). 10 cycles ($K = 10$) is chosen such that KN (=21 samples) is an integer number and the Nyquist frequency is 20Hz (epoch duration = 10 cycles=1s). B) RMS of $x(t) = \sin(2\pi10t + \frac{\pi}{6})$ versus sampling frequency. $RMS = \frac{1}{\sqrt{2}} = 0.707$ except at the frequency of signal (10Hz) and the Nyquist frequency (20Hz). At these two frequencies the $RMS = A\sin(\varphi) = 0.5$

Comparing RMS with ARV (i.e. see figure 2.6, figure 2.3 (panel "B"), figure 2.5, and figure 2.4) show that for a sinusoidal signal RMS is robust to the sampling frequency (number of samples/cycle) while ARV depends on number of samples/cycle even at a sampling frequency higher than the Nyquist frequency . As a consequence, the ARV for sum of sinusoids suffers from dependency to the number of samples. Therefore, in the next sections only the RMS of a signal (considered as sum of sinusoids (1D and 2D)) is studied and its dependency to the number of samples is investigated.

2.6 Root Mean Square Value of sum of sinusoids (RMS)

2.6.1 Continuous case

Let's consider a periodic signal which is the summation of sinusoids with harmonic frequencies and different phases.

$$x(t) = A_1 \sin(2\pi f_1 t + \varphi_1) + A_2 \sin(2\pi f_2 t + \varphi_2) + \cdots + A_i \sin(2\pi f_i t + \varphi_i)$$

This finite series of sinusoids can be shortened in the form of equation 2.34.

$$x(t) = \sum_{i=1}^{M} A_i \sin(2\pi f_i t + \varphi_i) \tag{2.34}$$

where M is the number of individual sinusoids (an integer number), f_i [Hz] and A_i [a.u.] are the frequency and amplitude of the ith sinusoid respectively. φ_i is the phase of the ith sinusoid ranging from 0 to 2π [rad] and t [s] is the time (continuous).
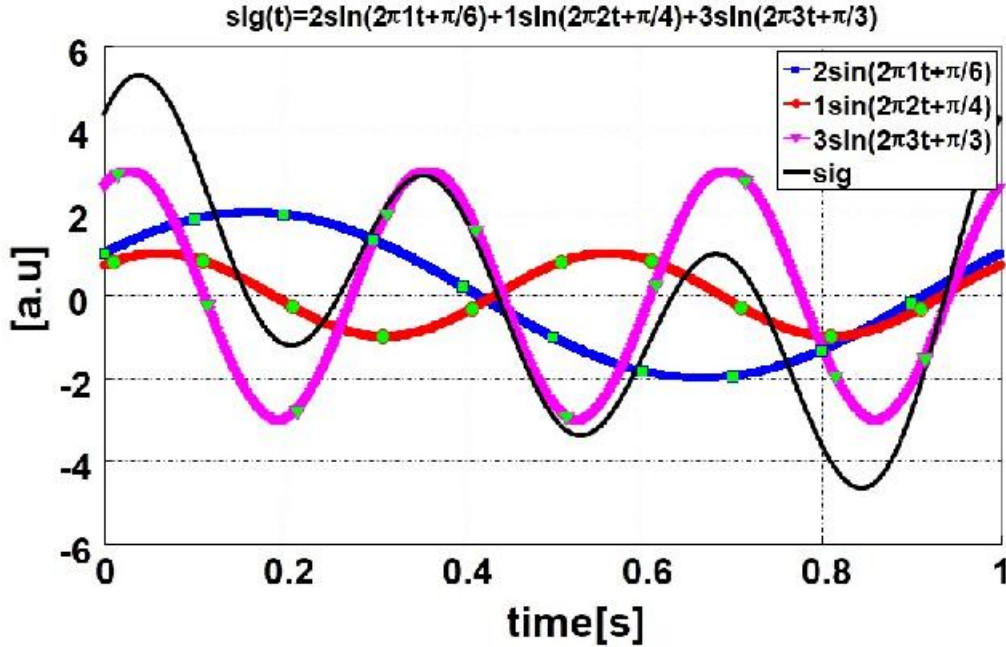
Figure 2.7: Three sinusoids with different phase and different amplitudes $(x_1(t) = 2\sin\left(2\pi t + \frac{\pi}{6}\right), x_2(t) = \sin\left(2\pi 2t + \frac{\pi}{4}\right), x_1(t) = 3\sin\left(2\pi 3t + \frac{\pi}{3}\right))$

RMS^2 of the $x(t)$ (see eq.(2.34)) is defined as follows:

$$RMS^2 = \frac{1}{T} \int_0^T x^2(t)\mathrm{d}t \qquad (2.35)$$

supposing $0 \le t < 1$, $T = 1[\mathrm{s}]$

we know that:

$$\left(\sum_{i=1}^M a_i\right)^2 = \sum_{i=1}^M a_i^2 + \sum_{i=0}^M \sum_{j=0}^M a_i a_j \quad , i \neq j \qquad (2.36)$$

therefore:

$$RMS^2 = \int_0^T \left(\sum_{i=1}^M A_i \sin\left(2\pi f_i t + \varphi_i\right)\right)^2 \mathrm{d}t = \int_0^T \sum_{i=1}^M A_i^2 \sin^2\left(2\pi f_i t + \varphi_i\right) \mathrm{d}t$$

$$+ \int_0^T \sum_{m=1}^M \sum_{l=1}^M A_m A_l \sin\left(2\pi f_m t + \varphi_m\right) \sin\left(2\pi f_l t + \varphi_l\right) \mathrm{d}t \quad , m \neq l \qquad (2.37)$$

Referring to the integral properties, eq.(2.37) can be rewritten as follows:

$$RMS^2 = \sum_{i=1}^M \int_0^T A_i^2 \sin^2\left(2\pi f_i t + \varphi_i\right) \mathrm{d}t$$

$$+ \sum_{m=1}^M \sum_{l=1}^M \int_0^T A_m A_l \sin\left(2\pi f_m t + \varphi_m\right) \sin\left(2\pi f_l t + \varphi_l\right) \mathrm{d}t \quad , m \neq l \qquad (2.38)$$

The first term of eq.(2.38) i.e. $\left(\int_0^T A_i^2 \sin^2\left(2\pi f_i t + \varphi_i\right) \mathrm{d}t\right)$ is the definition of the RMS^2 of the ith sinusoid. The integral part of the second term of eq.(2.38) i.e. $\left(\int_0^T A_m A_l \sin\left(2\pi f_m t + \varphi_m\right) \sin\left(2\pi f_l t + \varphi_l\right) \mathrm{d}t \quad , m \neq l\right)$ can be rewritten based on the trigonometric property (eq.(2.39))

$$\sin(\theta_1)\sin(\theta_2) = \frac{1}{2}\left[\cos(\theta_1 - \theta_2) - \cos(\theta 1 + \theta_2)\right] \qquad (2.39)$$

$$\int_0^T A_m A_l \sin\left(2\pi f_m t + \varphi_m\right) \sin\left(2\pi f_l t + \varphi_l\right) \mathrm{d}t$$

$$= \int_0^T \frac{A_m A_l}{2}\left[\cos\left(2\pi f_m t + \varphi_m - 2\pi f_l t - \varphi_l\right) - \cos\left(2\pi f_m t + \varphi_m + 2\pi f_l t + \varphi_l\right)\right]\mathrm{d}t$$

$$= \frac{A_m A_l}{2} \int_0^T \cos\left(2\pi(f_m - f_l)t + (\varphi_m - \varphi_l)\right) \mathrm{d}t - \frac{A_m A_l}{2} \int_0^T \cos\left(2\pi(f_m + f_l)t + (\varphi_m + \varphi_l)\right) \mathrm{d}t$$

The integral of a sine or cosine function over a period is always zero. Therefore, the second term of eq.(2.38) i.e. $\left(\sum_{m=1}^M \sum_{l=1}^M \int_0^T A_m A_l \sin\left(2\pi f_m t + \varphi_m\right) \sin\left(2\pi f_l t + \varphi_l\right) \mathrm{d}t \quad , m \neq l \right)$ is always zero and the eq.(2.38) is simplified as follows:

$$RMS^2 = \sum_{i=1}^M \int_0^T A_i^2 \sin^2\left(2\pi f_i t + \varphi_i\right) \mathrm{d}t = \sum_{i=1}^M RMS_i^2$$

Thus, for the continuous case:

$$RMS = \sqrt{\sum_{i=1}^M RMS_i^2} \tag{2.40}$$

where M is the number of sinusoids and RMS_i is the RMS of the ith sinusoid. In a descriptive way for continuous case, RMS squared of sum of sinusoids is the sum of squared RMSes.

2.6.2 Discrete case

Let's consider again the continuous function defined as $x(t) = A \sum_{i=1}^M \sin(2\pi f_i t + \varphi_i)$, where M is the number of individual sinusoids (an integer number), f_i [Hz] and A_i [a.u.] are the frequency and amplitude of the ith sinusoid respectively. φ_i is the phase of the ith sinusoid ranging from 0 to 2π [rad] and t [s] is the time. We have shown that in the continuous case the $RMS^2 = \sum_{i=1}^M RMS_i^2$. Now we want to show that this is true when we sample our signal provided certain conditions as follows:

Let N be the number of samples (integer) over 1s. Time interval between samples (Δt) is $\frac{1}{N}$ and therefore, the sampling frequency will be $F_{samp.} = \frac{1}{\Delta t} = N$. n is the sample index ranging from 0 to $N - 1$; $n = 0, 1, 2, \ldots, N - 1$

We sample our signal at time instants $n\Delta t = \frac{n}{N}$

Therefore, the sampled form of the signal can be shown as:

$$x[n] = \sum_{i=1}^M A_i \sin\left(\frac{2\pi f_i n}{N} + \varphi_i\right) = \sum_{i=1}^M A_i \sin\left(\frac{2\pi f_i n}{N} + \varphi_i\right) \tag{2.41}$$

To deal with sum of sinusoids, we assume the exponential form which is the general form of a sinusoid in both real and imaginary domain. The exponential form of eq.(2.41) is as follows:

$$x[n] = \sum_{i=1}^{M} A_i e^{j\left(\frac{2\pi f_i n}{N} + \varphi_i\right)} \tag{2.42}$$

the RMS^2 is:

$$RMS^2 = \frac{1}{N} \sum_{n=0}^{N-1} \left(\sum_{i=1}^{M} A_i e^{j\left(\frac{2\pi f_i n}{N} + \varphi_i\right)} \right)^2 \tag{2.43}$$

considering that $\left(\sum_{i=1}^{M} a_i \right)^2 = \sum_{i=1}^{M} a_i^2 + \sum_{i=1}^{M} \sum_{j=1}^{M} a_i a_j, i \neq j$ we can rewrite eq.(2.43) as:

$$RMS^2 = \frac{1}{N} \sum_{n=0}^{N-1} \left(\sum_{i=1}^{M} \left(A_i e^{j\left(\frac{2\pi f_i n}{N} + \varphi_i\right)} \right)^2 + \sum_{m=1}^{M} \sum_{l=1}^{M} A_m A_l e^{j\left(\frac{2\pi f_m n}{N} + \varphi_m\right)} e^{j\left(\frac{2\pi f_l n}{N} + \varphi_l\right)} \right), l \neq m \tag{2.44}$$

Applying the $\sum$ property, eq.(2.44) can be reformed as:

$$RMS^2 = \frac{1}{N} \sum_{n=0}^{N-1} \sum_{i=1}^{M} \left(A_i e^{j\left(\frac{2\pi f_i n}{N} + \varphi_i\right)} \right)^2 + \frac{1}{N} \sum_{n=0}^{N-1} \sum_{m=1}^{M} \sum_{l=1}^{M} A_m A_l e^{j\left(\frac{2\pi f_m n}{N} + \varphi_m\right)} e^{j\left(\frac{2\pi f_l n}{N} + \varphi_l\right)}, l \neq m \tag{2.45}$$

Applying the $\sum$ property, eq.(2.45):

$$RMS^2 = \frac{1}{N} \sum_{i=1}^{M} \sum_{n=0}^{N-1} \left(A_i e^{j\left(\frac{2\pi f_i n}{N} + \varphi_i\right)} \right)^2 + \frac{1}{N} \sum_{n=0}^{N-1} \sum_{m=1}^{M} \sum_{l=1}^{M} A_m A_l e^{j\left(\frac{2\pi f_m n}{N} + \varphi_m\right)} e^{j\left(\frac{2\pi f_l n}{N} + \varphi_l\right)}, l \neq m$$

Referring to the RMS definition of each sinusoid we can write:

$$\frac{1}{N} \sum_{i=1}^{M} \sum_{n=0}^{N-1} \left(A_i e^{j\left(\frac{2\pi f_i n}{N} + \varphi_i\right)} \right)^2 = \sum_{i=1}^{M} RMS_i^2$$

therefore, eq.(2.45) can be rewritten as:

$$RMS^2 = \sum_{i=1}^{M} RMS_i^2 + \frac{1}{N} \sum_{n=0}^{N-1} \sum_{m=1}^{M} \sum_{l=1}^{M} A_m A_l e^{j\left(\frac{2\pi f_m n}{N} + \varphi_m\right)} e^{j\left(\frac{2\pi f_l n}{N} + \varphi_l\right)}, l \neq m \tag{2.46}$$

Let's consider the second term of eq.(2.46) as eq.(2.47) and discuss it more as follows:

$$\frac{1}{N} \sum_{n=0}^{N-1} \sum_{m=1}^{M} \sum_{l=1}^{M} A_m A_l e^{j\left(\frac{2\pi f_m n}{N} + \varphi_m\right)} e^{j\left(\frac{2\pi f_l n}{N} + \varphi_l\right)}$$

$$= \frac{1}{N} \sum_{n=0}^{N-1} \sum_{m=1}^{M} \sum_{l=1}^{M} A_m A_l e^{j\left(\frac{2\pi (f_m + f_l) n}{N} + \varphi_m + \varphi_l\right)}, l \neq m \tag{2.47}$$

2. EMG AMPLITUDE INDICATORS IN SPACE AND TIME

Now we want to find condition such that eq.(2.47) is zero.

One term of $\sum_{m=1}^{M}\sum_{l=1}^{M} A_m A_l e^{j\left(\frac{2\pi(f_m+f_l)n}{N}+\varphi_m+\varphi_l\right)}$ can be considered as $A_m A_l e^{j\left(\frac{2\pi(f_m+f_l)n}{N}+\varphi_m+\varphi_l\right)}$ and we are going to find under what condition the value of $\frac{1}{N}\sum_{n=0}^{N-1} A_m A_l e^{j\left(\frac{2\pi(f_m+f_l)n}{N}+\varphi_m+\varphi_l\right)} = 0$, then we can indicate that eq.(2.47) = 0. In this manner:

$$\frac{A_m A_l}{N}\sum_{n=0}^{N-1} e^{j\left(\frac{2\pi(f_m+f_l)n}{N}+\varphi_m+\varphi_l\right)} = \frac{A_m A_l}{N} e^{j(\varphi_m+\varphi_l)}\sum_{n=0}^{N-1} e^{j\left(\frac{2\pi(f_m+f_l)n}{N}\right)}$$

and

$$\frac{A_m A_l}{N} e^{j(\varphi_m+\varphi_l)}\sum_{n=0}^{N-1} e^{j\left(\frac{2\pi(f_m+f_l)n}{N}\right)} = \frac{A_m A_l}{N} e^{j(\varphi_m+\varphi_l)}\sum_{n=0}^{N-1} \left(e^{j\left(\frac{2\pi(f_m+f_l)}{N}\right)}\right)^n \qquad (2.48)$$

if we think of $r = e^{j\left(\frac{2\pi(f_m+f_l)}{N}\right)}$ then eq.(2.48 can be considered as a geometric series. We already know[1] that $\sum_{n=m}^{h} ar^n = \frac{a(r^m-r^{h+1})}{1-r}, r \neq 1$, therefore by setting $h = N-1$, $m = 0$, $a = 1$, and $r = e^{j\left(\frac{2\pi(f_m+f_l)}{N}\right)}$ we can simply rewrite eq.(2.48) as:

$$\frac{A_m A_l}{N} e^{j(\varphi_m+\varphi_l)}\sum_{n=0}^{N-1} \left(e^{j\left(\frac{2\pi(f_m+f_l)}{N}\right)}\right)^n = \left(\frac{A_m A_l}{N} e^{j(\varphi_m+\varphi_l)}\right)\left(\frac{1-e^{j\left(\frac{2\pi(f_m+f_l)}{N}\right)^N}}{1-e^{j\left(\frac{2\pi(f_m+f_l)}{N}\right)}}\right)$$

$$= \left(\frac{A_m A_l}{N} e^{j(\varphi_m+\varphi_l)}\right)\left(\frac{1-e^{j(2\pi(f_m+f_l))}}{1-e^{j\left(\frac{2\pi(f_m+f_l)}{N}\right)}}\right) \quad , 1-e^{j\left(\frac{2\pi(f_m+f_l)}{N}\right)} \neq 0$$

Discussion on $\frac{1-e^{j\left(2\pi(f_m+f_l)\right)}}{1-e^{j\left(\frac{2\pi(f_m+f_l)}{N}\right)}}$

- **Discussion on the numerator** $\left(1-e^{j\left(2\pi(f_m+f_l)\right)}\right)$:

  f_m and f_l are considered as integer numbers, which implies an integer number of periods in observation time of 1s . The sum of two integer numbers $(f_m + f_l)$ is also an integer number and $2(f_m + f_l)$ is an even number. Therefore, if $h = f_m + f_l$ then:

$$e^{j(2\pi(f_m+f_l))} = e^{j2h\pi} = \cos(2h\pi) + j\sin(2h\pi) = 1 \qquad (2.49)$$

---

[1]http://mathworld.wolfram.com/Sine.html

Eq.(2.49) indicates that the numerator of $\left(\frac{1-e^{j\left(2\pi(f_m+f_l)\right)}}{1-e^{j\left(\frac{2\pi(f_m+f_l)}{N}\right)}} \right)$ is always zero. For

the cases that the denominator of $\left(\frac{1-e^{j\left(2\pi(f_m+f_l)\right)}}{1-e^{j\left(\frac{2\pi(f_m+f_l)}{N}\right)}} \right)$ is not zero (i.e.

$1 - e^{j\left(\frac{2\pi(f_m+f_l)}{N}\right)} \neq 0$) the $\left(\frac{1-e^{j\left(2\pi(f_m+f_l)\right)}}{1-e^{j\left(\frac{2\pi(f_m+f_l)}{N}\right)}} \right) = 0$ and therefore eq.(2.48) will be

zero and consequently eq.(2.47) is zero and finally we can simplify eq.(2.46) as
follows:

$$RMS^2 = \sum_{i=1}^{M} RMS_i^2 \tag{2.50}$$

Now we should check certain conditions such that the denominator is zero.

- **Discussion on the denominator** $\left(1 - e^{j\left(\frac{2\pi(f_m+f_l)}{N}\right)}\right)$:

$$1 - e^{j\left(\frac{2\pi(f_m+f_l)}{N}\right)} = 0$$

$$\Rightarrow e^{j\left(\frac{2\pi(f_m+f_l)}{N}\right)} = 1$$

$$\Rightarrow e^{j\left(\frac{2\pi(f_m+f_l)}{N}\right)} = \cos\left(\frac{2\pi(f_m+f_l)}{N}\right) + j\sin\left(\frac{2\pi(f_m+f_l)}{N}\right) = \cos(2k\pi)$$

where k is an integer number. Therefore:

$$\frac{2\pi(f_m+f_l)}{N} = 2k\pi \Rightarrow \frac{f_m+f_l}{k} = N \tag{2.51}$$

Referring to our setup (we assumed N is integer and the observation interval
$T = 1$[s], therefore time interval between samples (Δt) is $\frac{1}{N}$ and $F_{samp.} = \frac{1}{\Delta t} = N$
eq.(2.51) states that as N is an integer, when the sampling frequency is equal to
the sum of two frequencies or any combination such that $\frac{f_m+f_l}{K}$ is an integer,
the denominator is zero and $\frac{1-e^{j\left(2\pi(f_m+f_l)\right)}}{1-e^{j\left(\frac{2\pi(f_m+f_l)}{N}\right)}} = \frac{0}{0}$. In this case there will be an
additive term to the $\sum_{i=1}^{M} RMS_i^2$, when we compute RMS^2 (see eq.(2.46). The
additive term causes deviation from the expected value $\left(\sum_{i=1}^{M} RMS_i^2\right)$.

- **Discussion on** $\frac{f_m+f_l}{N}$
  if $\frac{f_m+f_l}{N} < 1$ then $N > f_m + f_l$. If we find the maximum value of $f_m + f_l$ then
  for any other values of f_m and f_l, the inequality is still true. The maximum of

f_m or f_l is the maximum frequency in the signal. Let's call f_c as the maximum frequency of $x(t)$.

$$max(f_m + f_l) = max(f_m) + max(f_l) = f_c + f_c = 2f_c$$

Thus, the inequality $N > f_m + f_l$ is holding if $N > 2f_c$. To check the value of denominator in this condition, let's consider $N = 2f_c + \epsilon$, $\epsilon > 0$ and $f_m + f_l = 2fc$. We can rewrite the denominator of $\left(\frac{1 - e^{j(2\pi(f_m+f_l))}}{1 - e^{j\left(\frac{2\pi(f_m+f_l)}{N}\right)}} \right)$ as follows:

$$e^{j\left(\frac{2\pi(f_m+f_l)}{N}\right)} = e^{j\left(\frac{2\pi(2f_c)}{2f_c+\epsilon}\right)} = e^{j(2\pi\alpha)} = \cos(2\pi\alpha) + j\sin(2\pi\alpha), 0 < \alpha < 1$$

where $\alpha = \frac{2f_c}{2f_c+\epsilon}$. Meanwhile,

$$\cos(2\pi\alpha) + j\sin(2\pi\alpha) \neq 1, 0 < 2\pi\alpha < 2\pi$$

therefore:

$$e^{j\left(\frac{2\pi(f_m+f_l)}{N}\right)} \neq 1 \tag{2.52}$$

Eq.(2.52) states that in case of $N > 2f_c$ the denominator is is not zero and:

$$\left(\frac{1 - e^{j(2\pi(f_m+f_l))}}{1 - e^{j\left(\frac{2\pi(f_m+f_l)}{N}\right)}} \right) = \frac{0}{1 - \cos\left(\frac{\pi\epsilon}{f_c}\right) - j\sin\left(\frac{\pi\epsilon}{f_c}\right)i} = 0, N > 2f_c, \epsilon > 0 \tag{2.53}$$

Eq.(2.53) states that eq.(2.48) is zero and consequently eq.(2.47) is zero. These findings imply that eq.(2.46) is simplified as follows:

$$RMS^2 = \sum_{i=1}^{M} RMS_i^2 \qquad \forall F_{samp.} > 2f_c, f_c = max.(f_i), i = 1, 2, \ldots, M \tag{2.54}$$

In other words observing the Nyquist sampling theorem guarantees no error in the RMS for a signal that can be synthesized to individual sinusoidal signals. Below the Nyquist frequency, as long as $\frac{f_m+f_l}{N} = 1$, which implies that $F_{samp.} = f_m + f_l$, the RMS is deviated from the expected value $\left(RMS^2 = \sum_{i=1}^{M} RMS_i^2 \right)$ by the following additive term (see also eq.(2.46).

$$\frac{1}{N} \sum_{n=0}^{N-1} \sum_{m=1}^{M} \sum_{l=1}^{M} A_m A_l e^{j\left(\frac{2\pi f_m n}{N} + \varphi_m\right)} e^{j\left(\frac{2\pi f_l n}{N} + \varphi_l\right)}, l \neq m \tag{2.55}$$
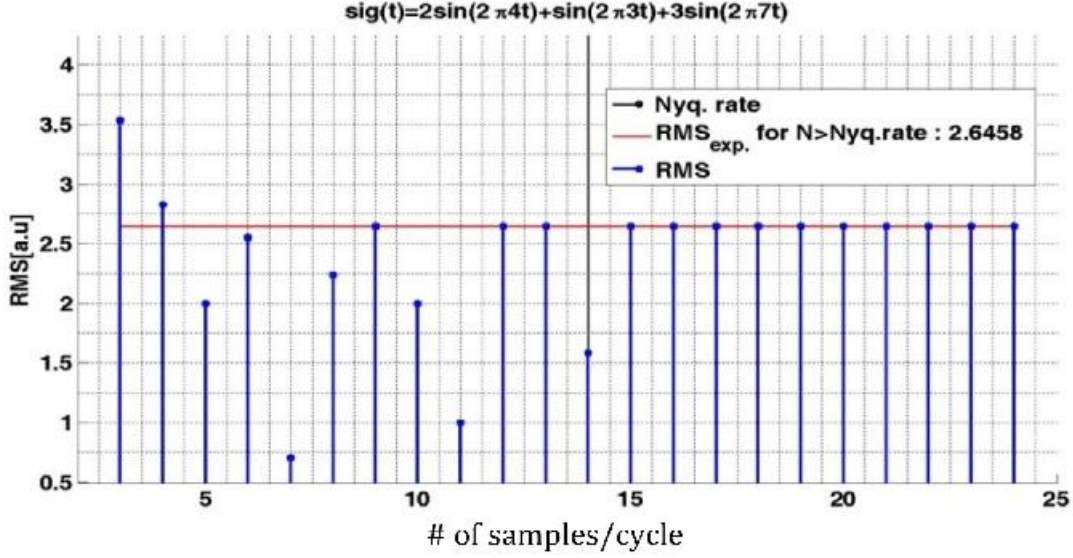
Figure 2.8: RMS of $sig(t) = 2\sin(2\pi 4t) + \sin(2\pi 3t) + 3\sin(2\pi 7t)$ versus number of samples/cycle. $RMS = \sqrt{\sum_{i=1}^{M} RMS_i^2} = \sqrt{\frac{2^2}{2} + \frac{1^2}{2} + \frac{3^2}{2}} = 2.6458$ for any value of sampling frequency above the Nyquist frequency (14Hz)

2.6.3 Conclusion for 1D (time) signals

It is shown that in the continuous form of $x(t) = A\sin(2\pi f_0 t + \varphi)$ the ARV and RMS are computed as follows:

$$ARV = \frac{2A}{\pi}$$

$$RMS = \frac{A}{\sqrt{2}}$$

and in the discrete form of $x(t) = A\sin(2\pi f_0 t + \varphi)$ the ARV and RMS value can be computed as follows:

for ARV:

$$ARV = \frac{2A}{N}\left(\frac{\cos\left(\frac{\pi}{N}\right)}{\sin\left(\frac{\pi}{N}\right)}\right) = \frac{2A}{N}\cot\left(\frac{\pi}{N}\right)$$

ARV depends on N (number of samples/cycle). When $N \to \infty$ then the $ARV \to \frac{2A}{\pi}$. Even if observing the sampling theorem ($F_{samp.} > 2f_0$), for cases that the N is not big enough ($N > 10$ samples/cycle provide less than 3.5% deviation from the expected value and $N > 18$ the error $< 1\%$) there is a deviation from the expected ARV.

for RMS:

- At the frequency of signal (f_0) and the Nyquist frequency $(2f_0)$:

$$RMS = A\sin(\varphi), \quad 0 \leq \varphi < 2\pi$$

- At all frequencies except the frequency of signal (f_0) and the Nyquist frequency $(2f_0)$:

$$RMS = \frac{A}{\sqrt{2}}$$

- For sum of sinusoids $\left(x(t) = \sum_{i=1}^{M} A_i \sin(2\pi f_i t + \varphi_i)\right), \quad 0 \leq \varphi_i < 2\pi$

  – **In continuous case:**

$$RMS = \sqrt{\sum_{i=1}^{M} RMS_i^2}$$

  – **In discrete case:**

  a) above the Nyquist frequency: $RMS = \sqrt{\sum_{i=1}^{M} RMS_i^2}$

  b) below the Nyquist frequency:

  $\cdot$ $RMS \neq \sqrt{\sum_{i=1}^{M} RMS_i^2}$ if $F_{samp.} = f_m + f_l, m \neq l, m = 1, 2, \ldots, M$

  $\cdot$ $RMS = \sqrt{\sum_{i=1}^{M} RMS_i^2}$ if $F_{samp.} \neq f_m + f_l, m \neq l, m = 1, 2, \ldots, M$

In a sampled sinusoid, the RMS does not depend on the number of samples in a cycle even if the signal is sampled below the Nyquist frequency and there is no deviation from the expected value $\left(\frac{A}{\sqrt{2}}\right)$, while ARV depends on the number of samples. As a result, RMS is more robust than ARV as an amplitude indicator when the signal is sampled, either in space or time.

2.7 Root Mean Square (RMS) and Average Rectified Value (ARV) of a 2D sinusoid

Considering an image $(f(x, y))$ that is defined as multiplication of two sinusoidal signals along x and y direction such that:

$$f(x, y) = A_x \sin\left(2\pi f_x x + \varphi_x\right) A_y \sin\left(2\pi f_y y + \varphi_y\right) \tag{2.56}$$

2.7 Root Mean Square (RMS) and Average Rectified Value (ARV) of a 2D sinusoid

where f_x and f_y are the frequencies [cycles/m], A_x, A_y are the amplitudes [a.u.], and φ_x, φ_y are the phases [rad] of the sinusoids along x and y directions respectively. Panel "A" in figure 2.9 shows an example image defined as eq.(2.56).

Analytically the RMS (in continuous case of the signal) can be computed as follows:

$$RMS^2 = \frac{1}{AB} \left(\int_0^A \int_0^B f^2(x,y) \mathrm{d}x \mathrm{d}y \right) \tag{2.57}$$

where A and B are specifying the region (along x an y respectively) that is being sampled

$$RMS^2 = \frac{1}{AB} \left(\int_0^A \int_0^B \left(A_x \sin\left(2\pi f_x x + \varphi_x\right) A_y \sin\left(2\pi f_y y + \varphi_y\right)\right)^2 \mathrm{d}x \mathrm{d}y \right) \tag{2.58}$$

The period of each row and each column of the image is the period of sinusoids along x and y directions respectively. In other words, $A = \frac{1}{f_x}$ ([cycle/m]$^{-1}$) and $B = \frac{1}{f_y}$([cycle/m]$^{-1}$).

As long as x and y are independent (i.e. changing parameters of the sinusoid along x direction does not affect the sinusoid along y), we can rewrite eq.(2.58) as follows:

$$RMS^2 = \left(\frac{1}{A} \int_0^A A_x^2 \sin^2(2\pi f_x x + \varphi_x) \mathrm{d}x \right) \left(\frac{1}{B} \int_0^B A_y^2 \sin^2(2\pi f_y y + \varphi_y) \mathrm{d}y \right)$$

$$= RMS_x^2 * RMS_y^2$$

where RMS_x and RMS_y are the RMS values of sinusoids along x and y directions.

$$RMS = RMS_x * RMS_y = \frac{A_x}{\sqrt{2}} * \frac{A_y}{\sqrt{2}} = \frac{A_x A_y}{2} \tag{2.59}$$

$$f(x, y) =$$
$$6 \sin \left(2\pi 5x + \frac{\pi}{3} \right) \sin \left(2\pi 3y + \frac{\pi}{4} \right)$$
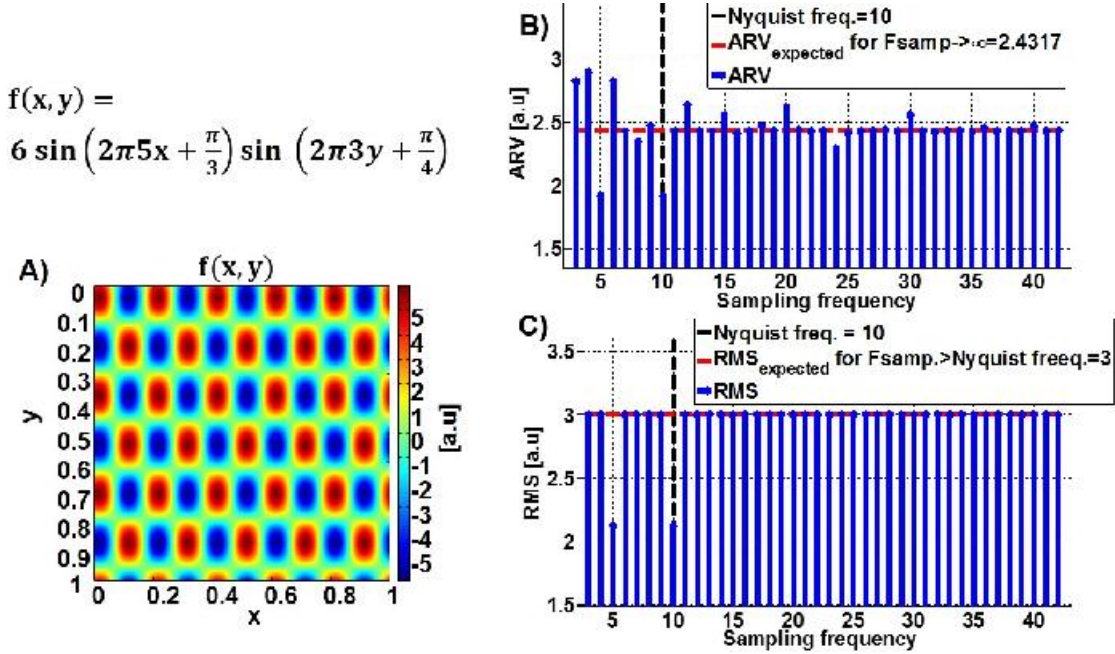
Figure 2.9: A) an image representing a 2D sinusoid that is the multiplication of two sinusoids with arbitrary amplitudes and phases($\left(f(x, y) = 2 \sin \left(2\pi 5x + \frac{\pi}{3} \right) * 3 \sin \left(2\pi 3y + \frac{\pi}{4} \right) \right)$). This image is over sampled with 1000 samples/cycle to be represented as a continuous case.B) ARV and C)RMS of the image shown in panel "A" versus sampling frequency

As long as observing the sampling theorem ($F_{samp} \geq Nyquist\,frequency$), eq.(2.59) is confirmed. Figure 2.9 shows RMS and ARV versus sampling frequencies. It shows that there are no changes in RMS values for any sampling frequency greater than the Nyquist rate, while this is not true for ARV. We have shown that in case of single sinusoid (1D) the ARV tends to the expected value if the number of samples (N) is quite enough ($N > 10$ samples/cycle provide less than 3.5% deviation from the expected value and $N > 18$ the error $< 1\%$) (see section 2.4.2 on page 31) .

2.8 Spatial aliasing in detected action potentials over skin (a simulation study)

2.8.1 Introduction

In signal processing and related disciplines, aliasing refers to an effect that causes different signals to become indistinguishable, when are sampled. It also refers to the distortion or artifact when the reconstructed samples of the signal are different from the original continuous signal.

A two-dimensional (2-D) high density (HD) electrode array is a grid of EMG contacts covering a portion of the skin surface above one or more muscles. In HDsEMG, the continuous surface potential distribution is sampled using a grid of N×M electrodes equally spaced along "x" and "y", providing N×M spatial samples of the instantaneous potential distribution analog image.

Despite the many applications described in the literature, a fundamental issue in HDsEMG related to the sampling and truncation of the image have not been sufficiently addressed.

HDsEMG electrodes are small (1 mm^2 to 25 mm^2). For the sake of simplicity, they will be considered in this section as point-like. To study the effect of sampling in space, a previously developed model (5) was used to simulate the monopolar potential distribution generated by the propagating action potential of a single muscle fiber parallel to the skin placed at different depth in the muscle. Skin and fat layers thicknesses were considered 1 mm and 3 mm respectively.

2.8.2 Spatial distribution of simulated action potential (space-time and frequency domain)

Non-homogeneous (layered), anisotropic volume conductor model constituted by muscle (anisotropic), fat (isotropic), and skin (isotropic) layers is considered for generation and detection of sEMG (5). The detection system was defined as a 128×128 electrodes (grid) with 1mm inter electrode distance (IED) as the reference. The center of detection grid was placed over the neuromuscular junction. The fiber length was considered 100mm (upper semi fiber length = 55mm, lower semi fiber length = 45mm). Different layers in the model were considered as 1mm skin layer and 3mm fat layer as mentioned before. The conductivities of the anisotropic volume conductor were set as

2. EMG AMPLITUDE INDICATORS IN SPACE AND TIME

$\sigma_{skin} = 20\sigma_{fat}$, $\sigma_{fat} = 0.5\sigma_{muscle_y}$, $\sigma_{muscle_x} = \sigma_{muscle_y}$, and $\sigma_{muscle_z} = 5\sigma_{muscle_y}$. The skin potentials were simulated in monopolar. Figure 2.10 shows the geometry of the model used for simulation.

When electromyograms are recorded with a bi-dimensional grid of electrodes, each electrode may be conceived as a pixel "p" with coordinates "x" and "y" given by the rows and columns in the grid. Muscle activity can be considered as a movie whose frames are generated by the instantaneous amplitude of each channel. Four frames (image) of the spatial distribution of simulated action potential were prepared. These images correspond to the start of depolarization (t_1 = time that the amplitude of the fiber action potential start decreasing from 0 at $t_2 = t_1 + 2.5$ms, at first ($t_3 = t_1 + 13$ms) and second ($t_4 = t_1 + 16$ms) end of fiber effects (see figure 2.11. The color of the pixels is the amplitude of the center point.
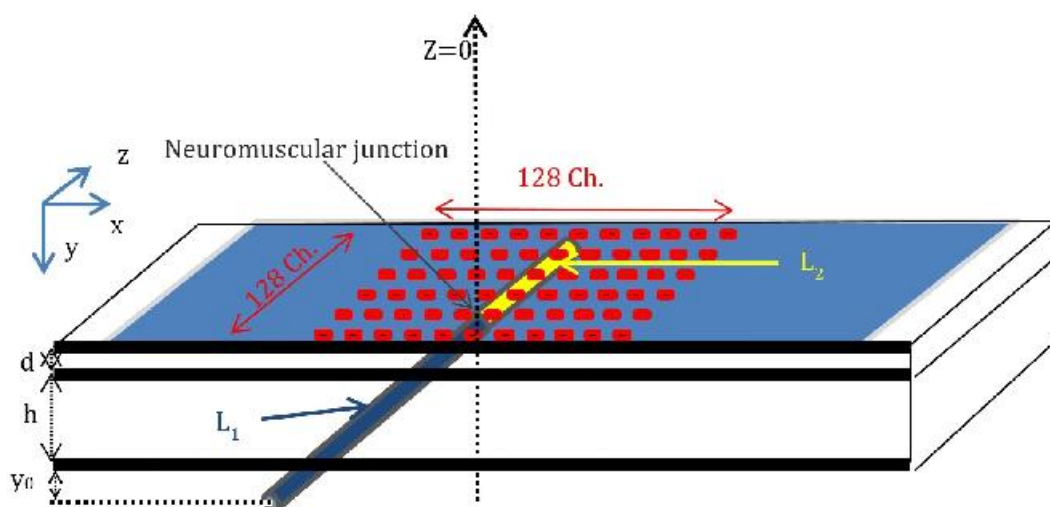
Figure 2.10: The geometry of the model used for simulating the monopolar action potential generated by 1 fiber placed at different depths in the muscle and detected by 128×128 electrodes (grid, IED=1mm) over the skin. Neuromuscular junction location in Z direction=0, d(skin thickness)=1mm, h(subcutaneous tissue thickness=3mm), L_1(lower semi-fiber length=45mm), L_2(upper semi-fiber length=55mm), y_0= depth of the fiber in the muscle in mm. The model is the planar model developed by Farina and Merletti (5).
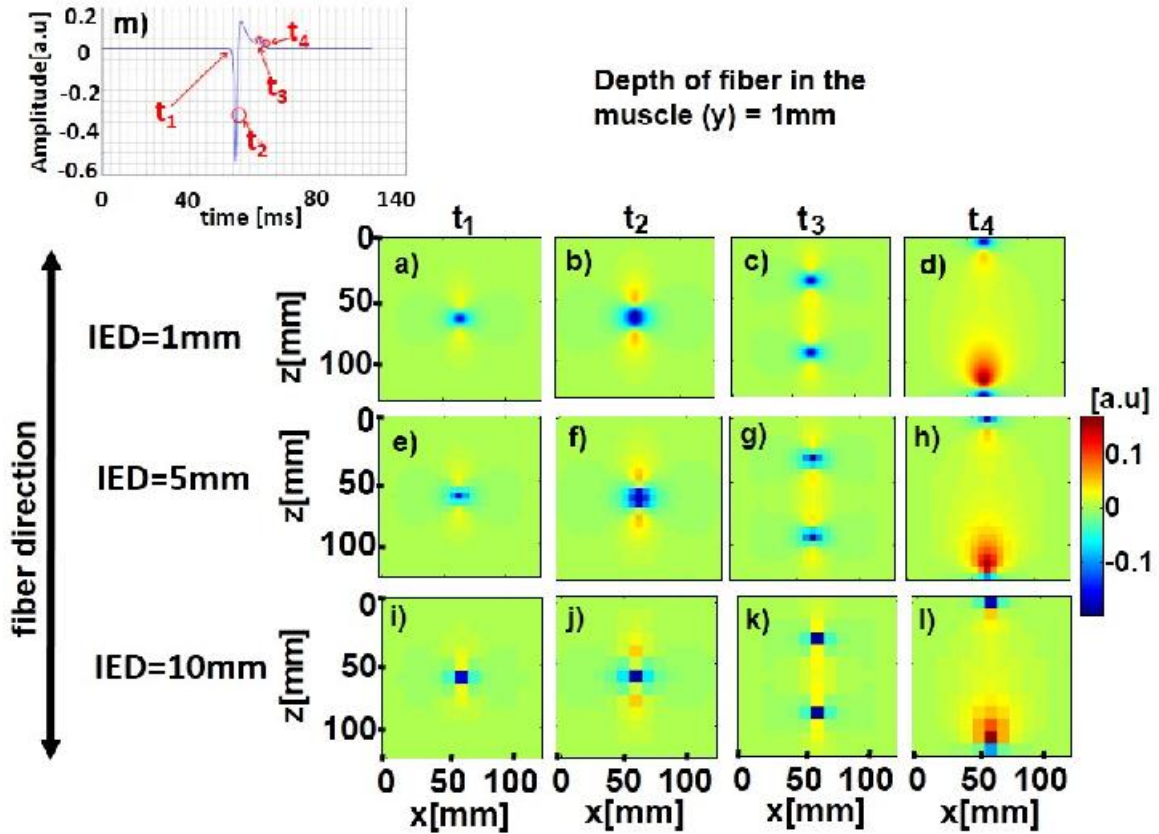
Figure 2.11: Distribution of the simulated monopolar surface potential from a single muscle fiber, 1 mm deep in the muscle (skin thickness 1 mm, subcutaneous tissue thickness: 3mm). The action potential are at a), e), i) start of depolarization(t_1); b), f), j) during depolarization(t_2); c), g), k) during the first end of fiber effect(t_3); d), h), l) at the second end of fiber effect(t_4). a), b), c), and d) are relating to inter electrode distance(IED)=1mm. Panels e), f), g), and h) are for IED=5mm; panels i), j), k), and l) are for IED=10mm. The detection system covers $127{\times}127$mm^2 in all images. m)Simulated action potential generated by the model shown in figure 2.10 and detected by the electrode over the neuromuscular junction. Four different times that indicate start of depolarization (t_1), during depolarization ($t2 = t1 + 2.5$ms), during first ($t3 = t1 + 13$ms) and second ($t4 = t1 + 16$ms) end of fiber effect are shown on panel "m"

2. EMG AMPLITUDE INDICATORS IN SPACE AND TIME

In order to have a better understanding of spatial aliasing as the IED increases, the magnitude of the 2-D Fourier transform of the spatial distribution of simulated monopolar surface potentials produced by a single fiber are prepared. Figure 2.12, shows one cycle of the amplitude spectrum in space for sampling frequency 1000, 200, and 100 cycles/m (i.e., IED=1, 5, and 10mm respectively) with harmonics spaced by 1.0/0.127=7.87 cycles/m of simulated skin potentials (monopolar detection) produced by a single muscle fiber (see figure 2.10). It is evident that aliasing is negligible for IED < 5 mm (figure 2.12. By increasing the depth of fiber in the muscle, a smoother action potential over the skin is expected. Therefore, aliasing is expected to occur in higher IEDs. For a simulated muscle fiber placed at just below the skin, 4mm and 10mm deep in the muscle (skin thickness=1mm, subcutaneous tissue thickness=3mm) aliasing starts from 7mm, 10mm and 15mm respectively(see figure 2.13). The presented frequency domain figures (figures 2.12 and 2.13) also imply that start of aliasing is different in different directions. Propagation of action potential in an anisotropic environment is the reason.
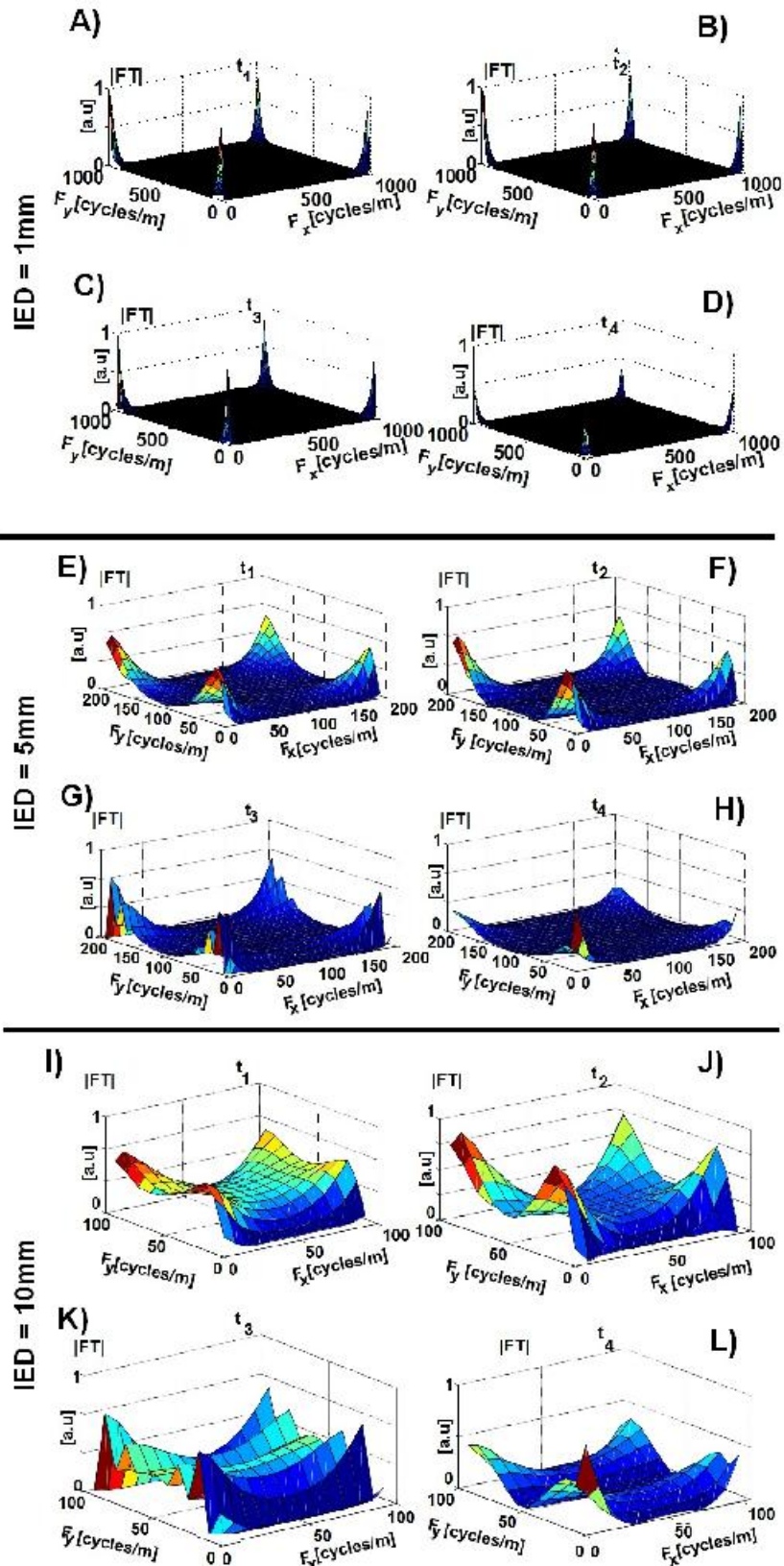
Figure 2.12: See caption on the next page . . .

Figure 2.12: **The magnitude of the 2-D Fourier transform (without removing the DC component) for spatial distribution of simulated monopolar surface potential produced by a single muscle fiber (skin thickness=1mm, subcutaneous tissue thickness=3mm) and 1mm deep into the muscle. Panels are corresponding to the images at different instantaneous time of the simulated action potential i.e. t_1, t_2, t_3, and t_4 respectively. (for spatial time domain images please see figure 2.11. The 127×127 mm^2 skin surface is sampled at A), B), C), and D) 1000 samples/m (reference case, IED=1mm); E), F), G), and H) 200 samples/m (reference case, IED=5mm); I), J), K), and L) 100 samples/m (reference case, IED=10mm).**
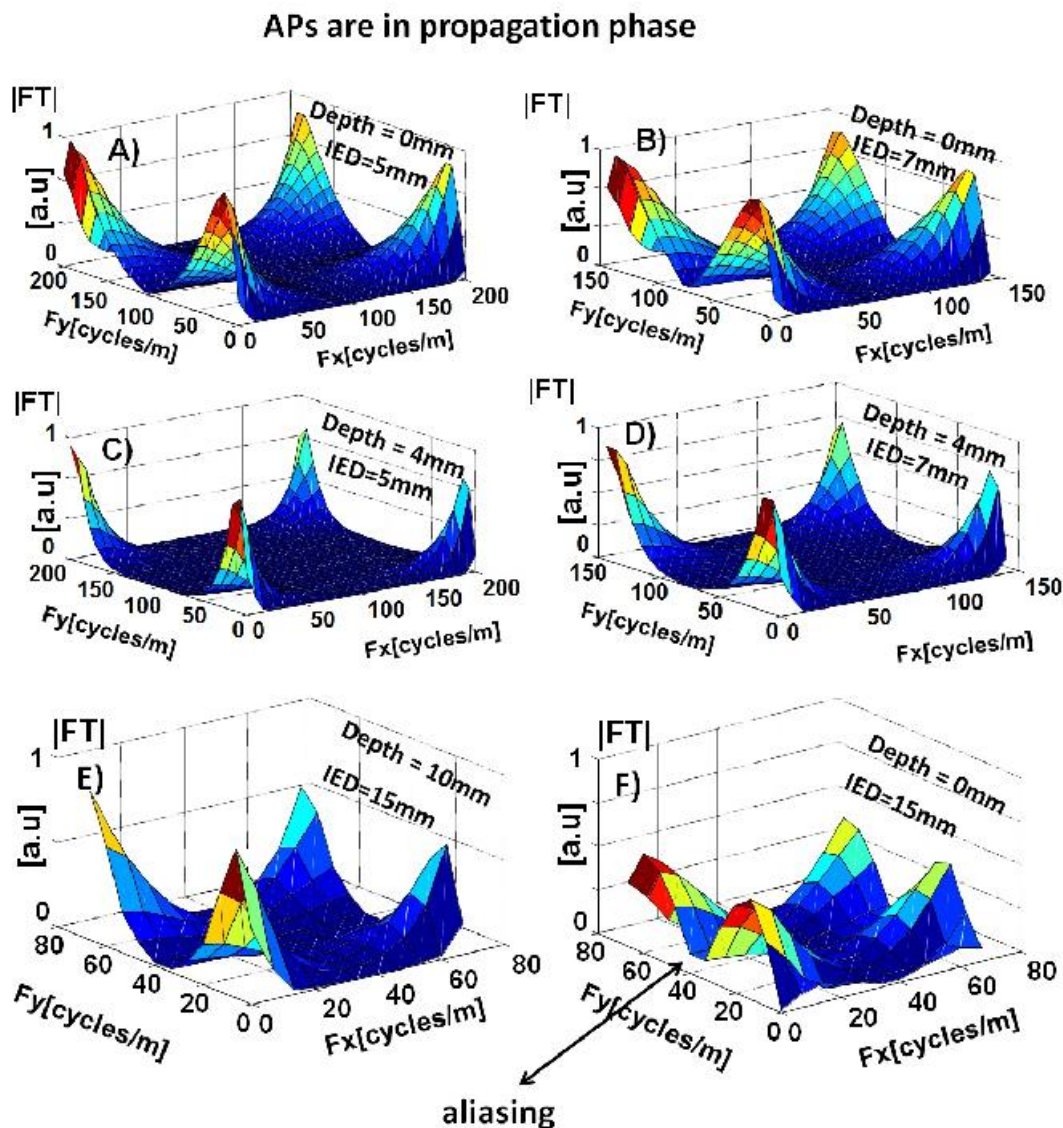
Figure 2.13: One cycle of the magnitude of the 2-D Fourier transform (up to sampling frequency) for spatial distribution...see the continue on the next page...

Figure 2.13: ... from the previous page: of simulated monopolar surface potential produced by a single fiber placed A), B) just below the skin(0mm deep in the muscle); C), D) 4mm deep in the muscle; E)10mm deep in muscle and F)just below the skin(0mm deep in the muscle). For A), C) IED=5mm and B), D) IED=7mm, and for panels E) and F) IED=15mm. Spatial images were obtained at propagation phase(t_2, see figure 2.11). Detection system was considered to cover 127×127mm^2

2.9 Spatial distribution (over the skin) of a simulated motor unit action potential (space-time and frequency domain)

The issue of aliasing in skin potentials produced by a motor unit (MU) is discussed in this section. This case is more general than aliasing of just a single fiber. In reality, the number of motor units per muscle in human may range from about 100 for a small hand muscle to 1000 or more for large limb muscles (3).

The size of a MU depends on the function of the muscle and can contain from 10 to over 3000 muscle fibers[1] . No significant difference is reported between the estimated number of Biceps Brachiis muscle fibers of young (253000) and old (234000) men (6). Muscle fiber number can be estimated by dividing the maximal area of the muscle (e.g. Biceps Brachii) which can be determined by magnetic resonance imaging (MRI) by the mean fiber area of that muscle determined in a muscle biopsy (6). With reference to the Biceps Brachii, a single MU may innervate on average 150 fibers. Considering 250,000 muscle fibers in Biceps Brachii, therefore, the muscle includes approximately 3300 MUs[2].

To study the aliasing in a simulated MU, 150 fibers were simulated using the model developed by Farina and Merletti (5). The fiber length was considered 125mm (60mm as lower and 65mm as upper semi-fiber length). Buchthal and colleagues estimated from electrophysiological evidence in the Biceps Brachii that an average MU innervation zone (IZ) is longitudinally spread over a distance roughly equal to 10% of the fiber length (7). For simulation, the IZ spread was set to 10mm. The skin potentials were simulated as monopolar. Two motor units were simulated individually. One with rather small

---

[1]www.biology.kenyon.edu/coursces/biol09/EMG/EMG.htm

[2]www.excercisephysiologists.com/skeletalmuscle/index.htm

2. EMG AMPLITUDE INDICATORS IN SPACE AND TIME

motor unit territory (radius =2mm) place 2mm deep in the muscle. The second motor unit is a large motor unit with 15mm radius in a circular territory with the center placed at 15.5mm deep into the muscle. Figure 2.14 shows the geometry of the model (motor unit with 15mm territory radius) and the parameters that were used in this study. Similar to the single fiber simulation study presented in the previous section, the spatial distribution of skin potentials at four instantaneous times (t_1, t_2, t_3, and t_4) were studied (t_1 to t_4 are corresponding to 1.5ms, 2.4 ms, 8.8ms, and 16.6ms after start of depolarization respectively). These times were chosen by visual inspection of the detected signal from the electrode placed at the center of detection grid and are related to the action potential at depolarization, repolarization, first end of fiber and second end of fiber. Figure 2.15 shows the simulated skin potential sampled by electrodes with IED=1mm, 5mm, 10mm, and 15mm.

Figure 2.16 show one cycle of the amplitude spectrum in space for sampling frequency 200, 100, and 67 samples/m (i.e. IED=5, 10, and 15mm respectively) with harmonics spaced by 1.0/0.128=7.81 cycles/m of simulated skin potentials (monopolar detection) produced by a single motor unit (see also figure 2.14).

For the IED = 15mm (see figure 2.16 panel "C") the presence of aliasing can be seen for all selected times corresponding depolarization, repolarization, first and second end of fiber. The aliasing is getting worse as the IED increases.
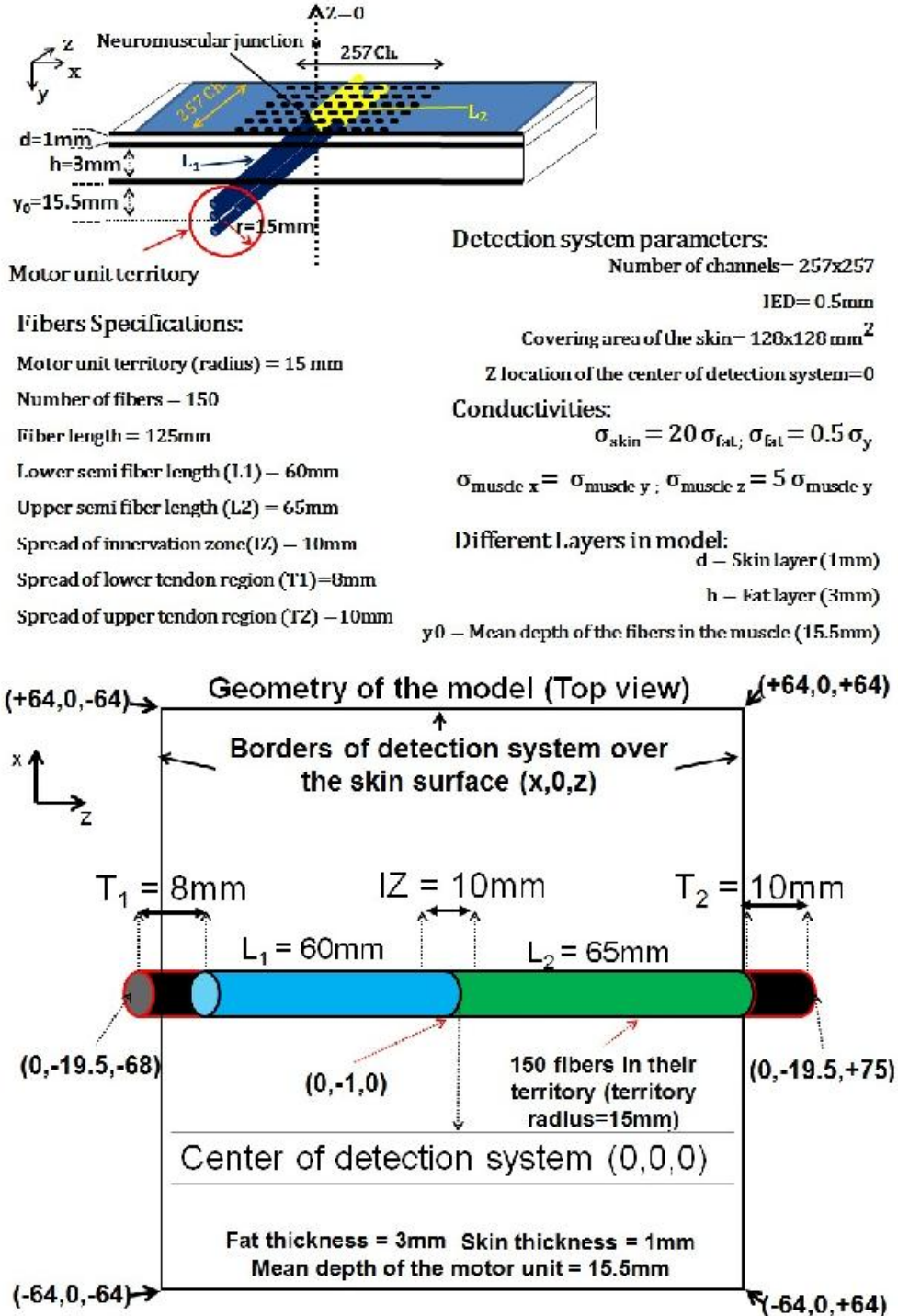
Figure 2.14: **Geometry of the model up) 3-D view and bottom) top view that is used for simulating a single MU including 150 fibers, which are uniformly distributed in the motor unit territory. Specific parameters can be found in the middle of plot. Uniform distribution for the spread of innervation zone (IZ), lower (T1), and upper (T2) tendon regions were considered.**
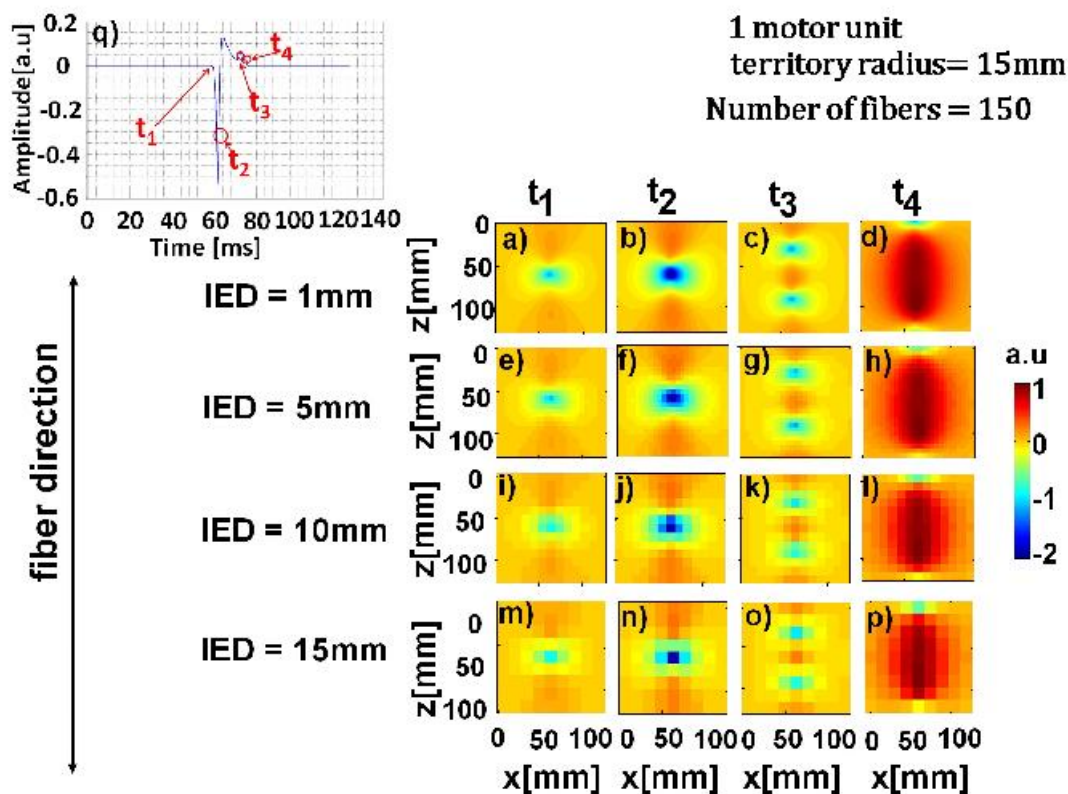
Figure 2.15: Distribution of the simulated monopolar surface potential from a motor unit including 150 fibers uniformly distributed in a circular territory (radius=15mm), the most superficial fiber among 150 fibers was placed 0.5mm deep in the muscle (skin thickness 1 mm, subcutaneous tissue thickness: 3mm). The action potential are at a), e), i), m) start of depolarization(t_1); b), f), j), n) during depolarization(t_2); c), g), k), o) during the first end of fiber effect(t_3); d), h), l), p) at the second end of fiber effect(t_4). a), b), c), and d) are relating to inter electrode distance(IED)=1mm. Panels e), f), g), and h) are for IED=5mm; panels i), j), k), and l) are for IED=10mm; panels m), n), o), and p) are for IED=15mm. The detection system covers 128×128mm^2 in all images. q)Simulated action potential generated by the model shown in figure 2.14 and detected by the electrode over the neuromuscular junction. Four different instant times, when the surface potential images were plotted, indicate start of depolarization (t_1), during depolarization ($t_2 = t_1 + 2.5$ms), during first ($t_3 = t_1 + 13$ms) and second ($t_4 = t_1 + 16$ms) end of fiber effect are also shown on panel q)
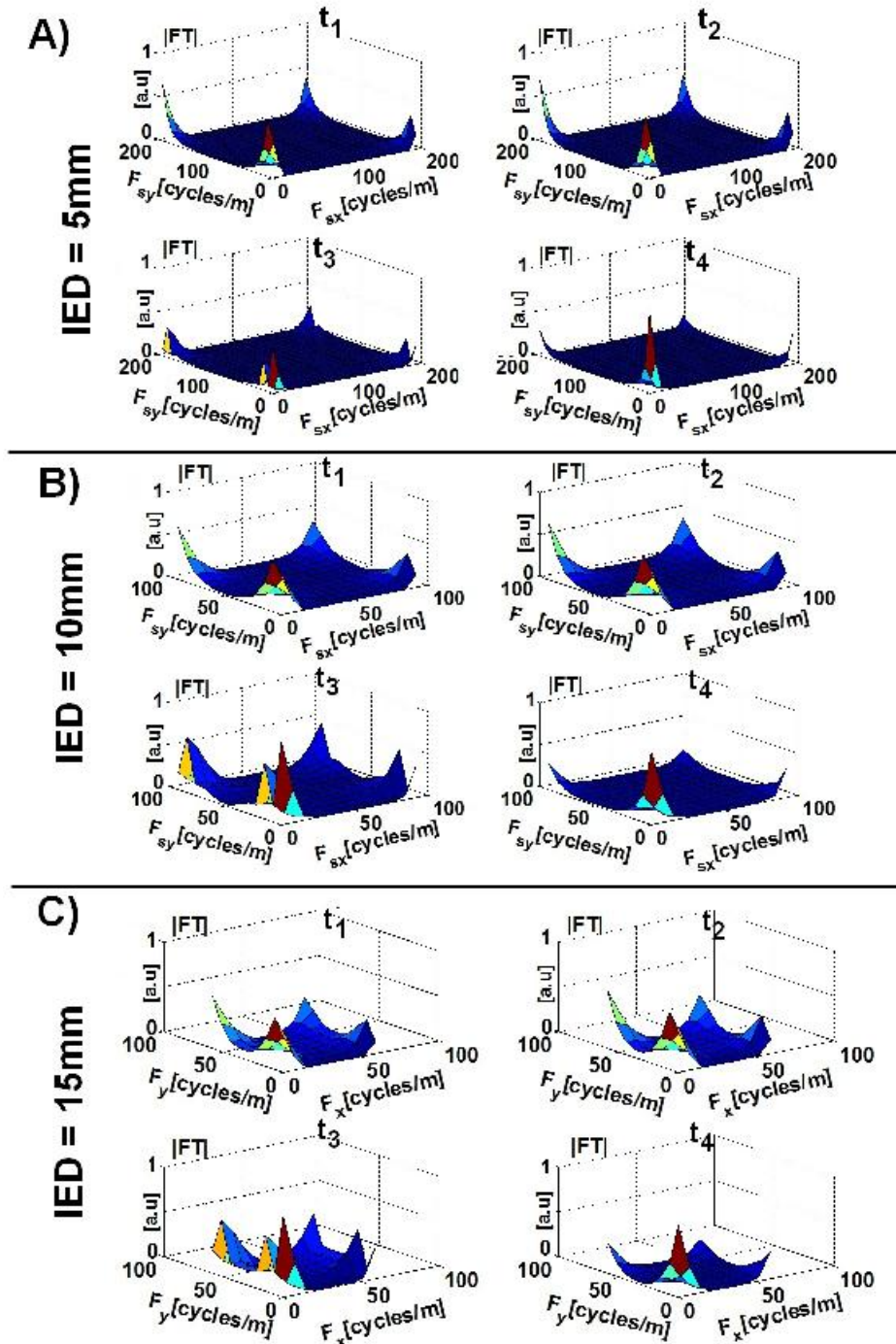
Figure 2.16: One cycle of the magnitude of the 2-D Fourier transform (up to sampling frequency) for spatial distribution of simulated monopolar surface potential produced by a single motor unit . . . continued on the next page...

Figure 2.16: ... from the previous page: including 150 fibers uniformly distributed in a circular territory 15mm radius, 15.5mm deep in the muscle, at 4 different instant times (t_1, t_2, t_3, t_4-see figure 2.15-panel "q") with reference to the action potential time generation (t_1) are represented. The simulated skin potentials ($128 \times 128 \text{mm}^2$) were sampled at A) 200 samples/m (IED=5mm), B) 100 samples/m (IED=10)mm, and C) 67sampls/m (IED=15mm). The spatial domain plots are shown in figure 2.15.

2.10 Symmetry issue in 2-D magnitude Fourier transform of skin potentials

Visual inspection of the magnitude spectrum shows that in one cycle there is no symmetry while it is expected to be as a property of the Fourier transform in a frequency cycle (one half of the Fourier transform of a function is the mirror and complex conjugate of the second half). Two dimensional Fourier transform (FT) of an image ($f(x, y)$) is obtained by two consecutive FT. One FT is done across columns (x-direction) and then the second FT is carried out across the rows (y-direction) of the input matrix (image). The Presence of a dc component (global average) is a unique value in the 3D spectrum plot at the location of (0,0,z). If each row and each column of the image includes a dc component then the 3D-plot will not be symmetric. Considering the simulated skin potential images shown in figure 2.16-panels a), b), c), and d), The average, minimum and maximum of the 4 images corresponding to time instants t_1, t_2, t_3, and t_4 can be found in table 2.1.

Table 2.1: the mean, minimum and maximum of the images shown in panels a), b), c), and d) of figure 2.15

Image at	Mean of the image	min.(Image)	max.(Image)
t_1	-0.0476	-1.1768	0.1290
t_2	-0.1062	-2.0955	0.2843
t_3	-0.1041	-1.2611	0.2124
t_4	0.3654	-1.0807	1.0472

This dc component (Mean of the image) is due to the limited dimension of the 2D

2.10 Symmetry issue in 2-D magnitude Fourier transform of skin potentials

detection grid that cause truncation in space. If the detection system is spread from $-\infty$ to $+\infty$, then the average of the images is expected to be zero.

In our simulated model the detection system covers the fibers in one side (shorter semi fiber) and does not cover 0.5mm of the fiber in other side (upper semi fiber). Also some portion of tendon in shorter part of semi fiber is covered while the upper tendon is placed outside of the detection system (see figure 2.14). Therefore, a "dc" component over the entire space of the grid is expected.

As an example, consider the skin surface potential simulated by the motor unit (see figure 2.14) sampled with the spatial sampling frequency =400 samples/m (IED=2.5 mm). The spatial time domain at t_4 (time instant at end of fiber-see figure 2.15-panel "q") and its 2D magnitude Fourier transform are shown in figure 2.17. It is expected to have a mirrored image (from 0 to 200cycles/m) of what is shown in figure 2.17 at the location from 200 to 400 cycles/m in both x and y directions. The observed asymmetry is due to the presence of dc component in each row and each column in the spatial domain where the action potentials are distributed. To show this fact, by removing the dc component row by row and column by column of the image plotted at panel "a" of figure 2.17, panel "c" will be the result with its 2D magnitude of Fourier transform(panel "d"), which is symmetric after removing the dc components.

As a conclusion, when a finite area of the skin surface is sampled by the detection system, the image of spatial distribution of muscle activity is truncated. Each row and each column of the image has also its own dc component. Removing these dc components (row by row and column by column) from the EMG maps provide a new skin potential map that is not similar to the original map (compare visually panels "a" and "c" of figure 2.17). It is clear that different skin potential maps provides different outputs from an image segmentation application. These imply that removing dc component should not be applied.

In the following section, the issue of image segmentation techniques and a comparison study between three segmentation methods(watershed, h-dome, and k-means algorithms) is discussed.
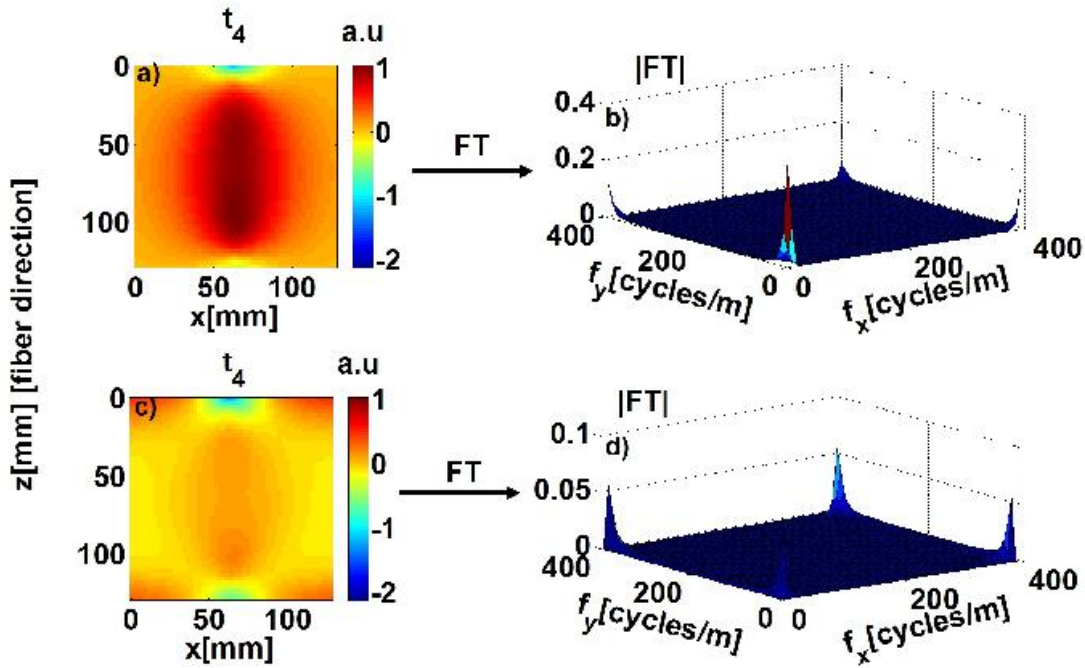
Figure 2.17: Panels a) and c): Skin potentials maps (128mm×128mm) at time instant = t_4 a) before and c) after removing the dc component of each row and column from its row and column respectively; panels b) and d): Magnitude of the 2-D Fourier transform of the images shown in panels "a" and "c" are displayed up to the sampling frequency. Spatial sampling frequency along both "x" and "z" directions is 400 samples/m

2.11 sEMG map segmentation

2.11.1 Introduction

The muscle activity recorded by conventional bipolar electrode configuration is not representative of the whole muscle activity. Using bi-dimensional detection system and electrode grid instead that can provide a spatial activity distribution (a map) is recommended (1). Usually an image (considering of N×M electrode grid) whose pixels are the amplitude (ARV or RMS) of recorded sEMG over a certain time epoch is created for analysis. Since often the whole map might not be of interest, the map needs to be partitioned to different regions of activity. Therefore, finding an automatic way for extracting the most active area over the skin and comparing some of these methods is necessary and is the main goal of this section.

Partitioning of an image is called image segmentation in image processing field. There are many methods that are used for data clustering and image segmentation (8). K-means, Watershed, and h-dome segmentations are three algorithms that have been used to segment the EMG maps in the literature (9, 10, 11). Vieira showed that local activation of skeletal muscles can be automatically tracked from EMGs acquired with a bi-dimensional grid (8×15) of surface electrodes. Vieira et al. also reported (10) that watershed segmentation provides a higher rate of correct classification of active region in ARV map of a simulated muscle activity comparing to simple thresholding technique. No comparison among applied segmentation algorithms is reported so far in the literature. The main questions that arise are:

- Among the segmentation algorithms presented in the literature, which one can identify active portion of a simulated muscle more accurately?

- Which method is more robust to the noise level?

- Which EMG parameters such as amplitude indicators, physiological parameters such as fat thickness and SNR can significantly affect the accuracy of the mentioned segmentation methods?

In this study k-means, watershed, and h-dome methods are studied and their performance are compared to each other in terms of their absolute accuracy and robustness to threshold that is defined over 5% to 90% of maximum of the EMG ARV map, fat

thickness (2 and 6mm), noise level (SNR = 0, 5, 10, 15, and 20 dB), and histogram equalization (with and without equalization).

2.11.2   Method

The signals used in this study are the same used by T. Vieira to validate the watershed algorithm for segmenting EMG images (10). When electromyograms are recorded with a bi-dimensional grid of electrodes, each electrode may be conceived as a pixel "p" with coordinates "x" and "y" given by the rows and columns in the grid. EMG activity is often represented with its average rectified value (ARV) or its root mean square (RMS). For EMG images generated with the ARV and RMS descriptors, pixels intensity (i.e. $IRMS_{emg}$ and $IARV_{emg}$) are computed as eq. (2.60) and (2.61) respectively.

$$IARV_{emg}[x, y, i] = \frac{1}{N} \sum_{n=1+(i-1)N}^{iN} |EMG[x, y, n]| \tag{2.60}$$

$$IRMS_{emg}[x, y, i] = \sqrt{\frac{1}{N} \sum_{n=1+(i-1)N}^{iN} (EMG[x, y, n])^2} \tag{2.61}$$

where i and N stand for the epoch number and the number of time samples in each epoch, respectively. In a gray scale EMG image, dark and light pixels indicate low and high EMG amplitudes respectively. The cluster of pixels with high intensity means a group of electrodes detecting high monopolar EMG activity and likely reflects the spatial selectivity of muscle activation.

For each (totally 30 different) MU population, monopolar surface EMGs (sEMG) from one muscle (60mm large) activated at 60% of maximal voluntary contraction (MVC) and with fat thickness varying between 2 and 6mm were simulated for 1s duration. The simulated detection system comprised 120 channels in a grid arranged in 8 rows by 15 columns with 10mm inter electrode distance(IED).

In Table 2.2, a summary of parameters for simulation is defined. The planar model proposed by Farina and Merletti (5) was used for EMG simulation.

Table 2.2: Description of the parameters used to simulate interference EMG (SD means standard deviation; (12)), EMGs were simulated using the planar model proposed in (5). see also (10)

Parameter	Value
Skin conductivity	4.3×10^{-4} S/m
Fat conductivity	4×10^{-4} S/m
Muscle longitudinal conductivity	40×10^{-4} S/m
Muscle axial conductivity	9×10^{-4} S/m
Fiber mean length	120 mm
Spread of innervation zone	1mm SD of Gaussian Distribution
Spread of tendon endings	2mm SD of Gaussian Distribution
Fiber density	20 fibers per mm^2
Fiber depth	From 0.15 to 15 mm
Motor unit (MU) dimension	Exponential distribution of number of fibers per MU, with ten-fold variation between smallest and largest MUs
Conduction Velocity (CV)	Gaussian distribution with 4m/s mean and 0.3 m/s SD
Recruitment order	From low to high CV
Force level where recruitment stops	60% of maximal voluntary contraction (MVC)
Range of discharge rate	8 to 30 pulses per second (pps)
Variation in discharge rate with force	0.5 pps/%MVC
Inter - pulse interval variability	Gaussian distribution with coefficient of variation 0.2

The geometry of the model used to simulate sEMG signals and an example of raw monopolar signals are presented in figure 2.18.

Five different noise (Gaussian, $\mu = 0, \sigma = 1$) levels ($SNR = 0$ dB to $SNR = 20$ dB in steps of 5dB) were considered as additive noise to the signals. The average of the RMS values (each RMS is calculated over 1s epoch) of those electrodes placed over the active portion of muscle (totally 36 electrodes of the detection grid) was used to calculate each of the noise level amplitude. Since the watershed method is validated for

ARV sEMG maps segmentation in the literature (10), the ARV maps were used as the images for partitioning in the next section. Although, it is shown (see section 2.6.3 and section 2.7) that an RMS indicator is more robust with respect to ARV, the comparison was done on ARV maps.
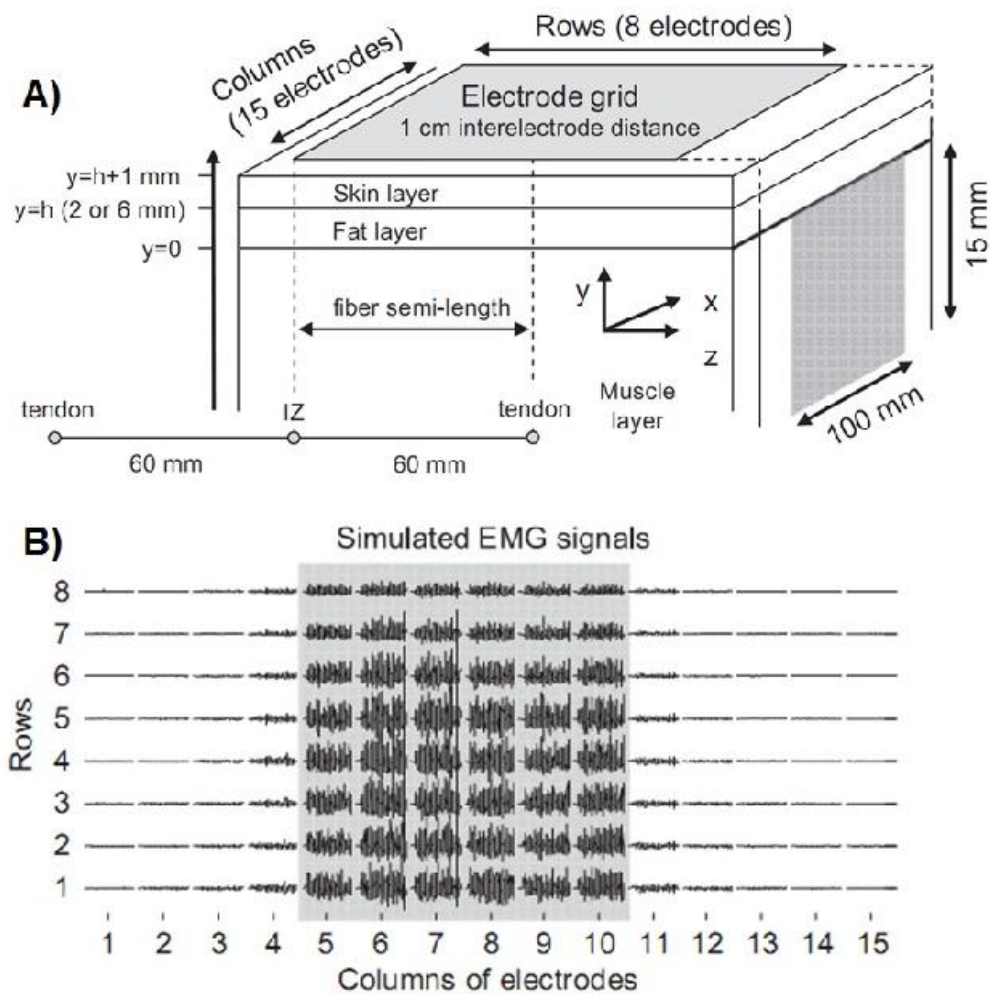
Figure 2.18: A) Schematic and specification of the simulated muscle portion and of the grid of electrodes. The standard area corresponds to the portion of muscle for which fiber potentials were simulated. B) Example of raw monopolar EMGs simulated for the muscle configuration shown in (A). Courtesy of Vieira and Merletti (10).

2.11.3   Watershed segmentation algorithm

The watershed technique segments gray scale images by considering pixels with high intensity as elevated surfaces and pixels with low intensity as catchment basins. Similarly, the intensity of pixels in EMG images can be represented as a topographical relief. The algorithm identifies the location of ridges (watersheds) in the gray scale image and labels each catchment basin (group of pixels), surrounded by such ridges, with a different number (13).

Since pixels with high ARV amplitude would be conceived as elevated surfaces, clusters of these pixels would be partitioned if the watershed algorithm was applied directly to EMG images. In this case, pixels with high gray intensity (i.e. high neuromuscular activity) would constitute the watershed line, which is not desired. Rather, watershed lines could be estimated by processing the gradient of I_{emg}. Assuming that pixels represent the spatial sampling of I_{emg}, the edges of subsets with low and high EMG activities are computed as the Euclidean norm of I_{emg} gradient (g_{emg}), which gives the rate of change in gray intensity

$$
g_x[m,n;i] = F^{-1}\left[S^T \sum_{m=1}^{N_r} \sum_{n=1}^{N_c} I_{emg}[m,n;i]e^{-j2\pi\left(\frac{k_x m}{N_r} + \frac{k_y n}{N_c}\right)} \right]
$$
$$
g_y[m,n;i] = F^{-1}\left[S \sum_{m=1}^{N_r} \sum_{n=1}^{N_c} I_{emg}[m,n;i]e^{-j2\pi\left(\frac{k_x m}{N_r} + \frac{k_y n}{N_c}\right)} \right]
$$
$$
g_{emg} = \sqrt{g_x^2 + g_y^2}
$$

(2.62)

where F^{-1} is the inverse of the Fourier transform operator, k_x and k_y indicate the spatial frequencies, N_r and N_c stand for the number of rows and columns of electrodes, T indicates the transpose operator, and S is the bi-dimensional Fourier transform of the zero-padded Sobel operator

$$
S = \begin{vmatrix} +1 & +2 & +1 \\ 0 & 0 & 0 \\ -1 & -2 & -1 \end{vmatrix}
$$

(2.63)

As the number of clusters produced by the watershed segmentation depends on the number of regional minima in the gradient, the problem of over segmentation can be minimized by flattening sharp transitions of gray intensity in g_{emg} with image opening followed by image closing operation (10). Opening and closing can be envisaged as the

attenuation and intensification of pixels with intensity exceeding or not reaching some threshold, respectively. Opening and closing g_{emg} by the structuring element "v" are defined (14) as:

$$g_{emg} \circ v = (g_{emg} \ominus v) \oplus v \tag{2.64}$$

$$g_{emg} \bullet v = (g_{emg} \oplus v) \ominus v \tag{2.65}$$

where $\circ$ and $\bullet$ indicate opening and closing, respectively. $\oplus$ and $\ominus$ are the Minkowski operators for addition and difference, defined as

$$(g_{emg} \oplus v =)(p) = \max_{z \in D_v}[g_{emg}(p+z)] \tag{2.66}$$

$$(g_{emg} \ominus v =)(p) = \min_{z \in D_v}[g_{emg}(p+z)] \tag{2.67}$$

where D_v is the domain of the structuring element v, which was chosen as a square grid (3×3) of zeros (which means that $z \in [-1, 0, 1] \times [-1, 0, 1]$.

The openedclosed gradient of I_{emg} provided a flattened surface for the segmentation. Clusters of EMG activity were then identified properly with the watershed algorithm (10). In this study, the validated method proposed by T. Vieira (10) is used for automatic identification of local variations in simulated sEMG activity with a bi-dimensional array of electrodes. It should be noted that this method consist of steps other than just applying the watershed algorithm.

2.11.4   h-dome segmentation algorithm

Mathematical morphology provides an operator called "reconstruction" that extracts connected components of an image which are marked by another image. A connected component is a set of connected pixels that share a specific property, "V". "V" can be pixel intensity value. Two pixels, "p" and "q" are connected if there is a path from "p" to "q" of pixels with property "V". A path is an ordered sequence of pixels such that any two adjacent pixels in the sequence are neighbors.

Reconstruction is a transformation defined in binary images extendable to gray scale images. Mathematically speaking, a gray scale image is a mapping from a finite rectangular subset D_I of the discrete plane $\mathbb{Z}^2$ into a discrete set of gray levels $[0, N-1]$. Pixels of a binary image can only take values 0 or 1. Segmentation is often regarded as

the set of pixels with value 1. Reconstruction of a binary image I from another binary image (J) which $J \subseteq I$, is the union of connected components of I which contain at least a pixel of J. I and J are usually called mask and marker respectively in the literature (15) and are defined on the same discrete domain.

$$\rho_I(J) = \cup_{J \cap I_K} = \phi^{I_K} \tag{2.68}$$

Figure 2.19 (panels "A" and "B") explain graphically the reconstruction in a binary image. The connected components (I_1, I_3, I_5) that are marked with marker J are extracted after reconstruction transformation. Reconstruction can also be defined as iterative geodesic dilation. Before describing geodesic dilation, let's define the geodesic distance term. Given a data set (e.g. image I), the geodesic distance (d_I) between two pixels p and q in I is the shortest paths of I joining p to q (see figure 2.19 panel "C") . The geodesic dilation of size $n \geq 0$ of a set J such that $J \subseteq I$ within $I \in \mathbb{Z}^2$ is the set of pixels (p) of I whose geodesic distance to J is smaller or equal to n (see eq. (2.69)).

$$\delta_I^{(n)}(J) = \{p \in I | d_I(p, J) \leq n\} \tag{2.69}$$

Geodesic dilation of size "n" can be obtained by iterating "n" elementary geodesic dilation. i.e.:

$$\delta_I^{(n)}(J) = \underbrace{\delta_I^{(1)} \circ \delta_I^{(1)} \circ \delta_I^{(1)} \circ \ldots \delta_I^{(1)}}_{n \text{ times}} \tag{2.70}$$

and elementary geodesic dilation is defined as:

$$\delta_I^{(1)}(J) = (J \oplus B) \cap I \tag{2.71}$$

where $\oplus$ is dilation operator and B denote structuring element. An example of the structure element B is a 3×3 square, that is:

$$B = [(-1, -1), (-1, 0), (-1, +1), (0, -1), (0, 0), (0, +1), (+1, -1), (+1, 0), (+1, +1)]$$

Therefore, reconstruction of I from $J \subseteq I$ is:

$$\rho_I(J) = \lim_{n \to \infty} \delta_I^{(n)}(J) \tag{2.72}$$

Reconstruction is an increasing transformation and any increasing transformation defined for binary images can be extended to gray scale images. Let's define the gray scale
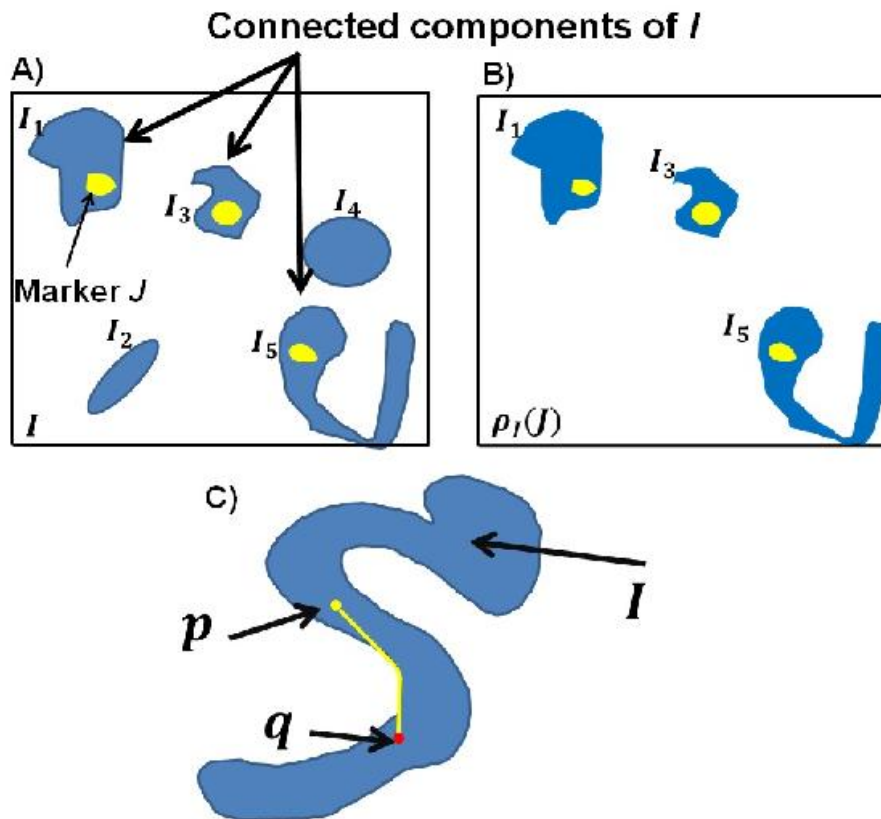
Figure 2.19: A) the binary image I is constituted of different components (I_1, I_2, I_3, I_4, I_5). The marker J is another binary image that satisfies $J \subseteq I$. **B)** I after applying the reconstruction transform($\rho_I(J)$). Reconstruction transform (the union of connected components of I, which contain at least a pixel of J) extracts the connected components of I. **C)** Geodesic distance in a data set (image I) is defined as the shortest joining paths of I between two pixels "p" and "q".

image I in the discrete domain $\mathbb{D}$ with values that are taken from $[0, N-1]$. Successive thresholds $T_K(I)$ of I is defined as:

$$T_K(I) = \{p \in \mathbb{D}_I | I(p) \geq K\}, \quad K \in [1, N-1] \tag{2.73}$$

Considering $T_K(I)$ sets of image I, the reconstruction for gray scale image I is computed as:

$$\forall p \in \mathbb{D}_I, \quad \rho_I(J)(p) = max\{K \in [1, N-1] \ \big| p \in \rho_{T_K(I)}(T_K(J))\} \tag{2.74}$$

In other words, reconstruction in a gray scale image is considered as an increasing transformation of the marker in the mask in a way of reaching to the local maximum level of the marker or boundaries of the mask.

Let's define the marker image as the mask such that each of its pixels value decreased by a constant value h (plateau altitude in the topographical image I) i.e. $J = I - h$ and then extract the connected components by applying the reconstruction. By subtracting the reconstructed image from the original image (I), the peaks which are also called domes can be extracted from the original image I (see figure 2.20). All this procedure is called h-dome transformation in image processing and is used to extract domes. h-dome transformation extract peaks of the connected components in the image without involving any size or shape criterion. The only parameter (h) is related to the height of these structures. Connected components of pixels with a given value h (plateau at altitude h in a topographical image like EMG) of a given gray scale image I are pixels belonging to regional maximum that is called M such that every pixel in the neighborhood M has a strictly lower value (15).

2.11.5 K-means segmentation algorithm

K-means (16) is one of the simplest unsupervised learning algorithms that solve the well-known clustering problem. The procedure follows a simple and easy way to classify a given data set through a certain number of clusters (assume "k" clusters) fixed a priori. The main idea is to define "k" centroids, one for each cluster. These centroids should be placed (arbitrarily) in a cunning way because different locations cause different result. So, the better choice is to place them as much as possible far away from each other. The algorithm is composed of the following steps:
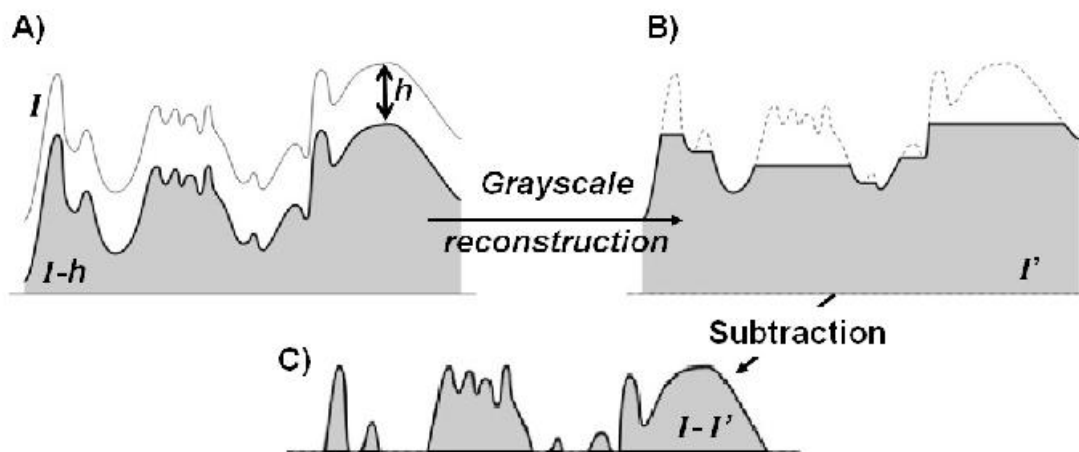
Figure 2.20: Grayscale reconstruction (B) from the topographical image I (A) and detection of the regional maximum by subtracting the gray scale reconstruction from I (C). The image which is defined as $I - h$, where h is a constant (plateau altitude in the topographical image I), is usually called marker and the image I is called mask in the literature (15).

1. Arbitrarily place K points into the space represented by the objects that are being clustered. These points represent initial group centroids.

2. Assign each object to the group that has the closest centroid.

3. When all objects have been assigned, recalculate the positions of the K centroids.

4. Repeat Steps 2 and 3 until the centroids no longer move. This produces a separation of the objects into groups.

Although it can be proved that the procedure will always terminate, the k-means algorithm does not necessarily find the optimal configuration, corresponding to the global objective function minimum. The algorithm is also significantly sensitive to the initial randomly selected cluster centers. The k-means algorithm can be run multiple times to reduce this effect[1].

---

[1] www.home.dei.polimi.it/matteucc/Clustering/tutorial_html/kmeans.html

2.11.6 Accuracy of the algorithms

Segmentation accuracy depends on the occurrence of false positive and false negative pixels. False positives correspond to electrodes positioned above inactive muscle portion and included in the active cluster after segmentation. Electrodes over active muscle portion and not included in the active cluster are false negatives. True positive is the number of those electrodes found by the segmentation algorithm as the active region and also belonging to the active portion of simulated muscle (placed under the electrode grid with corner electrodes positioned at (3,5), (3,10), (8,5), and (8,10) in Cartesian coordinate (x,y)).

Based on the simulation (see section 2.11.2 on page 68), there is only one active portion in the detection grid. The map of active region -the output of segmentation algorithm- is a binary image (an image with 0s and 1s, with 1s corresponding to channels over the active region of simulated muscle). The accuracy of segmentation of simulated EMG images was evaluated as the ratio between the sum of true positive and true negative electrodes and the total number of electrodes in the grid (totally 120 channels=8×15). True negative is the number of those electrodes that are found by the segmentation algorithm belonging to the inactive region and true positives is the number of those electrodes belonging to the active region of the simulated muscle portion.

$$Acc = 100 * \left(\frac{T_{Pos.} + T_{Neg.}}{N_{ch}} \right) \tag{2.75}$$

where Acc, T_{Pos}, $T_{Neg.}$, N_{ch} are accuracy in percentage, true positive, true negative and total number of channels in the detection grid, respectively.

2.11.7 Implementing algorithms

Accuracy for the algorithm proposed by Vieira (10) was recalculated using the same simulated EMG signals and compared with accuracy proposed by two other algorithms (K-means and h-dome). For the watershed algorithm those electrodes belonging to the watershed line which are connected (4-type connectivity) to the active portion of simulated muscles are also considered as active segmented part. Connectivity is defined as a connected set of pixels. In a 4-connectivity type, each pixel (p) has four connected neighbors (N) top, bottom, right and left. The diagonally touching pixels are not considered to be connected. In 8-connectivity, each pixel (p) has eight connected neighbors

(N) including the diagonally touching pixels (17).

2.11.8 Results and Discussion

An example of simulated ARV map (monopolar, 5th simulated subject (MU population), Fat thickness= 6 mm), its equalized form with two different noise (Gaussian) levels ($SNR = 0$ dB, $SNR = 20$ dB) is presented in panels "A", "B", "C", and "D" of figure 2.21.
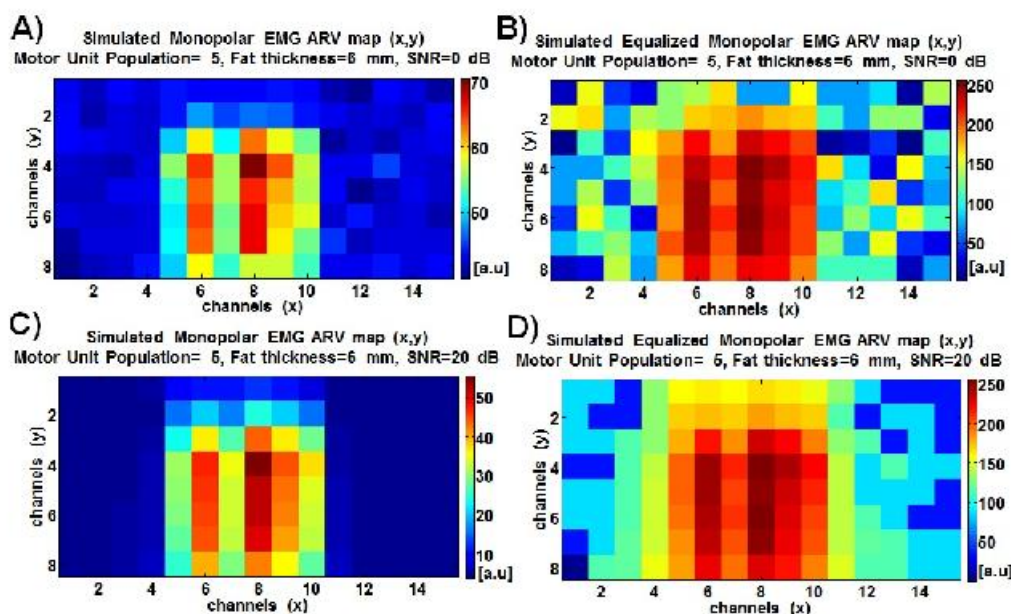
Figure 2.21: An example of simulated ARV maps (8x15) before A), C) and after B), D) equalization process with noise level A), B) $SNR = 0$ dB and C), D) $SNR = 20$ dB of the 5th MU population with fat thickness simulated at 6mm.

Equalization (adjusting contrast) usually increases the global contrast of an image especially when the image is represented by close contrast values. This allows for areas of lower local contrast to gain a higher contrast. Histogram equalization accomplishes this by effectively spreading out the most frequent intensity values (see figure 2.21). The outputs of the segmentation algorithms applied to an equalized simulated ARV

map are shown in figure 2.22. Figure 2.22 shows the ability of the 3 algorithms in detecting the active portion of the grid. In h-dome, threshold level was used to define the parameter h for providing the marker image ($M_{rk} = ARV - h$ where M_{rk} and ARV are the marker and ARV images (see section 2.11.4). The "h" parameter is defined as $h = thr * \max(ARV)$ where "thr" is the threshold level.
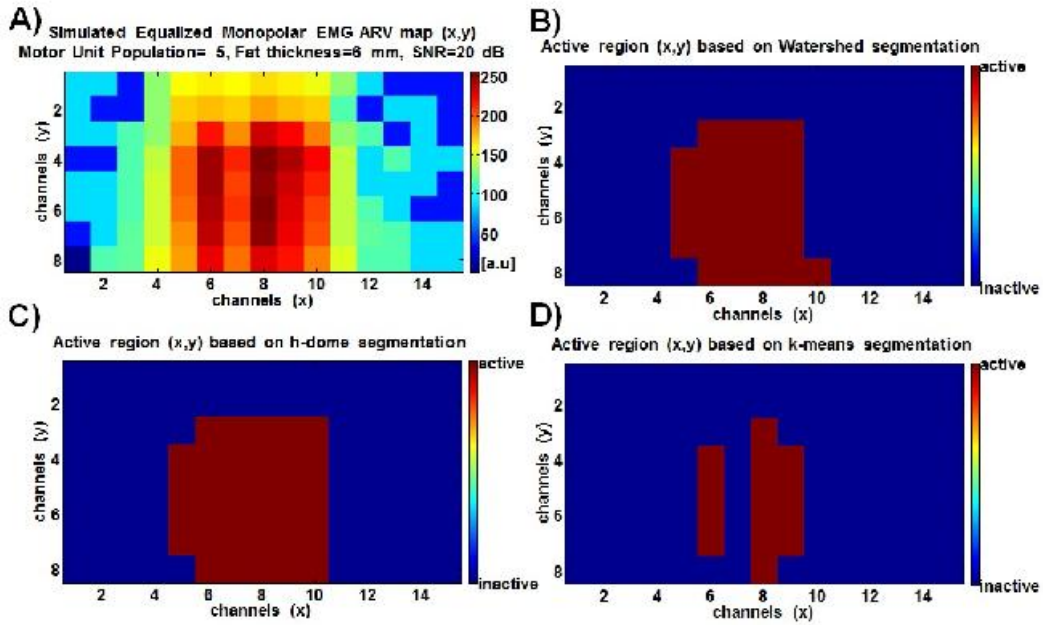
Figure 2.22: **An example that shows the ability of watershed, h-dome and K-means algorithms in detecting the active portion of a simulated EMG map of A) equalized simulated monopolar ARV map (8×15 channels, fat thickness = 6mm, SNR = 20dB) and the active (red) and inactive (blue) regions found by B) watershed, C) h-dome, and D) k-means segmentation. The three algorithms have been applied to the equalized ARV map (input image). The active region B) is defined as 70% of the maximum of the input image in watershed. h-dome marker is defined as subtraction of 30% of the maximum of input image from the input image. Five clusters assumed in k-means algorithm (panel D). Note that the parameters used in the three mentioned segmentation methods are just examples and different parameters might provide different results. Effects of these parameters on segmentation have been discussed in the text in order to compare the segmentation methods.**

Regardless of threshold, mean and standard deviation over 540 samples (540=18*30,

i.e. 18 threshold levels for 30 set of signals) of the accuracy of EMG image segmentation when the watershed and h-dome methods were applied with and without histogram equalization at five noise levels (SNR = 0, 5, 10, 15, and 20 dB) are reported in table 2.3. A peer to peer comparison between corresponding conditions (fat thickness, equalized/non-equalized (eq/non-eq), and SNR levels) in table 2.3 reveals that the average value of watershed segmentation accuracy is higher than h-dome except for non-equalized images of fat thickness = 2mm, SNR = 20 dB. At SNR = 20 dB with non-equalized ARV maps the average accuracy is slightly higher (about 2%) for h-dome. Table 2.3 also shows that watershed provides generally less variation (smaller standard deviation), which implies that watershed method is more robust to defining threshold, equalizing and noise level in partitioning the EMG maps with respect to h-dome.

Figure 2.23 shows the average value (across the SNR levels) of the accuracy resulting from watershed segmentation with equalization is higher or equal to those obtained without equalization. This is not true for the h-dome segmentation. The accuracy provided by h-dome segmentation with equalization is higher for noisy simulated ARV images or smaller in higher SNR levels in comparison with non-equalized images.

Changes of accuracy versus fat thickness conditions (2 and 6mm) for equalized and non-equalized simulated ARV images for both h-dome and watershed segmentation is shown in Figure 2.24. This figure shows that equalization has more effect on accuracy segmentation for fat thickness of 6mm for h-dome in comparison with watershed method.

For studying the effect of different factors such as fat thickness, equalization, and SNR levels, ANOVA and post hoc (Bonferroni) tests were applied. In h-dome method, the accuracy significantly ($p < 0.001$) depends on equalization for both fat thicknesses and all SNR levels except SNR=10 dB. In watershed segmentation, the equalization significantly ($p < 0.001$) improve the accuracy at SNR=0, 5, 10 dB for fat thickness=2mm and at SNR=0, 5 dB for fat thickness=6mm.

For h-dome segmentation method, Vincent reported that the choice of "h" is not critical, since a range of values yield correct results and this characteristic is of interest for complex segmentation problems (15). But in segmenting the EMG maps using h-dome, the threshold level ($h = thr * \max(ARV)$, $M_{rk} = ARV - h$ where thr is the threshold level, M_{rk} and ARV are the marker and ARV images; see also section 2.11.4

on page 72), which is used for creating "h" significantly ($p < 0.001$) affects (increase or decrease) the accuracy of the results as shown in figure 2.23. In both watershed and h-dome methods, the accuracy of simulated EMG image segmentation significantly depended on the noise level ($p < 0.001$) (see figure 2.23).

Table 2.3: **Mean values (SD; N=18 threshold levels from 5% to 90% of the maximum of simulated EMG-ARV map in steps of 5%) of the percentage accuracy (%) of EMG image segmentation when the h-dome and watershed methods were applied with (eq.) and without (non-eq.) histogram equalization. EMG images were created from simulated signals (n=30 sets of signals) with the fat thickness adjusted at 2 and 6 mm, with SNR levels varying from 0 to 20 dB in equal steps of 5 dB. The mean(SD) of accuracy in all conditions reported in this table is 73.1(19.55)% for h-dome and 82.2(9.48)% for watershed segmentation. In h-dome, threshold level was used to define the parameter h for providing the marker image ($M_{rk} = ARV - h$ where M_{rk} and ARV are the marker and ARV images. the h parameter is defined as $h = thr * \max(ARV)$ where "thr" is the threshold level. In the watershed algorithm, the active region is defined as $thr\%$ of the maximum of the image that is used for segmentation.**

	h-dome segmentation method				watershed segmentation method			
	Fat layer				Fat layer			
	2mm		6mm		2mm		6mm	
SNR	eq.	non-eq.	eq.	non-eq.	eq.	non-eq.	eq.	non-eq.
0	75(18)	53(27)	74(17)	54(27)	83(11)	71(13)	87(6)	72(15)
5	73(18)	65(26)	74(18)	66(27)	84(9)	77(14)	85(7)	79(13)
10	73(19)	76(22)	73(18)	76(22)	84(9)	81(13)	84(7)	82(12)
15	72(20)	82(15)	73(19)	83(16)	83(9)	84(11)	83(8)	85(11)
20	73(21)	88(8)	73(19)	86(9)	84(8)	85(10)	85(7)	86(9)
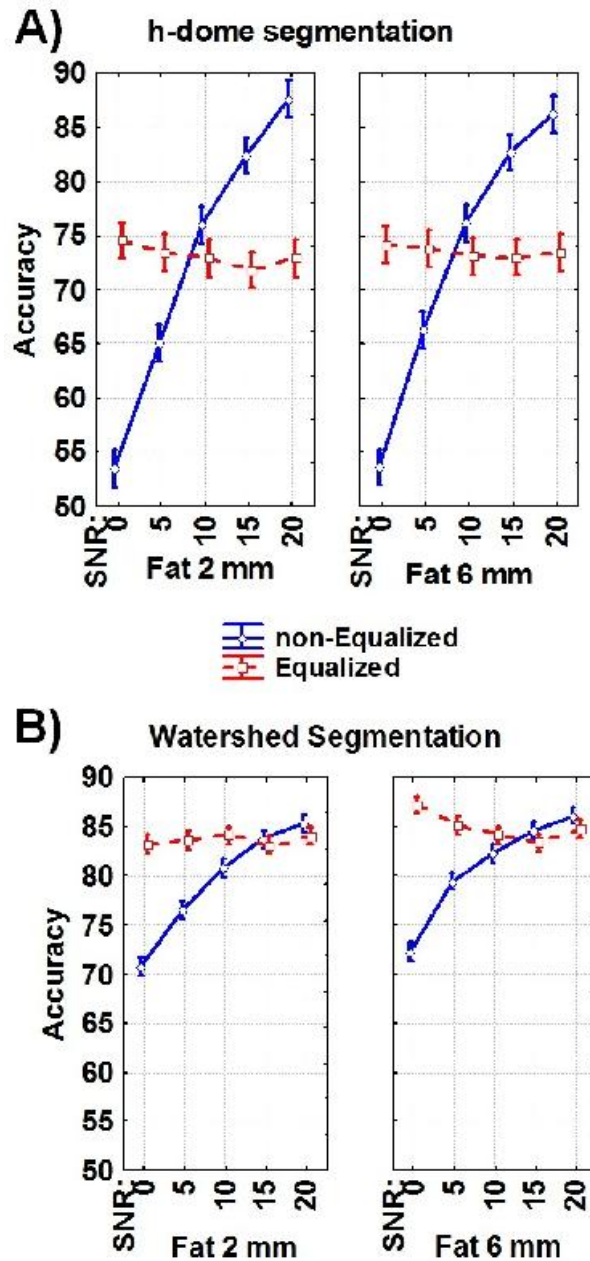
Figure 2.23: **Average accuracy (N=18 threshold levels, 30 set of signals; averaging was done over 540=18*30 values considering Fat thicknesses, SNR levels, and Equalization)versus SNR, when A) h-dome, B) watershed segmentation methods were applied. ARV EMG images were created from simulated signals (n=30 sets of signals) with the fat thickness simulated at 2 and 6mm and with SNR levels varying from 0 to 20 dB in equal steps of 5 dB. Vertical bars denote 0.95 confidence intervals.**
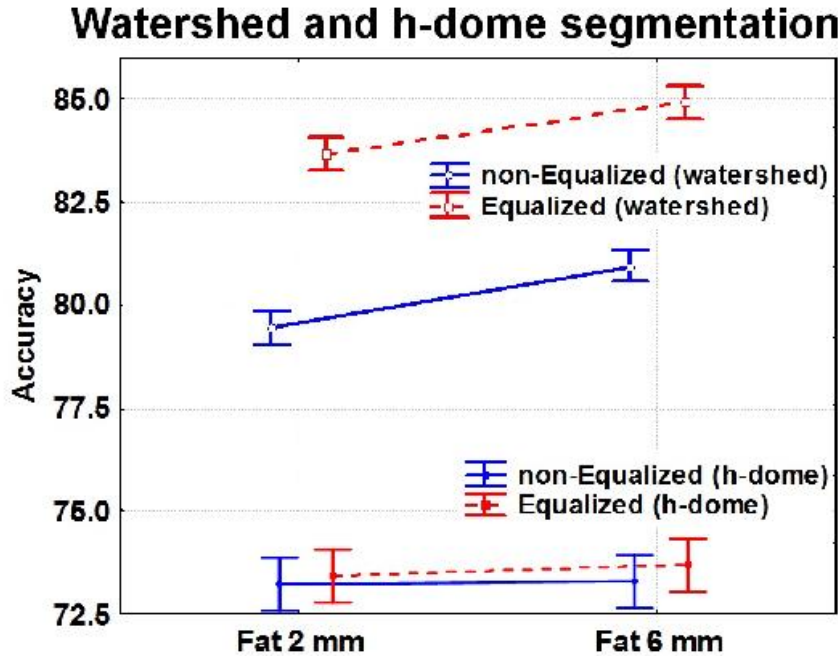
Figure 2.24: Average (N=30*18*5=2700; 30 set of signals, 18 threshold levels, 5 SNR levels) of accuracy (h-dome and watershed segmentation methods) versus fat thickness applied to the equalized and non-equalized simulated ARV maps considering five different noise levels (SNR =0, 5, 10, 15, and 20 dB) and threshold level ranging from (5 to 90% of maximum of simulated ARV map in steps of 5%). Vertical bars denote 0.95 confidence intervals. Filled circles and square representing h-dome. Unfilled circles and squares were used for watershed segmentation. Red dashed and blue solid lines representing segmentation with and without histogram equalization respectively.

In figures 2.25 and 2.26, average accuracy versus threshold is depicted when watershed and h-dome were applied respectively. In watershed the highest accuracy (average among 30 sets of MU populations) peaked at 70% for all five different noise levels after histogram equalization, while for non-equalized simulated ARV maps the accuracy peaked at different thresholds for different noise levels. In h-dome the highest average accuracy was observed at threshold = 30% of the maximum of ARV map for equalized ARV maps at the different noise levels. Figures 2.25 and 2.26 also show that the pattern of changes in accuracy versus threshold is similar for the fat thickness=2 and 6mm.
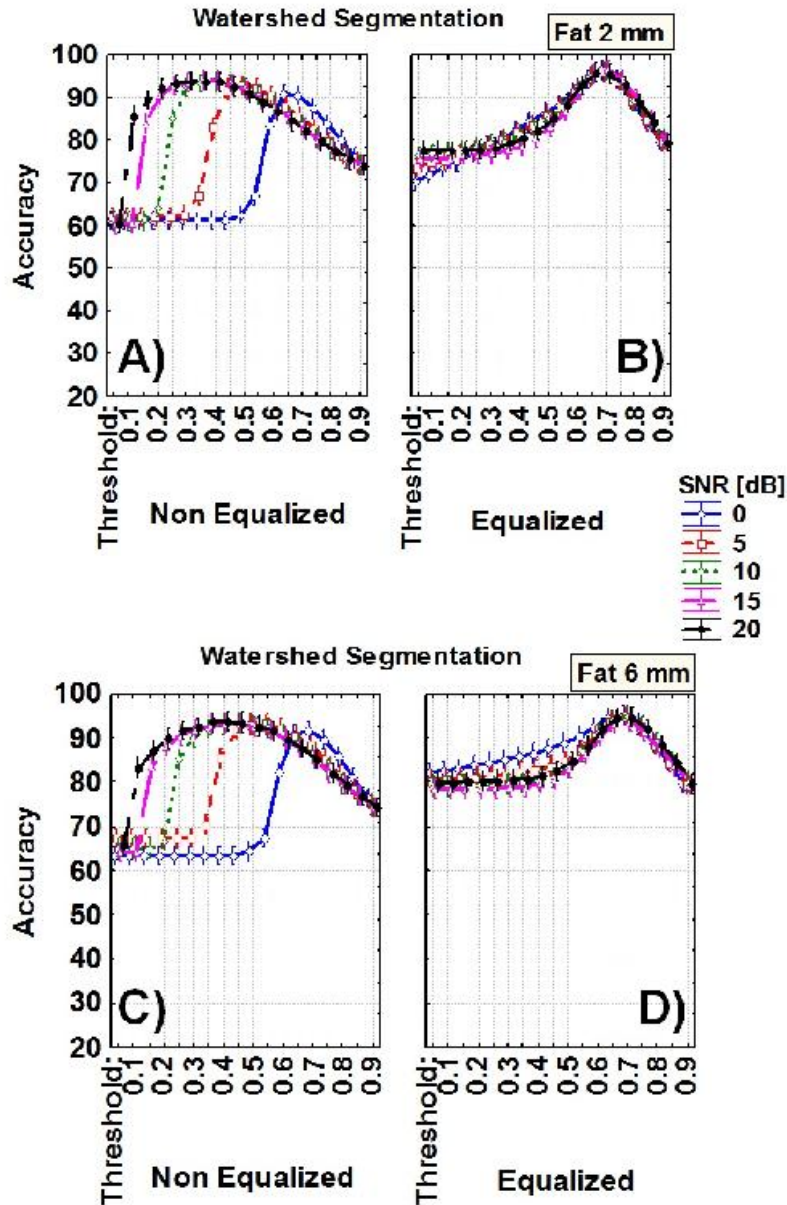
Figure 2.25: Average (N=30) accuracy versus threshold applying watershed segmentation method to the simulated ARV maps (30 different MU populations described in (10) for non-equalized (A and C), equalized (B and D), fat thickness 2 (A and B) and 6mm (C and D) in five different noise levels.
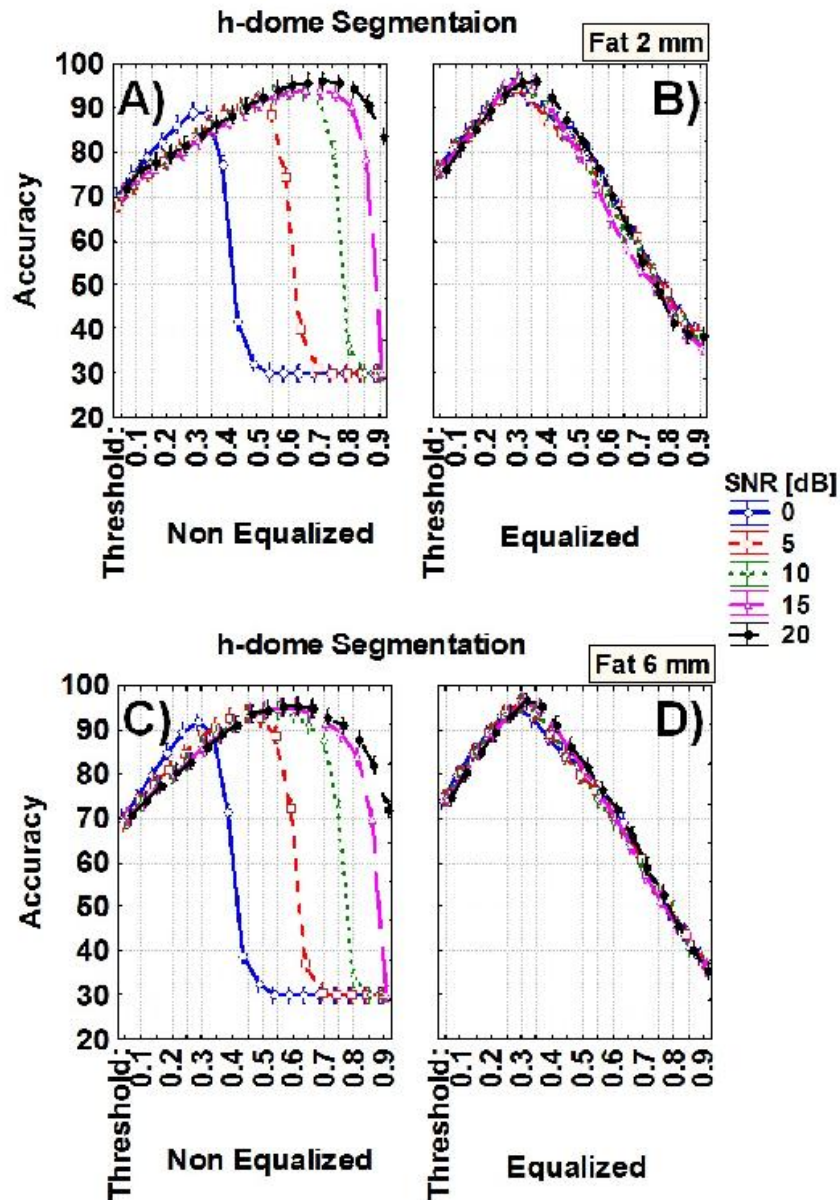
Figure 2.26: Average (N=30) accuracy versus threshold applying h-dome segmentation method to the simulated ARV maps (30 different MU populations) for non-equalized (A and C), equalized (B and D), fat thickness 2 (A and B) and 6 mm (C and D) in five different noise levels.
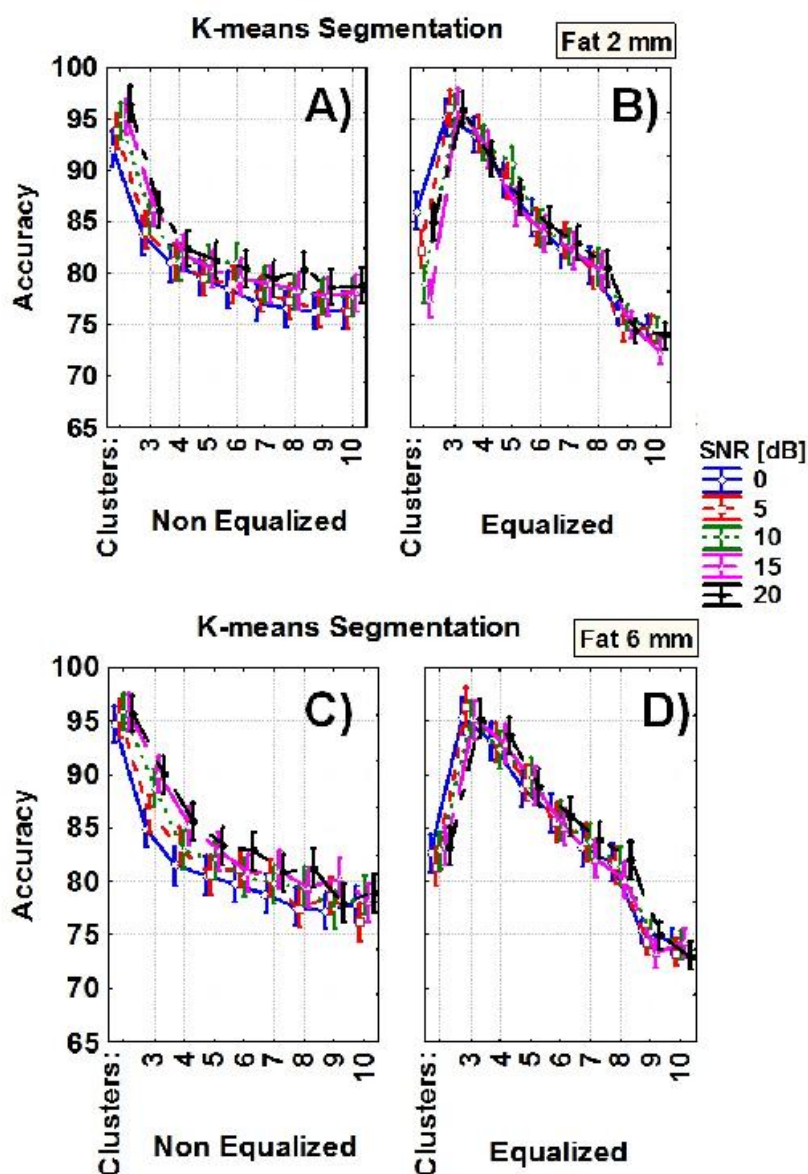
Figure 2.27: Average (among 30 different MU populations) accuracy versus number of clusters for five different noise levels (SNR=0, 5, 10, 15, and 20 dB) resulted from applying k-means segmentation method, regarding non-equalized (A and C), equalized (B and D), fat thickness 2 (A and B) and 6 mm (C and D). One active region is simulated; therefore two clusters (active and inactive) are present in the simulated ARV maps.

Figure 2.27 shows the accuracy versus number of clusters in k-means segmentation

algorithm. Note that in this segmentation the number of clusters must be defined before segmentation. From our simulated data any incorrect guess for the number of active regions in the detection grid provide less accuracy in non-equalized and lower or higher accuracy in segmenting of equalized simulated ARV maps. Here the best accuracy is obtained when two clusters (inactive and active regions) is considered as a priori for non-equalized simulated ARV maps. Regardless of SNR levels, fat thickness, equalization procedure, and number of clusters, k-means resulted 82.3% accuracy in average. Statistical test (ANOVA) shows that in k-means method, accuracy significantly depends ($p < 0.001$) on SNR, equalization, number of clusters, and fat thickness. Although this segmentation needs to know the number of clusters a priori, it has been used in the literature (9).

2.11.9 Conclusion

Three segmentation algorithms K-means, watershed, and h-dome have been tested using simulated EMG maps (30 simulated MU population for each of the two fat thickness (2mm and 6mm) in five different noise levels with and without equalization as described in (10)). They showed ability of detecting the active regions of the simulate EMG maps (8×15 electrodes). K-means segmentation method needs the number of clusters to be known a priori and this can be considered as its strong limitation. The advantage of watershed and h-dome is that they do not need any a priori knowledge about the number of active regions in the EMG maps. In general, equalization (see section 2.11.8 on page 78), provides higher accuracy with respect to the un-equalized ARV maps. In segmentation of 30 equalized simulated ARV images, the highest accuracy was obtained at 70% and 30% of the maximum of ARV map for fat thickness=2 and 6mm, at 5 different noise levels by applying watershed and h-dome respectively. Regardless of threshold in h-dome and watershed methods, number of clusters in k-means method, and considering factors such as fat thickness, noise level and histogram equalization, the average accuracy and its standard deviation across all mentioned conditions and all images described in table 2.3 (mean (SD)) for watershed, h-dome and k-means segmentation were 82.2(9.48), 73.1(19.55), and 82.3(8)%, respectively.

As indicated in section 2.11.8 (Results and Discussion), watershed is more robust to the changes of threshold and noise levels in comparison with the h-dome. Results show

that for simulated EMG ARV maps, the watershed segmentation (watershed segmentation+equalization+thresholding) is preferable to the h-dome and K-means algorithms. Last but not least, based on the application, the needs for simplicity and any a priori knowledge about the EMG images many other segmentation algorithms exist but they need to be validated for EMG partitioning before applying them to EMG maps.

References

[1] D. Staudenmann, Kingma Idsart, A. Daffertshofer, D. F. Stegeman, and J. H. van Dieen. **Improving EMG-based muscle force estimation by using a high-density EMG grid and principal component analysis**. *Biomedical Engineering, IEEE Transactions on*, **53**(4):712–719, 2006. 28, 67

[2] V. T. Inman, H. J. Ralston, J. B. Saunders, B. Feinstein, and Jr. Wright, E. W. **Relation of human electromyogram to muscular tension**. *Electroencephalogr Clin Neurophysiol*, **4**(2):187–194, 1952. 29

[3] R. Merletti and P. A. Parker. *ELECTROMYOGRAPHY Physiology, Engineering, and Noninvasive Applications*. IEEE PRESS, 2004. x, 29, 59

[4] Edward Shwedyk, R. Balasubramanian, and R. N. Scott. **A Nonstationary Model for the Electromyogram**. *Biomedical Engineering, IEEE Transactions on*, **BME-24**(5):417–424, 1977. x, 29

[5] D. Farina and R. Merletti. **A novel approach for precise simulation of the EMG signal detected by surface electrodes**. *Biomedical Engineering, IEEE Transactions on*, **48**(6):637–646, 2001. xii, xli, 53, 54, 59, 68, 69

[6] C. S. Klein, G. D. Marsh, R. J. Petrella, and C. L. Rice. **Muscle fiber number in the biceps brachii muscle of young and old men**. *Muscle Nerve*, **28**(1):62–68, 2003. 59

[7] Uwe Windhorst and H. Johansson. *Modern techniques in neuroscience research*. Springer, 1999. 59

[8] J. Ohser and K. Schladitz. *Image Processing and Analysis*. http://www.fbmn.h-da.de/ ohser/TomoBook.pdf. CLARENDON PRESS . OXFORD, 2006. 67

[9] D. Staudenmann, I. Kingma, A. Daffertshofer, D. F. Stegeman, and J. H. van Dien. **Heterogeneity of muscle activation in relation to force direction: A multichannel surface electromyography study on the triceps surae muscle**. *Journal of Electromyography and Kinesiology*, **19**(5):882–895, 2009. 67, 87

[10] Taian M. M. Vieira, Roberto Merletti, and Luca Mesin. **Automatic segmentation of surface EMG images: Improving the estimation of neuromuscular activity**. *Journal of biomechanics*, **43**(11):2149–2158, 2010. xv, xvii, xli, 67, 68, 69, 70, 71, 72, 77, 84, 87

[11] M. Rojas-Martinez, M. A. Mananas, J. F. Alonso, and R. Merletti. **Identification of isometric contractions based on High Density EMG maps**. *J Electromyogr Kinesiol*, **23**(1):33–42, 2013. 67

[12] A. J. Fuglevand, D. A. Winter, and A. E. Patla. **Models of recruitment and rate coding organization in motor-unit pools**. *Journal of Neurophysiology*, **70**(6):2470–2488, 1993. xli, 69

[13] L. Vincent and P. Soille. **Watersheds in digital spaces: an efficient algorithm based on immersion simulations**. *Pattern Analysis and Machine Intelligence, IEEE Transactions on*, **13**(6):583–598, 1991. 71

[14] H. Heijmans. **Mathematical Morphology: A Modern Approach in Image Processing Based on Algebra and Geometry**. *SIAM Review*, **37**(1):1–36, 1995. 72

[15] L. Vincent. **Morphological grayscale reconstruction in image analysis: applications and efficient algorithms**. *Image Processing, IEEE Transactions on*, **2**(2):176–201, 1993. xv, 73, 75, 76, 80

[16] J. MacQueen. **Some methods for classification and analysis of multivariate observations**. In *Proc. Fifth Berkeley Symp. on Math. Statist. and Prob.*, **1**, pages 281–297. Univ. of Calif. Press, 1967. 75

[17] Geoff Dougherty. *Digital Image Processing for Medical Applications*. CAMBRIDGE UNIVERSITY PRESS, 2009. 78

REFERENCES

3

Estimation of muscle force from EMG

3.1 Introduction

Despite many years of research, the issue of load sharing among muscles acting on the same joint is still unresolved and very controversial. There is a monotonic relationship between the EMG amplitude of a specific muscle and its force. Such relationship depends on the specific anatomical (subcutaneous thickness) and detection condition (electrode location, inter-electrode distance) and recruitment modality of motor units (random, superficial to deep, deep to superficial). The force produced by a specific muscle cannot be measured and what is measured is the total force provided by all the active muscles acting on a joint.

Researchers (1, 2) have reported linear and exponential like relations between force and sEMG. Considering also the recruitment order of fibers, it is possible to categorized the sEMG-force relation into three main patterns, which all are monotonic but a) linear, b) non-linear with upward concavity, and c) non-linear with downward concavity (see figure 3.1). A possible non-linear relationship between the EMG and force or torque is presented as eq.(3.1) that is reported in the literature (3, 4).

$$F_m = x_m \left(sEMG^{y_m} \right) \tag{3.1}$$

Where F_m is the force contributed by muscle "m", $sEMG$ is the surface EMG amplitude of muscle "m". x and y are suitable coefficients to be identified. Minimization

of the mean square error, between the measured and the total estimated force (with N muscles involved) provides an estimate of the model parameters x and y that in turn provide the force contributions of the individual muscles. The individual muscle torque of the Biceps Brachii, Brachioradialis, lateral and medial head of the Triceps Brachii during isometric voluntary flexions-extensions with the elbow flexed at 90° were estimated using optimization algorithms (3, 4).

Equation 3.1 discuss the contribution of each muscle to the the force. Two unknown parameters exist for each muscle. In load sharing issue, a non-linear system of equations is built based on the model. Using equation 3.1, the load sharing problem can be formulated as follows for N muscles:

$$F_c = \sum_{i=1}^{N} x_i V_{sEMG_i}^{y_i} \tag{3.2}$$

where F_c is the total force from all modeled muscles acting on a joint and it can be compared with the force that experimentally measured by a load cell. V_{sEMG_i} is the sEMG amplitude of muscle "i", x_i and y_i are the unknown parameters of the model corresponding to the ith muscle. By asking the subject to provide different values of isometric force (F_{c1}, F_{c1}, ..., F_{cN}) and assuming that x_i and y_i do not change when force changes, an non-linear system of "N" equations in "$2M$" unknowns is obtained, where "N" is the number of muscles and "M" is the number of contractions at different levels. Comparing the measured force with the model derived force of each muscle by minimizing the mean squared error between two vectors (i.e. between measured and estimated forces) leads us to find the "x" and "y" values of each muscle. Solving the load sharing problem (non-linear system of equations) is the main objective of this chapter. Two different approaches were investigated for finding the solutions of the system, which are:

- Analytical-Graphical Approach (AGA)

- Numerical Approach(NA) consisting of error minimization (between the estimated and measured force) applying optimization algorithms

These approaches(AGA and NA) are discussed in detail in this chapter. The term "force" will be used even if "torque" may occasionally be more appropriate.
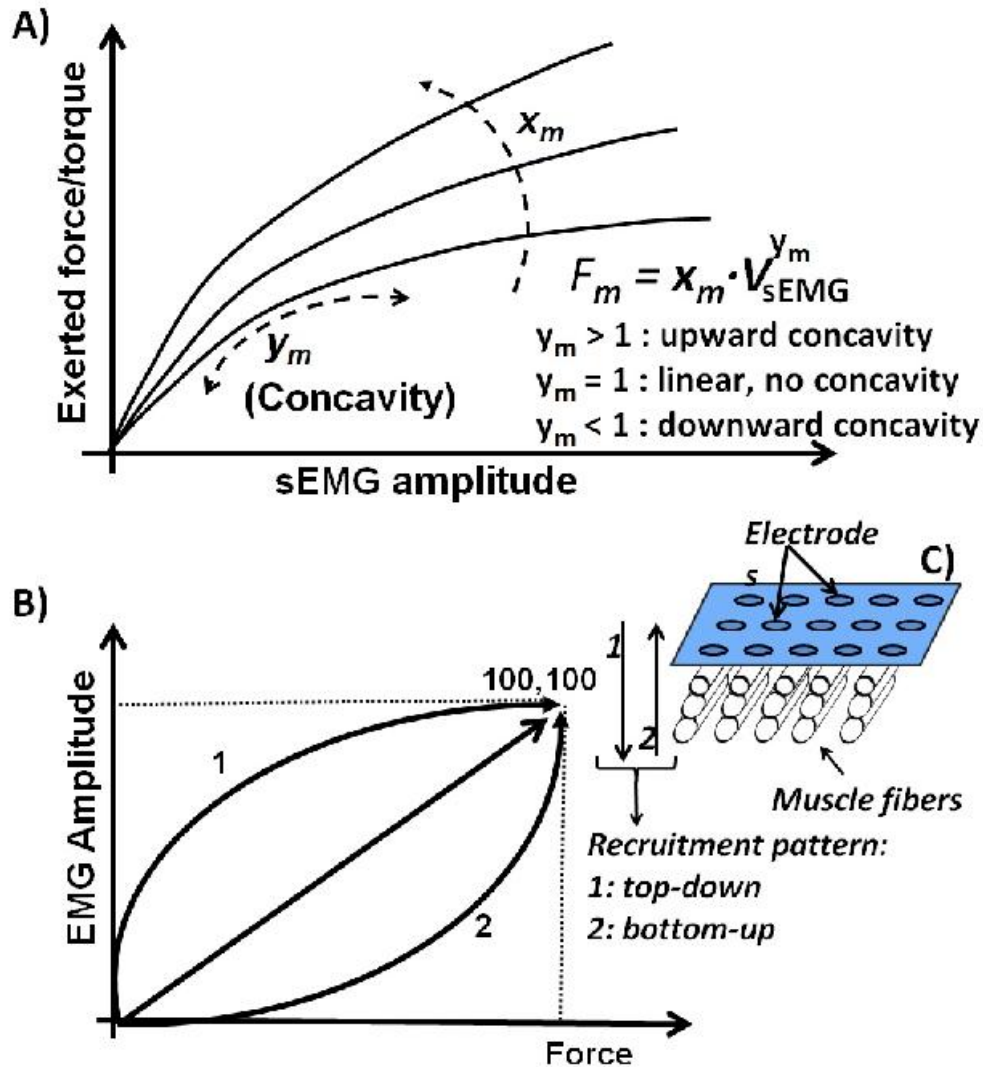
Figure 3.1: A)Model used to relate the force of each muscle to its EMG amplitude (V_{sEMG}) by means of the unknown coefficients x_m and y_m B) The EMG amplitude versus force in two different recruitment orders (1 and 2) that are presented in panel "C" .

3.2 Solving the load sharing problem

In this section the Analytical-Graphical Approach (AGA) and the Numerical approach (NA) for solving the load sharing problem is discussed. The AGA finds the model parameters of each muscle (i.e. "x_m" and "y_m") contributing to the force production on a joint by finding the intersection of the surfaces that can be obtained from sequential substitutions of the model parameters in the equations corresponding to each contraction level. Sequential substitutions help us to find the exponential parameter of one muscle (ex.: y_m) versus its corresponding parameter associated to the other muscles. The second approach (NA), based on minimization of the mean square error between the measured and the total estimated force or torque (with "N" muscles involved) provides an estimate of the model parameters "x_m" and "y_m" that in turn provides the force contributions of the individual muscles. The optimization algorithms can find the solutions of our system made of non-linear equations. Starting from different point (initial conditions), different solutions can be found, as predicted by the AGA approach for the two-muscle case.

3.2.1 Analytical-Graphical Approach (AGA) for two muscles

Considering the single muscle EMG-Force model:.

$$F_C = xV^y \tag{3.3}$$

where V is amplitude of the EMG signal (RMS, ARV, or Envelope) recorded from muscle at a certain contraction level, x and y are coefficients of the model that are unknown and are parameters of the muscle. F_C is the value (force or torque) predicted by the model which compared with the measured value at a known isometric contraction (C) level. F_C is known. Therefore, for each muscle we have the force and EMG amplitude as known parameters and two unknown parameters. For two muscles that are contributing in force production we can rewrite equation (3.3) for a certain contraction level(c) as:

$$F_C = x_1 V_1^{y_1} + x_2 V_2^{y_2} \tag{3.4}$$

where F_C is the total force from the two modeled muscles acting on a joint, V_1 and V_2 are the sEMG amplitude of muscle #1 and 2 respectively. x_1 and y_1 are the unknown parameters of the model associated to the muscle #1. x_2 and y_2 are the unknown

model parameters associated to the muscle #2. In AGA we are going to find the model parameters of each muscle (i.e. "x" and "y") contributing in force production on a joint by finding the intersection of those surfaces that can be obtained from sequential substitutions of the model parameters in the equations corresponding to each contraction level. Sequential substitutions help us to find the exponential parameter of one muscle (ex.: y_1) versus its corresponding parameter associated to the other muscles(ex.: y_2). Considering more than two muscles, in the graphical part of the AGA approach, we need more than 3 dimensions for plotting the model parameters of one muscle versus the other. Therefore, the AGA is discussed in detail considering two muscles.

Concerning two muscles, we are facing with four unknowns. In order to find the four unknowns, we need at least four equations based on the four different contraction levels. Let's rewrite equations of EMG-force model for the four different contraction levels as follows:

$$F_{C_1} = x_1 V_{11}^{y_1} + x_2 V_{12}^{y_2} \tag{3.5}$$

$$F_{C_2} = x_1 V_{21}^{y_1} + x_2 V_{22}^{y_2} \tag{3.6}$$

$$F_{C_3} = x_1 V_{31}^{y_1} + x_2 V_{32}^{y_2} \tag{3.7}$$

$$F_{C_4} = x_1 V_{41}^{y_1} + x_2 V_{42}^{y_2} \tag{3.8}$$

where V_{ij} is the modeled EMG amplitude produced by muscle "j" at contraction level "i", F_{C_1}, F_{C_2}, F_{C_3}, and F_{C_4} are the forces of four different contraction levels. x_1, y_1 are the model parameters of the first muscle and x_2, y_2 are the model parameters of the second muscle. In order to simplify the load sharing problem, our first assumption is that all measured forces are > 0, which implies all muscles involving in producing force are agonists and no antagonist muscle is present.

Let's also consider (3.6) and (3.8) for computing x_1 and x_2 and then by substitution, we are going to find the two surfaces obtained from (3.5) and (3.7) to find y_1 and y_2: By computing x_1 from (3.6)

$$x_1 = \frac{F_{C_2} - x_2 V_{22}^{y_2}}{V_{21}^{y_1}} \tag{3.9}$$

and substituting in (3.8), we will have:

$$F_{C_4} = F_{C_2} \left(\frac{V_{41}}{V_{21}} \right)^{y_1} - x_2 V_{22}^{y_2} \left(\frac{V_{41}}{V_{21}} \right)^{y_1} + x_2 V_{42}^{y_2}$$

then

$$x_2 = \frac{F_{C_4} - F_{C_2} \left(\frac{V_{41}}{V_{21}} \right)^{y_1}}{V_{22}^{y_2} \left(\left(\frac{V_{42}}{V_{22}} \right)^{y_2} - \left(\frac{V_{41}}{V_{21}} \right)^{y_1} \right)} \tag{3.10}$$

Let's substitute eq.(3.9) and (3.10) in (3.5). We will have:

$$F_{C_1} = \left(\frac{F_{C_2} - x_2 V_{22}^{y_2}}{V_{21}^{y_1}} \right) V_{11}^{y_1} + x_2 V_{12}^{y_2} \Rightarrow$$

$$F_{C_1} = F_{C_2} \left(\frac{V_{11}}{V_{21}} \right)^{y_1} - x_2 V_{22}^{y_2} \left(\frac{V_{11}}{V_{21}} \right)^{y_1} + x_2 V_{12}^{y_2} \Rightarrow$$

$$F_{C_1} = F_{C_2} \left(\frac{V_{11}}{V_{21}} \right)^{y_1} + V_{22}^{y_2} \left(\left(\frac{V_{12}}{V_{22}} \right)^{y_2} - \left(\frac{V_{11}}{V_{21}} \right)^{y_1} \right) x_2 \Rightarrow$$

$$F_{C_1} = F_{C_2} \left(\frac{V_{11}}{V_{21}} \right)^{y_1} + V_{22}^{y_2} \left(\left(\frac{V_{12}}{V_{22}} \right)^{y_2} - \left(\frac{V_{11}}{V_{21}} \right)^{y_1} \right) \left(\frac{F_{C_4} - F_{C_2} \left(\frac{V_{41}}{V_{21}} \right)^{y_1}}{V_{22}^{y_2} \left(\left(\frac{V_{42}}{V_{22}} \right)^{y_2} - \left(\frac{V_{41}}{V_{21}} \right)^{y_1} \right)} \right) \Rightarrow$$

$$F_{C_1} = F_{C_2} \left(\frac{V_{11}}{V_{21}} \right)^{y_1} + \left(\left(\frac{V_{12}}{V_{22}} \right)^{y_2} - \left(\frac{V_{11}}{V_{21}} \right)^{y_1} \right) \left(\frac{F_{C_4} - F_{C_2} \left(\frac{V_{41}}{V_{21}} \right)^{y_1}}{\left(\frac{V_{42}}{V_{22}} \right)^{y_2} - \left(\frac{V_{41}}{V_{21}} \right)^{y_1}} \right) \Rightarrow$$

$$\Rightarrow F_{C_1}\left(\left(\frac{V_{42}}{V_{22}}\right)^{y_2} - \left(\frac{V_{41}}{V_{21}}\right)^{y_1}\right) = F_{C_2}\left(\frac{V_{11}}{V_{21}}\right)^{y_1}\left(\frac{V_{42}}{V_{22}}\right)^{y_2} - F_{C_2}\left(\frac{V_{11}}{V_{21}}\right)^{y_1}\left(\frac{V_{41}}{V_{21}}\right)^{y_1}$$

$$+F_{C_4}\left(\left(\frac{V_{12}}{V_{22}}\right)^{y_2} - \left(\frac{V_{11}}{V_{21}}\right)^{y_1}\right) - F_{C_2}\left(\frac{V_{41}}{V_{21}}\right)^{y_1}\left(\frac{V_{12}}{V_{22}}\right)^{y_2} + F_{C_2}\left(\frac{V_{11}}{V_{21}}\right)^{y_1}\left(\frac{V_{41}}{V_{21}}\right)^{y_1} \Rightarrow$$

By simplification of the above equation we obtain:

$$F_{C_1}\left(\left(\frac{V_{42}}{V_{22}}\right)^{y_2} - \left(\frac{V_{41}}{V_{21}}\right)^{y_1}\right) + F_{C_2}\left(\left(\frac{V_{41}}{V_{21}}\right)^{y_1}\left(\frac{V_{12}}{V_{22}}\right)^{y_2} - \left(\frac{V_{11}}{V_{21}}\right)^{y_1}\left(\frac{V_{42}}{V_{22}}\right)^{y_2}\right)$$

$$+F_{C_4}\left(\left(\frac{V_{11}}{V_{21}}\right)^{y_1} - \left(\frac{V_{12}}{V_{22}}\right)^{y_2}\right) = 0 \tag{3.11}$$

Let's define surface $S_{1_{13}}$ (read it as S_1 computed from the first and the third contraction levels) as follows:

$$S_{1_{13}} = f(y_1, y_2) := F_{C_1}\left(\left(\frac{V_{42}}{V_{22}}\right)^{y_2} - \left(\frac{V_{41}}{V_{21}}\right)^{y_1}\right)$$

$$+F_{C_2}\left(\left(\frac{V_{41}}{V_{21}}\right)^{y_1}\left(\frac{V_{12}}{V_{22}}\right)^{y_2} - \left(\frac{V_{11}}{V_{21}}\right)^{y_1}\left(\frac{V_{42}}{V_{22}}\right)^{y_2}\right) + F_{C_4}\left(\left(\frac{V_{11}}{V_{21}}\right)^{y_1} - \left(\frac{V_{12}}{V_{22}}\right)^{y_2}\right)$$
$$\tag{3.12}$$

and rewrite (3.11) as:

$$S_{1_{13}} = z \quad for \quad z = 0 \tag{3.13}$$

Now we are going to find another surface that can be obtained by substituting eq.(3.9) and (3.10) in (3.7).

$$F_{C_3} = \left(\frac{F_{C_2} - x_2 V_{22}^{y_2}}{V_{21}^{y_1}}\right) V_{31}^{y_1} + x_2 V_{32}^{y_2} \Rightarrow$$

$$F_{C_3} = F_{C_2}\left(\frac{V_{31}}{V_{21}}\right)^{y_1} - x_2 V_{22}^{y_2}\left(\frac{V_{31}}{V_{21}}\right)^{y_1} + x_2 V_{32}^{y_2} \Rightarrow$$

$$F_{C_3} = F_{C_2}\left(\frac{V_{31}}{V_{21}}\right)^{y_1} + V_{22}^{y_2}\left(\left(\frac{V_{32}}{V_{22}}\right)^{y_2} - \left(\frac{V_{31}}{V_{21}}\right)^{y_1}\right) x_2 \Rightarrow$$

$$F_{C_3} = F_{C_2}\left(\frac{V_{31}}{V_{21}}\right)^{y_1} + V_{22}^{y_2}\left(\left(\frac{V_{32}}{V_{22}}\right)^{y_2} - \left(\frac{V_{31}}{V_{21}}\right)^{y_1}\right)\left(\frac{F_{C_4} - F_{C_2}\left(\frac{V_{41}}{V_{21}}\right)^{y_1}}{V_{22}^{y_2}\left(\left(\frac{V_{42}}{V_{22}}\right)^{y_2} - \left(\frac{V_{41}}{V_{21}}\right)^{y_1}\right)}\right) \Rightarrow$$

$$F_{C_3} = F_{C_2}\left(\frac{V_{31}}{V_{21}}\right)^{y_1} + \left(\left(\frac{V_{32}}{V_{22}}\right)^{y_2} - \left(\frac{V_{31}}{V_{21}}\right)^{y_1}\right)\left(\frac{F_{C_4} - F_{C_2}\left(\frac{V_{41}}{V_{21}}\right)^{y_1}}{\left(\frac{V_{42}}{V_{22}}\right)^{y_2} - \left(\frac{V_{41}}{V_{21}}\right)^{y_1}}\right) \Rightarrow$$

$$F_{C_3}\left(\left(\frac{V_{42}}{V_{22}}\right)^{y_2} - \left(\frac{V_{41}}{V_{21}}\right)^{y_1}\right) = F_{C_2}\left(\frac{V_{31}}{V_{21}}\right)^{y_1}\left(\frac{V_{42}}{V_{22}}\right)^{y_2} - F_{C_2}\left(\frac{V_{31}}{V_{21}}\right)^{y_1}\left(\frac{V_{41}}{V_{21}}\right)^{y_1}$$

$$+F_{C_4}\left(\left(\frac{V_{32}}{V_{22}}\right)^{y_2} - \left(\frac{V_{31}}{V_{21}}\right)^{y_1}\right) - F_{C_2}\left(\frac{V_{41}}{V_{21}}\right)^{y_1}\left(\frac{V_{32}}{V_{22}}\right)^{y_2} + F_{C_2}\left(\frac{V_{41}}{V_{21}}\right)^{y_1}\left(\frac{V_{31}}{V_{21}}\right)^{y_1} \Rightarrow$$

By simplification of the above equation we obtain:

$$F_{C_2}\left(\left(\frac{V_{31}}{V_{21}}\right)^{y_1}\left(\frac{V_{42}}{V_{22}}\right)^{y_2} - \left(\frac{V_{41}}{V_{21}}\right)^{y_1}\left(\frac{V_{32}}{V_{22}}\right)^{y_2}\right) + F_{C_3}\left(\left(\frac{V_{41}}{V_{21}}\right)^{y_1} - \left(\frac{V_{42}}{V_{22}}\right)^{y_2}\right)$$

$$+F_{C_4}\left(\left(\frac{V_{32}}{V_{22}}\right)^{y_2} - \left(\frac{V_{31}}{V_{21}}\right)^{y_1}\right) = 0 \tag{3.14}$$

Let's define surface $S_{2_{13}}$ (read it as S_2 computed from the first and the third contraction levels) as follows:

$$S_{2_{13}} = g(y_1, y_2) :=$$

$$F_{C_2}\left(\left(\frac{V_{31}}{V_{21}}\right)^{y_1}\left(\frac{V_{42}}{V_{22}}\right)^{y_2} - \left(\frac{V_{41}}{V_{21}}\right)^{y_1}\left(\frac{V_{32}}{V_{22}}\right)^{y_2}\right) + F_{C_3}\left(\left(\frac{V_{41}}{V_{21}}\right)^{y_1} - \left(\frac{V_{42}}{V_{22}}\right)^{y_2}\right)$$

$$+F_{C_3}\left(\left(\frac{V_{41}}{V_{21}}\right)^{y_1} - \left(\frac{V_{42}}{V_{22}}\right)^{y_2}\right) + F_{C_4}\left(\left(\frac{V_{32}}{V_{22}}\right)^{y_2} - \left(\frac{V_{31}}{V_{21}}\right)^{y_1}\right) \tag{3.15}$$

and rewrite (3.14) as:

$$S_{2_{13}} = z \quad for \quad z = 0 \tag{3.16}$$

Now, we have two surfaces(equations 3.13 and 3.16), whose intersection with the y_1y_2 plane i.e. where the $S_{1_{13}} = 0$ and $S_{2_{13}} = 0$ generate two curves $y_1 = f(y_2)$ and $y_1 = g(y_2)$. These curves intersect in "k" points, which are the solutions(i.e. the exponents of the sEMG-force model, i.e. y_1 and y_2) of the non-linear system consisting of equations 3.13 and 3.16 (see eq. 3.17).

$$System \quad A = \begin{cases} S_{1_{13}} = z = 0 \\ S_{2_{13}} = z = 0 \end{cases} \tag{3.17}$$

Each of the "k" points satisfies the "system A" (eq. 3.17) and provides a pair of coordinates that satisfies the equations 3.13 and 3.16. x_1 ad x_2 can be found based on y_1 and y_2 using equations 3.9 and 3.10 respectively.

Before providing an example, let's continue with some questions that might come into mind. We derived the two surfaces (equations 3.12 and 3.15) from the first and third

contraction levels. Generally, there are six possible combinations to derive the surfaces (ex:. eqs. equations 3.12 and 3.15) from the four equations those we wrote based on the four contraction levels(see eqs. 3.5 to 3.8). Now, the questions are: Are the surfaces that can be derived from different contraction levels (other possible combination of our four contraction levels) equivalent? Should we expect similar x and y solutions from different surfaces? To answer these questions, Let's find the other surfaces in the same manner that is explained for deriving equations 3.12 and 3.15. All possible cases from two muscles and four contraction levels can be summarized into six possible combinations. Note that this six combinations are equivalent for a system of linear equations, but they may not be in case of system of non-linear equations.

3. ESTIMATION OF MUSCLE FORCE FROM EMG

Case 1: Surfaces derived from contraction levels 1 & 3 (see eq. 3.5 and 3.7):

$S_{1_{13}} = f(y_1, y_2) = z =$

$$F_{C_1}\left(\left(\frac{V_{42}}{V_{22}}\right)^{y_2} - \left(\frac{V_{41}}{V_{21}}\right)^{y_1}\right) + F_{C_2}\left(\left(\frac{V_{41}}{V_{21}}\right)^{y_1}\left(\frac{V_{12}}{V_{22}}\right)^{y_2} - \left(\frac{V_{11}}{V_{21}}\right)^{y_1}\left(\frac{V_{42}}{V_{22}}\right)^{y_2}\right)$$

$$+ F_{C_4}\left(\left(\frac{V_{11}}{V_{21}}\right)^{y_1} - \left(\frac{V_{12}}{V_{22}}\right)^{y_2}\right) = 0 \qquad (3.18)$$

$S_{2_{13}} = g(y_1, y_2) = z =$

$$F_{C_2}\left(\left(\frac{V_{31}}{V_{21}}\right)^{y_1}\left(\frac{V_{42}}{V_{22}}\right)^{y_2} - \left(\frac{V_{41}}{V_{21}}\right)^{y_1}\left(\frac{V_{32}}{V_{22}}\right)^{y_2}\right) + F_{C_3}\left(\left(\frac{V_{41}}{V_{21}}\right)^{y_1} - \left(\frac{V_{42}}{V_{22}}\right)^{y_2}\right)$$

$$+ F_{C_4}\left(\left(\frac{V_{32}}{V_{22}}\right)^{y_2} - \left(\frac{V_{31}}{V_{21}}\right)^{y_1}\right) = 0 \qquad (3.19)$$

Case 2: Surfaces derived from contraction levels 1 & 4 (see eq. 3.5 and 3.8):

$S_{1_{14}} = f(y_1, y_2) = z =$

$$F_{C_1}\left(\left(\frac{V_{32}}{V_{22}}\right)^{y_2} - \left(\frac{V_{31}}{V_{21}}\right)^{y_1}\right) + F_{C_2}\left(\left(\frac{V_{31}}{V_{21}}\right)^{y_1}\left(\frac{V_{12}}{V_{22}}\right)^{y_2} - \left(\frac{V_{11}}{V_{21}}\right)^{y_1}\left(\frac{V_{32}}{V_{22}}\right)^{y_2}\right)$$

$$+ F_{C_3}\left(\left(\frac{V_{11}}{V_{21}}\right)^{y_1} - \left(\frac{V_{12}}{V_{22}}\right)^{y_2}\right) = 0 \qquad (3.20)$$

$S_{2_{14}} = g(y_1, y_2) = z =$

$$F_{C_2}\left(\left(\frac{V_{41}}{V_{21}}\right)^{y_1}\left(\frac{V_{32}}{V_{22}}\right)^{y_2} - \left(\frac{V_{31}}{V_{21}}\right)^{y_1}\left(\frac{V_{42}}{V_{22}}\right)^{y_2}\right) + F_{C_3}\left(\left(\frac{V_{42}}{V_{22}}\right)^{y_2} - \left(\frac{V_{41}}{V_{21}}\right)^{y_1}\right)$$

$$+ F_{C_4}\left(\left(\frac{V_{31}}{V_{21}}\right)^{y_1} - \left(\frac{V_{32}}{V_{22}}\right)^{y_2}\right) \qquad (3.21)$$

Case 3: Surfaces derived from contraction levels 2 & 3 (see eq. 3.6 and 3.7):

$$S_{1_{23}} = f(y_1, y_2) = z =$$

$$F_{C_1}\left(\left(\frac{V_{21}}{V_{11}}\right)^{y_1}\left(\frac{V_{42}}{V_{12}}\right)^{y_2} - \left(\frac{V_{41}}{V_{11}}\right)^{y_1}\left(\frac{V_{22}}{V_{12}}\right)^{y_2}\right) + F_{C_2}\left(\left(\frac{V_{41}}{V_{11}}\right)^{y_1} - \left(\frac{V_{42}}{V_{12}}\right)^{y_2}\right)$$

$$+ F_{C_4}\left(\left(\frac{V_{22}}{V_{12}}\right)^{y_2} - \left(\frac{V_{21}}{V_{11}}\right)^{y_1}\right) = 0 \tag{3.22}$$

$$S_{2_{23}} = g(y_1, y_2) = z =$$

$$F_{C_1}\left(\left(\frac{V_{31}}{V_{11}}\right)^{y_1}\left(\frac{V_{42}}{V_{12}}\right)^{y_2} - \left(\frac{V_{41}}{V_{11}}\right)^{y_1}\left(\frac{V_{32}}{V_{12}}\right)^{y_2}\right) + F_{C_3}\left(\left(\frac{V_{41}}{V_{11}}\right)^{y_1} - \left(\frac{V_{42}}{V_{12}}\right)^{y_2}\right)$$

$$+ F_{C_4}\left(\left(\frac{V_{32}}{V_{12}}\right)^{y_2} - \left(\frac{V_{31}}{V_{11}}\right)^{y_1}\right) = 0 \tag{3.23}$$

Case 4: Surfaces derived from contraction levels 2 & 4 (see eq. 3.6 and 3.8):

$$S_{1_{24}} = f(y_1, y_2) = z =$$

$$F_{C_1}\left(\left(\frac{V_{21}}{V_{11}}\right)^{y_1}\left(\frac{V_{32}}{V_{12}}\right)^{y_2} - \left(\frac{V_{31}}{V_{11}}\right)^{y_1}\left(\frac{V_{22}}{V_{12}}\right)^{y_2}\right) + F_{C_2}\left(\left(\frac{V_{31}}{V_{11}}\right)^{y_1} - \left(\frac{V_{32}}{V_{12}}\right)^{y_2}\right)$$

$$+ F_{C_3}\left(\left(\frac{V_{22}}{V_{12}}\right)^{y_2} - \left(\frac{V_{21}}{V_{11}}\right)^{y_1}\right) = 0 \tag{3.24}$$

$$S_{2_{24}} = g(y_1, y_2) = z =$$

$$F_{C_1}\left(\left(\frac{V_{41}}{V_{11}}\right)^{y_1}\left(\frac{V_{32}}{V_{12}}\right)^{y_2} - \left(\frac{V_{31}}{V_{11}}\right)^{y_1}\left(\frac{V_{42}}{V_{12}}\right)^{y_2}\right) + F_{C_3}\left(\left(\frac{V_{42}}{V_{12}}\right)^{y_2} - \left(\frac{V_{41}}{V_{11}}\right)^{y_1}\right)$$

$$+ F_{C_4}\left(\left(\frac{V_{31}}{V_{11}}\right)^{y_1} - \left(\frac{V_{32}}{V_{12}}\right)^{y_2}\right) = 0 \tag{3.25}$$

3. ESTIMATION OF MUSCLE FORCE FROM EMG

Case 5: Surfaces derived from contraction levels 3 & 4 (see eq. 3.7 and 3.8): $S_{1_{34}} = f(y_1, y_2) = z =$

$$F_{C_1}\left(\left(\frac{V_{31}}{V_{11}}\right)^{y_1}\left(\frac{V_{22}}{V_{12}}\right)^{y_2} - \left(\frac{V_{21}}{V_{11}}\right)^{y_1}\left(\frac{V_{32}}{V_{12}}\right)^{y_2}\right) + F_{C_2}\left(\left(\frac{V_{32}}{V_{12}}\right)^{y_2} - \left(\frac{V_{31}}{V_{11}}\right)^{y_1}\right)$$

$$+ F_{C_3}\left(\left(\frac{V_{21}}{V_{11}}\right)^{y_1} - \left(\frac{V_{22}}{V_{12}}\right)^{y_2}\right) = 0 \tag{3.26}$$

$S_{2_{34}} = g(y_1, y_2) = z =$

$$F_{C_1}\left(\left(\frac{V_{41}}{V_{11}}\right)^{y_1}\left(\frac{V_{22}}{V_{12}}\right)^{y_2} - \left(\frac{V_{21}}{V_{11}}\right)^{y_1}\left(\frac{V_{42}}{V_{12}}\right)^{y_2}\right) + F_{C_2}\left(\left(\frac{V_{42}}{V_{12}}\right)^{y_2} - \left(\frac{V_{41}}{V_{11}}\right)^{y_1}\right)$$

$$+ F_{C_4}\left(\left(\frac{V_{21}}{V_{11}}\right)^{y_1} - \left(\frac{V_{22}}{V_{12}}\right)^{y_2}\right) = 0 \tag{3.27}$$

Case 6: Surfaces derived from contraction levels 1 & 2 (see eq. 3.5 and 3.6):

$S_{1_{12}} = f(y_1, y_2) = z =$

$$F_{C_1}\left(\left(\frac{V_{42}}{V_{32}}\right)^{y_2} - \left(\frac{V_{41}}{V_{31}}\right)^{y_1}\right) + F_{C_3}\left(\left(\frac{V_{41}}{V_{31}}\right)^{y_1}\left(\frac{V_{12}}{V_{32}}\right)^{y_2} - \left(\frac{V_{11}}{V_{31}}\right)^{y_1}\left(\frac{V_{42}}{V_{32}}\right)^{y_2}\right)$$

$$+ F_{C_4}\left(\left(\frac{V_{11}}{V_{31}}\right)^{y_1} - \left(\frac{V_{12}}{V_{32}}\right)^{y_2}\right) = 0 \tag{3.28}$$

$S_{2_{12}} = g(y_1, y_2) = z =$

$$F_{C_2}\left(\left(\frac{V_{41}}{V_{31}}\right)^{y_1} - \left(\frac{V_{42}}{V_{32}}\right)^{y_2}\right) + F_{C_3}\left(\left(\frac{V_{21}}{V_{31}}\right)^{y_1}\left(\frac{V_{42}}{V_{32}}\right)^{y_2} - \left(\frac{V_{41}}{V_{31}}\right)^{y_1}\left(\frac{V_{22}}{V_{32}}\right)^{y_2}\right)$$

$$+ F_{C_4}\left(\left(\frac{V_{22}}{V_{32}}\right)^{y_2} - \left(\frac{V_{21}}{V_{31}}\right)^{y_1}\right) = 0 \tag{3.29}$$

Example 1: we simulated the sEMG-force relation of two muscles based on the equations 3.3 and 3.4 by setting muscle parameters as $x_1 = 4$, $y_1 = 0.5$, $x_2 = 2$, and $y_2 = 1.2$ (see figure3.2 and figure 3.1 condition: downward concavity ($y_1 < 1$) for the first muscle(M_1) and upward concavity ($y_2 > 1$) for the second muscle(M_2)). We also assigned the four contraction levels (see eqs. (3.5) to 3.8) for each muscle based on table 3.1.

Table 3.1: Example 1: Assuming $x_1 = 4$, $y_1 = 0.5$, $x_2 = 2$, and $y_2 = 1.2$, values that were considered for EMG and force in different contraction levels for muscle 1 and 2 are presented; Total forces are 7.7269, 15.7454, 21.2934, and 28.6895 at first, second, third and fourth contraction levels respectively

Muscle	Contraction level	EMG amplitude [a.u]	Force [a.u]
Muscle 1	1	2.4	6.1968
	2	4.4	8.3905
	3	5.9	9.716
	4	7.9	11.2428
Muscle 2	1	0.8	1.5302
	2	2.96	7.355
	3	4.32	11.5774
	4	6.08	17.4467
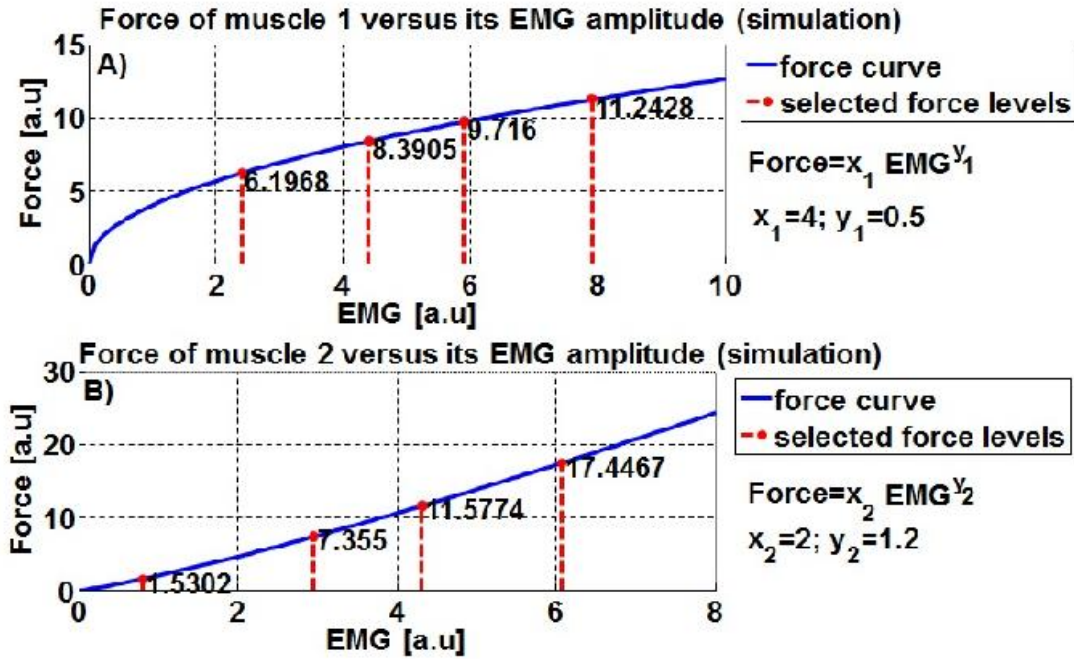
Figure 3.2: Example 1: Force-EMG relation of muscle 1 and muscle 2 (assuming $x_1 = 4$, $y_1 = 0.5$, $x_2 = 2$, and $y_2 = 1.2$), the EMG of four contraction levels and their corresponding forces are depicted by dashed red bars. Values are in arbitrary unit.
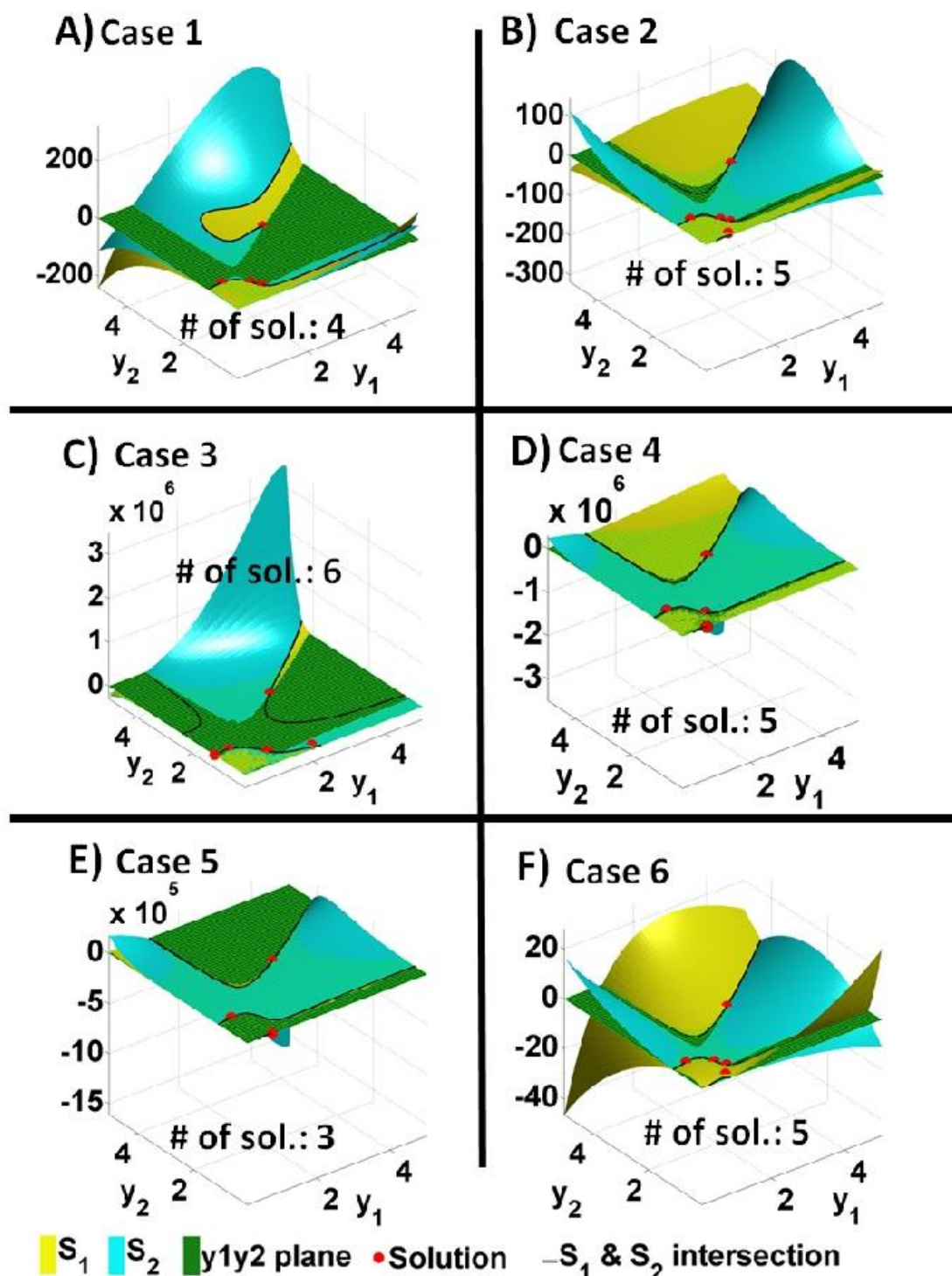
Figure 3.3: Example 1: Surfaces ($f(y_1, y_2)$ and $g(y_1, y_2)$) derived from the contraction levels A) 1 and 3 (see eqs. 3.18 and 3.19), B) 1 , 4 (see eqs. 3.20 and 3.21), C) 2 and 3(see eqs.3.22 and 3.23), D) 2 and 4(see eqs. 3.24 and 3.25), E) 3 and 4 (see eqs. 3.26 and 3.27), F) 1 and 2 (see eqs. 3.28 and 3.29); their intersection (solid line), and intersection with the plane $y_1 y_2$ (solutions, red circles)

Different possible combinations of equations in order to derive the surfaces whose intersection provide the solutions, offers different number of solutions (see figure 3.3). Totally, solutions found from the six cases are equivalent. In some cases due to the discretization and numerical error, the number of solutions are different. The most important message from the figure 3.3 is that in all cases, there is more than one solution to the load sharing problem.

Example 2 is provided such that the concavity of the force-EMG relation for both muscles are downward i.e. $y_1 < 1$ and $y_2 < 1$.

Example 2:

Assumptions: $x_1 = 2$, $y_1 = 0.3$, $x_2 = 3$, and $y_2 = 0.7$

The second example (simulation study) is designed such that the concavity in the force-EMG amplitude curvature (see figure 3.1) of both muscles(M_1 and M_2) are downward (i.e. $y_1 < 1$ and $y_2 < 1$), but with different curvature.

The selected values for EMG and force considering the second example (Example 2) are presented in table 3.2. The EMG-force relations of the first and second muscles (M_1 and M_2) are also depicted in figure 3.4

3. ESTIMATION OF MUSCLE FORCE FROM EMG

Table 3.2: Example 2: Assuming $x_1 = 2$, $y_1 = 0.3$, $x_2 = 3$, and $y_2 = 0.7$, values that were considered for EMG and force in four contraction levels for muscle 1 and 2 are presented; Total forces are 5.1669, 9.5318, 11.7616, and 14.3315 at first, second, third and fourth contraction levels respectively

Muscle	Contraction level	EMG amplitude [a.u]	Force [a.u]
Muscle 1	1	2.4	2.6007
	2	4.4	3.1194
	3	5.9	3.4063
	4	7.9	3.7181
Muscle 2	1	0.8	2.5662
	2	2.96	6.4125
	3	4.32	8.3553
	4	6.08	10.6134
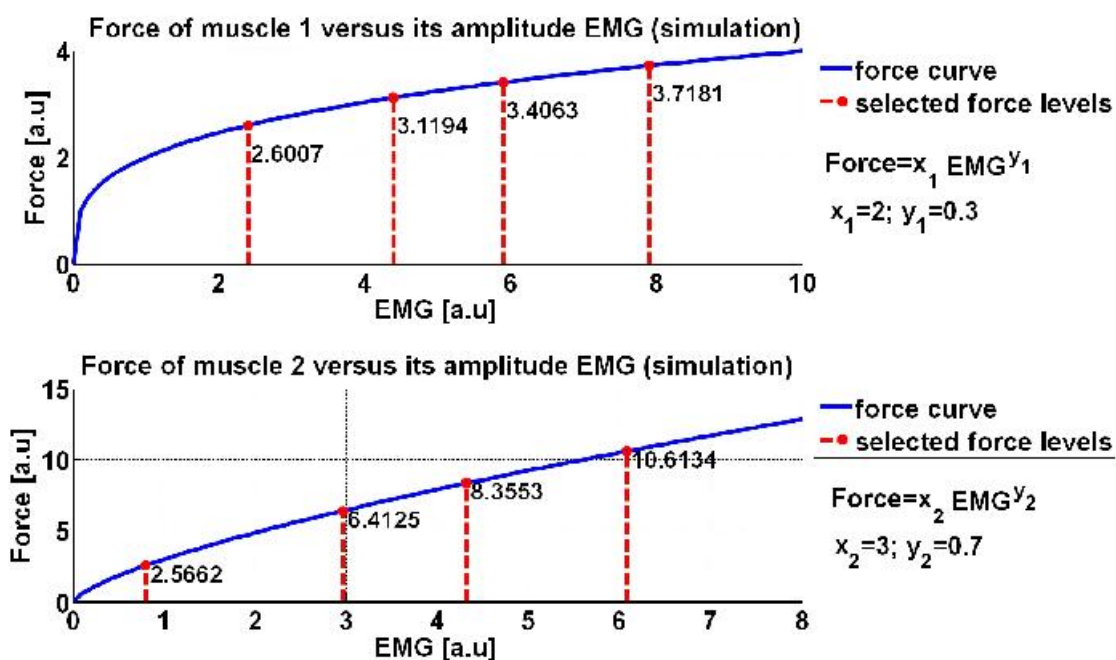
Figure 3.4: Example 2: Force-EMG relation of muscle 1 and muscle 2 (assuming $x_1 = 2$, $y_1 = 0.3$, $x_2 = 3$, and $y_2 = 0.7$), the EMG of four contraction levels and their corresponding forces are depicted by dashed red bars. Values are in arbitrary unit.

Figure 3.5: Example 2: Surfaces ($f(y_1, y_2)$ and $g(y_1, y_2)$) derived from the contraction levels A) 1 and 3 (see eqs. 3.18 and 3.19), B) 1 and 4 (see eqs. 3.20 and 3.21), C) 2 and 3 (see eqs.3.22 and 3.23), D) 2 and 4 (see eqs. 3.24 and 3.25), E) 3 and 4 (see eqs. 3.26 and 3.27), F) 1 and 2 (see eqs. 3.28 and 3.29); their intersection (solid line), and intersection with the plane y_1y_2 (solutions, red circles)

3.2.2 Numerical Approach (Optimization algorithms)

Practical mathematical theory of optimization has been developed since the Sixties when computers became available. In mathematics, computer science and economics, optimization, or mathematical programming, refers to choosing the "best" solution from some set of available alternatives. The "best" solution is the one that minimizes a cost function (in our problem the cost function is defined as the mean squared error (MSE) between the measured and predicted forces using the model mentioned in eq. 3.2). Creating reliable methods to catch the extremum of a function by an intelligent arrangement of its evaluations (measurements) in an acceptable amount of time is the main goal of the optimization theory.

There are different methods capable of finding solutions to optimization problems including exact methods, Heuristics and Meta heuristics (5). Exact methods solve optimization problems by searching the entire solution space exhaustively. However, in a large number of optimization problems, solutions cannot be found by exact methods except for a few cases. For example, in load sharing problem to minimize the error between the measured and predicted (predicted based on the model mentioned as eq. 3.2) muscles'(acting on elbow joint) forces, the objective function (MSE) has 8 continuous input parameters; using the absolute input ranges of "A" to "B" (ex.: 0 to 10) for linear coefficients (in steps of 0.1) and a range of 0 to 1 for exponential coefficients (in steps of 0.01), more than 1.45×10^{20} cases should be taken into account to find the global optimum by brute-force approach (4). This is quite time-consuming and impractical. Also, its accuracy depends on the resolution (step) chosen for each input variable.

Approximation methods in optimization, on the other hand, provide the approximate solution in a reasonable amount of time but imply the risk of not finding the global optimum. In Heuristics, e.g. local search, the best possible solution is found close to the starting point. Local search does not guarantee the finding of the best solution; it is only able to find the best one in the neighborhood of the starting point. Thus, it is quite probable to get stuck in the local optimum. Evolutionary Computations (EC) simulates some of the known mechanisms of evolution. They differ from the traditional search methods in the following three concepts: they use a population of potential solutions, decision making processes are guided by minimizing the objective function alone and decisions are probabilistic rather than deterministic. In EC, the possibility

of getting stuck in local optimum is decreased by introducing a population of possible solutions and the randomness of their behavior to approaching the "best" solution (the solution that minimize the objective function). A particle by itself has almost no power to solve any problem; progress occurs when the particles interact (6). Particle swarm optimization (PSO) is one of the recent EC techniques introduced and its application has increased exponentially in the last decade (7).

To solve the load sharing problem PSO algorithm was studied and compared with previous approaches using the Interior-Reflective Newton Algorithm (IRNA) (3).

The PSO algorithm eliminates the problems of initialization and has an intrinsically higher likelihood of finding the global minimum and nearby relative minima that might be worth of consideration. However, the computational load of PSO is greater than that of IRNA (4).

Particle Swarm Optimization

Particle Swarm Optimization (PSO) is a meta-heuristic population-based stochastic optimization technique inspired by social behavior of a flock of birds. The initial ideas on particle swarms of Kennedy (a social psychologist) (6) and Eberhart (an electrical engineer) (6) were essentially aimed at producing computational intelligence by exploiting simple analogues of social interaction, rather than purely individual cognitive abilities. Bird flocks searching for corn developed into a powerful optimization method. In the past several years, PSO has been successfully applied in many research and application areas such as antennas, biomedical, comunication networks, control, clustering and qualification (6, 7). Within little more than a decade hundreds of papers have reported successful applications of PSO. An investigation on PSO application based on IEEE paper database (1100 papers) have been done in 2007 and 2008 by Riccardo Poli et al (6, 7). They divided PSO applications into 26 different categories. Based on this research, Biomedical science is very popular with approximately 4.3% of all application papers in the IEEE Xplore database (7).

In PSO a number of particles, are placed in the parameter space (x_i and y_i in our case; see eq. 3.2) of some problem or function, and each evaluates the fitness at its current location. Each particle then determines its movement through the parameter space by combining some aspect of the history of its own fitness values (particle's best solution: *pbest*) with those of one or more members of the swarm (swarm's best solution or global
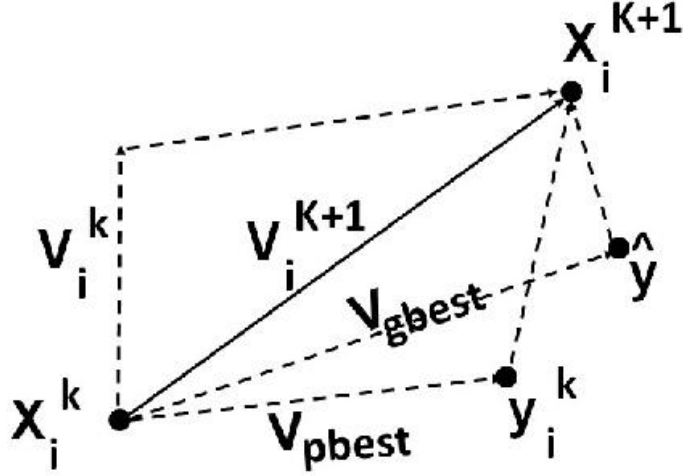
Figure 3.6: Concept of modification of a searching point (i^{th} particle in the solution space) by particle swarm optimization (PSO), X_i^k states the current position of the ith particle. X_i^{k+1} is the modified position; y_i is the particle's best position until now, and $\hat{y}$ is the best position (the best position means the solution (a set of model parameters) that minimizes the cost function) discovered by any of the particles until now; V_i^K is current velocity and V_i^{k+1} is the modified velocity. V_{pbest} and V_{gbest} are velocities based on particle's best and swarm's best velocities respectively.

best: *gbest*), and then moving through the parameter space with a velocity determined by the locations and processed fitness values according to particle's best (*pbest*) and global best (*gbest*) of those other members, along with some random perturbations (7) (Poli, 2008). The term of "best" solution is defined as the solution that minimizes the objective function (i.e. the MSE between the measured force and model-based predicted force in our case). Concept of modification is plotted in figure 3.6. Defining X_i as the current position, V_i as the current velocity vector, y_i as the particle's best position of the ith particle, and $\hat{y}$ as the best position (i.e. the solution (set of model parameters) that minimizes the objective function) discovered by any of the particles so far, then the update of the velocity and particle's position at each iteration of the algorithm can be formulated as follows:

$$X_i^j = X_i^{j-1} + V_i^{j-1} \tag{3.30}$$

$$y_i^j = \begin{cases} y_i^{j-1} & \text{if } f(X_i^j) \geq f(y_i^{j-1}) \\ X_i^j & \text{if } f(X_i^j) < f(y_i^{j-1}) \end{cases} \qquad (3.31)$$

$$\hat{y}^j \in \{y_1^j, y_2^j, \ldots, y_{n_p}^j\} | f(\hat{y}^j) = min\left(f(y_1^j), f(y_2^j), \ldots, f(y_{n_p}^j)\right) \qquad (3.32)$$

$$V_i^j = wV_i^{j-1} + c_1 r_1 \bullet (y_i^j - X_i^j) + c_2 r_2 \bullet \left(\hat{y}_i^{\,j} - X_i^j\right) \qquad (3.33)$$

Where $f(.)$ is the objective function, j is the iteration number, n_p is the number of particles in the swarm, and $\bullet$ denotes element-by-element multiplication. The new velocity depends on the previous velocity and on the distances of the particle from the personal and neighborhood best positions, with the coefficient w being the inertia weight, c_1 and c_2 are two constants, known as the acceleration coefficients, which control the relative proportion of cognition and social interaction in the swarm (7). r_1 and r_2 are random vectors whose elements are uniformly distributed in $U(0, 1)$. A large value of inertia weight favors global search (exploration), while a small value favors local search (exploitation) (4).

By applying the particle swarm optimization to the example 2 presented in page 106 (simulated study with $x_1 = 2$, $y_1 = 0.3$, $x_2 = 3$, and $y_2 = 0.7$) and defining the cost function as eq. 3.34, solutions can be found. Table 3.3 shows the solutions found through 50 calls of the PSO-function starting from different random points.

$$E_{rr} = \sqrt{\sum_{i=1}^{4} (F_{meas._i} - F_{C_i})^2} \qquad (3.34)$$

where E_{rr} is the cost function that is going to be minimized in order to find solutions. "i" is the contraction level ($i \in [1, 2, 3, 4]$). F_{C_i} is the total force of ith contraction level computed (estimated) from equations 3.5 to 3.8. $F_{meas._i}$ is the known total force (measured or simulated) of the ith contraction level.

As seen in the table 3.3, five solutions have been found for the example 2. The first solution in the table (note that the first solution does not mean it is the first solution found by the PSO) is the exact solution of the system (the one that we set for our simulation example). Other four solutions were also found by PSO through minimizing the cost function (eq. 3.34).

Table 3.3: Five solutions (set of "x" and "y" parameters of the muscle force estimation model presented as eq. 3.2 on page 92) of system of non-linear equations (see eqs. (3.5) to (3.8)) found by particle swarm optimization (PSO) algorithm considering example 2 (see page 106). The five solutions were found through 50 calls of PSO function starting from different random points. Note that some solutions (solution #2, 3, and 4), which were found mathematically are not physiologically meaningful (i.e. solutions whose y_m or $x_m < 0$, where "m" (the muscle number) here = 1 or 2)

Sol.#	x_1	y_1	x_2	y_2	Cost function Evaluation(eq. 3.34)
1	2	0.3	3	0.7	0
2	4.1452	0.6165	-1.672	-0.6770	$1.9 * 10^{-9} \approx 0$
3	5.5485	-2.0292	4.8326	0.5990	$1.7 * 10^{-9} \approx 0$
4	0.5095	2.7939	-1.3843	2.6363	$9.7 * 10^{-7} \approx 0$
5	1.0247	0.78081	3.5306	0.52972	$6.6 * 10^{-10} \approx 0$

The solutions #2, 3, and 4 are not physiologically meaningful (although they are mathematically acceptable solutions), because in our model (see eq. 3.2) y_1 or y_2 can not be < 0 (Force of a muscle can not decrease when its amplitude EMG increases). Meanwhile, a muscle with $x < 0$, implies (physiologically) that the muscle is acting as an antagonist muscle ($x < 0$ produce a negative muscle force based on our model; a muscle can only pull when it contracts i.e. "force> 0"), where we assumed only the presence of agonist muscles in the example. Solution #5 is an acceptable solution goes with the first solution to be considered as two different solutions of the example 2. Note that solution #5 is not an exact solution, but it minimizes the cost function to $6.6 * 10^{-10}$, which can be considered as "0" from the engineering point of view.

Levenberg-Marquardt Method

The Levenberg-Marquardt (LM) method is a standard technique used to solve nonlinear least squares problems. Least squares problems arise when fitting a parameterized function to a set of measured data points by minimizing the sum of the squares of the errors between the data points and the function. Nonlinear least squares problems arise when the function is not linear (as we are facing with load sharing problem, see equations 3.2) in the parameters (i.e. "x"es and "y"s of the model presented as eq. 3.2 on page 92). Nonlinear least squares methods involve an iterative improvement to

parameter values in order to reduce the sum of the squares of the errors between the function and the measured data points. The Levenberg-Marquardt (LM) curve-fitting method is actually a combination of two minimization methods: the gradient descent method and the Gauss-Newton method. In the gradient descent method, the sum of the squared errors is reduced by updating the parameters in the direction of the greatest reduction of the least squares objective. In the Gauss-Newton method, the sum of the squared errors is reduced by assuming the least squares function is locally quadratic, and finding the minimum of the quadratic. The LM method acts more like a gradient-descent method when the parameters are far from their optimal value, and acts more like the Gauss-Newton method when the parameters are close to their optimal value (8). Considering example 2 (see page 107; simulated study with model parameters: $x_1 = 2$, $y_1 = 0.3$, $x_2 = 3$, and $y_2 = 0.7$) and applying the LM method, more than one solution was found (similar to PSO and Analytical-Graphical approach). Even if we do not consider physiologically meaningless solutions(i.e. y_1 or $y_2 \leq 0$), still there is more than one solution for the load sharing problem. Table 3.4 shows the "x" and "y" of the first and second muscle, which were found by the LM algorithm. Under the last column of this table entitled (Solution's Evaluation) the difference between the estimated force (see eqs. 3.5 to 3.8) and real force(the simulated value) at four contraction levels are reported. Solutions were found through 50 calls of LM method starting at different random points. It should be noted that, table 3.4 reports all solutions, which are mathematically meaningful while some are physiologically meaningless.

Figure 3.7 shows the solutions found by optimization approach (Levenberg-Marquardt) Method.
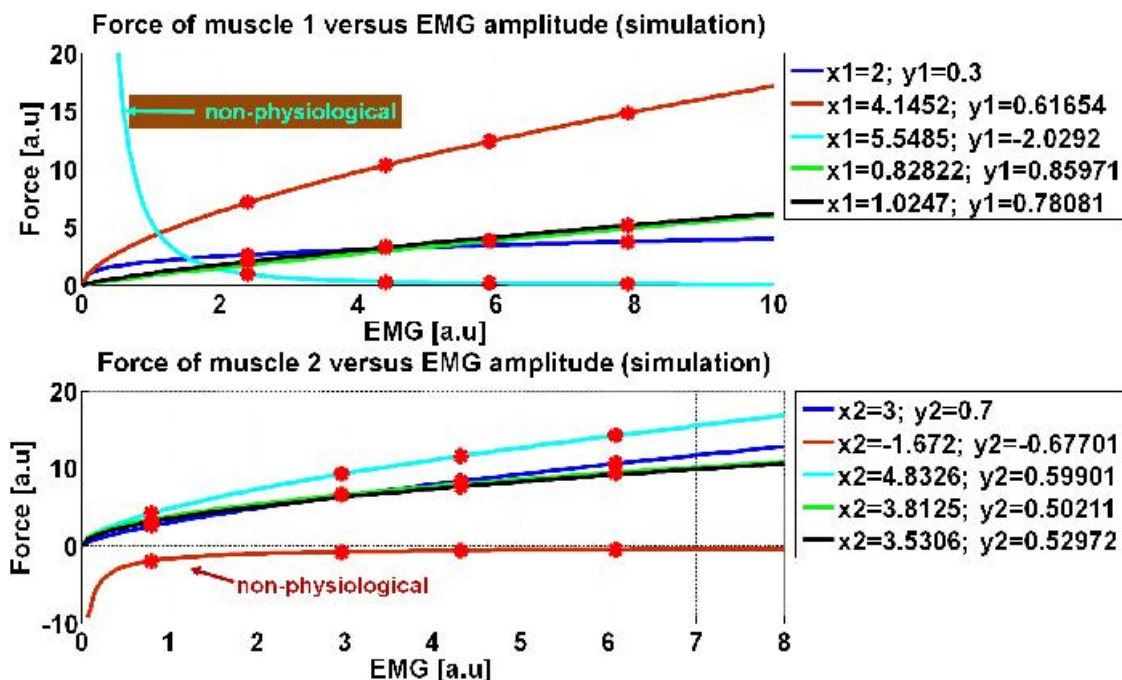
Figure 3.7: Possible load sharing strategies (see example 2 presented in page 106) found by solving the non-linear system of equations (see eq. 3.5 to 3.8) by optimization approach. Solutions (x and y of each muscle) were found using optimization algorithms (Levenberg-Marquardt method) from random starting points. Negative values for "y" are physiologically meaningless, but they exists mathematically as solutions to the non-linear system. Putting aside these solutions still, there is more than one acceptable solution

Comparing tables 3.3 and 3.4, leads to the fact that different algorithms might provide different solutions. Solution found by LM method (i.e. $x_1 = 0.82822$, $y_1 = 0.85971$, $x_2 = 3.8125$, $y_2 = 0.50211$) was not found by the PSO; and also, solution found by PSO (i.e. $x_1 = 0.5095$, $y_1 = 2.7939$, $x_2 = -1.3843$, $y_2 = 2.6363$) was not found by the LM method. Note that these solutions were found in 50 calls of the optimization algorithm. By increasing the number of calls, more solutions might be found from each optimization algorithm. Meanwhile, theoretically, similar solutions (in value and number of solutions) will be expected if the number of calls for PSO and LM methods $\rightarrow \infty$.

Table 3.4: Possible solutions found by Levenberg-Marquardt(LM) method after 50 calls (random different starting points) of the LM function. Solution's Evaluation column is reporting the difference between the estimated forces from the found solutions and the simulated forces mentioned in example 2(see page 106) for each contraction level

Contraction level	x_1	y_1	x_2	y_2	Solution's Evaluation
1	2	0.3	3	0.7	0
	4.152	0.61654	-1.672	-0.67701	$-1.0*10^{-13}$
	5.5485	-2.0292	4.8326	0.59901	$-4.0*10^{-11}$
	0.82822	0.85971	3.8125	0.50211	$-4.7*10^{-4}$
	1.0247	0.78081	3.5306	0.52972	$-4.8*10^{-8}$
2	2	0.3	3	0.7	0
	4.152	0.61654	-1.672	-0.67701	$2.3*10^{-12}$
	5.5485	-2.0292	4.8326	0.59901	$7.2*10^{-11}$
	0.82822	0.85971	3.8125	0.50211	$-2.7*10^{-3}$
	1.0247	0.78081	3.5306	0.52972	$-1.1*10^{-7}$
3	2	0.3	3	0.7	0
	4.152	0.61654	-1.672	-0.67701	$-4.4*10^{-12}$
	5.5485	-2.0292	4.8326	0.59901	$-9.0*10^{-11}$
	0.82822	0.85971	3.8125	0.50211	$-3.6*10^{-3}$
	1.0247	0.78081	3.5306	0.52972	$-2.2*10^{-7}$
4	2	0.3	3	0.7	0
	4.152	0.61654	-1.672	-0.67701	$1.4*10^{-12}$
	5.5485	-2.0292	4.8326	0.59901	$4.0*10^{-11}$
	0.82822	0.85971	3.8125	0.50211	$1.2*10^{-3}$
	1.0247	0.78081	3.5306	0.52972	$-2.5*10^{-7}$

3.3   Effect of increasing the number of equations

A model based on linear system of equations is solveable if the number of unknowns is equal to the number of independent equations. In case of existence of greater number of independent equations than the number of model's unknown parameters, the system has no solution. In a non-linear system of equation, the story is different. Since we can measure the force and sEMG at different contraction levels, in our nonlinear force-EMG relation (see eq. 3.2) we can have greater number of equations with respect to the number of unknowns (two unknowns for each muscle: "x" and "y"). It can by hypothesized that we can constrain the optimization algorithm to converge into only one solution by increasing the number of equations contributed in solving the non-linear system of equations. In order to show this, example 3 is provided such that two muscle and five Force-EMG equations were considered in solving the load sharing problem (eq. 3.2).

Example 3: Muscle parameters are considered the same as example 2 in page 105

- two muscle are involved. $x_1 = 2$, $y_1 = 0.3$, $x_2 = 3$, and $y_2 = 0.7$

- Known parameters: F_C, V_{im}, where F_C is the total force measured (or simulated) at a joint (produced from all muscles acting on the joint), V_{im} is the amplitude of sEMG signal, "i" represents the contraction level and "m" is the muscle number.

- Unknowns are "x_1", "y_1", which are the parameters of the first muscle and "x_2", "y_2", which are the parameters of the second muscle.

$$F_{C_1} = x_1 V_{11}^{y_1} + x_2 V_{12}^{y_2} \tag{3.35}$$

$$F_{C_2} = x_1 V_{21}^{y_1} + x_2 V_{22}^{y_2} \tag{3.36}$$

$$F_{C_3} = x_1 V_{31}^{y_1} + x_2 V_{32}^{y_2} \tag{3.37}$$

$$F_{C_4} = x_1 V_{41}^{y_1} + x_2 V_{42}^{y_2} \tag{3.38}$$

$$F_{C_5} = x_1 V_{51}^{y_1} + x_2 V_{52}^{y_2} \tag{3.39}$$

Table 3.5: Example 3: Values assumed for EMG and force relation in five contraction levels for muscle 1 and 2 considering $x_1 = 2$, $y_1 = 0.3$, $x_2 = 3$, and $y_2 = 0.7$ are presented; Total forces are 5.1669, 9.5318, 11.7616, 14.3315, and 15.6410 at first, second, third, fourth, and fifth contraction levels respectively

Muscle	Contraction level	EMG amplitude [a.u]	Force [a.u]
Muscle 1	1	2.4	2.6007
	2	4.4	3.1194
	3	5.9	3.4063
	4	7.9	3.7181
	5	8.4	3.7872
Muscle 2	1	0.8	2.5662
	2	2.96	6.4125
	3	4.32	8.3553
	4	6.08	10.6134
	5	7.12	11.8538
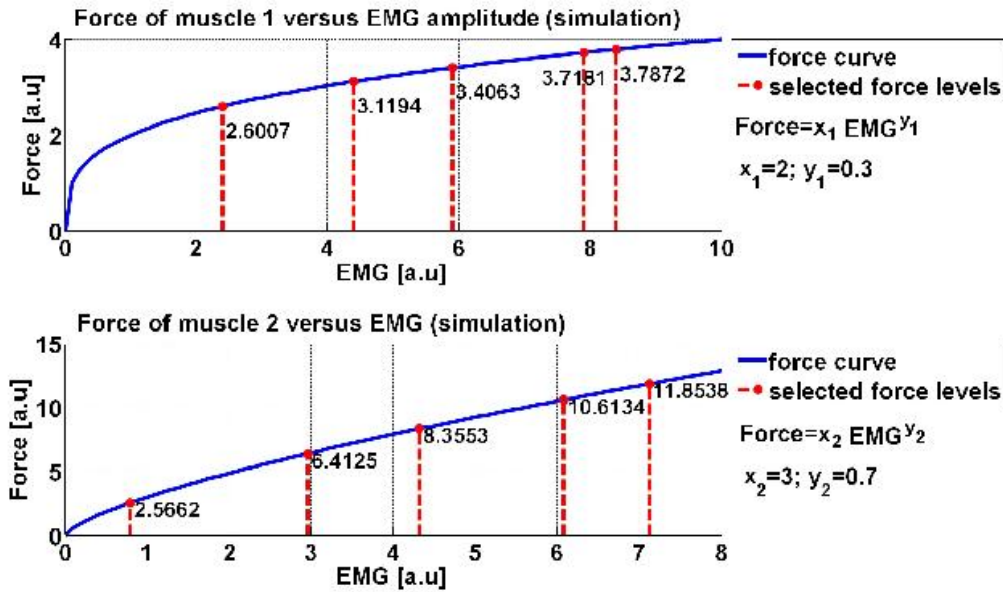
Figure 3.8: Example 3: Force-EMG relation of muscle 1 and muscle 2 (assuming $x_1 = 2$, $y_1 = 0.3$, $x_2 = 3$, and $y_2 = 0.7$), the EMG of five contraction levels and their corresponding forces are depicted by dashed red bars. Values are in arbitrary unit.

Applying PSO algorithm to example 3 for 50 times (each call started from different random point within a specific range (0–50)) provides us with only one solution, which is what we set as the simulated model's parameters. This is interesting and can be described as , when more equations (than the model's parameters) in our non-linear system of equations (example 3) are considered, optimization algorithm is forced to converge to only one solution, if the optimization algorithm does not get stuck in a local minimum. Another interesting issue is that this is true only when the exponent parameters of the model (i.e. "y_1" and "y_2") are not linearly related to each other. This condition is discussed in the following section.

3.4 Condition of existence of a linear relation between the exponent parameter of the model at all contraction levels

Coming back to the Analytical-Graphical approach and considering two muscles and four equations corresponding to four contraction levels (see eqs.3.5 to 3.8), and then computing x_1 from (3.5) we obtained:

$$x_1 = \frac{F_{C_1} - x_2 V_{12}^{y_2}}{V_{11}^{y_1}} \tag{3.40}$$

by substituting x_1 (eq. 3.40) in (3.6), we will have:

$$F_{C_2} = F_{C_1} \left(\frac{V_{21}}{V_{11}}\right)^{y_1} - x_2 V_{12}^{y_2} \left(\frac{V_{21}}{V_{11}}\right)^{y_1} + x_2 V_{22}^{y_2}$$

then

$$x_2 = \frac{F_{C_2} - F_{C_1} \left(\frac{V_{21}}{V_{11}}\right)^{y_1}}{V_{12}^{y_2} \left(\left(\frac{V_{22}}{V_{12}}\right)^{y_2} - \left(\frac{V_{21}}{V_{11}}\right)^{y_1}\right)} \tag{3.41}$$

Let's check the condition such that the denominator of equation (3.41) $= 0$

$$V_{12}^{y_2} \left(\left(\frac{V_{22}}{V_{12}}\right)^{y_2} - \left(\frac{V_{21}}{V_{11}}\right)^{y_1}\right) = 0$$

since $V_{12}^{y_2} \neq 0$ then

$$\left(\frac{V_{22}}{V_{12}}\right)^{y_2} - \left(\frac{V_{21}}{V_{11}}\right)^{y_1} = 0$$

3.4 Condition of existence of a linear relation between the exponent parameter of the model at all contraction levels

Let's consider:

$$\left(\frac{V_{22}}{V_{12}}\right)^{y_2} = \left(\frac{V_{21}}{V_{11}}\right)^{y_1} = K_1 \tag{3.42}$$

(3.42) implies that:

$$V_{22}^{y_2} = K_1 V_{12}^{y_2} \quad \& \quad V_{21}^{y_1} = K_1 V_{11}^{y_1} \tag{3.43}$$

by substituting (3.43) in (3.6) we obtain:

$$F_{C_2} = x_1 K_1 V_{11}^{y_1} + x_2 K_1 V_{12}^{y_2} = K_1 F_{C_1} \tag{3.44}$$

equation (3.44) and (3.41) lead us to:

$$x_2 = \frac{K_1 F_{C_1} - K_1 F_{C_1}}{V_{12}^{y_2}(K_1 - K_1)} = \frac{0}{0} \tag{3.45}$$

equation 3.45 implies that x_2 can not be determined as a deterministic value (we should get close to the solution) and may have any value.

In a similar manner, considering the six possible combinations of four contraction levels to compute x_1 and x_2 (six cases) we can summarize conditions where $x_2 = \frac{0}{0}$:

Case 1:
$$\left(\frac{V_{21}}{V_{11}}\right)^{y_1} = \left(\frac{V_{22}}{V_{12}}\right)^{y_2} = K_1 \tag{3.46}$$

Case 2:
$$\left(\frac{V_{41}}{V_{31}}\right)^{y_1} = \left(\frac{V_{42}}{V_{32}}\right)^{y_2} = K_2 \tag{3.47}$$

Case 3:
$$\left(\frac{V_{31}}{V_{11}}\right)^{y_1} = \left(\frac{V_{32}}{V_{12}}\right)^{y_2} = K_3 \tag{3.48}$$

Case 4:
$$\left(\frac{V_{41}}{V_{21}}\right)^{y_1} = \left(\frac{V_{42}}{V_{22}}\right)^{y_2} = K_4 \tag{3.49}$$

Case 5:
$$\left(\frac{V_{31}}{V_{21}}\right)^{y_1} = \left(\frac{V_{32}}{V_{22}}\right)^{y_2} = K_5 \tag{3.50}$$

Case 6:
$$\left(\frac{V_{41}}{V_{11}}\right)^{y_1} = \left(\frac{V_{42}}{V_{12}}\right)^{y_2} = K_6 \tag{3.51}$$

by taking the logarithm of the eq.(3.46), (3.47), (3.48), (3.49), (3.50), and (3.51), we can have conditions (lines) in which $x_2 = \frac{0}{0}$ (for example the line "$y_2 = H_1 y_1$" is a

119

special line in which $x_2 = \frac{0}{0}$, see eq. 3.52).

eq.(3.46)$\Rightarrow$
$$y_2 = \frac{log(V_{21}) - log(V_{11})}{log(V_{22}) - log(V_{12})} y_1 = H_1 y_1 \tag{3.52}$$

eq.(3.47)$\Rightarrow$
$$y_2 = \frac{log(V_{41}) - log(V_{31})}{log(V_{42}) - log(V_{32})} y_1 = H_2 y_1 \tag{3.53}$$

eq.(3.48)$\Rightarrow$
$$y_2 = \frac{log(V_{31}) - log(V_{11})}{log(V_{32}) - log(V_{12})} y_1 = H_3 y_1 \tag{3.54}$$

eq.(3.49)$\Rightarrow$
$$y_2 = \frac{log(V_{41}) - log(V_{21})}{log(V_{42}) - log(V_{22})} y_1 = H_4 y_1 \tag{3.55}$$

eq.(3.50)$\Rightarrow$
$$y_2 = \frac{log(V_{31}) - log(V_{21})}{log(V_{32}) - log(V_{22})} y_1 = H_5 y_1 \tag{3.56}$$

eq.(3.51)$\Rightarrow$
$$y_2 = \frac{log(V_{41}) - log(V_{11})}{log(V_{42}) - log(V_{12})} y_1 = H_6 y_1 \tag{3.57}$$

Currently, we have six lines (for two muscles that are contributing in force production at a certain joint) in which $x_2 = \frac{0}{0}$ (see (3.52) to (3.57)).

Example 4 is provided such that the conditions mentioned in equations (3.52) to (3.57) are met (i.e. $x_2 = \frac{0}{0}$). We already know that with four contraction levels (four equations), more than one solution can be found for our Force-EMG model. Meanwhile, we saw that increasing the number of equations to five (considering five contraction level) helps us to find the solution (one solution) that was set in simulation. In example 4, we considered also five contraction levels to check if still under the new conditions, the optimization algorithms can find the solution or not.

Example 4:

Assumptions:

- two muscle are involved.

- Known parameters: F_C, $V_i m$, where F_C is the total force measured (or simulated) at a joint (produced from all muscles acting on the joint), V is the amplitude of sEMG signal, "i" represents the contraction level and m represents the muscle number.

Table 3.6: **Example 4: Values assumed for EMG and force relation in five contraction levels for muscle 1 and 2 considering $x_1 = 2$, $y_1 = 0.3$, $x_2 = 3$, and $y_2 = 0.15$ are presented; Total forces are 5.8277, 6.5815, 7.9178, 8.5662, and 9.1168 at first, second, third, fourth, and fifth contraction levels respectively**

Muscle	Contraction level	EMG amplitude [a.u]	Force [a.u]
Muscle 1	1	1.8000	2.3857
	2	2.7000	2.6943
	3	5.0000	3.2413
	4	6.5000	3.5067
	5	8.0000	3.7321
Muscle 2	1	2.5000	3.4420
	2	5.6250	3.8872
	3	19.2901	4.6765
	4	32.6003	5.0595
	5	49.3827	5.3846

- Unknown parameters: x_1, y_1, which are the parameters of muscle 1 and x_2, y_2, which are the parameters of muscle 2.

let's assume the parameters of the model as $x_1 = 2$, $y_1 = 0.3$, $x_2 = 3$, and $y_2 = 0.15$ and five contraction level. Table 3.6 show the values assumed for EMG and force relation. The values were chosen such that the conditions mentioned in equations (3.46) to (3.51) are satisfied.

$$eq.(3.46) \Rightarrow \left(\frac{V_{21}}{V_{11}}\right)^{y_1} = \left(\frac{V_{22}}{V_{12}}\right)^{y_2} = K_1 = 1.1293$$

$$eq.(3.47) \Rightarrow \left(\frac{V_{41}}{V_{31}}\right)^{y_1} = \left(\frac{V_{42}}{V_{32}}\right)^{y_2} = K_2 = 1.0819$$

$$eq.(3.48) \Rightarrow \left(\frac{V_{31}}{V_{11}}\right)^{y_1} = \left(\frac{V_{32}}{V_{12}}\right)^{y_2} = K_3 = 1.3587$$

$$eq.(3.49) \Rightarrow \left(\frac{V_{41}}{V_{21}}\right)^{y_1} = \left(\frac{V_{42}}{V_{22}}\right)^{y_2} = K_4 = 1.3016$$

$$eq.(3.50) \Rightarrow \left(\frac{V_{31}}{V_{21}}\right)^{y_1} = \left(\frac{V_{32}}{V_{22}}\right)^{y_2} = K_5 = 1.2030$$
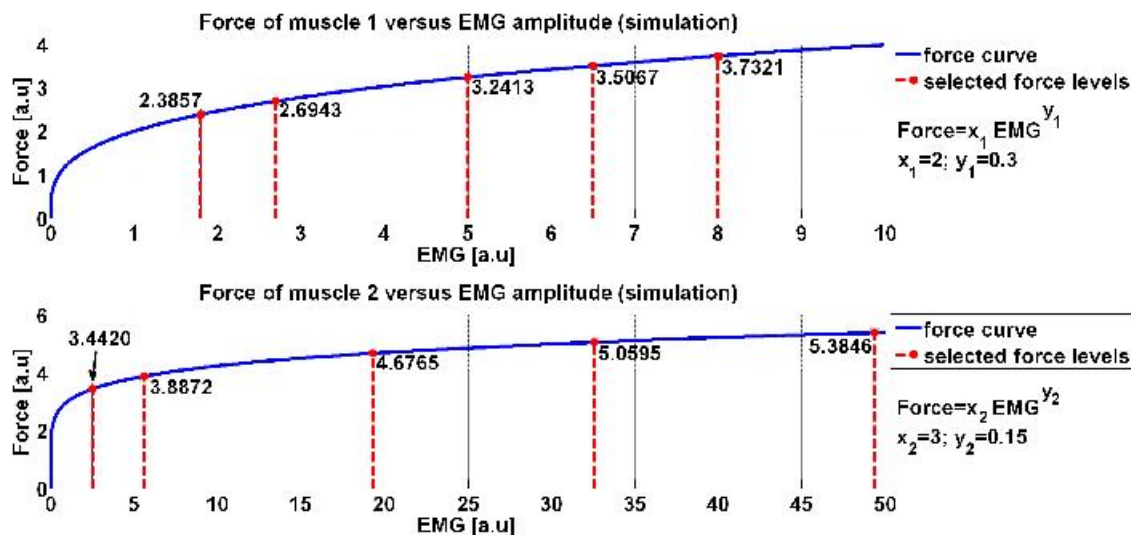
Figure 3.9: Example 4: Force-EMG relation of muscle 1 and muscle 2 (assuming $x_1 = 2$, $y_1 = 0.3$, $x_2 = 3$, and $y_2 = 0.15$), the EMG of five contraction levels and their corresponding forces are depicted by dashed red bars. Values are in arbitrary unit.

$$eq.(3.51) \Rightarrow \left(\frac{V_{41}}{V_{11}}\right)^{y_1} = \left(\frac{V_{42}}{V_{12}}\right)^{y_2} = K_6 = 1.4699$$

Panel "A" of figure 3.10 shows the y_2 versus y_1 i.e. the relation between exponent parameters of the non-linear system of equations presented in example 4. This relations have been reported as eq.(3.53) to eq.(3.57). To have a comparison between example 4 and example 3 (see page 116 for example 3) the y_1y_2 relation in six cases are plotted in panel "B" of figure 3.10.

Like example 3, we considered condition such that number of equations was more than number of unknowns, but for example 4, the Levenberg-Marquardt (LM) method found more than one solution after 50 calls of LM function when in each call the error minimization procedure between the real (simulated) and the estimated force were started from different points. These possible solutions and the difference between the simulated and estimated forces are reported in table 3.7.
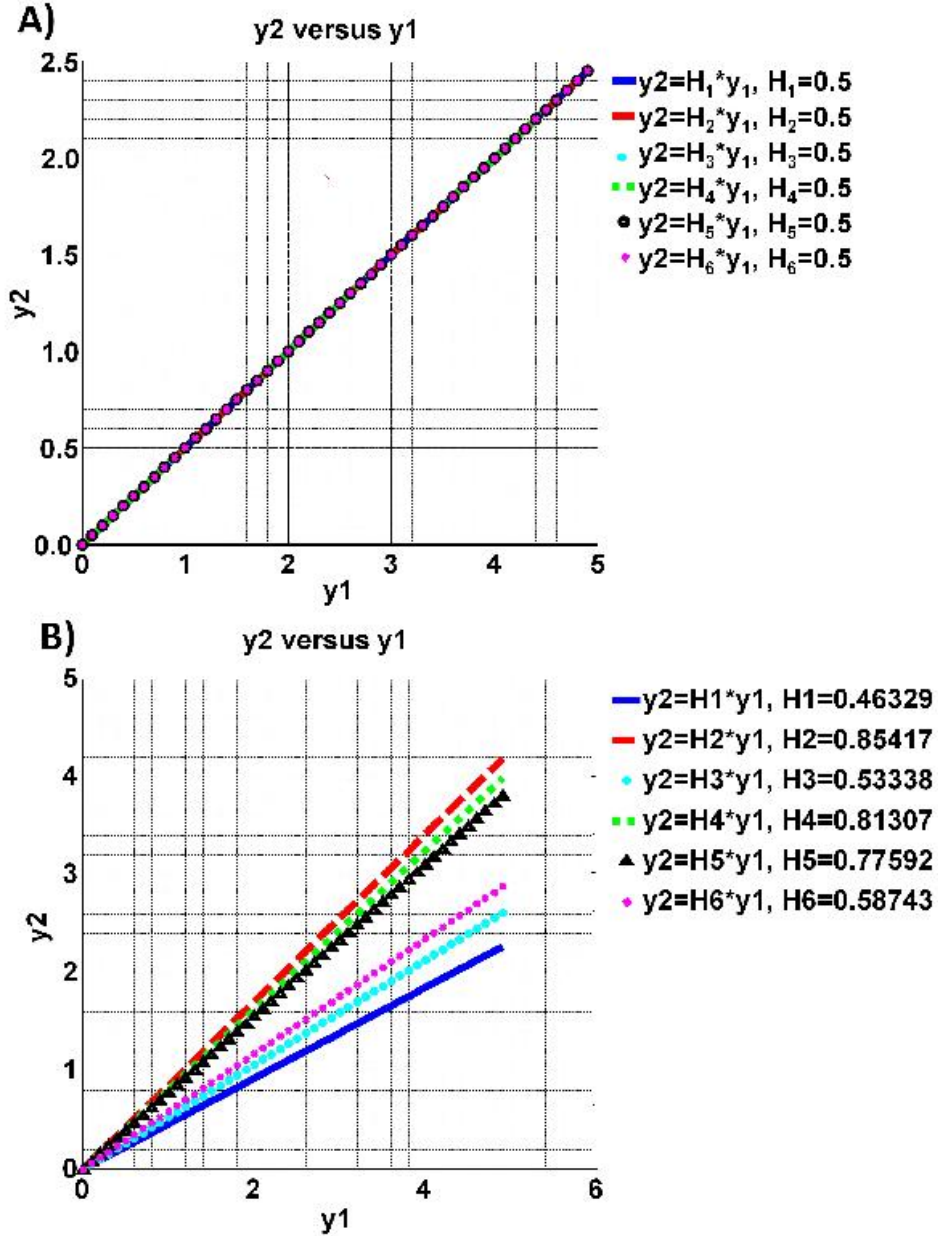
Figure 3.10: y2 versus y1 in conditions (six cases) mentioned in eq. (3.46) to (3.51)). See also eq.(3.53) to eq.(3.57) related to A) example 4(see page 120) and B)example 3(see page 116).

Table 3.7: Solutions of example 4 (see page 120) found by the Levenberg-Marquardt method in 50 runs of the algorithm (each call was started from different random starting point). Difference between the simulated and estimated forces for five contraction levels are also presented. Note that the exact solution for example 4 is: $x_1 = 2$, $y_1 = 0.3$, $x_2 = 3$, and $y_2 = 0.15$

Muscle parameters (unknowns)				$E_{rr} = F_{simulated} - F_{estimated}$				
x_1	y_1	x_2	y_2	level 1	level 2	level 3	level 4	level 5
2.8790	0.3003	2.0860	0.1498	-3.46E-07	6.96E-07	-5.20E-07	-1.80E-08	1.88E-07
2.8693	0.3003	2.0961	0.1498	-3.46E-07	6.96E-07	-5.20E-07	-1.81E-08	1.88E-07
3.5133	0.2997	1.4268	0.1503	-3.46E-07	6.96E-07	-5.20E-07	-1.86E-08	1.87E-07
2.1139	0.2995	2.8818	0.1502	-3.46E-07	6.96E-07	-5.20E-07	-1.82E-08	1.87E-07
1.7012	0.3006	3.3105	0.1499	-3.46E-07	6.96E-07	-5.20E-07	-1.85E-08	1.87E-07
2.4438	0.3004	2.5385	0.1498	-3.46E-07	6.96E-07	-5.20E-07	-1.82E-08	1.87E-07
4.6209	0.2999	0.2752	0.1508	-3.47E-07	6.96E-07	-5.20E-07	-1.86E-08	1.87E-07
3.2328	0.3003	1.7181	0.1497	-3.46E-07	6.96E-07	-5.20E-07	-1.82E-08	1.87E-07
2.5416	0.3004	2.4368	0.1498	-3.46E-07	6.96E-07	-5.20E-07	-1.82E-08	1.87E-07
2.9672	0.3003	1.9943	0.1497	-3.46E-07	6.96E-07	-5.20E-07	-1.82E-08	1.87E-07
4.3009	0.2999	0.6079	0.1505	-3.46E-07	6.96E-07	-5.20E-07	-1.82E-08	1.87E-07
2.4705	0.3004	2.5107	0.1498	-3.46E-07	6.96E-07	-5.20E-07	-1.82E-08	1.87E-07
2.5305	0.2996	2.4486	0.1502	-3.46E-07	6.96E-07	-5.20E-07	-1.82E-08	1.87E-07
4.8856	0.2999	1.44E-06	0.3969	-3.84E-07	7.25E-07	-4.90E-07	-1.64E-08	1.62E-07
3.0550	0.2997	1.9032	0.1503	-3.46E-07	6.96E-07	-5.20E-07	-1.81E-08	1.87E-07
3.8846	0.3002	1.04056	0.1496	-3.46E-07	6.96E-07	-5.20E-07	-1.82E-08	1.87E-07
2.5605	0.3003	2.41719	0.1498	-3.46E-07	6.96E-07	-5.20E-07	-1.79E-08	1.88E-07
4.3263	0.2999	0.58152	0.1506	-3.46E-07	6.96E-07	-5.20E-07	-1.84E-08	1.87E-07
3.4964	0.3003	1.44408	0.1497	-3.48E-07	6.93E-07	-5.23E-07	-2.02E-08	1.86E-07
2.3583	0.2996	2.62765	0.1502	-3.46E-07	6.96E-07	-5.20E-07	-1.81E-08	1.87E-07
3.6934	0.2998	1.23959	0.1504	-3.46E-07	6.96E-07	-5.20E-07	-1.83E-08	1.87E-07
2.8810	0.2997	2.08419	0.1502	-3.46E-07	6.96E-07	-5.20E-07	-1.82E-08	1.87E-07
2.3864	0.2996	2.59843	0.1502	-3.46E-07	6.96E-07	-5.20E-07	-1.83E-08	1.87E-07
2.5721	0.3004	2.40512	0.1498	-3.46E-07	6.96E-07	-5.20E-07	-1.81E-08	1.87E-07
2.5627	0.2996	2.41509	0.1502	-3.46E-07	6.96E-07	-5.20E-07	-1.80E-08	1.88E-07
2.5362	0.3004	2.44236	0.1498	-3.46E-07	6.96E-07	-5.20E-07	-1.81E-08	1.87E-07
2.5434	0.3003	2.43492	0.1498	-3.46E-07	6.96E-07	-5.20E-07	-1.83E-08	1.87E-07
2.2930	0.3004	2.69521	0.1498	-3.46E-07	6.96E-07	-5.20E-07	-1.82E-08	1.87E-07
2.6648	0.3004	2.30865	0.1498	-3.46E-07	6.96E-07	-5.20E-07	-1.79E-08	1.88E-07
2.5266	0.3004	2.45239	0.1498	-3.46E-07	6.96E-07	-5.20E-07	-1.82E-08	1.87E-07

Table 3.7: Solutions of example 4 (see page 120) found by the Levenberg-Marquardt method in 50 runs of the algorithm (each call was started from different random starting points). Difference between the simulated and estimated forces for five contraction levels are also presented. Note that the exact solution for example 4 is: $x_1 = 2$, $y_1 = 0.3$, $x_2 = 3$, and $y_2 = 0.15$

				...from the previous page				
Muscle parameters (unknowns)				**$E_{rr} = F_{simulated} - F_{estimated}$**				
x_1	y_1	x_2	y_2	level 1	level 2	level 3	level 4	level 5
2.4450	0.3004	2.53202	0.1498	-3.46E-07	6.96E-07	-5.20E-07	-1.82E-08	1.87E-07
2.8042	0.3003	2.16373	0.1497	-3.46E-07	6.96E-07	-5.20E-07	-1.82E-08	1.87E-07
2.2056	0.3004	2.78616	0.1498	-3.46E-07	6.96E-07	-5.20E-07	-1.89E-08	1.87E-07
3.5946	0.2998	1.34228	0.1503	-3.46E-07	6.96E-07	-5.20E-07	-1.84E-08	1.87E-07
2.7954	0.3004	2.17293	0.1498	-3.46E-07	6.96E-07	-5.20E-07	-1.83E-08	1.87E-07
2.6940	0.3004	2.27838	0.1498	-3.46E-07	6.96E-07	-5.20E-07	-1.81E-08	1.87E-07
2.7195	0.3004	2.25178	0.1498	-3.46E-07	6.96E-07	-5.20E-07	-1.82E-08	1.87E-07
2.8804	0.2997	2.08486	0.1502	-3.46E-07	6.96E-07	-5.20E-07	-1.82E-08	1.87E-07
2.8625	0.3003	2.10319	0.1498	-3.46E-07	6.96E-07	-5.20E-07	-1.83E-08	1.87E-07
2.8037	0.3003	2.16430	0.1498	-3.46E-07	6.96E-07	-5.20E-07	-1.82E-08	1.87E-07

Some solutions that were found for example 4 (see table 3.7) are very close to each other and they are very similar. This is due to the fact that the optimization algorithm found them as the values could observe the condition of $E_{rr} = F_{simulated} - F_{estimated} < 10^{-6}$. If we increase the precision (setting a smaller value than 10^{-6} for E_{rr}), the similar values are expected to converge to one value. Increasing the precision of the solutions will increase the computational time. Therefore, there will be a compromise between the computational time and the precision of solution that we need (please also see section 3.2.2 on page 108).

figure 3.11 shows the solutions found for example 4, considering the first four contraction levels and applying Analytical-Graphical approach.
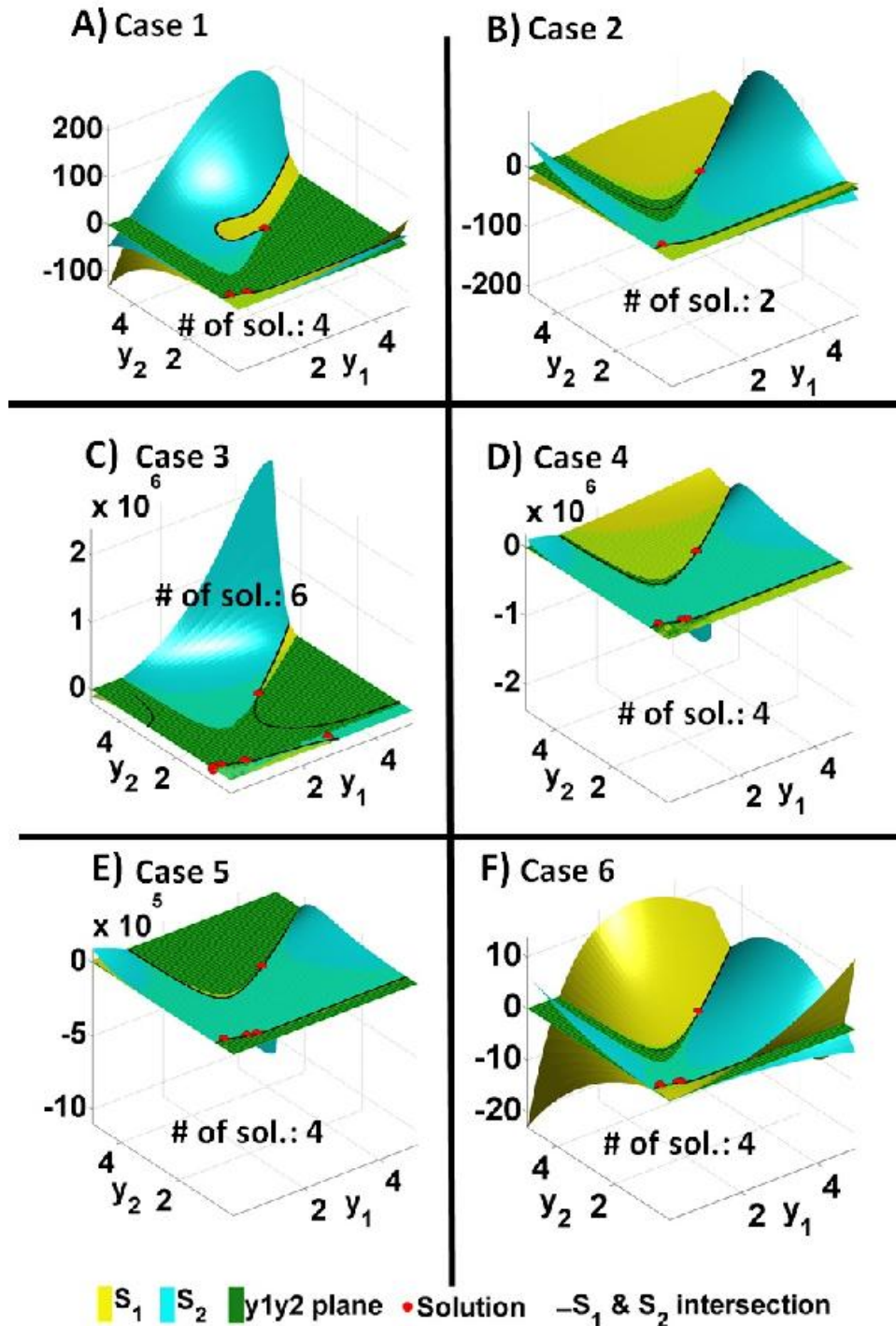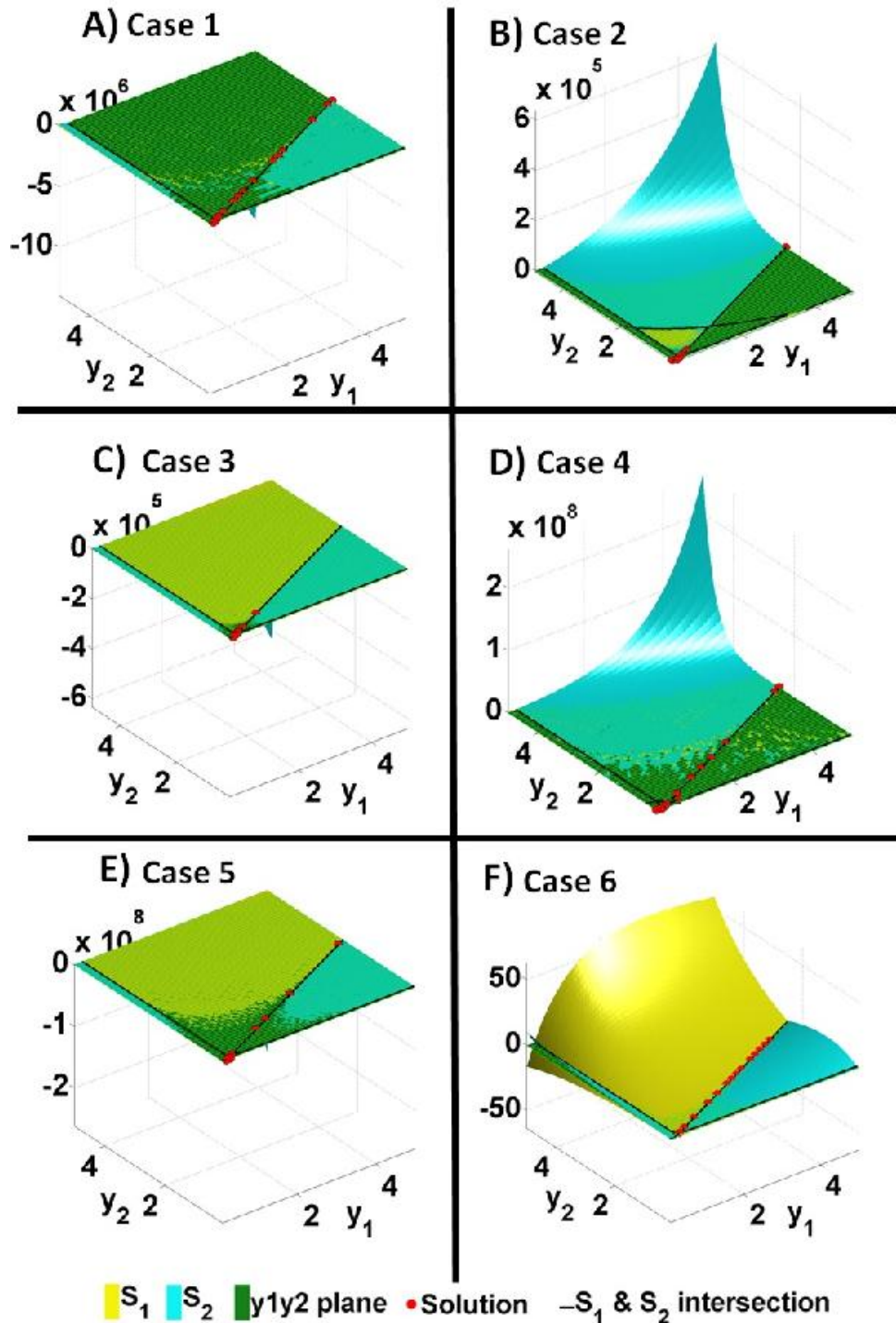
Figure 3.11: Example 4: Surfaces $(f(y_1, y_2)$ and $g(y_1, y_2))$ derived from the contraction levels A) 1 and 3 (see eqs. 3.18 and 3.19), B) 1 , 4 (see eqs. 3.20 and 3.21), C) 2 and 3(see eqs.3.22 and 3.23), D) 2 and 4(see eqs. 3.24 and 3.25), E) 3 and 4 (see eqs. 3.26 and 3.27), F) 1 and 2 (see eqs. 3.28 and 3.29); their intersection (solid line), and intersection with the plane $y_1 y_2$ (solutions, red circles)

3.5 Investigating the load sharing among muscles acting on elbow joint using particle Swarm Optimization: An experimental study

3.5.1 Introduction

In section 3.2.1 (see page 94), we discussed the Analytical-Graphical Approach (AGA) and its ability in solving the load sharing problem and finding the exact solutions for the force prediction model(see eq. 3.2 on page 92) concerning two muscles. The dimension of the model presented for force prediction (see eq. 3.2 on page 92) is twice the number of muscles. Solving load sharing problems using the AGA in cases of considering more than two muscles is not a trivial task. Plotting and visualizing the solutions for the cases with four dimensions or even more is another issue in AGA. Although, it is possible to decrease the number of muscles by merging them (ex.: considering the two heads of Biceps Brachii muscle as only one muscle) based on their function, this simplification increases the force estimation error. Therefore, the solutions found using AGA will not be the exact solutions anymore. Moreover, there are some muscles in the human body whose surface EMG is hard to be detected by recent technologies (ex.: the Brachilalis muscle, which is placed under the Biceps Brachii and is a deep muscle, spanned on the elbow joint and acts as an elbow flexor). The difficulty in detecting the sEMG of these muscles (deep, or very short muscles) is another source of error in load sharing estimation. Therefore, apart from the usefulness of AGA in theoretical and simulation studies, the AGA is not suitable in finding the exact solutions because of its simplifications that do not apply in real cases. For a real case, we investigated the load sharing problem of muscles acting on the elbow joint using an optimization algorithm (particle swarm method). In the following sections we discuss about method, materials, results and conclusions.

3.5.2 Experimental recordings

The muscles of our interest are muscles, which are acting on the elbow joint to produce force during elbow flexion and extension (i.e. elbow flexors and elbow extensors). Elbow flexors are "Biceps Brachii" (including the long and short heads) muscle, "Brachialis" muscle, and "Brachioradialis". The elbow extensors are "Triceps Brachii" (including

3. ESTIMATION OF MUSCLE FORCE FROM EMG

three heads: Medial, long, and lateral heads) and the "Anconeus" muscle (9) (please see figure 3.12).

Five healthy male subjects (mean $\pm$ std , age: 21.3 ± 2.8 years; stature 174.3 ± 2.6 cm; body mass 71.0 ± 3.4 kg) participated in the study after giving written informed consent in accordance with the Declaration of Helsinki.

sEMG signals were recorded from the Biceps Brachii (BB), Brachioradialis (BR), lateral and medial head of the Triceps Brachii (TBL and TBM) during isometric voluntary flexions-extensions with the elbow flexed at 90 degree. A two-dimensional adhesive array of 65 electrodes of circular shape (5 columns and 13 rows, 8 mm inter-electrode distance, LISiN Spes Medica, Battipaglia, Salerno, Italy) was used to detect signals from the BB muscle distal half. Three linear arrays of 8 electrodes (5 mm inter-electrode distance) were used to acquire signals from BR, TBL, and TBM.

The main innervation zone (IZ) was located for each muscle prior to the electrode-array placement and the adhesive arrays were placed either proximally or distally from the main IZ location depending on anatomical features of the subject. The reference electrode was placed at the wrist. The skin was abraded with a paste (MeditecEvery, Parma, Italy). Monopolar surface EMG signals were amplified (multichannel surface EMG amplifier, EMG-USB, LISiN-OT Bioelettronica, Torino, Italy), band-pass filtered (3 dB bandwidth, 10750 Hz), and sampled at 2048 Hz with a resolution of 12 bits.

The torque signal was measured by the isometric brace used for limb fixation, amplified (Force Amplifier MISO-II, LISiN, Politecnico di Torino, Italy), sampled at 2048 Hz, displayed in real-time on a computer screen as feedback to the subjects, and recorded concurrently with the EMG signals. Three maximal voluntary isometric flexion and extension contractions (fMVC, eMVC) lasting five seconds were performed at the beginning of the experimental session, and the highest was selected as the reference MVC for each direction (please see figure 3.13).
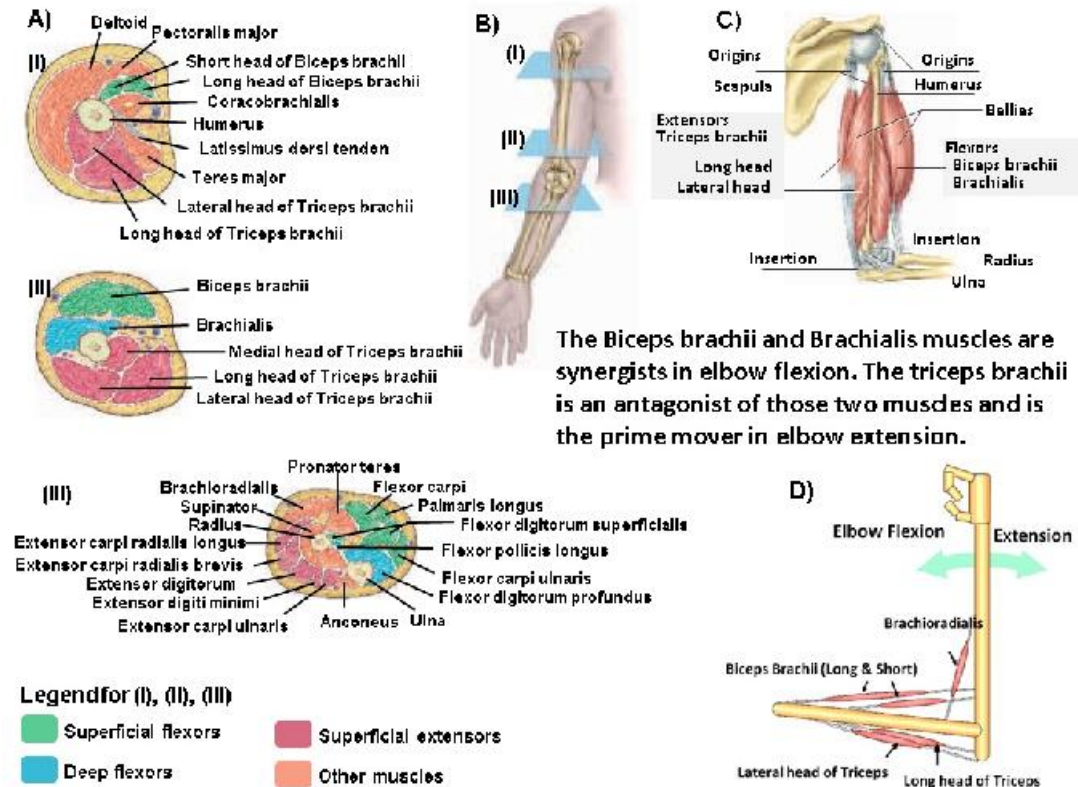
Figure 3.12: A)Serial Cross Sections Through the Upper Limb. Each section (I, II, and III) is taken at the correspondingly labeled level in the figure at panel "B". C) Side view of the right arm showing the Biceps Brachii and Brachialis muscles, which are synergists in elbow flexion. The Triceps Brachii is an antagonist of those two muscles and is the prime mover in elbow extension. D) Muscles analyzed in the study. Biceps Brachii (BB) short and long heads, Brachioradialis (BR), and Triceps Brachii lateral head (TBL) and medial (TBM) heads. BB and BR act as flexors. TBL and TBM act as extensors. Panels "A", "B" and "C" are from (9).

Let's consider eMVC as the maximum voluntary contraction in elbow extension and fMVC as the maximum voluntary contraction in elbow flexion. The subjects were requested to perform three series of flexion-extension force ramps lasting 24 s each. Each series consisted of four isometric ramps from n% eMVC to n% fMVC and back (with n = 30, 50, 70). Few ramps were performed before the beginning of the protocol to train the subjects to track the ramp target on the biofeedback screen. Monopolar

3. ESTIMATION OF MUSCLE FORCE FROM EMG

(MN) sEMG signals were digitally band-pass filtered (20–450 Hz, 4th order Butterworth filter, zero phase) and the force signal was low-pass filtered with a cut-off frequency of 1 Hz (4th order non-causal Butterworth filter). Single differential (SD) and double differential (DD) signals were computed along the fiber direction, thus obtaining three sets of signals (MN, SD, and DD). The envelope of sEMG signals was extracted by non-causal digital low-pass filtering (1 Hz, 4th order Butterworth filter) of the rectified signals. For each muscle (i.e. detection system) the global envelope was computed as the spatial average of the corresponding recorded signals.

In this work, the estimated torque produced by the muscles acting on the elbow is described by equation 3.58

$$\hat{T}[n] = \sum_{m \in muscles} x_m (V_m[n])^{y_m} \tag{3.58}$$

Where "n" is the n th sample of the envelope "V_m"(μV), "$\hat{T}[n]$" is the estimated torque[Nm], "$muscles$" identify the set of muscles considered. In this model, "x_m" is the linear weight associated with the muscle "m", and "y_m" is the exponential weight that takes into account the non-linearity of the relationship between sEMG and torque of muscle "m". To estimate the model parameters (x_m, y_m), the sEMG-torque relationship can be formulated as an optimization problem by minimization of the objective function defined in equation 3.59,

$$E_{rr} = \sum_{n=1}^{K} (T[n] - \hat{T}[n])^2 \tag{3.59}$$

where "$T[n]$" is the measured torque, "$\hat{T}[n]$" is the estimated torque (see eq. 3.58), "n" is the sample index, and "K" is the number of samples in the signal.
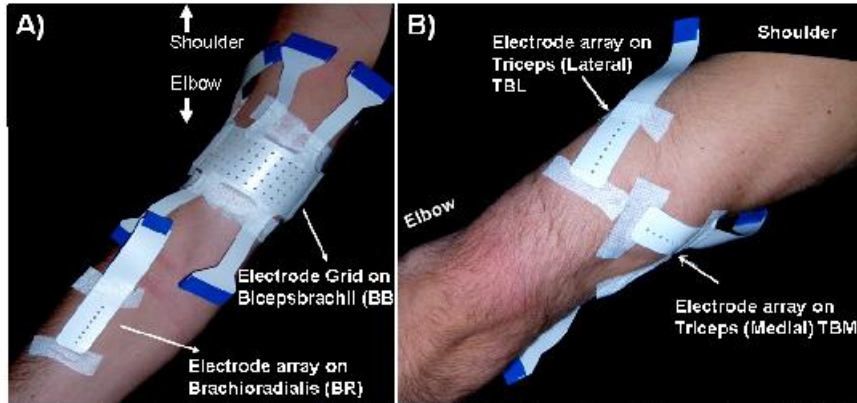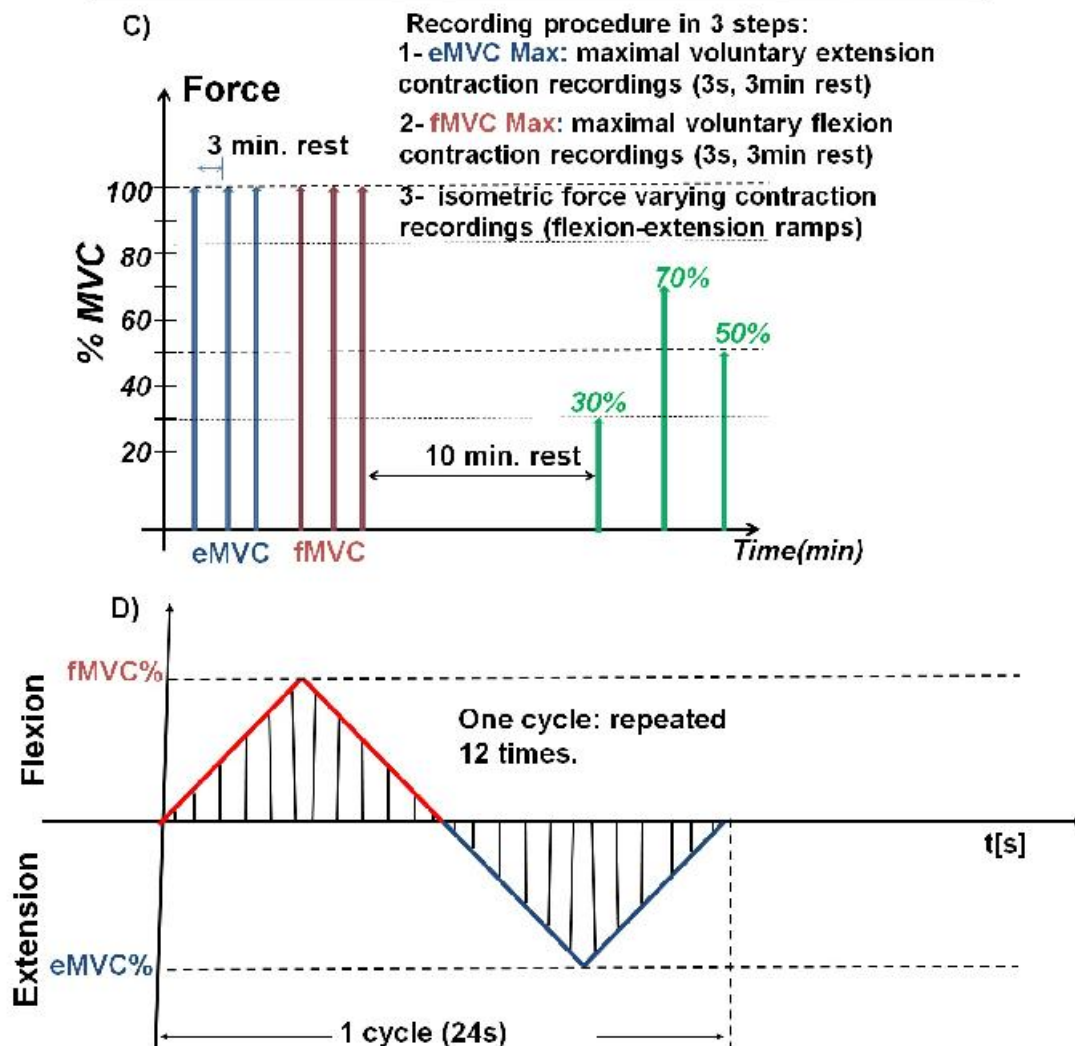
Figure 3.13: Please see the caption of this figure on the next page ...

Figure 3.13: ... from the previous page: A) and B) Placement of electrode arrays (1D and 2D) over the elbow flexors and extensors. The sEMG envelope was the spatial average of the single differential envelopes along the fiber direction with the arrays placed on one side of the innervation zone. C) Representation of the contractions performed within the protocol by each subject. The groups of contractions are reported on the x–axis ordered with respect to chronology: eMVCs that are maximal voluntary extension contractions, 3s each, with three minutes rest in between, fMVCs that are maximal voluntary flexion contractions ,3s each, with three minutes rest in between; D) One of the 12 cycles of flexion–extension ramp in voluntary isometric contractions, whose peak value is in the 30% to 70%MVC range with steps of 20%MVC.

3.5.3 Constraint optimization

The values of the linear weights x_m resulting from the training phase are expected to be positive for flexor muscles and negative for extensor muscles. The values of y_m are expected to be in the range (0,1] (1, 10, 11). The objective function customized for our study is reported in equation 3.60. The constraint optimization is formulated using helping variables to find x_m and y_m:

$$E_{rr} = \frac{\sum_{n=1}^{K_t} \left(T[n] - \sum_{m=1}^{4} z_m(|x_m|) V_m[n]^{|\frac{y_m}{R}|} \right)^2}{\sum_{n=1}^{K_t} (T[n])^2} \tag{3.60}$$

where variables x_m and y_m are real numbers ranging within [-R,R] (R=100, in our study), the first and second muscles are the elbow flexors ($m = 1, 2$; $z_m = 1$: Biceps Brachii, and Brachioradialis) while the third and forth muscles are elbow extensors ($m = 3, 4$; $z_m = -1$: the medial and lateral heads of Triceps Brachii). Twenty four seconds (the first cycle of flexion-extension) were used to estimate the linear and exponential weights. K_t is the number of samples corresponding to the first cycle of flexion-extension. The accuracy of the algorithm was assessed in terms of relative errors (in percent), defined as $100\sqrt{E_{rr}}$.

The performance of the algorithm was measured using number of evaluations of the objective function which was called "Evals" (see table 3.8) and the total execution time of the algorithm used to solve the optimization problem.

Recalling equations 3.30 to 3.33 (see page 111), for updating the position (eq. 3.30 on

page 111) and velocity (eq. 3.33 on page 111) at each iteration, the coefficient "$c1$" as the cognitive acceleration coefficient (7) was set to $0.2(c1 = 2.0)$ and $c2$ as the social acceleration coefficient (7) was considered 0.5 ($c2 = 0.5$). $r1$ and $r2$ were considered as random vectors whose elements were uniformly distributed in U(0,1).

A large value of inertia weight favors global search ("exploration"), while a small value favors local search ("exploitation"). Our strategy was to set the value high initially (1.2) to encourage exploration, and then reducing it towards a low value (0.1) to fine tune the final solution. To prevent oscillations, the velocity components were limited to [-4,4]. Whenever the absolute value of the positions "x" reaches the limit 100, the velocity components were clamped and the sign of the corresponding velocities was changed to continue searching within the defined ranges. The maximum number of iterations ("max_ iter") was $500K + 200$, where "K" is the number of muscles. The number of particles in the swarm was set to $20 + 10\sqrt{2K}$. Several extensions and modifications to the standard method were used to speed convergence and discourage premature convergence to a non-global minimum as follows:

- Multi-start PSO Approach: the PSO algorithm was run twice (12). The best result found at the first iteration was used as a particle in the second run. Increasing the number of runs increases the chance of finding the global minimum, but at the cost of increased computation time.

- Sobol's quasi-random sequence: 60% of the particles were filled with uniform random values, while the remaining 40% were filled with Sobol's quasi-random sequence (13), in order to cover the search space regularly.

- Random PSO Approach (12): Randomized particles were introduced in the swarm as follows every 40 iterations, the positions of the particles filled with the Sobolian Sequence, are re-initialized using the next generation of Sobol's sequence.

- Breeding Algorithm: breeding (arithmetic cross-over) operator was taken from the genetic algorithm to increase the performance of the PSO (14). In every iteration, there is a 20% chance that two offspring particles are generated using the arithmetic mean of two randomly chosen (from the non-Sobolian partition) parent particles.

- Swarm Regeneration and Multi-Swarm Strategy (15): if a swarm's best solution did not change for 200 iterations, then a new, randomly initialized swarm was created to increase the exploration while the original swarm was kept to further tuning the solution found. The maximum number of Swarms was set to the number of muscles. After the initialization of PSO, two swarms were generated. A swarm was deleted if all of its particles converged to a single solution. Finally, a multi-criteria for terminating the PSO (based on the maximum number of iterations and the diameter of the swarm) was used (16).

3.5.4 Results

Figure 3.14(panel "A") shows the comparison between the recorded and estimated torques. The contribution of the four muscles acting on the elbow joint is also reported. Panel "B" of figure 3.14 depicts the single differential(SD) sEMG envelops of the above mentioned muscles. Table 3.8 reports the results of PSO on SD recording for five subjects during elbow flexion-extension isometric ramps on the training and test sets at 30%, 50% and 70% Maximum Voluntary Contractions (MVC). The cross-checking results of PSO on Monopolar, Single-Differential, and Double Differential recordings for elbow flexion-extension at 30% and 70% MVC are reported in table 3.9. The missing data in the tables correspond with the conditions in which subjects could not follow the force target and the force variations were not acceptable.

As it can be seen from figure 3.14, the total estimated force (presented in dotted red in the figure) tracks well the recorded torque. Based on the estimated parameters of the model presented as equation 3.58, the torque of each muscle was computed. The results show that in elbow flexion phase the torque of BB is greater than the BR while the single differential sEMG envelope of BR is greater than BB. Moreover, the lateral head of the Triceps Brachii (TBL) is producing greater torque in elbow extension than the medial head of the Triceps Brachii (TBM).
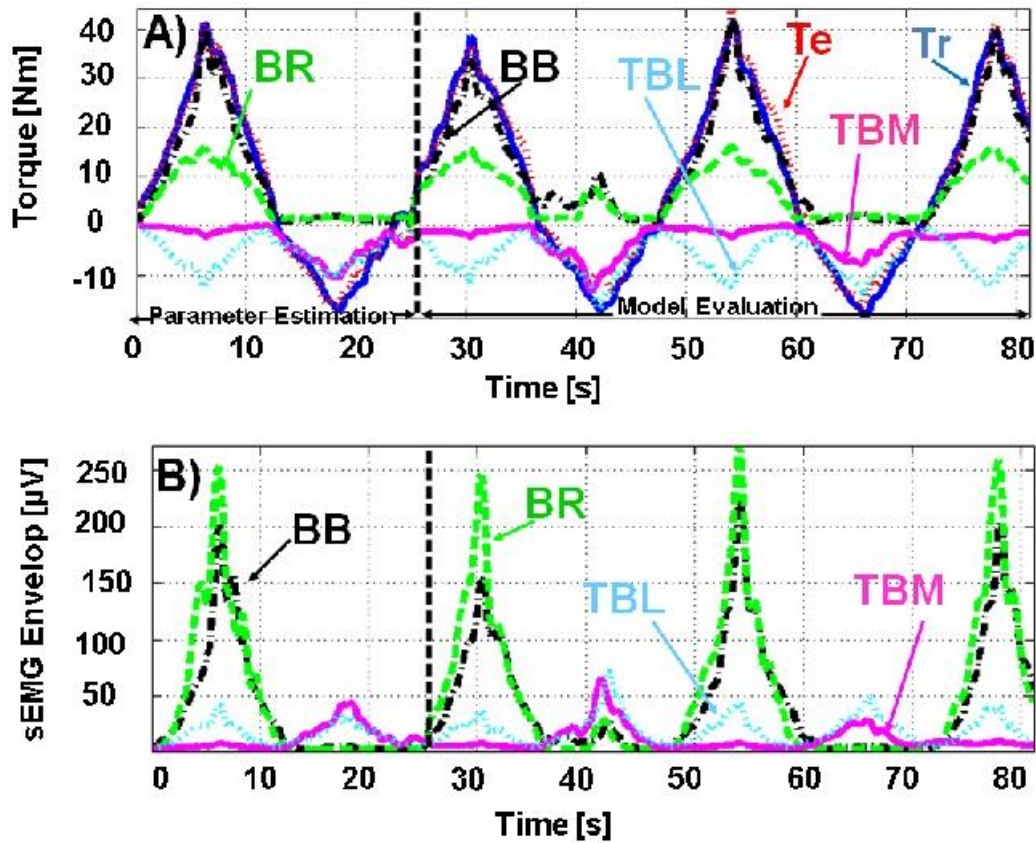
Figure 3.14: A) recorded Torque "Tr" (solid blue) and estimated Torque "Te" (dotted red) in addition to the reconstructed Torques for each muscle (top). B) Single differential sEMG envelopes for Biceps Brachii (BB, dashdot black), Brachioradialis (BR, dashed green), medial and lateral heads of the Triceps Brachii (TBM=solid magenta and dotted cyan=TBL) for subject No. 5 during a 70 %MVC elbow flexion-extension isometric ramp. The sEMG signals and measured torque up to 25.6 s (shown by the tick dashed black line) were used to estimate the parameters of EMG based force estimation model i.e. "x_m" and "y_m" in the equation 3.58 (phase 1) and the rest was used for the test (phase 2).

Table 3.8: Result of Particle Swarm Optimization (PSO) on single differential (SD) recording for five subjects during elbow flexion-extension isometric on the training and test sets at 30%, 50% and 70% maximum voluntary contraction (MVC); Average($\pm$SD) relative error obtained in the training and test sets were $10.2 \pm 3.5(\%)$ and $14.4 \pm 4.5(\%)$ respectively. # Swarms=number of swarms generated in the PSO algorithm for the first and second runs respectively, Evals= number of evaluations of the objective function ($\times 10^6$), Time= total execution time of the PSO at the first and second runs, Rel Err= the RMS of the force prediction error divided by the RMS of the measured force.

	Subjects		S1	S2	S3	S4	S5
30%MVC	Training Set	# Swarms	2,4	4,4	2,4	–	2,4
		Evals	0.80	1.08	0.80	–	0.80
		Time[s]	465	619	460	–	478
		RelErr(%)	10.8	7.4	14.3	–	18.6
	Test Set	RelErr(%)	14.6	10.6	13.9	–	22.2
50%MVC	Training Set	# Swarms	3, 4	2, 4	2, 4	2, 4	4, 4
		Evals	1.92	0.08	0.80	0.80	0.97
		Time[s]	1121	461	475	508	478
		RelErr(%)	9.5	6.6	6.6	10.1	10.7
	Test Set	RelErr(%)	12.3	10.3	11.1	11.4	24.0
70%MVC	Training Set	# Swarms	2, 4	–	4, 3	–	2,4
		Evals	0.80	–	1.52	–	1.58
		Time[s]	467	–	956	–	979
		RelErr(%)	11.8	–	7.6	–	6.5
	Test Set	RelErr(%)	14.7	–	16.4	–	11.3

Table 3.9: The cross-checking results of Particle Swarm Optimization (PSO) on Monopolar(MN), Single Differential(SD), and Double Differential(DD) recordings for five subjects during elbow flexion-extension isometric ramps on the training and test sets (using the coefficients obtained at 50% MVC to estimate the force at 30% and 70%). Rel Err= the RMS of the force prediction error (using the coefficients obtained at 50% MVC) divided by the RMS of the measured force.

	Subjects		S1	S2	S3	S4	S5	Mean±Std Total
MN	Rel Err(%)	30% MVC	33.6	19.4	32.3	–	17.9	26.0±7.2
		70% MVC	0.80	1.08	0.80	–	0.80	N = 7
SD	Rel Err(%)	30% MVC	23.8	13.7	21.9	–	35.1	25.3±6.7
		70% MVC	28.1	–	26.1	–	28.4	N = 7
DD	Rel Err(%)	30% MVC	29.7	16.4	15.2	–	42.2	28.7 ±10.0
		70% MVC	37.0	–	30.9	–	29.5	N = 7

3.5.5 Discussion

The issue of muscle force prediction from EMG has been addressed in the literature, e.g. (17, 18, 19). Unlike other methods that considered linear relationship between EMG and force (17, 18), a non-linear model was proposed in this chapter. As evidenced by Clancy et al. (17), using non-linear models is possible to capture additional subtle behavior in EMG-force relationship. Also, our model does not require preset musculoskeletal parameters (e.g. parallel elastic stiffness and damping (19)).

When solving an optimization problem, the goal is to find the global optimal solution in an acceptable amount of time. There are different methods capable of finding solutions to optimization problems, including exact methods, heuristics and meta heuristics (5). Exact methods solve optimization problems by searching the entire solution space exhaustively and often exhausting available resources.

With respect to previously tested methods (3), the PSO algorithm eliminates the problems of initialization and has an intrinsically higher likelihood of finding the global minimum and nearby relative minima that might be worth of consideration. However, the computational load of PSO is greater than that of Interior-Reflective Newton Algorithm (IRNA). The fact that the EMG of some deep muscles cannot be collected

with surface electrodes (e.g. brachialis muscle) remains a strong limitation and major cause of error. The error in reconstructing the total torque with the two algorithms (IRNA and PSO) is not that different (13.2 3 % for IRNA, and 10.2 4 % for PSO in the training set). However, IRNA required several initialization and tighter constraints found by trial-and-errors for the input variables to find a suitable optimum which was not the case for PSO, whose parameters initialization can be randomly chosen.

3.6 Conclusion

Analytical-Graphical and Numerical approaches were presented and discussed in this chapter in order to solve the load sharing problem (EMG based muscle force estimation) formulated in equation 3.2. Both approaches can solve the problem and find the model parameters of the muscle. The Analytical-Graphical Approach (AGA) finds the exact solutions. If the number of muscles in the model increases, deriving the equation of the surfaces whose intersection provides the solutions, will be too complex.

The dimension of the model is twice the number of muscles, therefore plotting the solutions in real cases which at least four muscles (two agonists and two antagonists) act on a joint (i.e. 8 unknowns should be identified), is a limitation. For simulation studies, AGA graphically shows that there is more than one solution to the load sharing problem even for the simplest theoretical case (i.e. a joint spanned with two muscles). Different possible combinations of equations in order to derive the surfaces whose intersection provide the solutions, offer different number of solutions to the load sharing problem. Totally, solutions found from different cases are equivalent. In some cases due to the discretization and numerical error, the number of solutions are different. All of the solutions found by the AGA were also found by Numerical Approach (NA) using optimization algorithms. In optimization algorithms, starting from different point (initial conditions), different solutions were found. It should be noted that optimization algorithms

- do not guarantee that the solution is the exact solution.

- might get stuck in local minima finding wrong solutions or no solution.

- might be designed to search the entire solution space exhaustively, but it would be quite time consuming and impractical.

- depend on the initial conditions and starting points.

The main conclusion of this study is that the load sharing strategy is not unique. Physiologically, for each muscle, the model parameters "x" and "y" might be set by the muscle through minimizing the energy consumption to carryout a certain task. This can be a hypothesize for future studies. Meanwhile, the presented model is a mathematical model that describes the relation between the force and sEMG amplitude. Finding a physiological explanation of "x" and "y" can be another topic for further studies.

References

[1] J. H. Lawrence and C. J. De Luca. **Myoelectric signal versus force relationship in different human muscles**. *Journal of Applied Physiology*, **54**(6):1653–1659, 1983. 91, 132

[2] Catherine Disselhorst-Klug, Thomas Schmitz-Rode, and Günter Rau. **Surface electromyography and muscle force: Limits in sEMGforce relationship and new approaches for applications**. *Clinical Biomechanics*, **24**(3):225–235, 2009. 91

[3] R. Merletti and Matteo Aventaggiato. **EMG-force relationship: preliminary data on load sharing**. In *XVIII Congress of the International Society of Electrophysiology and Kinesiology (ISEK)*, 2010. 91, 92, 109, 137

[4] A. Botter, H. R. Marateb, B. Afsharipour, and R. Merletti. **Solving EMG-force relationship using Particle Swarm Optimization**. *Conf Proc IEEE Eng Med Biol Soc*, **2011**:3861–4, 2011. 91, 92, 108, 109, 111

[5] Mendes; Rue. *Population Topologies and Their Influence in Particle Swarm Performance*. Thesis, 2004. 108, 137

[6] Riccardo Poli, James Kennedy, and Tim Blackwell. **Particle swarm optimization**. *Swarm Intelligence*, **1**(1):33–57, 2007. 109

[7] Riccardo Poli. **Analysis of the Publications on the Applications of Particle Swarm Optimisation**. *Journal of Artificial Evolution and Applications*, **2008**, 2008. 109, 110, 111, 133

[8] Henri P. Gavin. **The Levenberg-Marquardt method for nonlinear least squares curve-fitting problems**, 2013. 113

[9] Kenneth S. Saladin. *Anatomy & Physiology: The Unity of Form and Function, 3/e*. New York, NY : McGraw-Hill, 2003. xx, 128, 129

[10] P. J. Sparto, M. Parnianpour, W. S. Marras, K. P. Granata, T. E. Reinsel, and S. Simon. **Effect of electromyogram-force relationships and method of gain estimation on the predictions of an electromyogram-driven model of spinal loading**. *Spine (Phila Pa 1976)*, **23**(4):423–429, 1998. 132

[11] H Peter Clamann. **Motor Unit Recruitment and the Gradation of Muscle Force**. *Physical Therapy*, **73**(12):830–843, 1993. 132

[12] Frans Van Den Bergh. *An analysis of particle swarm optimizers*. Thesis, 2002. 133

[13] Bennett L. Fox. **Algorithm 647: Implementation and Relative Efficiency of Quasirandom Sequence Generators**. *ACM Trans. Math. Softw.*, **12**(4):362–376, 1986. 133

[14] Thiemo Krink and Morten Løvbjerg. *The LifeCycle Model: Combining Particle Swarm Optimisation, Genetic Algorithms and HillClimbers*, **2439** of *Lecture Notes in Computer Science*, book section 60, pages 621–630. Springer Berlin Heidelberg, 2002. 133

[15] K. E. Parsopoulos and M. N. Vrahatis. *Modification of the Particle Swarm Optimizer for Locating All the Global Minima*, book section 80, pages 324–327. Springer Vienna, 2001. 134

[16] Karin Zielinski and Rainer Laur. **Stopping Criteria for a Constrained Single-Objective Particle Swarm Optimization Algorithm**. *Informatica*, **31**(1), 2007. 134

[17] E. A. Clancy, O. Bida, and D. Rancourt. **Influence of advanced electromyogram (EMG) amplitude processors on EMG-to-torque estimation during constant-posture, force-varying contractions**. *Journal of biomechanics*, **39**(14):2690–2698, 2006. 137

[18] Marco J. M. Hoozemans and Jaap H. van Dieën. **Prediction of handgrip forces using surface EMG of forearm muscles**. *Journal of electromyography and kinesiology : official journal of the International Society of Electrophysiological Kinesiology*, **15**(4):358–366, 2005. 137

[19] Luciano Luporini Menegaldo and Liliam Fernandes de Oliveira. **Effect of muscle model parameter scaling for isometric plantar flexion torque prediction**. *Journal of biomechanics*, **42**(15):2597–2601, 2009. 137

4

Applications of surface electromyography: a single case study of Yoga relaxation

4.1 Introduction

Modern society and lifestyles impose severe stresses on human beings, young and old from all walks of life. Medical researches had demonstrated with ample proofs that prolonged stresses, whether physical, mental or emotional, can adversely impact a person's health and well being. To help us manage and reduce our stress levels, there have been numerous medical, psychological, physical, alternative medical, medicinal, dietary and even philosophical and spiritual methods, techniques and schools. It is generally accepted and agreed that, whatever the technique employed, the more relaxed a person can achieve physically and mentally, the more peace, joy and physical, mental and spiritual well being can be achieved. Recently, enhances on expression of genes associated with energy metabolism, mitochondrial function, insulin secretion and telomere (a telomere is a region of repetitive DNA at the end of a chromosome, which protects the end of the chromosome from deterioration[1]) maintenance were reported as the effect of relaxation (ex. meditation and yoga) by Bhasin and Dusek (1).

Yoga is a commonly known generic term for the physical, mental, and spiritual practices or disciplines which originated in ancient India with a view to attain a state of

---

[1]http://www.news-medical.net/health/Telomere-What-are-Telomeres.aspx

permanent peace. Apart from the spiritual goals the physical postures of yoga are used to alleviate health problems, reduce stress and make the spine supple in contemporary times. Yoga is also used as a complete exercise program and physical therapy routine. Nambi and Shah (2) reported the effect of yoga and EMG biofeedback on pain and functional disability in chronic unilateral knee osteoarthritis. They reported a significant difference(p=0.001) in pain reduction of a group who received yoga practice for 8 weeks as an additional treatment to the EMG biofeedback comparing to the second group, who received only EMG biofeedback. In another study, Wagner et.al (3) investigated the effect of laughter yoga on trunk muscles and reported a positive effect on trunk muscle activation. They stated that the activation level of internal oblique muscle during laughter yoga is higher in comparison with the traditional exercises. Although, some scientific studies such as those mentioned above have been conducted on yoga, no study is reported applying a high density sEMG (HDsEMG)detection system to analyze the effect of muscle relaxation on distribution of muscle activity. The idea of this study comes from finding a noninvasive way for relaxing a certain muscle. Muscle self-relaxation (if it happens) can simplify the load sharing problem by decreasing the number of muscles acting on a joint avoiding invasive approaches. This simplification, can also lead us to validate force-sEMG model (see chapter 3 of this thesis). It is hypothesized that, long term yoga relaxation might provide yogis (a yogi is a practitioner of yoga) to control organs that ordinary people can not control voluntarily. We started from the following research questions:

1. Is there any significant change in sEMG amplitude distribution (or other features such as conduction velocity, mean and median frequencies) over the skin, when the muscle of interest is relaxed applying yoga relaxation techniques? If yes, how is this change?

2. Can a long time yoga practice provide the ability of controlling voluntarily the activity of a certain muscle?

A single case study has been carried out to answer the questions mentioned above. This chapter covers the method, results, and conclusion of effect of yoga relaxation on sEMG amplitude distribution.

4.2 Materials and Method

A yoga master(male, weight: 83 Kg, height: 181cm) participated to the study. We studied the sEMG amplitude distribution of two compartments of the Biceps Brachii (BB) muscle. Figure 4.1 shows the muscle of interest (panel "A"), the ultrasound image of the subject's right BB (panel "B"), and the location of the sEMG detection (panel "C").

A high density sEMG (HDsEMG) detection system including 64 channels (one 8×8
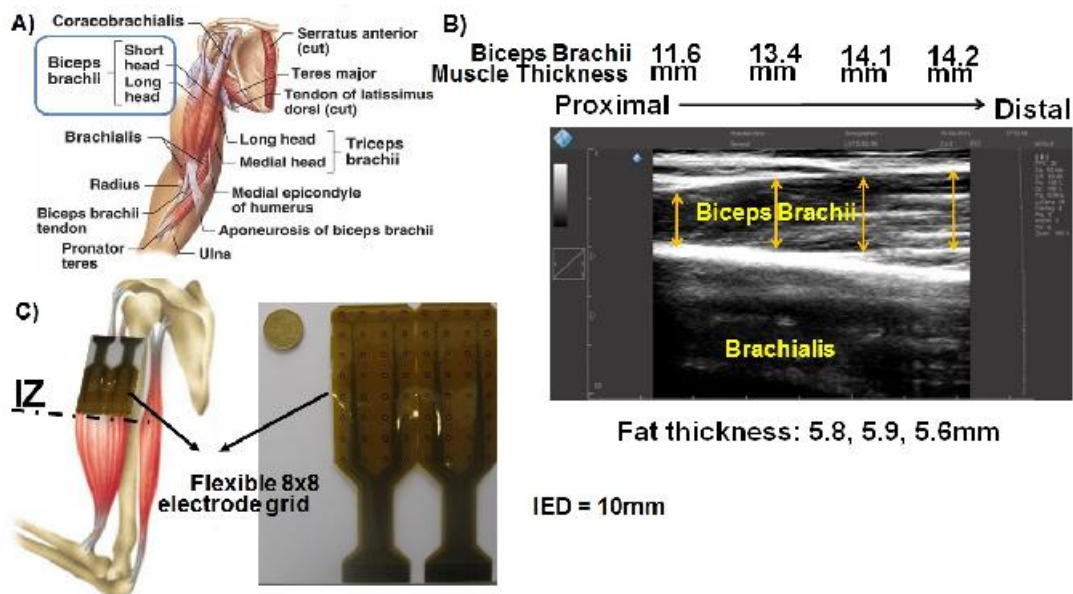
Figure 4.1: A)The muscle of interest for studying the effect of yoga relaxation on sEMG amplitude is presented (Courtesy of McGraw-Hill Companies). B) The ultrasound image taken from the subject's right arm (BB and Brachialis are identified). The BB's thickness from proximal to distal and fat thicknesses from three different parts of the image are also reported. C) One 8×8 flexible electrode grid was placed above the BB's innervation zone(IZ)

flexible grid) with 10mm inter electrode distance (IED) was applied to the right arm (proximal to the shoulder) of the subject (subject is a right handed person) above the innervation zone. As it was expected (4), the innervation zone was identified in about the middle of the BB, using a 16 electrode array (dry electrode, IED=5mm), before applying the 8×8 grid.

4. APPLICATIONS OF SURFACE ELECTROMYOGRAPHY: A SINGLE CASE STUDY OF YOGA RELAXATION

Monopolar surface EMG signals were amplified (multichannel surface EMG amplifier, Gain=2K, EMG-USB, LISiN-OT Bioelettronica, Torino, Italy), band-pass filtered (3 dB bandwidth, 10 – 750 Hz), and sampled at 2048 Hz with a resolution of 12 bits. Totally three recording sessions were performed. The first session was conducted such that the subject tried to change (transfer) the spatial distribution of the muscle activity from the short compartment to the long compartment by mental concentration. The map of muscle activity was shown to the subject as biofeedback. In the map of muscle activity (biofeedback), the active portion of muscle was specified by red color while the inactive portion was blue. The subject was asked to make the blue region (inactive portion of muscle) red (active portion of muscle) and make the red blue by mental concentration on the muscle. Through a 2 hours effort (first session), no changes were seen in transferring the muscle activity from short to long head of BB. In the second session, the subject did a self-relaxation (5min.) and signals were recorded before and after yoga relaxation in isometric condition while holding a weight (2Kg and 8Kg). Based on the subject's word, he was able to reach to deep yoga relaxation phase if a third party (a yoga practitioner, subject's friend) could help him. Therefore, by help from the third party, the third session was conducted and monopolar sEMG signals were recorded from a relaxed BB muscle. Figure 4.2 shows the procedure of sEMG recording considering before relaxation, after relaxation and after recovery from the yoga relaxation phase. Recovery time is the time that the subject declare he is in normal condition.

4.2.1 Signal processing

sEMG signals were acquired in monopolar configuration. Before computing the time and frequency domain parameters of the sEMG signals, the pre-processing procedure was carried out as the following steps:

1. Mean removal: Removing the average(dc component) of the signal from the signal.

2. Band pass filtering: sEMG signals were filtered by applying a fourth order digital zero phase filter (second order in each direction). The high and low pass cut-off frequencies were set to 20Hz and 400Hz respectively.

3. Spectral interpolation: The power line interference and its harmonics(up to 10) were attenuated by spectral interpolation technique.
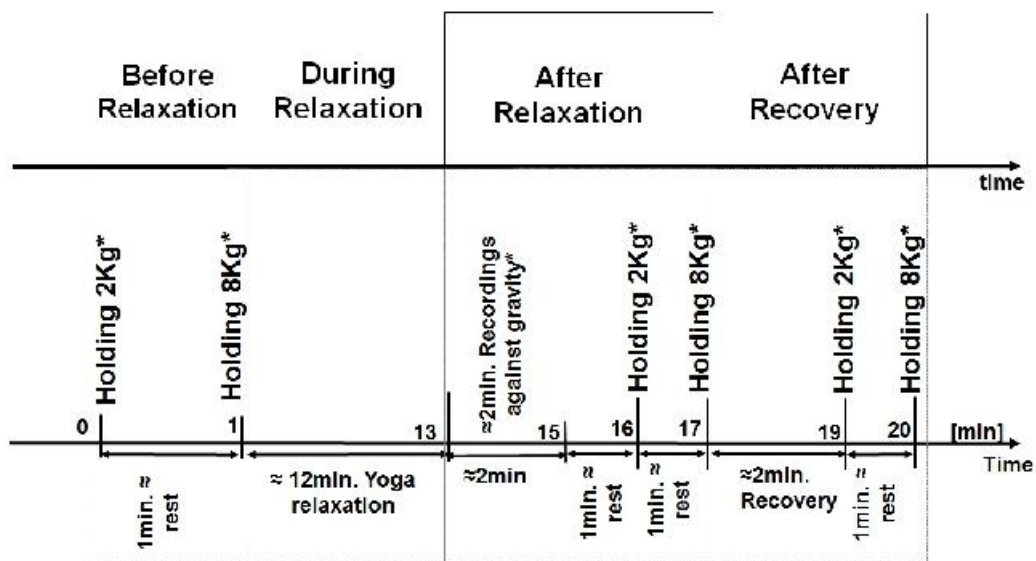
Figure 4.2: The sEMG recording procedure in study the effect of yoga relaxation on the sEMG amplitude distribution over the skin. sEMG signals were recorded for 15s(length of signals) when the subject held a weight(2Kg or 8Kg) in isometric condition, 90 degree elbow flexion, supinated forearm, before, after yoga relaxation, and after recovery time. Recovery time is the time after relaxation when the subject declares he is in normal condition.

145

After the pre-processing, root mean square(RMS) of the signals were considered as the channel's amplitude indicators. The frequency domain parameters such as mean and median frequencies were also computed based on the following equations from the time samples (1s epoch time, $X[n] = [x_0, x_1, x_2, \ldots, x_N], \quad n \in [1, N-1]$) and signal in frequency domain (Fourier transform) :

$$RMS^2 = \frac{1}{N} \sum_{i=1}^{N-1} x[i]^2 \tag{4.1}$$

$$f_{mean} = \frac{\sum_{i=1}^{M} f_i P_i}{\sum_{i=1}^{M} P_i} \tag{4.2}$$

$$\sum_{i=1}^{f_{med}} P_i = \sum_{i=f_{med}}^{M} P_i = \frac{1}{2} \sum_{i=1}^{M} P_i \tag{4.3}$$

where, "N" is the number of samples in 1s epoch time, "P_i" is the ith line of the power spectrum, and "M" is the highest harmonic considered.

Median frequency (f_{med}) divides the spectrum of a signal in two portions of equal power, the lower and higher 50th percentile of the distribution. Interpolation maybe needed for estimating the f_{med} when the epoch time is shorter than 1s and the power spectrum lines are therefore separated by more than 1Hz. Mean frequency (f_{mean}) is corresponding to the line that goes through the center of gravity (Centroid or moment of the first order) as shown in figure 4.3.

4.3   Results and Discussion

An example of time domain sEMG signals (third column of the detection grid), which was placed along the Biceps Brachii's fiber direction, are presented in figure 4.4. The propagation of sEMG action potentials can be seen from the channel 1 to channel 8 of the single differential (SD) signals. Single differential signals were computed (off line) from the acquired monopolar signals of the channels placed along the fiber direction. Channel 1, which is shown on the figure 4.4 is near to the innervation zone(IZ), where channel 8 is proximal to the shoulder.   The RMS sEMG maps (monopolar) corresponding to before and after yoga relaxation and after recovery, are shown in the figure 4.5.
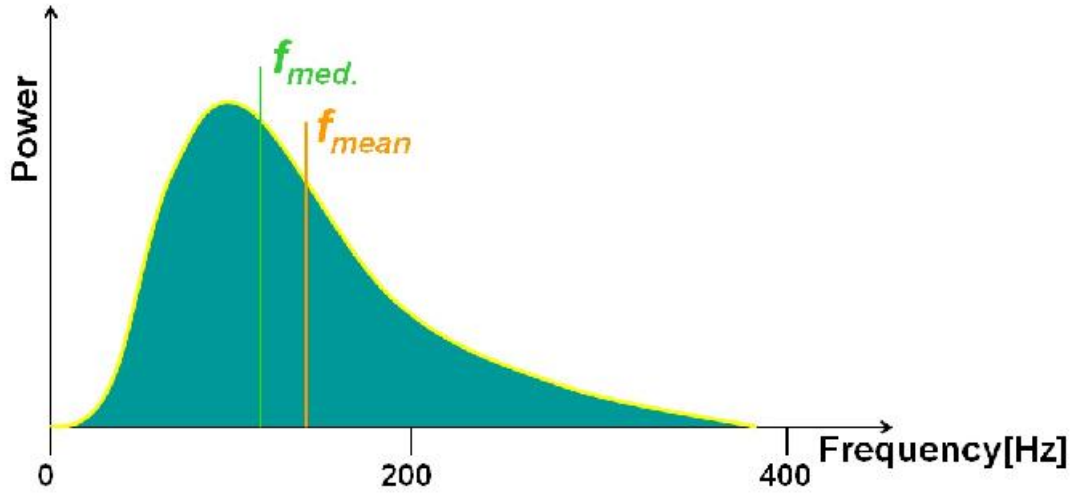
Figure 4.3: A schematic of the power spectrum of a sEMG signal with mean and median frequency lines(see also eqs.(4.2 and 4.3)).

sEMG signals were also recorded during yoga relaxation. No propagation was found in sEMG time domain signals(see figure 4.6). Meanwhile, the level of RMS is in the range of noise level. The RMS map of monopolar signals, the mean and median frequency maps were provided. As it was expected, the RMS increased when the load (weight) increased from 2Kg to 8Kg. No changes in the distribution of sEMG activity was seen when different loads(2Kg and 8Kg weights) were applied to the elbow joint. From the RMS maps (ex. figure 4.5), it can be observed that in all conditions i.e. before yoga relaxation, after yoga relaxation, and after recovery time, the short head of Biceps Brachii is more active comparing to the muscle's long head.

Yoga relaxation provides changes in map of slopes of the time and frequency domain indicators (RMS, mean and median frequencies). Panels "A", "B", and "C" of figure 4.7 show that the RMS increases as the time passes for both before yoga relaxation and after recovery, however speed of changes in RMS value is faster before relaxation with respect the map of after recovery. It seems that after yoga relaxation, muscle is fresh with respect to before relaxation time and can participate in producing force to hold the weight(8Kg) without increasing RMS value (see panel "B" of figure 4.7).
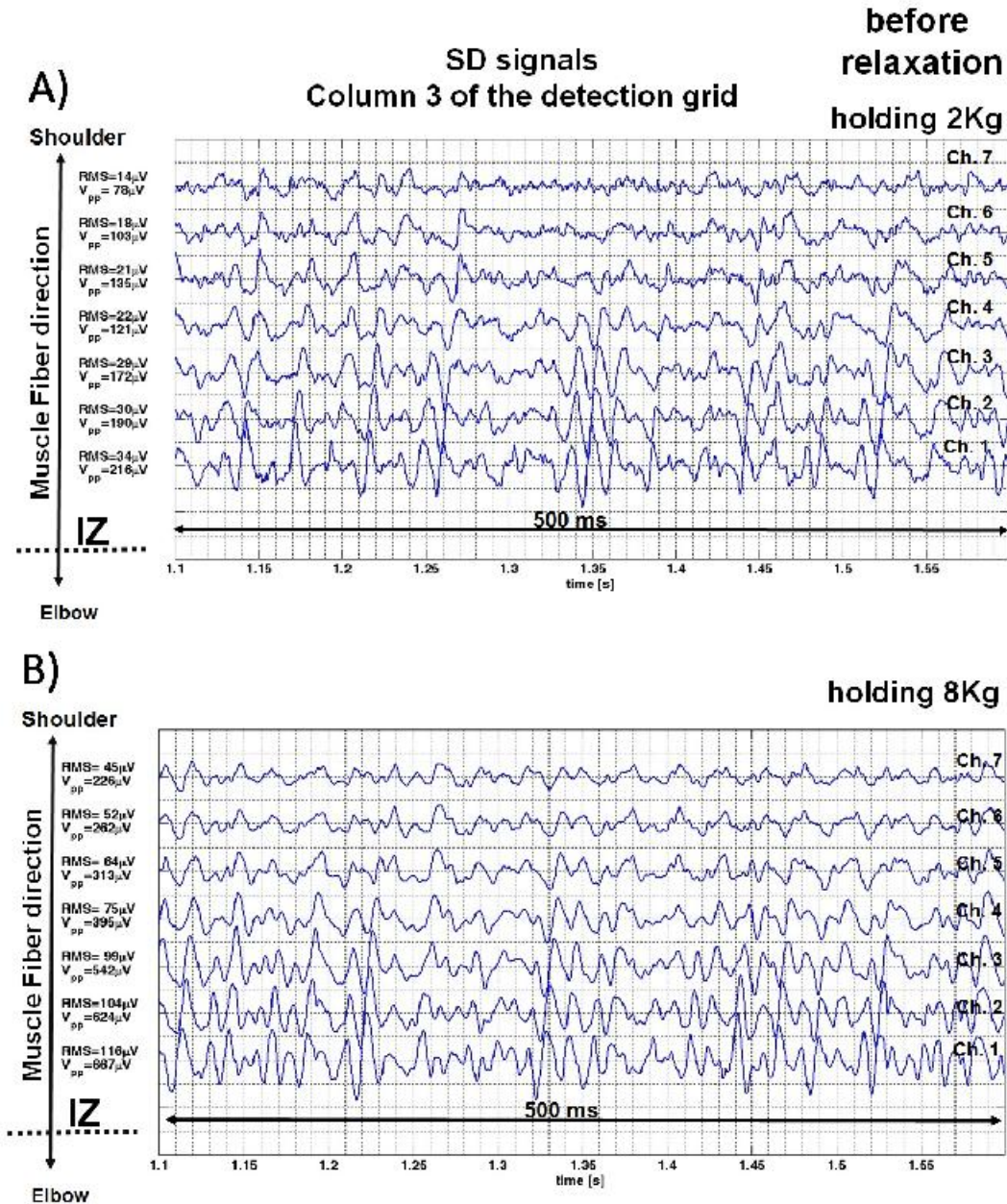
Figure 4.4: 500ms time window of single differential signals (computed offline from acquired monopolar sEMG signals) belonging to the third column of the 8×8 detection grid placed over the Biceps Brachii muscle (proximal to the shoulder) when subject held a A) 2Kg, B) 8Kg weight in 90 degree elbow flexion (isometric), supinated forearm for 15s. Monopolar signals were acquired before yoga relaxation. The innervation zone region, muscle fiber direction, RMS and peak to peak voltage of the signals in the 500ms epoch window are also shown on the plots.
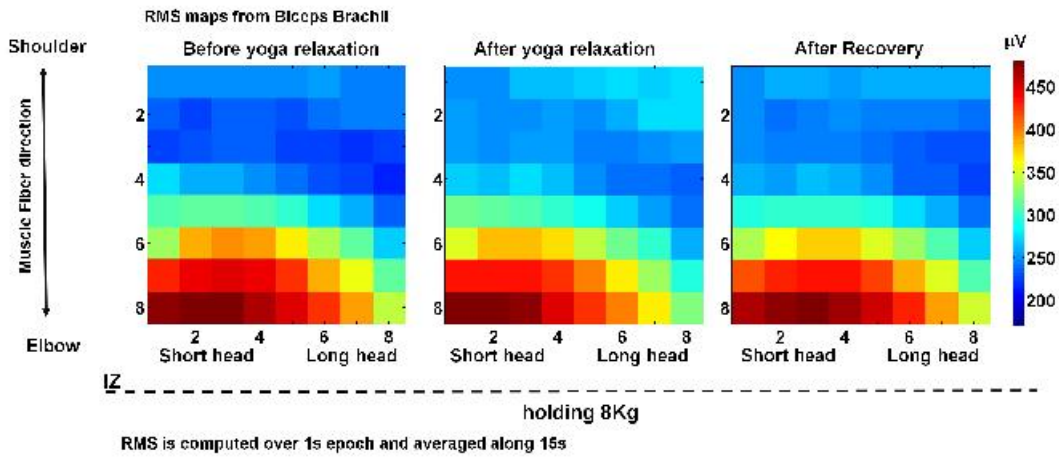
Figure 4.5: Monopolar sEMG RMS maps obtained from the Biceps Brachii's sEMG signals computed over the total length of the recorded signal (15s). The subjects held an 8Kg weight for 15s in 90 degree elbow flexion, supinated forearm isometric condition; See also figure 4.2 on page 145
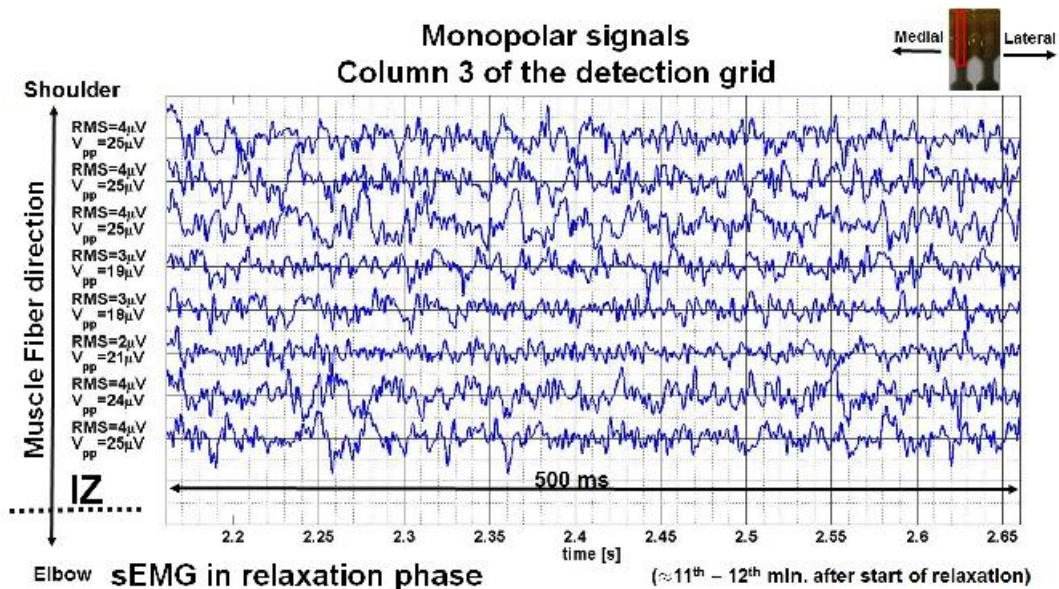
Figure 4.6: Monopolar signals during yoga relaxation belonging to the 3rd column of the 8×8 detection grid. RMS of the noise level≈ 4μV

149
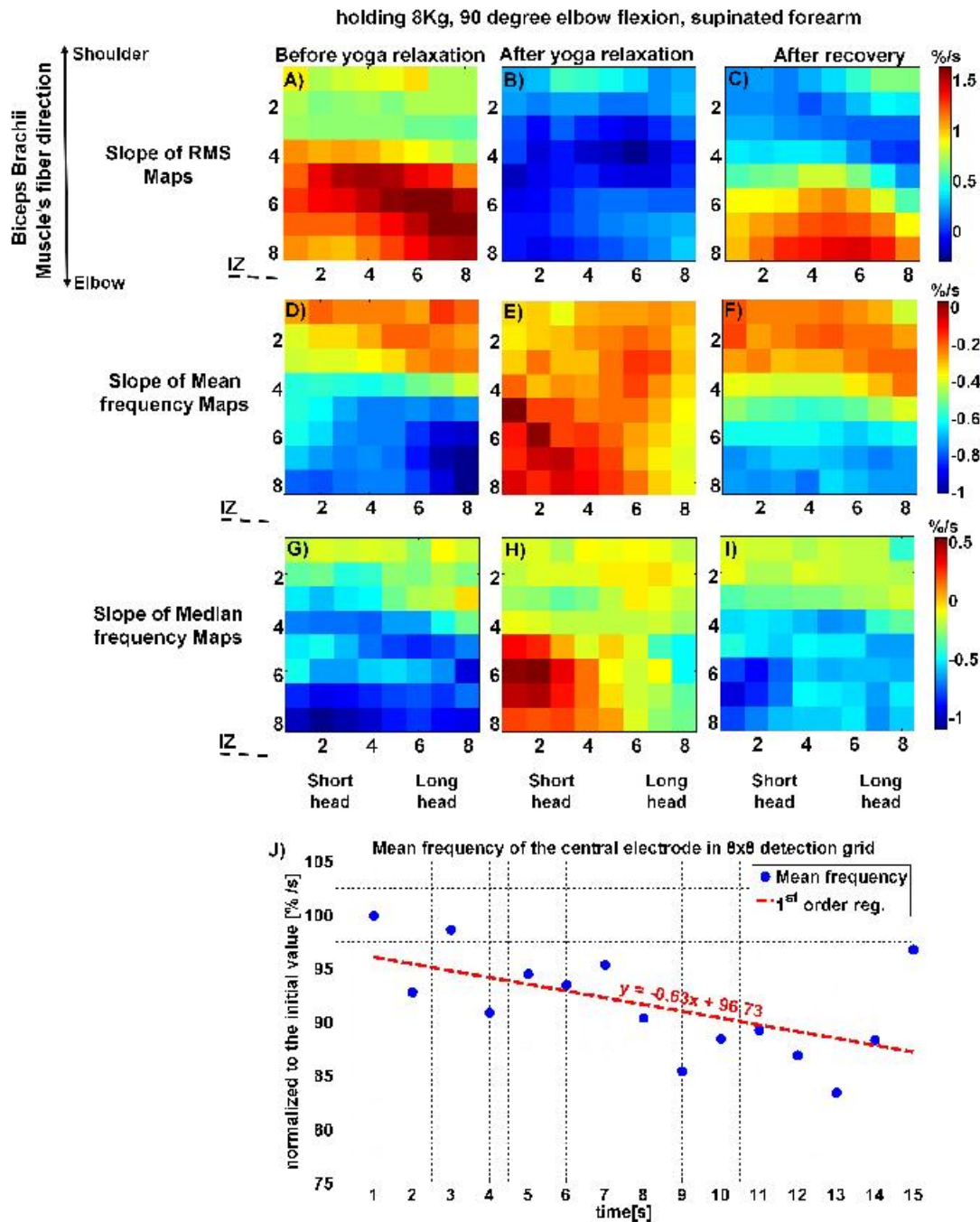
**Figure 4.7: Slope map of changes (%/s) the A), B), C) RMS; D), E), F) Mean
frequency; G), H), I)Median frequencies of monopolar signals recorded from
Biceps Brachii applying an 8×8 detection grid before and after yoga relaxation
and after recovery. Subject held an 8Kg weight for 15s in 90 degree elbow
flexion, supinated forearm, isometric condition. Slope is computed as the slope
of 1st order regression line from RMS(panels A, B, C), Mean (panels D, E, F),
and median (panels(G, H, I)) frequencies considering 1s epoch length over 15s
length of monopolar signals. J) The plot is representing the ... please see the
continue on the nex page ...**

Figure 4.7: . . . form the previous page: 15 mean frequency values (blue circles) computed for 15 time epochs over the total length (15s) of recorded sEMG signal related to the central electrode(row = 4, column = 4) in the electrode grid, and the mean frequency trend found by the first order regression line (dashed red line in "J"). Row and column numbers of each map are also depicted on the plots

The slope map of the mean frequency (panels "E" of figure 4.7) show almost no changes or small decreases of the mean frequency(see also eq. 4.2, when subject held an 8Kg weight for 15 seconds. Almost, similar pattern of changes (versus time) in the mean frequency can be observed for the conditions "before yoga relaxation and "after recovery". In both cases a decreasing trend is observed, which is also can be seen in the median frequency maps.

Merletti and Lo Conte have reported (5) a decreasing trend in mean and median frequency and an increasing trend in RMS from when a muscle start producing force. These trends and also decreasing trend in the conduction velocity are considered as manifestation of fatigue in a muscle. Smaller changes in the time domain (RMS) and frequency domain (f_{mean} and f_{median}) indicators after yoga relaxation strengthen the hypothesis that yoga might relief the muscles from fatigue and make them fresh.
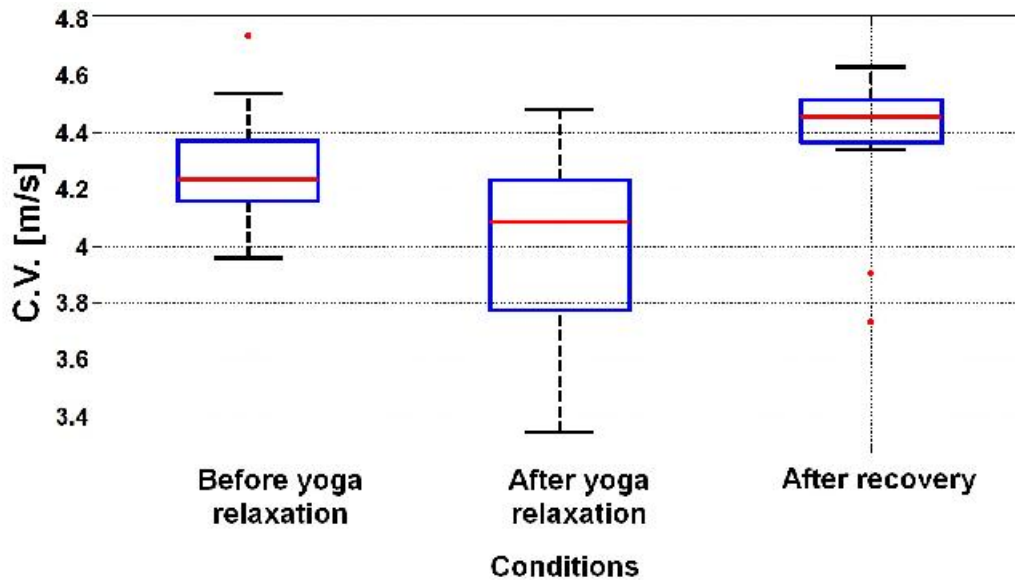
Figure 4.8: Distribution(15 values) of conduction velocity(CV) along 15s considering conditions: before/after yoga relaxation and after recovery of Biceps Brachii muscle. CVs were computed as the average of the CVs over 8 columns of the detection grid from double differential(DD) signals. DD signals were obtained off line from recorded monopolar sEMG signals along fiber direction when subject held 8Kg weight for 15s in 90 degree elbow flexion, supinated forearm, isometric condition; Red line shows the median value, the horizontal blue lines of the boxplots show the first and third quartiles.

Figure 4.8 shows the distribution of conduction velocities (15 values corresponding to 15s) in the three conditions(before and after yoga relaxation and after recovery time). Conduction velocity (CV) of the Biceps Brachii was estimated (6) as the average of the CVs over 8 columns of the detection grid from double differential(DD) signals. In figure 4.8, differences in the median of CVs corresponding to different conditions can be seen. It seems that after relaxation the median of CVs is smaller with respect to before yoga relaxation and after recovery, but this difference is not significant as it can be seen from figure 4.9.
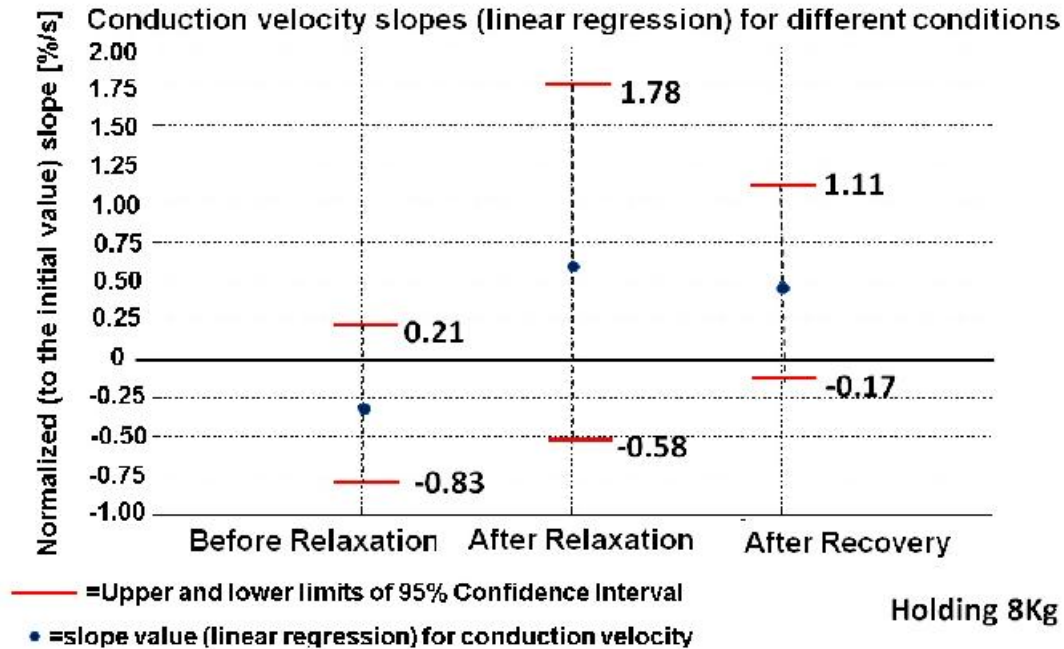
Figure 4.9: Conduction velocity(C.V.) slopes for three conditions are presented (blue circles). Red lines show the limits of 95% of confidence interval (CI) of the estimated slopes. The slopes were computed as the linear regression of the normalized(to the initial value) C.V.s. Conduction velocities were computed as the average of the C.V.s over 8 columns of the detection grid from double differential(DD) signals. DD signals were obtained off line from recorded monopolar sEMG signals along fiber direction when subject held 8Kg weight for 15s in 90 degree elbow flexion, supinated forearm, isometric condition.

4.4 Conclusion

We tested the effect of yoga relaxation on the muscle activity of a yoga master. Since this is a single case study, generalizing the conclusions is not possible, but based on our single subject we observed that:

- After relaxation the mean frequency shows no trend (slope = almost zero) during the 15s sEMG recordings in 90 degree elbow flexion, isometric contraction (holding 2Kg and 8Kg weights).

- No changes in the sEMG activity pattern distribution was seen among before, after yoga relaxation, and after recovery time.

- In both before and after yoga relaxation, the short head of Biceps Brachii(BB) was more active than the BB's long head.

- Maps of RMS's slope while subject held weights (2Kg and 8Kg) for 15s in 90 degree elbow flextion, isometric contraction, (after relaxation) show a uniform spatial distribution of slopes with values ≈ 0, while before relaxation, it is not uniform and the slope of RMS > 0 (increase of RMS with respect to time in a constant load, isometric condition)

- Myoelectric manifestations of fatigue are smaller after relaxation.

- Myoelectric manifestations of fatigue approach the normal pattern after recovery.

Note that to generalize the above conclusions, more recording sessions and more subjects are needed. The purpose of this chapter is only to show the feasibility of the measurements.

References

[1] M. K. BHASIN, J. A. DUSEK, B. H. CHANG, M. G. JOSEPH, J. W. DENNINGER, G. L. FRICCHIONE, H. BENSON, AND T. A. LIBERMANN. **Relaxation response induces temporal transcriptome changes in energy metabolism, insulin secretion and inflammatory pathways**. *PLoS One*, **8**(5):e62817, 2013. 141

[2] G. S. NAMBI AND A. A. SHAH. **Additional effect of iyengar yoga and EMG biofeedback on pain and functional disability in chronic unilateral knee osteoarthritis**. *Int J Yoga*, **6**(2):123–127, 2013. 142

[3] HEIKO WAGNER, ULRICH REHMES, DANIEL KOHLE, AND CHRISTIAN PUTA. **Laughing: A Demanding Exercise for Trunk Muscles**. *Journal of Motor Behavior*, **46**(1):33–37, 2013. 142

[4] MARCO BARBERO, ROBERTO MERLETTI, AND ALBERTO RAINOLDI. *Atlas of muscle innervation zones*. Springer, New York, 2012. 143

[5] ROBERTO MERLETTI AND LOREDANA R. LO CONTE. **Surface EMG signal processing during isometric contractions**. *Journal of Electromyography and Kinesiology*, **7**(4):241–250, 1997. 151

[6] D. FARINA, M. POZZO, E. MERLO, A. BOTTIN, AND R. MERLETTI. **Assessment of average muscle fiber conduction velocity from surface EMG signals during fatiguing dynamic contractions**. *Biomedical Engineering, IEEE Transactions on*, **51**(8):1383–1393, 2004. 152

5

A study of muscle activity in musicians playing string instruments

5.1   Introduction and literature review

Industrial workers, musicians, and populations whose job requires daily intensive repetitive tasks may suffer from musculoskeletal disorders after some years (work-related musculoskeletal disorders (WRMDs). Musicians are a large population who may start their work and their training from early ages. The optimal playing technique includes efficient motion patterns but avoids unnecessary movements and muscle activity (1). Therefore, becoming a professional player can be considered as a goal which motivates this population to work as hard as possible in a repetitive task that leads to playing-related musculoskeletal disorders (PRMDs) on muscle activity. Musicians are often compared to athletes because of their superior sensorimotor integration skills (2), neuro-musculoskeletal coordination and amount of training and practice required to achieve mastery. This large amount of practice makes musicians prone to high physical injury rates, as shown by several large epidemiological studies (3). Although musicians may suffer injury from non-performance related causes such as lifting and carrying

———————————————————

* This study is carried out in collaboration with Massimo Testone, RAI, EPA, and Conservatorio G. Verde di Torino

awkward or heavy instruments and suitcases (when on tour), demanding work schedules, sitting on poorly designed orchestral chairs, and temperature variations (3), the majority of musicians' injuries are overuse injuries with soft-tissue symptoms predominating. This is likely due to their postures, as stressful positions are required to play musical instruments due to their design, practice and performance techniques associated with their chosen vocation. Indeed, known performer-related risk factors for injury include poor posture, poor physical condition, inadequate instrument set-up, long hours of playing, insufficient rest breaks and inefficient movement patterns (or poor technique) (4).

5.1.1 Risk factors of injury in instrumentalists

Musculoskeletal disorders are one of the most important pathology in string instrumentalists. The responsible factors of these disorders can be grouped as follows (5) (Lledó et al., 2012):

Intrinsic factors:

- age

- gender

- professional life

Extrinsic factors:

- Large number of practicing hours or sudden increases in time of the instrumental practice

- Lack of breaks during instrumental practice

- Lack of training exercises in some of the several body segments involved in instrumental practice

- Physical tension, which requires a relatively strong pressure executed by fingers or finger tips on strings and against the fingerboard

- Incorrect body position or posture: it is important to consider the fact that a good posture during instrumental practice would imply a transfer of body weight to the half front of the spine. Many musicians have these functions altered and they transfer their weight to their halfback, being this one of the main causes of pain in the lumbar area;

- Teacher replacement: this circumstance can imply an injury risk for the instrumentalist due to various changes in some specific aspects of her/his instrumental practice. As an example, with regard to the replacement of a teacher, it can happen that the instrumentalist may have to hold the instrument in a different way, or even to undergo important changes in several aspects of his own playing technique.

- Instrument replacements: generally there is a large number of outstanding physical and mechanical differences from one instrument to another, such as the distance from the strings to the fingerboard, implying considerable variation of the pressure exerted by one's fingers on the strings. These changes in instrument size and shape are very noticeable, for example, in violas.

5.1.2 Analysis of the main musculoskeletal disorders

Musicians are susceptible to musculoskeletal disorders such as muscle-tendon overuse, acromiohumeral impingement, shoulder instability (6). In general, the most frequents disorders and musculoskeletal injuries can be summarized as follows (5, 7, 8):

- **Tendonitis** is conceptualized as an inflammatory degenerative process of a tendon. In its first stages is characterized by a diffused pain during practice, and in more advanced stages, by a constant pain, even after practising. Among the possible causes that originate this type of injury are the mechanical overload and also general traumatisms.

- **Joint injuries** in musicians are degenerative, likely to be related to repetitive use, but more specifically to regional overload. For example, the right thumb of a clarinetist carries the whole weight of the instrument and shows early degenerative changes. Ergonomic devices such as a neck strap to carry the weight of the

clarinet may effectively reduce strain on the thumb, although long term effects of transmitting this load through the neck are unclear.

- **Nervous trapping syndrome:** Among the nerve entrapment syndromes, we can mention the carpal tunnel syndrome (STC) and the cubital tunnel syndrome (CTS) as the most frequent and important. STC refers to the symptoms by compression of the median nerve in the hand, affecting the base of the thumb and as well as some areas of the index and middle fingers. The symptoms of this syndrome are associated with pain, numbness, tingling, and in the most severe cases, muscular atrophy. On occasion, pain or electric shock-like sensation is observed in the hand or the arm by lightly tapping over the wrist nerve, a test known as Tinels sign[1]. Violinists, violists, guitarists, pianists and percussionists are the people who have the highest probability to develop STC, because of the special movements they performed in each one of these instruments.

- **Dystonia:** Dystonia is the result of an abnormal process of liberation of chemical neurotransmitter substances in an area of the brain, as consequence of repetitive movements or by adopting an incorrect body posture. Basically the symptoms are involuntary muscular contractions. The three main aspects that show dystonia symptoms are: deterioration in handwriting after writing several lines, foot cramps or fast eye blinking. Focal dystonia in string instrumentalist is understood as the loss of voluntary motor control when playing the instrument. The involuntary movements done with the left hand fingers and the right arm are some of the most important coordinating injuries that affect violinists and violists. It is a painless muscle dis-coordination where the symptoms persist for many years. Among violinists and violists affected by dystonia, only 38% were capable

---

[1]Tinel's sign is a way to detect irritated nerves. It is performed by lightly tapping over the nerve to elicit a sensation of tingling or "pins and needles" in the distribution of the nerve. It takes its name from French neurologist Jules Tinel (1879-1952). For example, in carpal tunnel syndrome where the median nerve is compressed at the wrist, Tinel's sign is often "positive" causing tingling in the thumb, index, middle finger and the radial half of the fourth digit. Tinel's sign is sometimes referred to as "distal tingling on percussion" or DTP. This distal sign of regeneration can be expected during different stage of somatosensory recovery [http://en.wikipedia.org/wiki/Tinel_sign]

of keeping up with their musical career (9). Moreover, 57% of these instrumentalists had precedents at the beginning of the symptoms, such as a change in their instrumental execution technique, instrument and/or teacher replacement or an increase of instrumental practice time (10).

5.1.3   Movement analysis

Instruments played dynamically or held statically, put stress on musicians' bodies. Let's consider a violin, held with the left arm of a violinist, has an average length of 38cm from the top of the neck to the edge of the chin rest and the total weight ranges from 400 to 450gr. The left hand also governs intonation. In order to produce proper intonation at all times, a violinist must mindfully alter the position of his/her fingers on the fingerboard of the violin so as to determine the fundamental pitches of the notes played. While doing so, they must also adapt the character of the vibrato the rapid and subtle variation of pitch to produce the appropriate tone color (11). The right arm controls a bow that weighs about 270gr. (12). The right arm, used to facilitate the bowing, is more dynamic comparing the left hand. In the right arm there is a constant pattern of gross motor movement at the shoulder and elbow (greater motion occurring using larger muscle groups), while fine motor movement occurred at the wrist (slight movements using smaller muscle groups) and the resulting pattern was individualized (13). The posture the violinist assumes when playing is stressful on the body in itself, even without holding the weight of the violin and bow for a period of time. Typically, playing posture requires a raised left shoulder, with the instrument supported in the left supraclavicular fossa. The head is rotated to the left and the neck is in a position of left lateral flexion. The left arm is abducted and externally rotated, and the left forearm is supinated. On the bowing arm, the right shoulder is dropped, internally rotated and abducted, and the forearm is pronated (14). When the demands of playing the violin are combined with the required body posture and weight of the instrument, the stresses placed on the body are greater than those needed to simply support the violin (15).

To control the violin and the sounds being produced it is primarily muscles in the upper body which are active. The neck and shoulder muscles are most active when holding up the violin (16). The Sternocleidomastoid is used during rotation and depression movement of the chin to support the violin (15). On the left side of the body the Trapezius is used to support and secure the violin, holds the head in place during playing, and

is a stabilizer muscle for the constantly abducted left arm (12, 17). The left shoulder muscles, particularly the anterior Deltoid, are used to support the raised left arm (12). In the left arm the Biceps Brachii is the principal muscle being used while playing as it facilitates and sustains supination and flexion of the elbow. The left Triceps Brachii acts antagonistically to the Biceps Brachii as it stabilizes and holds the partially extended position of the elbow. As no large extension movements occur in the left arm during playing, the Triceps Brachii is primarily used for defined technical tasks such as vibrato (which is a quick repeated increase and decrease in the frequency and pitch of a note) (12). On the right side of the body, the Trapezius muscle is responsible for facilitating the bowing motion (12). The right shoulder muscles, such as the Deltoid, have been described as being active during the constant movement of the right arm when playing. They have the greatest muscle activity when the shoulder is horizontally adducted and flexed at the beginning of a down-bow, especially at low speeds (12, 13). The Biceps Brachii in the right arm is active in both the down and up-bow movement, although it is more forceful during the up-bow (flexion of the elbow and shoulder) as it works against gravity during that motion (13).

Two easy, simple, and repeatable movements, which are the most used for the study of musculoskeletal disorders (among violinists or cellist) are shown in figure 5.1. More information about the movement of the violinists while playing, such as the kinematic and dynamic analysis, can be found on the work carried out by Jennifer Wales (11).
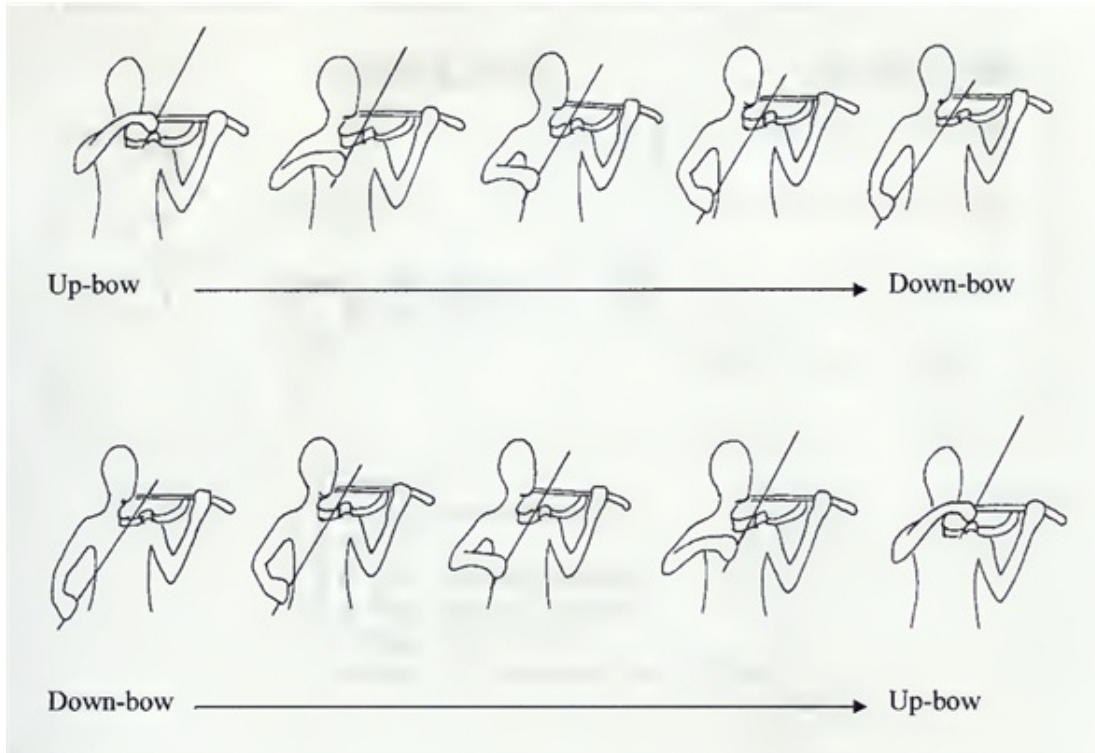
Figure 5.1: Two simple movements that are the most used for studying musculoskeletal disorders of the violinists as they are very simple, large and easily repeatable(courtesy of J. Wales, 2007 (11)).

5.2 Electromyography studies of musicians

In musicians' electromyography (EMG) based studies, the use of EMG as a method of discovery can be found in a wide variety of purposes. In a preliminary study conducted by Fjellman-Wiklund, et al. (2004a) (1), EMG was used to study variations (patterns) of the activity of Trapezius muscle from 12 string players (9 violin players, 2 viola players and 1 cello player). Musicians performed a piece of music at two playing sessions separated by a ten-week interval. The Trapezius muscle activity pattern was reported similar in the first and second playing sessions, showing that each musician repeated his/her own muscular activity pattern. However, there was considerable variability in the muscle activity pattern between cello, violin and viola players and between individual violin players.

In a another study, Fjellman-Wiklund, et al. (2004) (17) used EMG to examine vari-

5. A STUDY OF MUSCLE ACTIVITY IN MUSICIANS PLAYING STRING INSTRUMENTS

ability in string players' technique and to discover if there was intra-individual reproducibility in right and left upper Trapezius muscle activity during playing (two sessions separated by eight weeks). The surface EMG (sEMG) signals were detected by two electrodes (Ag-AgCl, diamter 6mm) attached at two-thirds of the distance from the spinous process of the seventh cervical vertebra (C7) to the lateral edge of the acromion. A reference electrode was attached to the neck (at C7). The researchers found that the right and left Trapezius muscles activity were different. The left Trapezius showed a constant load and the right Trapezius activity was varied with respect to the duration and amplitude of the measured EMG signal. There was no significant variability (intra-individual reproducibility in right and left upper Trapezius muscle activity when playing) within each player individually on the two testing days, whereas significant variability between the different players was found. This study showed that different playing techniques can be identified using EMG data. Philipson et al.(1990) (18) compared muscle load levels, using average rectified EMG, of Biceps and Triceps Brachii, Deltoid and Trapezius, during playing violin in different positions: standing relaxed without the violin, playing a piece of music at a fixed pace while sitting in a chair with support, without support, and in standing. No differences in the load levels of the muscles assessed were found during playing in the different postures.

Berque and Gray (2002) (14) investigated muscle activity (rectified EMG) of upper Trapezius muscles (figure 5.2) in string players (violin and viola) with and without pain in their shoulders and neck, at rest, during playing an easy piece, and playing a difficult piece. In contrast to Philipson et. al, (1990) (18), they found that musicians who were pain-free had more upper Trapezius activity during playing than the ones experiencing pain, and they also determined that variability between subjects was large. During the rest condition, the musicians with pain had a higher level of upper Trapezius activity. When observing only the uninjured violinists and viola players, there was more activity while playing in comparison to rest condition. Meanwhile, higher level of activity was reported during playing the more difficult piece of music. The final observation came from separating the right and left Trapezius activity. Although differences were not significant, the musicians had more activity in the right Trapezius when playing the more difficult piece of music, while at rest, the left Trapezius muscle was slightly more active.

Levy et al. (1992) (15) assessed whether using a shoulder rest would relieve some of
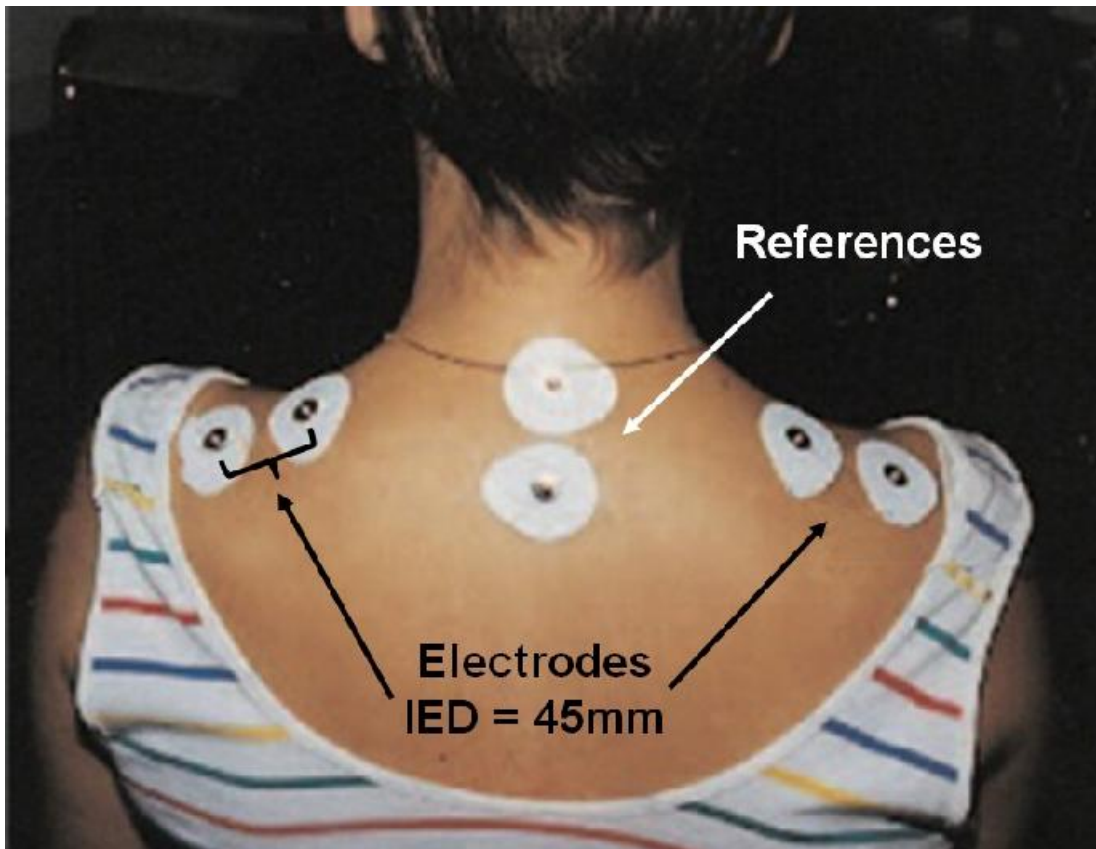
Figure 5.2: electrode placement in Berques study. Bilateral bipolar recordings were made using self-adhesive electrodes (blue sensor disposable electrodes, type M-00-S, 4mm diameter, Medicotest UK Ltd., St. Ives, England) placed on the descending fibers of the UT, with inter electrode distance(IED)=45mm center to center. The electrodes were oriented parallel to the muscle fibers, and placed on either side of a point 2 cm lateral to the midpoint of the line between the seventh cervical spinous process (C7) and the lateral edge of the acromion process. The two ground electrodes were placed on the spinous processes of C7 and T2 (14).

the tension in the upper Trapezius and Sternocleidomastoid muscles in a group of violinists, some of who had experienced pain in the past but had no problems at the time of testing. Muscle activity data were collected from right Sternocleidomastoid, left Trapezius, anterior Deltoid, and Biceps Brachii while playing with and without a shoulder rest. Levy et al. (1992) (15) reported that using a shoulder rest decreases the level of activity of the Trapezius and Sternocleidomastoid.

The purpose of Ackermann et al. study (2002) (4) was to evaluate the effects of taping the scapulae of violinists into a position that prevented excessive elevation and protraction whilst playing. Eight professional violinists played three different musical excerpts with and without scapula taping applied in random order. sEMG activity was recorded from the upper Trapezius, the scapula retractors and the right Sternocleidomastoid muscles using a series of 2cm diameter Ag-AgCl disc surface electrodes. The electrodes were placed 2cm apart over the mid-line in the center of the selected muscle belly in the direction of the muscle fibers. Compared to the control condition, scapula taping[1] increased sEMG amplitude of the left upper Trapezius muscle during playing by 49% as an overall effect, with a 60% increase in the most physically demanding piece played. Lower music quality was detected in the same piece by masters blinded to performance conditions. Taping also had significant negative effects on subjects' reports of concentration and comfort. Short-term application of scapula taping did not enhance selected scapula stabilising muscles during playing and was not well tolerated by professional violinists.

The purpose of Guettler et.al(1997) (19) study was to establish knowledge about the dynamic and static normalized (with respect to MVC) EMG levels of six muscles (left and right upper Trapezius, right Infraspinatus, right Deltoidus, right Pectoralis and right ext. Carpi Radialis) during performance of a standardized set of basic bowing patterns. 25 violinists, who were subdivided into females versus males and professionals versus advanced student groups. When comparing groups, their cyclic muscular patterns showed remarkable uniformity while significant differences were found in the EMG levels of some muscles. Significant dependence on skeletal properties such as arm length was also found.

---

[1]Taping is a form of strapping. It is a procedure that uses tape, attached to the skin, to physically keep in place muscles or bones at a certain position. This reduces pain and aids recovery. Taping is usually used to help recover from overuse and other injuries.

Yarbrough (20) studied the effects of sEMG biofeedback training in reducing musculoskeletal symptoms in music performance. The subjects were university-level violinists and cellists. Over a period of 2–4 weeks, all participants underwent sEMG biofeedback training while performing their instrument using audio feedback. All participants sat with the electrodes placed bilaterally across the upper Trapezius in line with the seventh cervical vertebrae (C7) and a ground electrode placed on the ankle. Paired t-tests were used to compare sEMG data between the base-test and post-test for each individual, and two-way analysis of variance (ANOVA) tests were used to compare sEMG data between the subjects. No significant results were found, but patterns of decreased muscles' sEMG amplitude was observed.

5.3 Objectives and research questions

Recent developments in sEMG have taken in many areas. Most of these developments concern the design of electrode arrays, solution of number of technical, processing and interpolation problems concerning the signals acquired with 2-D arrays of closely spaced electrodes (High Density surface EMG(HDsEMG)). These problems are much more serious than those encountered with the classical single electrode pair. On the other hand, the time evolution of the spatial distribution of sEMG potentials is providing much more information about activation of the underlying muscle(s) than the classical pair of electrode (21).

In this study, sEMG signals of seven musicians (two professional and five student players, male and female, violin, viola, and cello players) were analysed in terms of their muscle activation during playing individual strings. All subjects were right handed. The muscles considered in this study are right (bowing arm) and left (non-bowing arm) upper Trapezius, right lower Trapezius and the left and right lumbar muscles.

The aim of this study is to investigate the sEMG activity of the Trapezius and erector spine muscles by applying HDsEMG covering larger portion of the muscle and with a higher density of the electrodes with respect to previous works mentioned in the introduction and literature review section. The main research questions of this study are as follows:

1. Are the sEMG amplitude (root mean square(RMS)) of Trapezius and erector
   spine muscles spatially distributed similarly in cello, violin and viola players?

2. How is the distribution of sEMG detected over the skin of Trapezius and erector
   spine muscles during playing single strings?

3. Does the spatial distribution of muscle activity depend on the type of bowing?

4. Does backrest support affect the sEMG amplitude during playing strings?

In the next session the issue of materials, protocol of measurement, and procedure of
signal processing are discussed.

5.4   Materials and method

5.4.1   Muscles of interest

Trapezius muscle

The Trapezius is named for its trapezoidal shape. It is flat and broad, covering the
upper back and part of the neck and shoulders, but it's actually part of the thorax.
In fact, Trapezius is a large superficial muscle that extends longitudinally from the
occipital bone to the lower thoracic vertebrae and laterally to the spine of the scapula
(shoulder blade). The Trapezius has three functional regions: the superior region
(descending part), the intermediate region (transverse part) and the inferior region
(ascending part). The superior or upper fibers of the Trapezius arise from the external
Occipital Protuberance, the medial third of the superior Nuchal line of the Occipital
bone (both in the back of the head), and the ligamentum Nuchae. From this origin they
proceed downward and laterally to be inserted into the posterior border of the lateral
third of the clavicle. The middle fibers of the Trapezius arise from the spinous process
of the seventh cervical (both in the back of the neck), and the spinous processes of the
first, second, and third thoracic vertebrae. They are inserted into the medial margin
of the acromion, and into the superior lip of the posterior border of the spine of the
scapula.
The inferior or lower fibers of the Trapezius arise from the spinous processes of the
remaining thoracic vertebrae (T4-T12). From this origin they proceed upward and
laterally to converge near the scapula and end in an aponeurosis, which glides over

the smooth triangular surface on the medial end of the spine, to be inserted into a tubercle at the apex of this smooth triangular surface. At its occipital origin, the Trapezius is connected to the bone by a thin fibrous lamina, firmly adherent to the skin. The superficial and deep epimysia are continuous with an investing deep fascia that encircles the neck and also contains both Sternocleidomastoid muscles. At the middle, the muscle is connected to the spinous processes by a broad semi-elliptical aponeurosis, which reaches from the sixth cervical to the third thoracic vertebrae and forms, with that of the opposite muscle, a tendinous ellipse. The rest of the muscle arises by numerous short tendinous fibers (see figure 5.3). The Trapezius muscle abducts and extends the neck; superior fibers elevate the scapula or rotate it to tilt the glenoid cavity upward; middle fibers retract the scapula; inferior fibers depress the scapula. When the scapula is fixed, one Trapezius acting alone flexes the neck laterally and both Trapezius muscles working together extend neck (22) (see figure 5.3).

Erector Spinae muscles

The Erector Spinae is a muscle group of the back in humans and animals, which extends the vertebral column (bending the spine such that the head moves posteriorly while the chest protrudes anteriorly) (figure 5.4). It is also known as sacrospinalis in older texts. A more modern term is extensor spinae, though this is not in widespread use. It is not just one muscle, but a bundle of muscles and tendons (see figure 5.4, panel "C"). It is paired and runs more or less vertically. It extends throughout the lumbar, thoracic and cervical regions, and lies in the groove to the side of the vertebral column. Erector spinae is covered in the lumbar and thoracic regions by the Thoracolumbar fascia, and in the cervical region by the nuchal ligament.

A)

Trapezius muscle abducts and extends neck. Superior fibers elevate scapula or rotate it to tilt glenoid cavity upward. Middle fibers retract scapula. Inferior fibers depress scapula. When scapula is fixed, one trapezius acting alone flexes neck laterally and both trapezius muscles working together extend neck.

B)

Superior or upper fibers of the trapezius
Middle fibers of the trapezius
Inferior or lower fibers of the trapezius

Origin:
external occipital protuberance, nuchal ligament, spinous processes of vertebrae C7–T12.

Insertion:
clavicle, acromion, scapular spine

Figure 5.3: A)Trapezius muscles[http://www.sciencephoto.com, F004/8855] and B) it's compartments are presented in different colours [http://en.wikipedia.org/wiki/Trapezius_muscle]. Trapezius is a large superficial muscle that extends longitudinally from the occipital bone to the lower thoracic vertebrae and laterally to the spine of the scapula; Origin: external occipital protuberance, nuchal ligament, spinous processes of vertebrae C7T12; Insertion: clavicle, acromion, scapular spine; Functions: Abducts and extends neck, Superior fibers elevate scapula or rotate it to tilt glenoid cavity upward; middle fibers retract scapula; inferior fibers depress scapula. When scapula is fixed, one Trapezius acting alone flexes neck laterally and both Trapezius muscles working together extend neck (**22**).
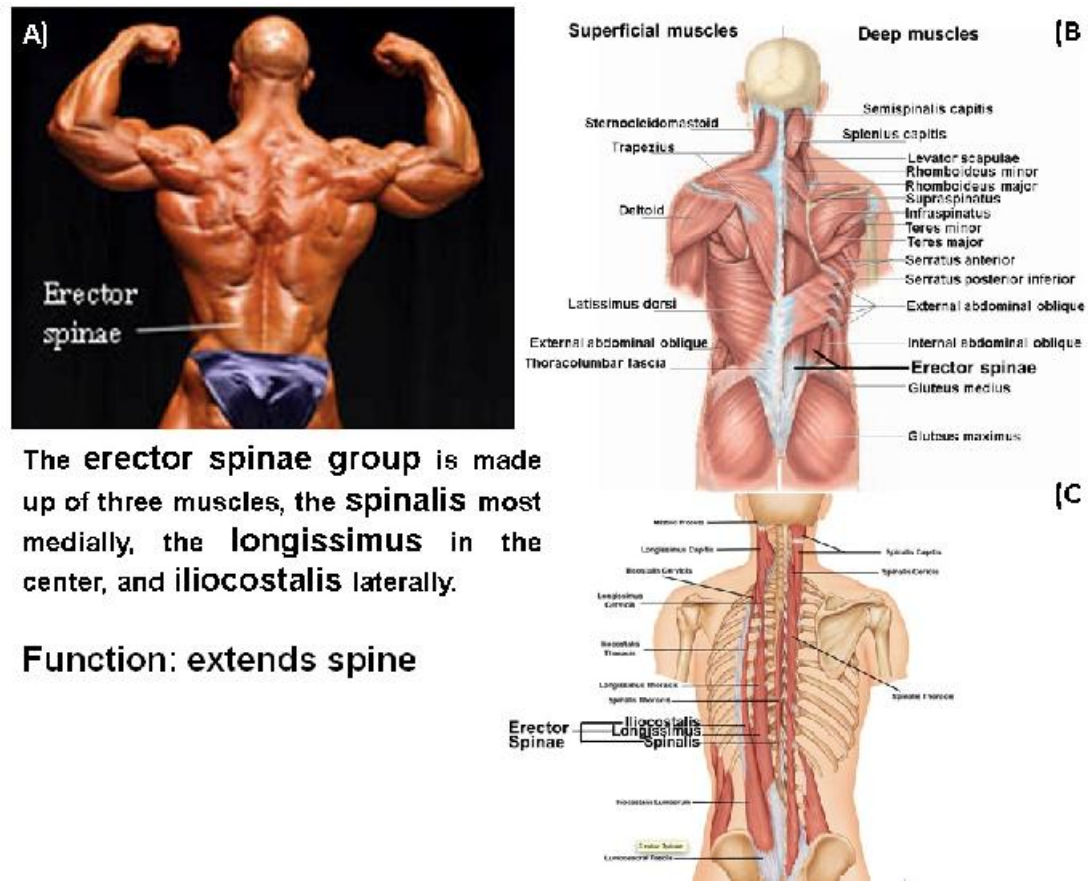
Figure 5.4: A)Erector spinae on a bodybuilder[http://skinnybulkup.com/abdominal-exercises-training-abs-core]. B)Erecor Spinae muscle is a deep muscle made up of three muscles shown in "C". "B" and "C" are from (22).

This large muscular and tendinous mass varies in size and structure at different parts of the vertebral column. In the sacral region it is narrow and pointed, and at its origin chiefly tendinous in structure. In the lumbar region it is larger, and forms a thick fleshy mass, which on being followed upward, is subdivided into three columns; these gradually diminish in size as they ascend to be inserted into the vertebra and ribs. The erector spinae arises from the anterior surface of a broad and thick tendon, which is attached to the medial crest of the sacrum, to the spinous processes of the lumbar and the eleventh and twelfth thoracic vertebra, and the supraspinous ligament, to the back part of the inner lip of the iliac crests and to the lateral crests of the sacrum, where it blends with the sacrotuberous and posterior sacroiliac ligaments. Some of its fibers are

171

continuous with the fibers of origin of the Gluteus maximus.

5.4.2 Subjects

Six (one subject played two different instruments and was considered as the seventh subject) healthy sting players, including two professional and four student players (two males and two females) participated in this study. Table 5.1 shows the gender, age, instrument, weight and height, [age (mean $\pm$ SD): 33.8 ± 18.0 height: 173.5 ± 6.2 cm, weight: 65.5 ± 16.2 kg] of participants in this study.

Table 5.1: sex , age(years), weight(kg), height(cm), level of proficiency and the musical instrument of the subjects participated in the study.

Subject	Sex	Age(years)	Weight(kg)	Height(cm)	L. proficiency	Instrument
1	Male	57	90	177	Professional	Viola
2	Male	57	62	179	Student	Cello
3	Male	22	80	180	Student	Cello
4	Female	22	51	172	Student	Violin
5	Female	25	50	165	Student	Violin
6	Male	20	60	168	Student	Violin
7	Male	20	60	168	Student	Viola

One of the participant played two instruments (violin and viola). He was considered as two subjects playing different instruments. He is indicated as subject 6 and 7 in table 5.1. Subjects were pain-free at the time of the experiment and they provided a written, informed consent before starting the experimental session. All subjects were right handed.

The experiments took place at the AUDITORIUM RAI for the first subject and at LISiN (Laboratory of Engineering of Neuromuscular System and Motor Rehabilitation) for the others. Subjects played the instrument in sitting position (using adjustable height chair) and they were asked to play an easy sequence of movements with and without backrest support.

The Movements performed are defined as follows:

- **Large bowing:** Action of bowing that starts from the tail of the bow and the total length of bow slides on an instrument's string and comes back to the starting

position. Each bow (i.e. bowing up or bowing down) last 1s (bowing speed = 1 bow/s).

- **Legato tail bowing:** Action of bowing that starts from the tail of the bow and the bow slides shortly (about 2-5 cm) on an instrument's strings. It is done repeatedly in fast movement (6 bows/s).

- **Legato tip bowing:** Action of bowing that starts from the tip of the bow and the bow slides shortly (about 2-5 cm) on an instrument's strings. It is done repeatedly in fast movement (6 bows/s).

The mentioned bowing movements are easy to play and were selected because they are very common and easily repeatable by each subject according to the instrument played (please see figure 5.5).

Subjects were asked to perform notes of the four strings (each string corresponds to a different note for each instrument played) for each movement. As a reference numbering in this study, the first string (string #1) was considered as the closest string to sagittal plane (the most medial string to the subject's body). The farthest string to the sagittal plane (the most lateral string to the subject's body) is called string #4. Other strings are numbered as the strings between the first and the fourth strings. These mentioned bowing movements were first performed without backrest support posture, and then they were repeated with the back leaning on the backrest. Lastly, all movements were repeated after about 30 minutes of playing a fatiguing piece of music. To control the speed of playing, a metronome was used. Each performance was carried out at constant speed. The metronome was set to 60 beats per minute (1 beat = 1s). Totally 48 (four notes, three bowing types, two sitting conditions, two fatigue conditions) signals for each subject in one session were recorded. Two recording sessions, which they were conducted in two different days, were considered for each subject (see figure 5.6).
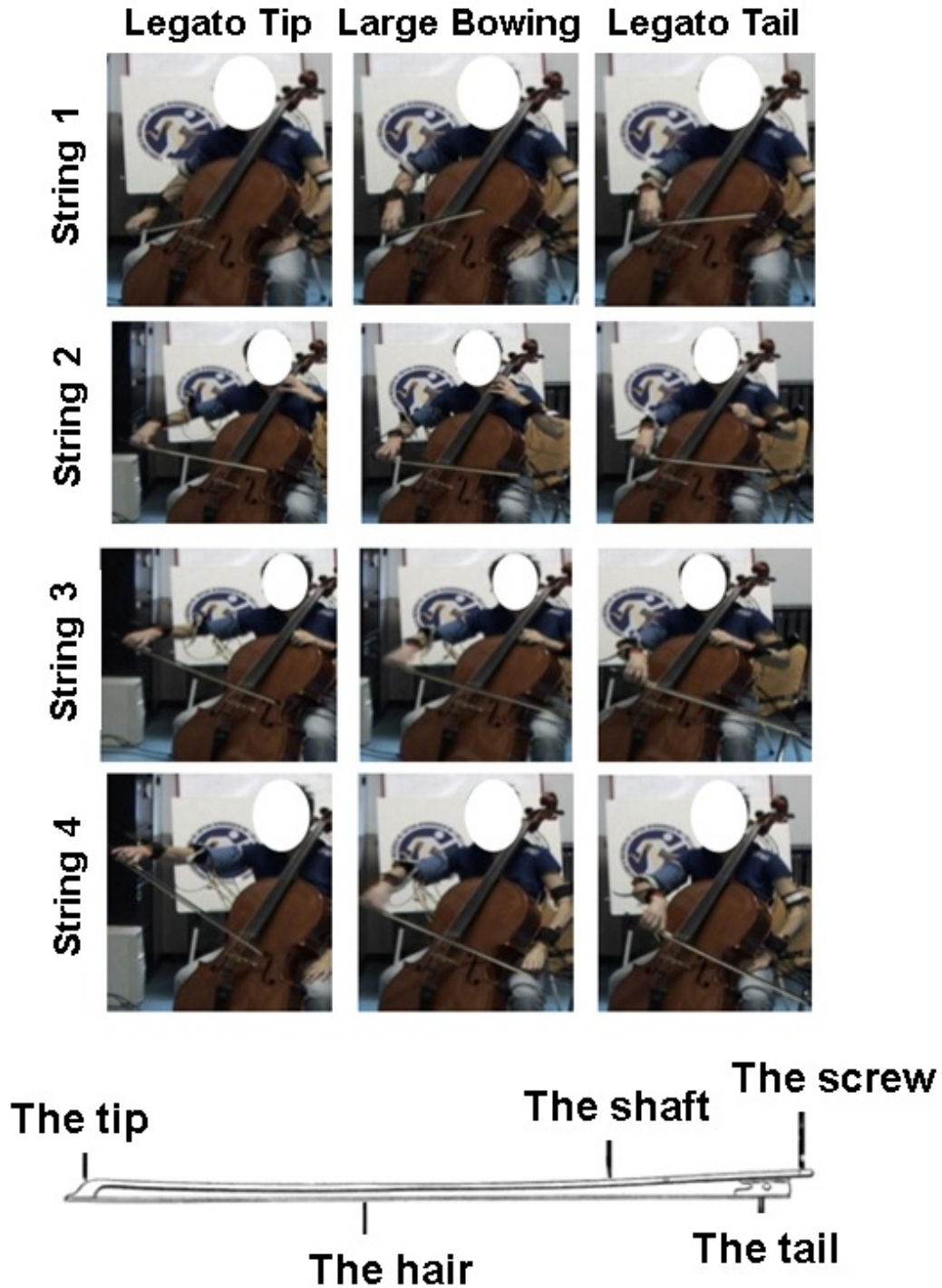
Figure 5.5: Pictures of cello performance, sorted by strings. Each row is a different string, from the first (top) to the fourth (bottom). In each row, the left picture corresponds to the legato tip technique, the picture on the right to the legato tail, the central one to a mid-range position of the large bowing technique. Please see the continue on the nextpage ...

Figure 5.5: ... from the previous page. We could observe that big differences exist in position of the bowing arm: depending on the string that is played, and on the technique used, different combinations of shoulder abduction, flexion and rotation are required, as well as different degrees of elbow flexion and pronation. Bottom graph shows the bow and technical names of its sections.

During each session, subjects were asked whether they were feeling comfortable with the setup. Occasional uncomfortable feelings related to the large number of cables were solved by fixing them to the subjects using elastic bands.
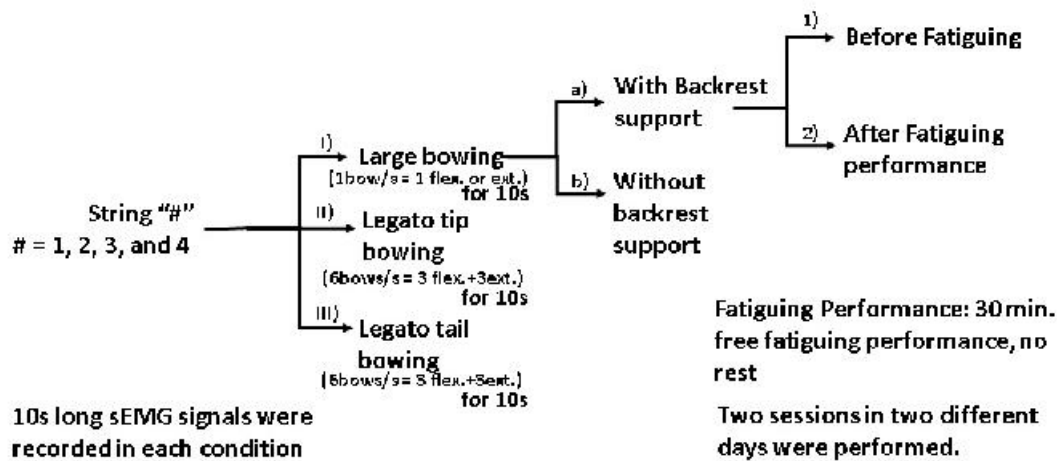
Figure 5.6: Schematic representation of the measurement protocol. Totally 48 (four notes, three bowing types, two sitting conditions, two fatigue conditions) signals for each subject in one session were recorded. Two recording sessions, which were conducted in two different days, were considered for each subject.

5.5 Surface EMG acquisition

Surface EMGs were collected from both upper and lower Trapezius of the bowing arm (right hand) using a 32-flexible electrode matrix (4×8 electrodes with 10mm inter electrode distance (IED) and each electrode was a circular electrode with 3mm diameter). The electrodes were arranged in a grid of four columns (medial-lateral direction) and eight rows (cranium-caudal direction). Two electrode grids were placed on the upper

Trapezius muscles of both sides with the rows in the direction of the muscle fibers. One electrode grid was placed on the lower Trapezius of bowing arm just below the upper Trapezius grid (figure 5.7). To avoid placing the innervation zones (IZ) under the detection area, the position of the IZs were identified by visual inspection from the signals detected by applying a linear dry electrode array (including 16 electrodes, IED=5mm) in single differential recording configuration along the fiber direction. For the upper Trapezius muscle the IZ was identified on the line connecting the acromion and C7 vertebra of both muscles (right and left side) and two other parallel lines 8cm caudal with respect to the previous one to identify the IZ of lower Trapezius of the bowing arm (for right side only).

The grid was positioned according to the literature, with muscle fibers aligned with the rows, and the third row aligned with the line C7-acromion. This placement of the grid was chosen because it allows analysing both muscle sub-portion (upper and lower Trapezius of bowing arm). The grid over the left upper Trapezius was placed to analyze the holding's arm's(instrument's holder) activity of the players. sEMG of the lumbar muscles were collected using two linear 16-electrode arrays (IED=10mm) (please see figure 5.7), placed laterally to the lumbar spine (the distal electrodes were placed at the level of the superior iliac spine, approximately at the level of L5 vertebra). The regions of the skin under the detection grid were slightly abraded with abrasive paste and rinsed with water to remove the abrasion flaky residuals like as suggested in the European Project on "Surface EMG for non Invasive Assessment of Muscles" (SE-NIAM). The matrices were fixed to the skin using adhesive tape. Signals were acquired in monopolar configuration by EMG-USB amplifier, LISiN and OT-Bioelettronica (128 channels, sample frequency of 2048 Hz, programmable gain of 2000, band-pass filter [10–750]Hz and 12 bit A/D converter). An arbokiddy electrodes (Kendall, $\phi = 20mm$) was placed over C7 vertebra as the reference point in sEMG monopolar configuration recordings.

5.5.1 Preprocessing step

Mean value removing, band pass digital filtering [20-450]Hz, zero lag Butterworth 2nd order in each direction) and spectral interpolation (to reduce power line interference up to 10 harmonics) were carried out for each recorded signal. The pre-processing steps were carried out offline using Matlab 7.1 environment.
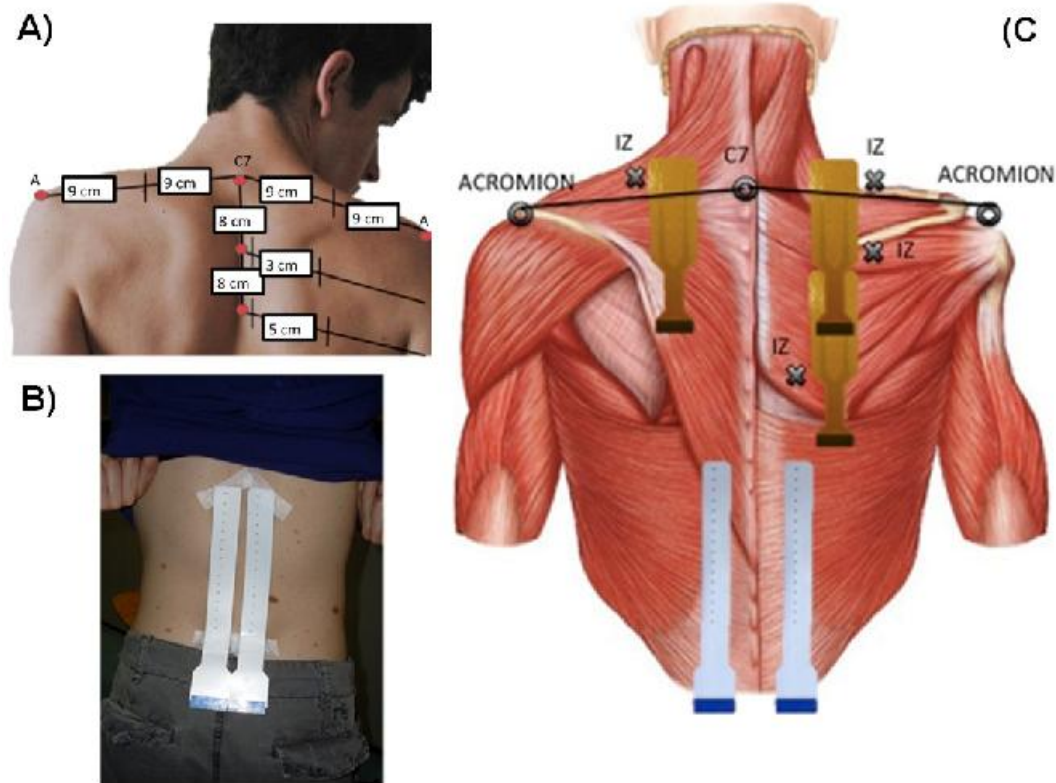
Figure 5.7: A) Schematic representation (not in scale) of innervation zone (**IZ**) detection. Left and right red points represent the acromion bone ("**A**"). Three vertical red points are over the spinal column, spaced with 8cm, where the upper is over the C7 vertebra. Vertical black sticks represent IZ position. Three parallel lines with respect to the C7-acromion line start from each vertical red point. **B)** Position of electrode array(16 channels) on left and right Erector Spinae of a subject. **C)** Position of the electrode grids on upper Trapezius of right and left side, right side of lower Trapezius and electrode arrays on Erector Spinae (right and left side) muscles. Both upper Trapezius matrices were positioned on the basis of some anatomical reference point: the acromion, the C7 vertebra and the position of IZs. The position of each IZ (black X) was identified using a linear electrode array in three different location of the right side and just one location for the left side. Both upper Trapezius matrices were positioned between the innervation zone and the spine. The third row of the these electrode grids were aligned with the line connecting C7 to acromion. Lower Trapezius matrix was positioned just below the upper Trapezius matrix in the right side. Two linear 16-electrode arrays were placed laterally, approximately 1 cm, to the lumbar spine (the distal electrode was placed at the level of the superior iliac spine, approximately at the level of L5 vertebra).

After recording the sEMG signals, visual inspection was done (offline) channel by channel in both time and frequency domain. Figure 5.8 shows monopolar and single differential signals, recorded from the fifth subject (student violin player), when she played the fourth string (large bowing), in sitting without backrest. Signals are from the upper Trapezius of the bowing arm (right side). Propagation can be seen clearly in the zoomed version(250ms time window) of panel "B" of the figure 5.8.

Generally, in HDsEMG recordings (here 128 channels) some channels appears as bad channels. Some popular sources of bad channels are because of bad-contacts (electrode to the skin), presence of large power-line interference, un-balance in electrode-gel-skin impedance, and short-circuits that cause near-zero single differential signals when using gels (23). These channels are also called as "outliers". Outliers indicate signals that have a very different trend or amplitude with respect to the other nearby channels.

We collected 48 set of signals (each set including 128 channels) in each session for each subject. Totally we collected 6144 (6144=48*128) sEMG signals during each session. The number of bad channels depended on the set of signals. A mean value of number of bad channels that we found over one session is 213±180; 679:15 (mean ± SD; max value:min value). This number of bad channels represent 3.5% ± 2.9%; 0.24% : 11.35% (mean±SD; max value:min value) of signals recorded (=6144) for each session.

All bad channels were removed and replaced with an interpolation of all available spatial neighbours in time domain (neighbours were defined by a 3×3 mask). An isolated bad channel was replaced by the average value of its eight neighbours in time domain. In case of presence of a bad channel in the edges of electrode grid, the average of the available neighbours was considered. In case of presence of two adjacent bad channels, the bad channels were removed at first, and then the bad channel with greater number of available neighbors, was interpolated first and then interpolation was done on the other bad channel.

5.6 Results and discussions

The effect of the note (string) that was played, the effect of the posture (supporting with and without backrest) and the effect of the fatigue session on muscle activity are described for each instrument in this section. The effects are presented for each electrode
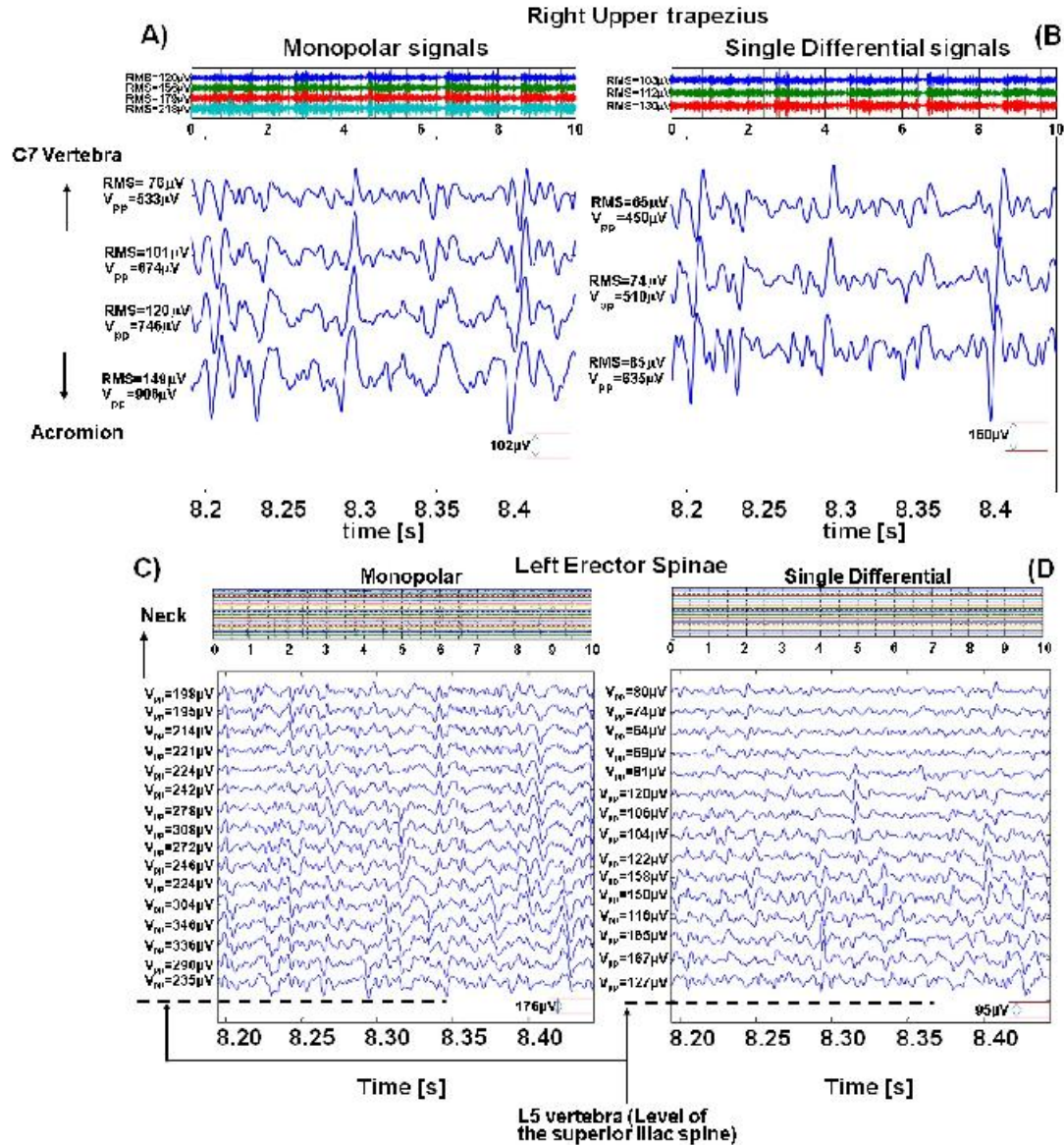
Figure 5.8: Plots show signals recorded from A), B) the upper Trapezius of the bowing arm (right arm), C) and D) the left Erector Spinae muscle concerning subject#5(student violin player), when the fourth string was played in large bowing, sitting without backrest. A) and C) Show monopolar signals related to the first row of electrode grid for 10s length of signal and a zoomed version (250ms) time window. RMS and peak to peak (V_{pp}) values calculated over the plotted time windows for each signal are shown. B) and D) Show differential signals calculated with respect to the columns (8×3, where 8 is a number of rows), along fiber direction for 10s and 250ms time windows.

179

grid (covering different muscles, upper Trapezius right and left side, lower Trapezius right side and right and left Erector Spinae) using Kruskal-Wallis test. "String number" (1, 2, 3, and 4), "posture condition" (with and without backrest) and "fatigue condition" (before and after playing a difficult piece) were considered as dependent variables for the muscle's activity index(MAI). The MAI was defined as the average RMS of the channels detected in the active region. The active region was detected using the modified watershed segmentation algorithm (see chapter 2, section 2.11 on page 67) applied to the RMS maps (calculated over 10s for each grid) of each signal recorded. Some representative RMS maps are shown as examples in the following sessions. In these maps we see how the activity areas are changing (in amplitude and shape) for different strings and for different bowing types. Studies about the size of the activity area or the changing position of center of gravity were not carried out in this study.

5.6.1 Violin players (subject 5 and subject 6)

Effect of the string(note) on the muscle activity index

- **Upper Trapezius muscle of the bowing arm:**

  There was a significant effect($p < 0.001$) for note(string number) that was played by violin players on the muscle's activity index (MAI) of the bowing arm's upper Trapezius(please see figure 5.9) during large bowing. The activity index of muscle increased as the string number increased (i.e. largest MAI is related to playing the string 4, while the minimum activity was obtained in playing the first string. String 4 is the most lateral string with respect to the sagittal plane of subject's body, see also figures 5.10, 5.11, 5.12, and 5.13).
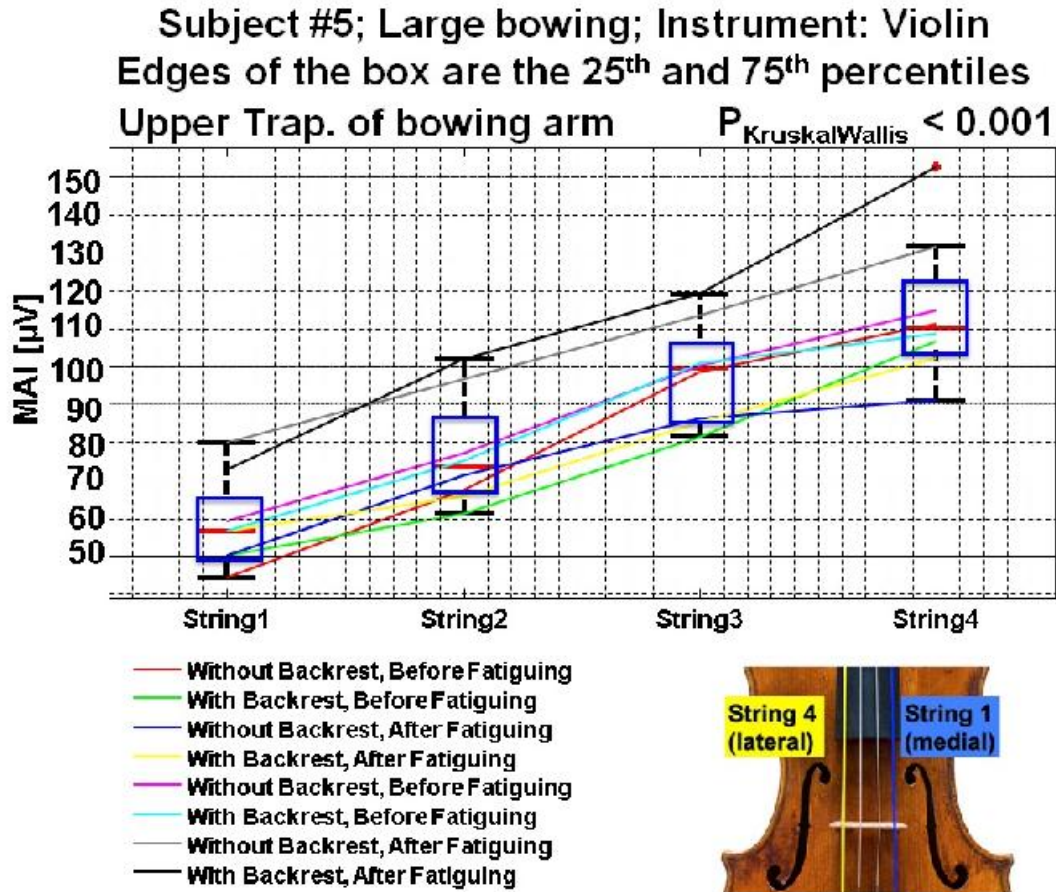
Figure 5.9: Boxplots represent the distribution of muscle activity index(MAI) of the fifth subject (student violin player) in large bowing from upper Trapezius muscle of the bowing arm versus the instrument's string number. The KruskalWallis test shows significant difference on the MAI, when subject played different strings (p = 0.001). MAI was defined as the spatial average of RMS values of the muscle active region detected by modified watershed segmentation technique (watershed + equalization + 70% of the maximum value thresholding). The RMS was computed in time, for each channel of the active region, over the total length of single differential signal (10s). RMS of noise was about $5\mu V$ and was computed from recorded signals in relaxed sitting position. See also figure 5.26 on page 212.
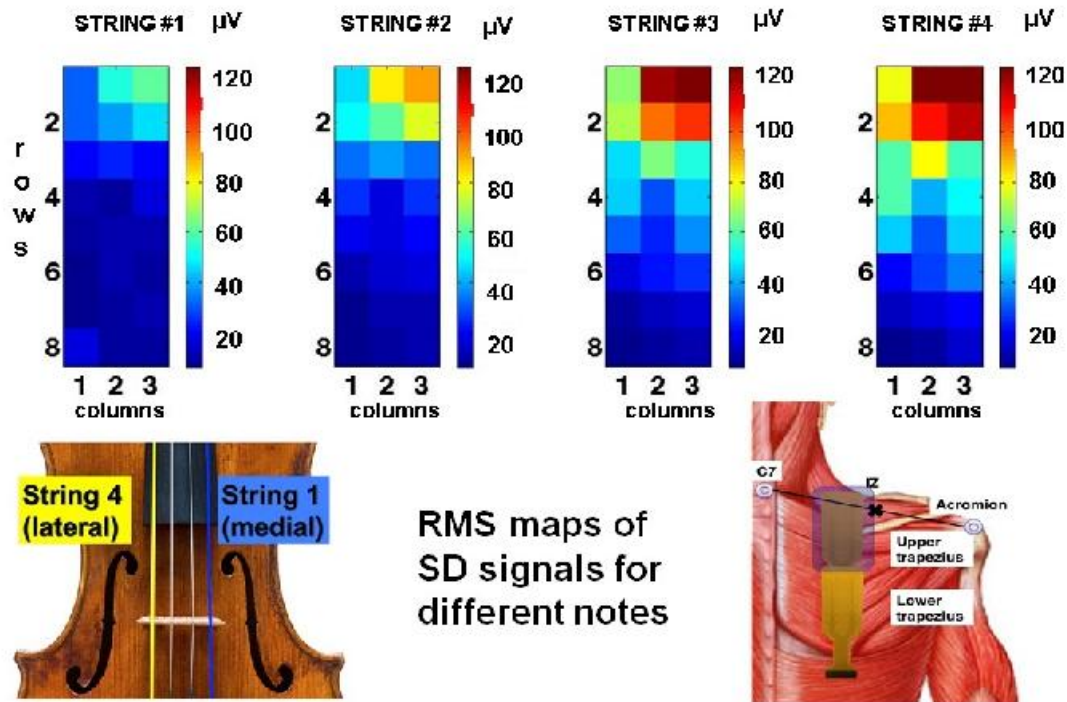
Figure 5.10: sEMG amplitude distributions obtained for the fifth subject (student violin player) performing four violin strings in large bowing. Each map (8 rows and 3 columns) represent the RMS values (calculated over 10s) of single differential signals(SD). sEMG signals were recorded from upper Trapezius (bowing arm side). Signals were acquired in monopolar configuration using 8×4 electrode grid. SD signals were computed offline.
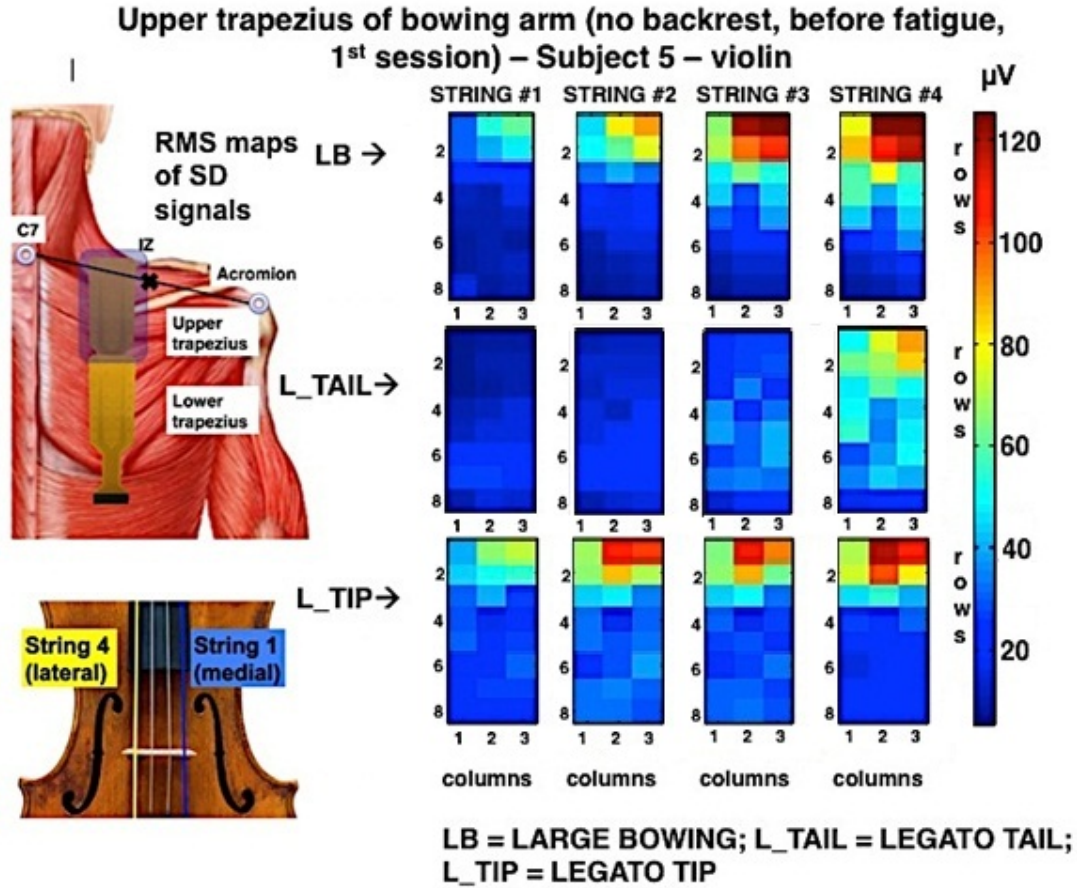
Figure 5.11: sEMG amplitude distributions obtained for subject #5 performing four violin strings in different bowing types(large, legato tip and legato tail bowing movements). Each map (8 rows and 3 columns) represent the RMS values (calculated over 10s) of single differential signals(SD). sEMG signals were recorded from upper Trapezius (bowing arm side). Signals were acquired in monopolar configuration using 8×4 electrode grid. SD signals were computed offline.
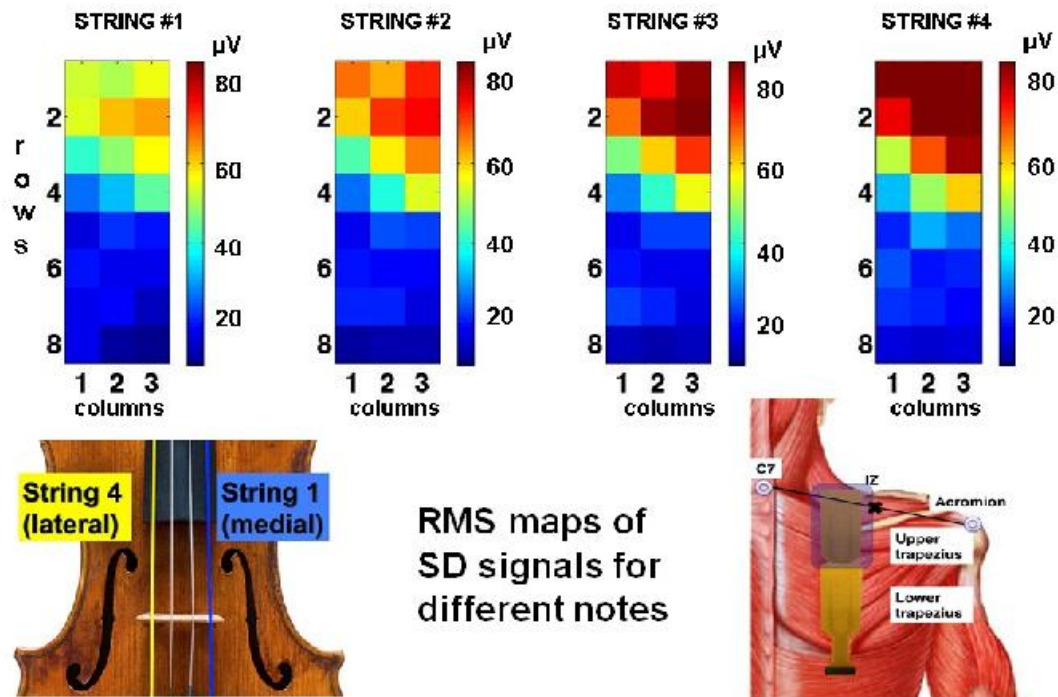
Figure 5.12: sEMG amplitude distributions obtained for the sixth subject performing four violin strings in large bowing. Each map (8 rows and 3 columns) represent the RMS values (calculated over 10s) of single differential signals(SD). sEMG signals were recorded from upper Trapezius (bowing arm side). Signals were acquired in monopolar configuration using 8×4 electrode grid. SD signals were computed offline.
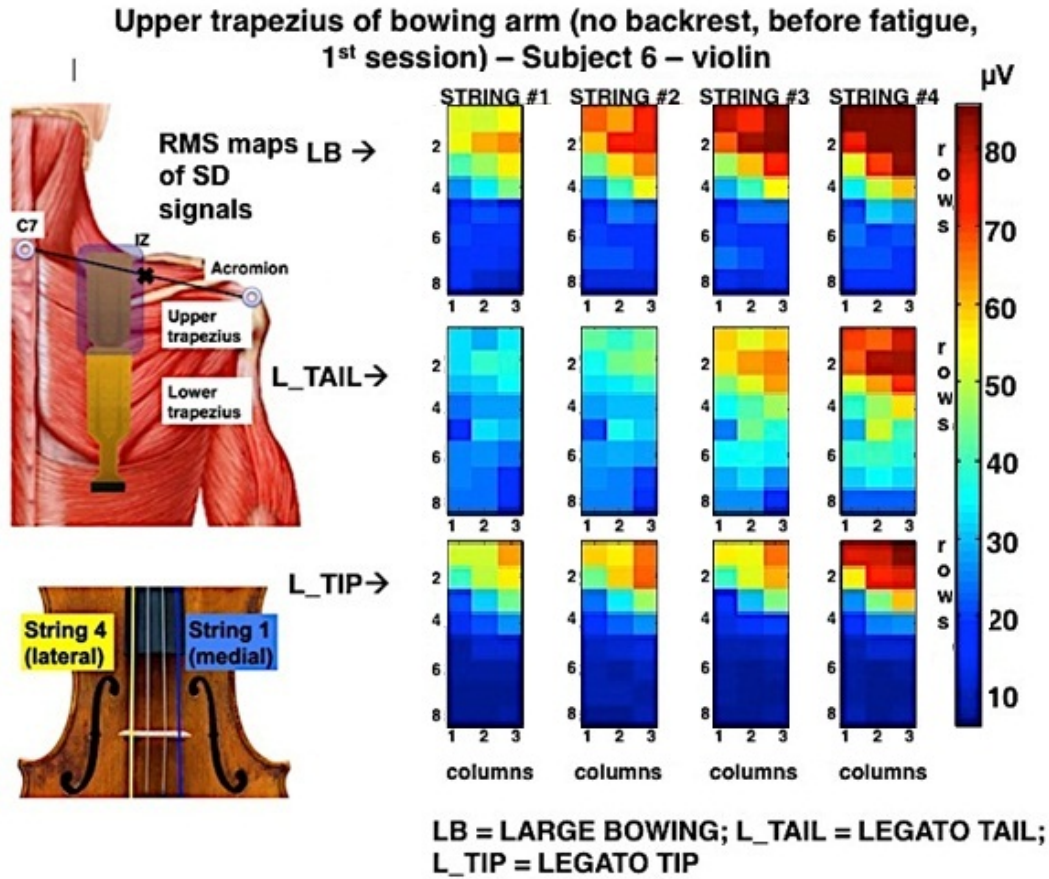
Figure 5.13: sEMG amplitude distributions obtained for subject #6 performing four violin strings in different bowing types(large, legato tip and legato tail bowing movements). Each map (8 rows and 3 columns) represent the RMS values (calculated over 10s) of single differential signals(SD). sEMG signals were recorded from upper Trapezius (bowing arm side). Signals were acquired in monopolar configuration using 8×4 electrode grid. SD signals were computed offline.

- **Lower Trapezius muscle of the bowing arm:**

  Figure 5.14 shows the trend of muscle activities and distribution of lower Trapezius activity index versus string numbers. The trend of MAI (increase of MAI as an increase in the string number) was seen in both subjects #6 and 7, but statistically significant difference($p < 0.001$) between the MAIs of the right lower Trapezius considering string numbers (notes) was found only for the sixth subject.
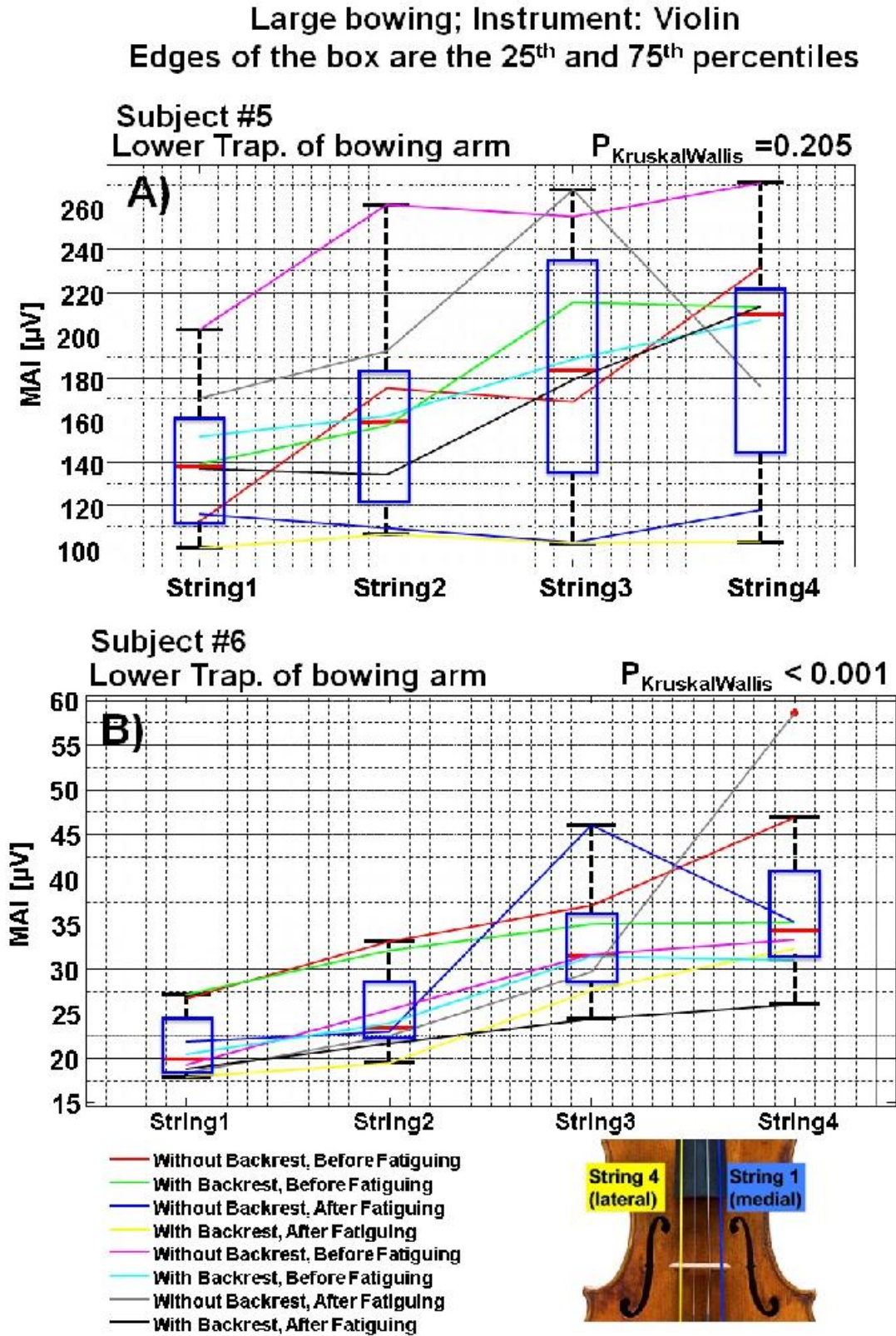
Figure 5.14: Please see the caption on the next page. . .

Figure 5.14: ...from the previous page: Boxplots represent the distribution of muscle's activity index (MAI) of A) subject 5 and B) subject 6 (student violin players) in large bowing from the lower Trapezius muscle of the bowing arm. The KruskalWallis test shows significant difference ($p < 0.001$) for the MAI of case "B", when subject played different strings. The trend of muscle activity index corresponding to the string number is the same for both "A" and "B" (case "A" shows a trend for the median values (solid red lines within the boxplots) with $p = 0.205$). The MAI was defined as the average of RMS values of the channels detected in the muscle active region. Muscle active region was detected by modified watershed segmentation technique (watershed+equalization+70% of the maximum value thresholding). The RMS was computed in time, for each channel of the active region, over the total length of single differential signal (10s). RMS of noise level (about 5 to 6μV) was computed from the recorded sEMG signals in relaxed sitting position.

In violin players, the upper Trapezius of the bowing arm was more active, when the fourth string was played and the muscle's activity index (MAI) decreases as the string number decreases (from lateral to medial strings). This is due to the different posture of the arm that is needed for producing different notes. In fact, to play different notes, subjects change the position of the bowing arm and control their shoulder rotation. In particular, playing from string #1 to 4 needs an increased scapular protraction. To quantify the position of bowing arm and its angles with respect to a predefined body reference during playing different notes, further studies with applying the XSENS or motion analyzers for recording the arm's position, synchronized with sEMG recording is suggested and needed.

Figures 5.14 and 5.15 (see page 186, and 190) show boxplots of the muscle activity index(MAI) from lower Trapezius of the bowing arm and left Erector Spinae muscle, when different notes (i.e. four strings) were played by the fifth and sixth subjects (student violin players) respectively. The MAI of subjects #6 and 5 show an increasing trend based on the string number from 1 to 4, but the KruskalWallis p-value of the fifth subject is 0.2, which implies no significant difference between the MAIs in the lower Trapezius of the bowing arm. Although both players are student players, greater p-value for the fifth subject might be due to different reasons such as more ability in controlling the upper Trapezius, or different styles of playing (different positioning

of bowing arm's joint angles) in comparison to subject #6. Discussion about these reasoning and validating them needs more recording sessions and more subjects.

- **Upper Trapezius muscle of the non-bowing arm:**

  The non-bowing arm (left hand) was only used for holding and supporting the instrument during playing. Therefore, the MAI of left upper Trapezius muscle was not affected significantly by playing the strings. The p-values (KruskalWallis test) computed for subject #5 and 6 are $p = 0.79$ and $p = 0.44$ respectively.

- **Left and right Erector Spinae muscles:**

  Table 5.2 shows the KruskalWallis p-values for two violin players (subjects 5 & 6). Both subjects are student players. Significant effect ($p < 0.001$) of the played string in two different types of bowing (legato tip and large bowing, please see figure 5.15) were observed for the sixth subject.

  Significant effect ($p < 0.001$) of the string on the MAIs, computed from both Erector Spinae muscles when subject #6 played in legato tip bowing; and also in large bowing for the MAIs of left Erector Spinae muscle(figure 5.15) were found. Meanwhile, sEMG from the right Erector Spinae, associated to the first (medial) string showed greater MAI, comparing to the fourth (lateral) string for the fifth subject, when she played in legato tip(see figure 5.16 panel "B").

Table 5.2: The p-value corresponding to the KruskalWallis test for two Violin players (subjects 5&6, student) for different bowing types for left and right Erector Spinae muscles in order to compare the muscle activity index(MAI), when different notes were played. For each subject, each bowing type and each muscle the p-values were computed over 8 values (two sessions, in each session before and after fatiguing, with and without backrest posture conditions were considered). MAI was defined as average of RMS values of the muscle active region detected by thresholding technique (70% of the maximum value). The RMS was computed in time, for each channel of the active region, over the total length of signal(10s). The $p < 0.05$ values are highlighted.

Subject No.	Muscle name	Bowing type	p-value
5	Left Erector Spinae	Legato tail	0.31
		Legato tip	< 0.001
		Large bowing	0.014
	Right Erector Spinae	Legato tail	0.86
		Legato tip	< 0.001
		Large bowing	0.56
6	Left Erector Spinae	Legato tail	0.38
		Legato tip	< 0.001
		Large bowing	< 0.001
	Right Erector Spinae	Legato tail	0.89
		Legato tip	0.88
		Large bowing	0.069
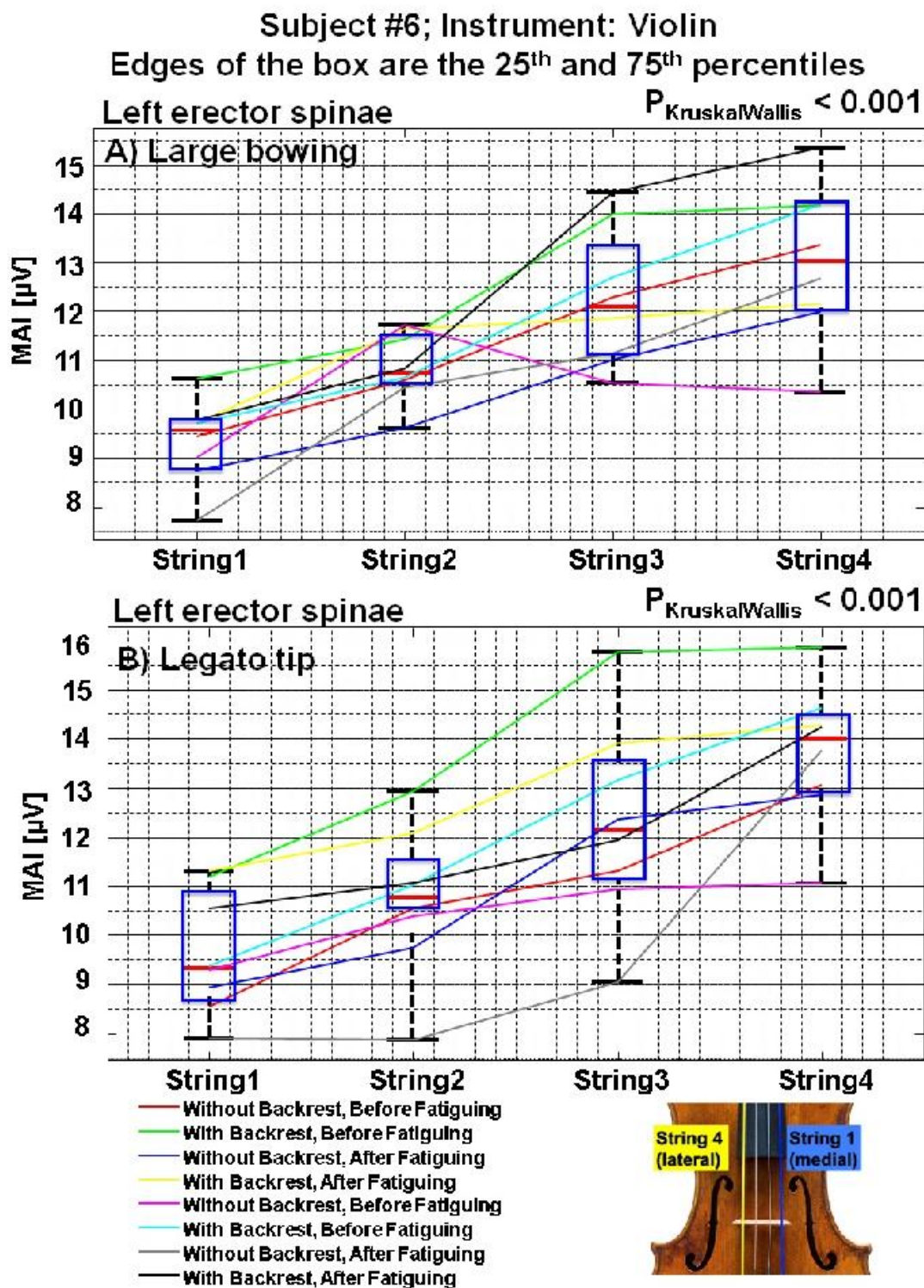
Figure 5.15: Boxplots represent the distribution of muscle activity index(MAI) of the sixth subject (student violin player) in A)large bowing and B) legato tip from left Erector Spinae muscle versus the instrument's string number. ...please see the continue on the next page ...

Figure 5.15: . . . continue from the previous page: The KruskalWallis test shows significant difference on the MAI, when subject played different strings ($p < 0.001$) in both "A" and "B". MAI was defined as the spatial average of RMS values of the muscle active region detected by thresholding technique (70% of the maximum value). The RMS was computed in time, for each channel of the active region, over the total length of single differential signal (10s). RMS of noise level was about 5 μV and was computed from recorded signals in relaxed sitting position.

Significant differences ($p < 0.001$) between MAIs from different types of bowing, legato tip and large bowing (see figure 5.15), from the left Erector Spinae plots concerning subject #6, can be seen. This might be due to some turning of the torso to the left since the holding arm(for the instrument) is the left. Playing the notes in legato tip, normally needs more control. Intrinsically, if the bowing arm is right, the player tends to turn its torso to the left. Since the sixth subject also plays viola, analyzing his data shows the same results (significant difference ($p < 0.001$) for legato tip, tail and large bowing). To check and quantifying the amount of leaning or turning to the left during playing the strings in different bowing types, further studies using the XSENS is suggested.
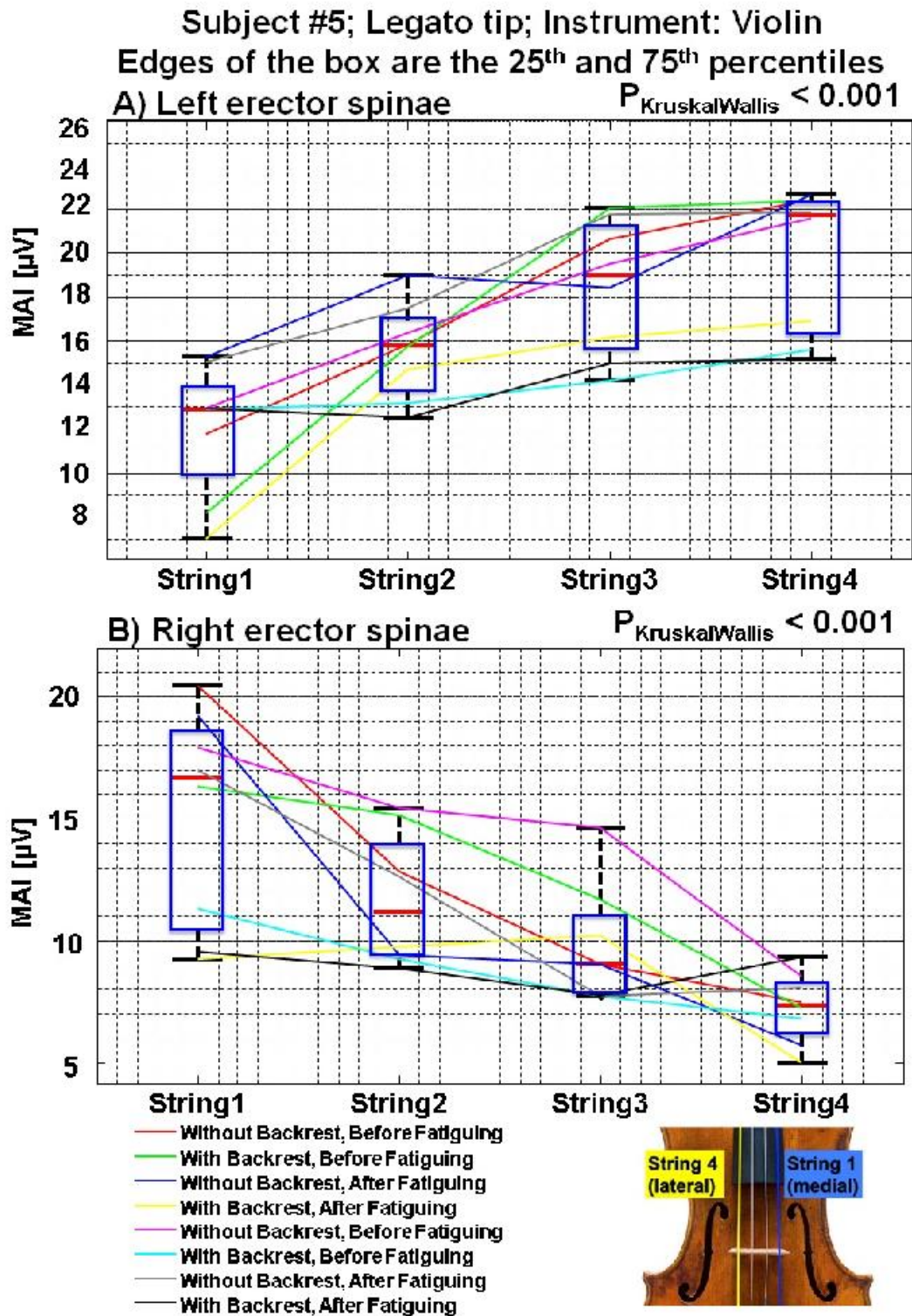
Figure 5.16: Boxplots represent the distribution of muscle activity index(MAI) of the fifth subject (student violin player) in legato tip bowing from A) left Erector Spinae and B) Right Erector Spinae muscles, versus the instrument's string number. ...please see the continue on the next page ...

Figure 5.16: ...continue from the previous page: The KruskalWallis test shows significant difference between the MAIs, when subject played different strings ($p < 0.001$) in both "A" and "B". MAI was defined as the spatial average of RMS values of the muscle active region detected by thresholding technique(70% of the maximum value). The RMS was computed in time, for each channel of the active region, over the total length of single differential signal (10s). RMS of noise was about 5μV and was computed from recorded signals in relaxed sitting position.

Effect of backrest support on muscle activity index:

In order to study the effect of backrest, subjects were asked to play the four strings individually in three different bowing types with and without backrest support during two recording sessions. Table 5.3 shows the p-values associated to different muscles and different bowing types, in study the effect of backrest support on the MAIs. Leaning on a backrest support provided a significant difference ($p < 0.05$) between the MAIs from left Erector Spinae muscle in all bowing types and from the right Erector Spinae in large bowing and legato tail for subjects #5 and 6.

Figures 5.17 shows the boxplot for the MAI of the left and right Erector Spinae muscle of fifth subject in large bowing. Figures 5.18 and 5.19 show the effect of backrest support for subject 5 in legato tail and legato tip bowing conditions respectively. Same information for subject 6 are plotted in the figures 5.20, 5.21, and 5.22.

Table 5.3: The *p*-values of the KruskalWallis test for violin players (subjects 5 & 6) are exposed in order to study the effect of backrest support on the the muscle activity index(MAI). For each subject, each bowing type and each muscle, the *p*-values were computed over 16 values (two sessions, in each session before and after fatiguing, and four different strings were considered). Conditions, which the *p*-value are presented with "*" indicates that MAI with no backrest support $<$ MAI with backrest. The $p < 0.05$ values are highlighted.

Subject No.	Muscle name	Bowing type	*p*-value
5	Left Erector Spinae	Legato tail	0.024
		Legato tip	0.013
		Large bowing	0.001
	Right Erector Spinae	Legato tail	< 0.001
		Legato tip	0.243
		Large bowing	0.014
	Upper Trapezius of the bowing arm	Legato tail	0.498
		Legato tip	0.522
		Large bowing	0.940
	Lower Trapezius of the bowing arm	Legato tail	0.598
		Legato tip	0.007
		Large bowing	0.187
	Upper Trapezius of the non-bowing arm	Legato tail	0.083
		Legato tip	0.651
		Large bowing	0.007
6	Left Erector Spinae	Legato tail	0.007*
		Legato tip	0.004*
		Large bowing	0.035*
	Right Erector Spinae	Legato tail	0.006*
		Legato tip	0.152
		Large bowing	0.035*
	Upper Trapezius of the bowing arm	Legato tail	0.763
		Legato tip	0.940
		Large bowing	0.792
	Lower Trapezius of the bowing arm	Legato tail	0.06*
		Legato tip	0.327
		Large bowing	0.200
	Upper Trapezius of the non-bowing arm	Legato tail	0.851
		Legato tip	0.91
		Large bowing	0.309
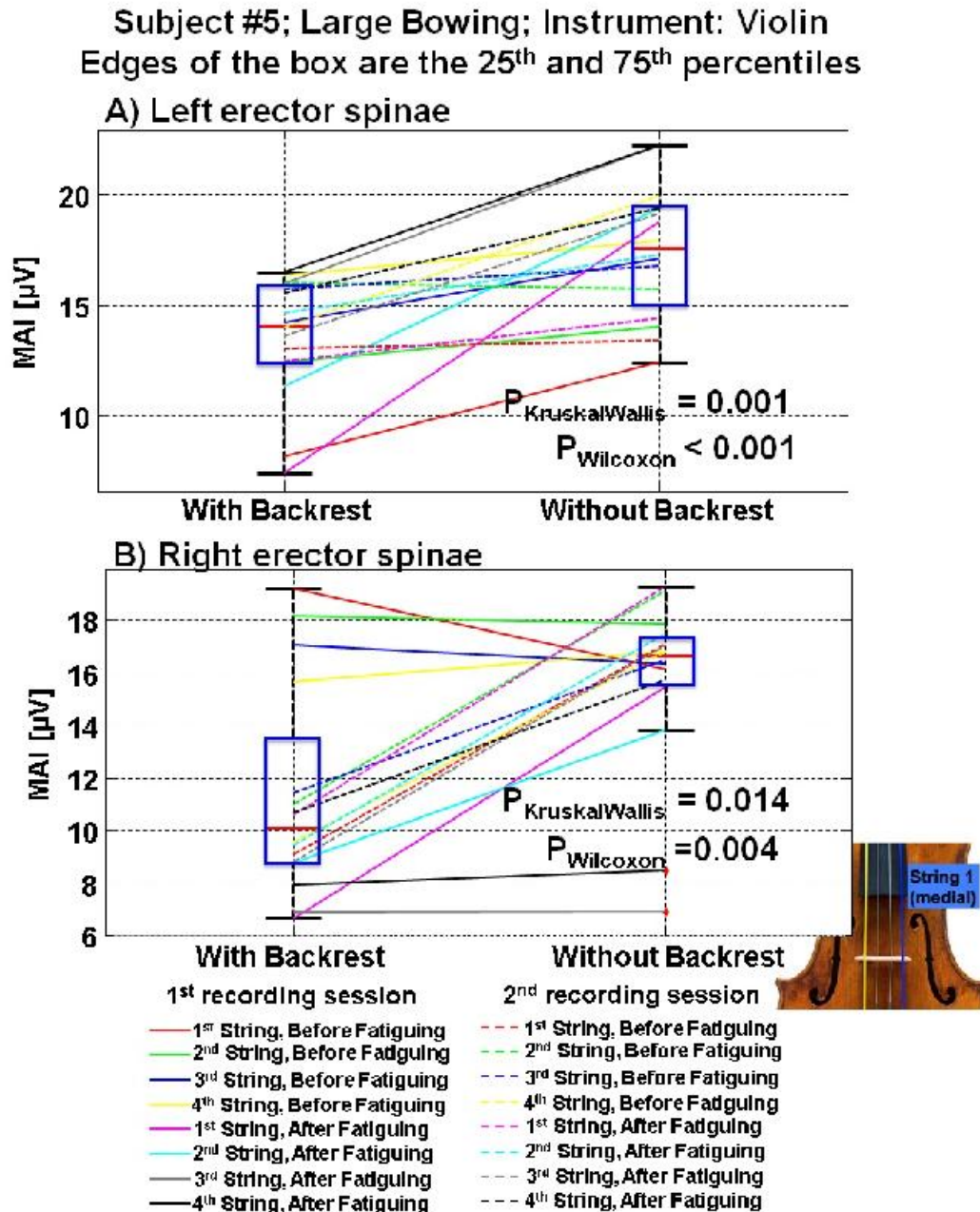
Figure 5.17: The boxplots represent the distribution of muscle activity index (MAI) of the subject 5 for A) left and B) right Erector Spinae muscles in large bowing. KruskalWallis test shows significant difference in the MAI between the conditions of backrest and no backrest as $p = 0.001$ for "A" and $p = 0.014$ for "B". The MAI was defined as average of RMS values of the muscle active region detected by thresholding technique (channels with RMS¿70% of max(RMS)). The RMS was computed in time, for each channel of the active region, over the total length of single differential signal (10s). RMS of noise was computed (about $5\mu V$) from recorded sEMGs in relaxed sitting position.
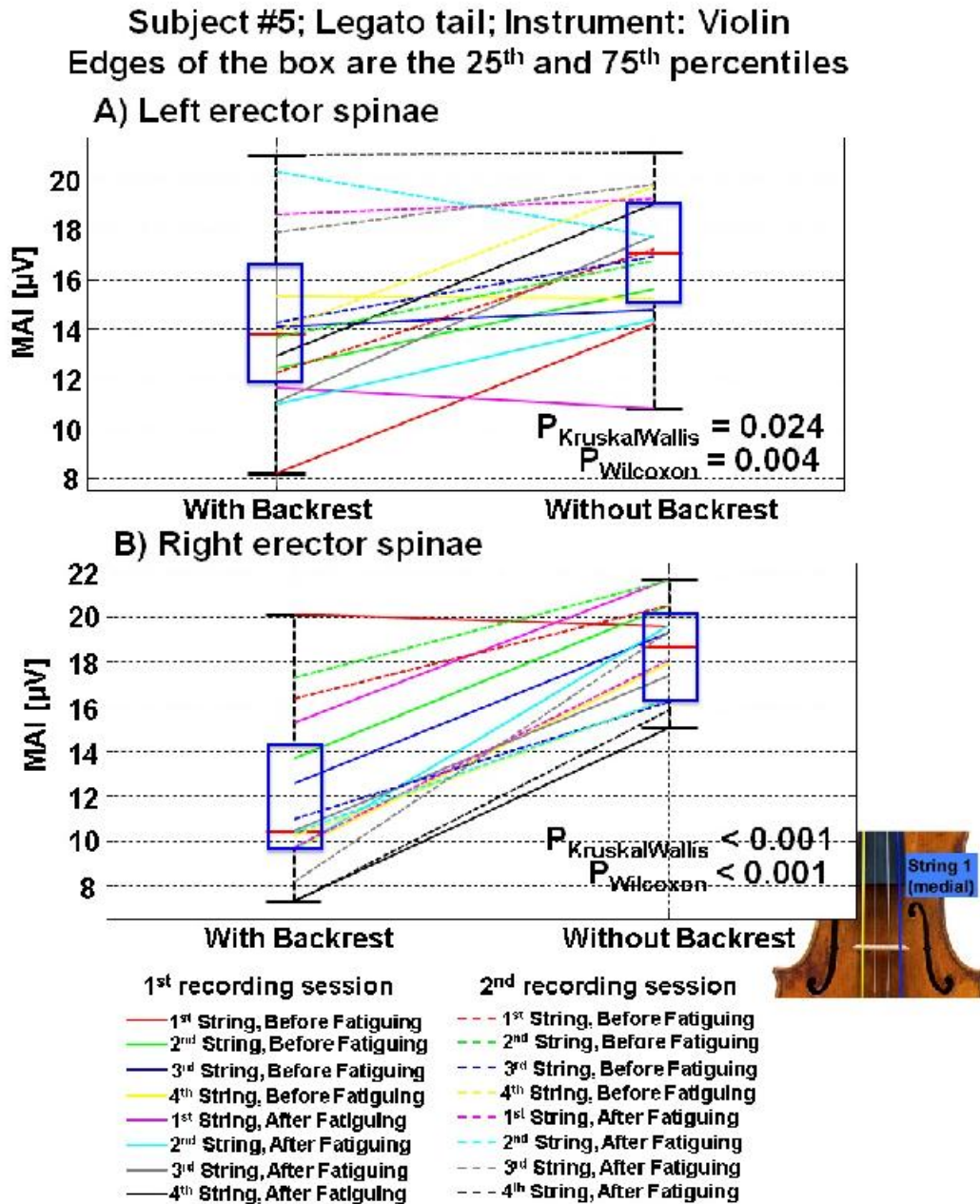
Figure 5.18: The boxplots represent the distribution of muscle activity index (MAI) of the subject 5 for A) left and B) right Erector Spinae muscles in legato tail bowing. KruskalWallis test shows significant difference in the MAI between the conditions of backrest and no backrest as $p = 0.024$ for "A" and $p < 0.001$ for "B". The MAI was defined as average of RMS values of the muscle active region detected by thresholding (channels with RMS>70% of max(RMS)). The RMS was computed in time, for each channel of the active region, over the total length of single differential signal (10s). Noise level(RMS) was computed about $5\mu V$ from recorded sEMGs in relaxed sitting position.
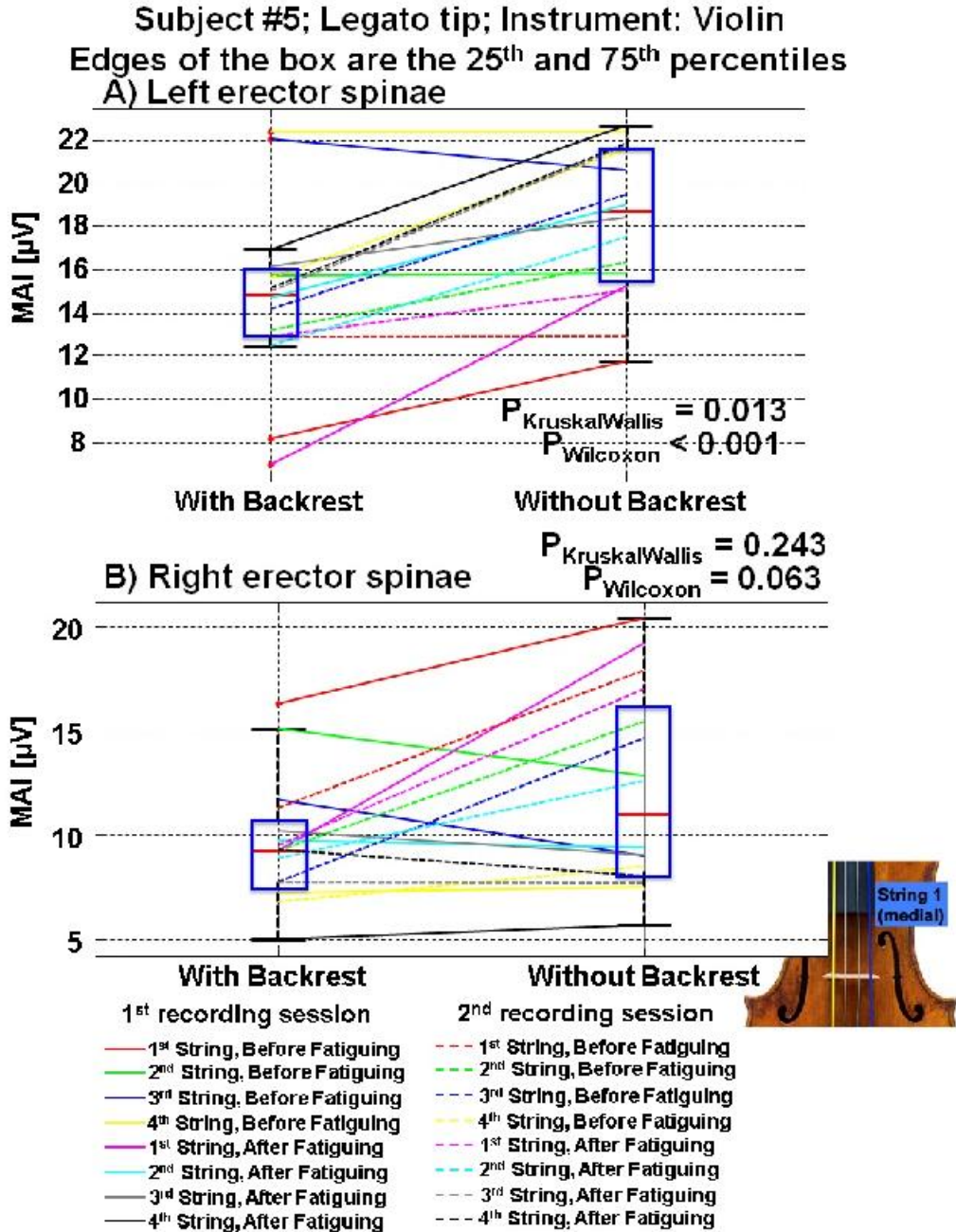
Figure 5.19: The boxplots represent the distribution of muscle activity index (MAI) of the fifth subject for A) left and B) right Erector Spinae muscles in legato tip bowing. KruskalWallis test shows significant difference in the MAI between the conditions of backrest and no backrest as $p = 0.013$ for "A" and $p = 0.243$ for "B". The MAI was defined as average of RMS values of the muscle active region detected by thresholding (channels with RMS>70% of max(RMS)). The RMS was computed in time, for each channel of the active region, over the total length of single differential signal (10s). Noise level(RMS) was computed about 5μV from recorded sEMGs in relaxed sitting position.
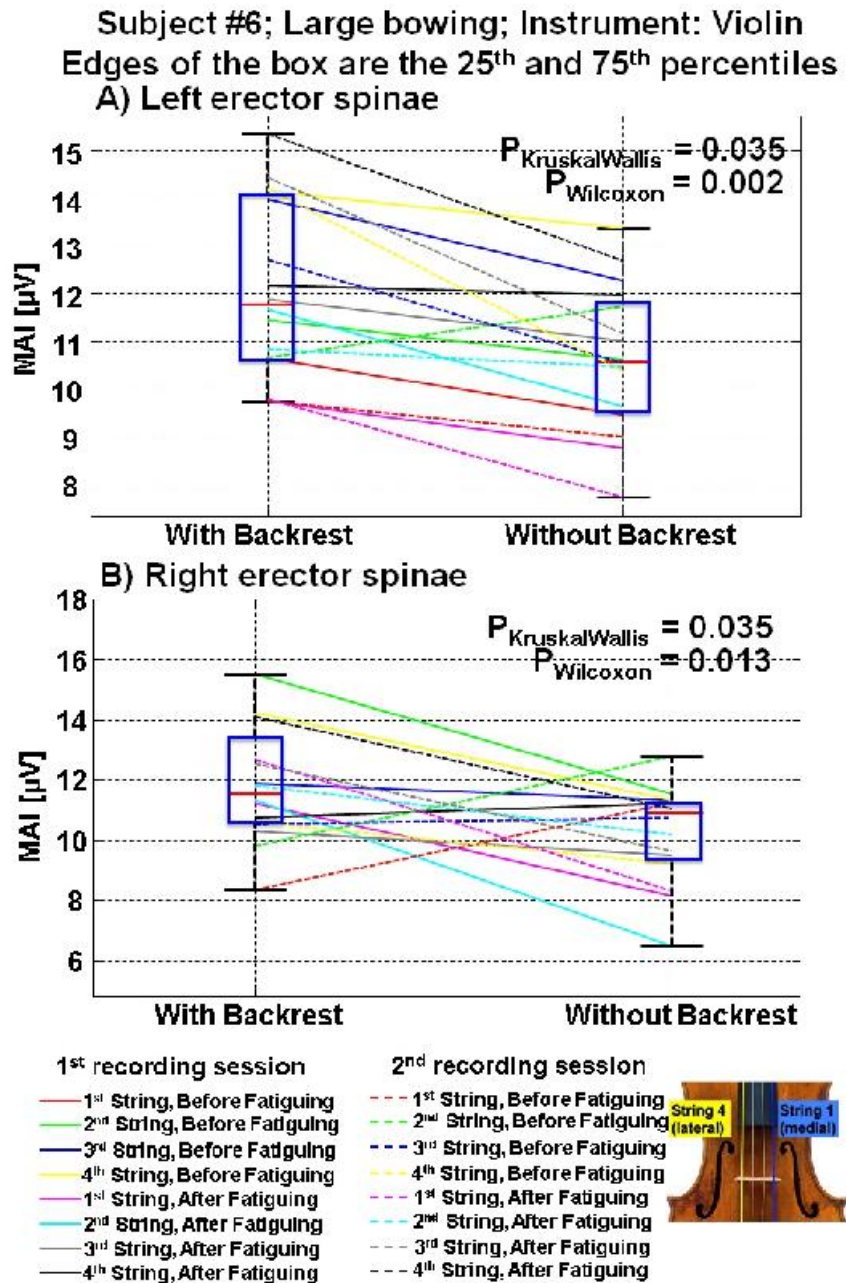
Figure 5.20: The boxplots represent the distribution of muscle activity index (MAI) of the subject 6 for A) left and B) right Erector Spinae muscles in large bowing. KruskalWallis test shows significant difference in the MAI between the conditions of backrest and no backrest as $p = 0.035$ for both "A" and "B". The MAI was defined as average of RMS values of the muscle active region detected by thresholding technique(channels with RMS>70% of max(RMS)). The RMS was computed in time, for each channel of the active region, over the total length of single differential signal (10s). Noise level(RMS) was computed (about 5μV) from recorded sEMGs in relaxed sitting position.
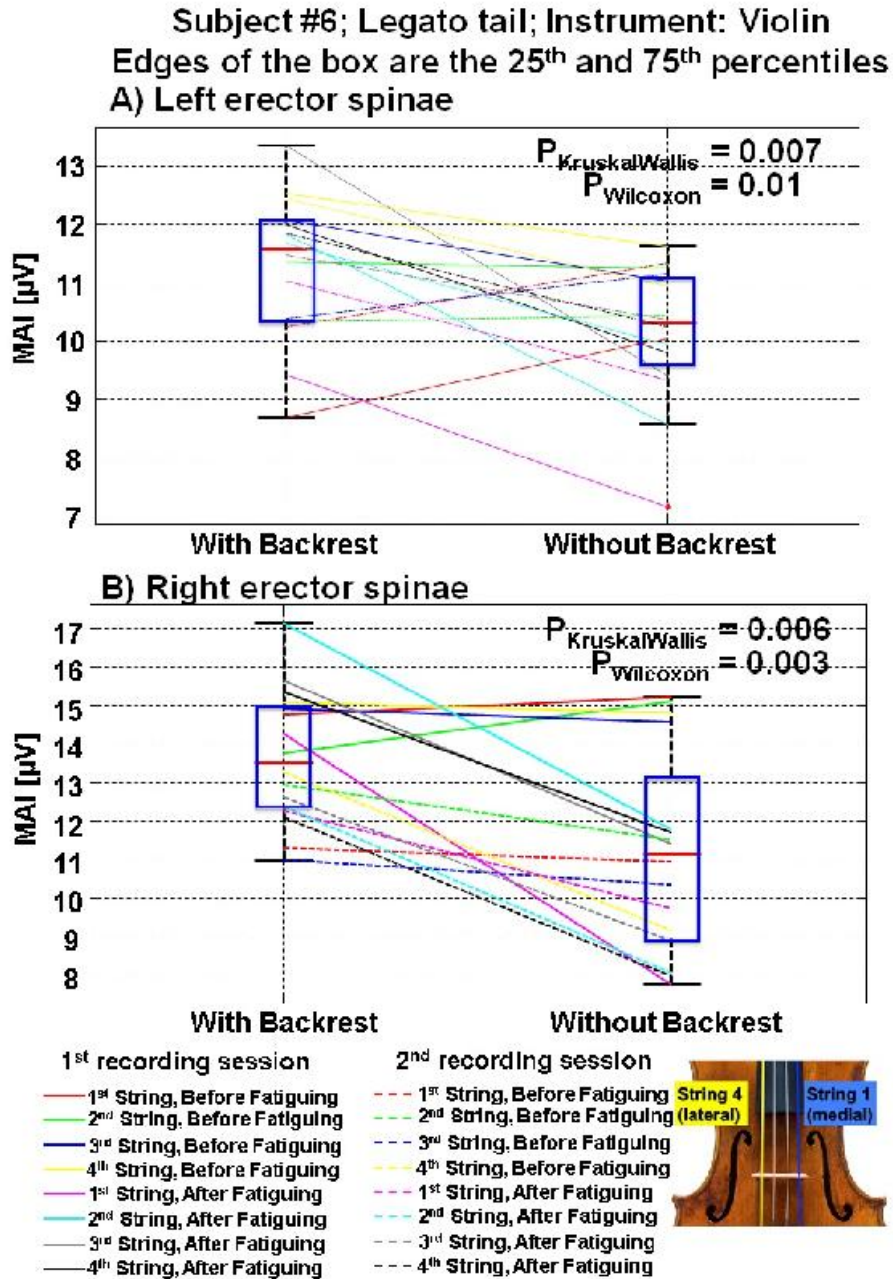
Figure 5.21: The boxplots represent the distribution of muscle activity index (MAI) of the subject 6 for A) left and B) right Erector Spinae muscles in legato tail bowing. KruskalWallis test shows significant difference in the MAI between the conditions of backrest and no backrest as $p = 0.007$ for "A" and $p = 0.006$ for "B". The MAI was defined as average of RMS values of the muscle active region detected by thresholding technique (channels with RMS>70% of max(RMS)). The RMS was computed in time, for each channel of the active region, over the total length of single differential signal (10s). Noise level(RMS) was computed (about 5μV) from recorded sEMGs in relaxed sitting position.
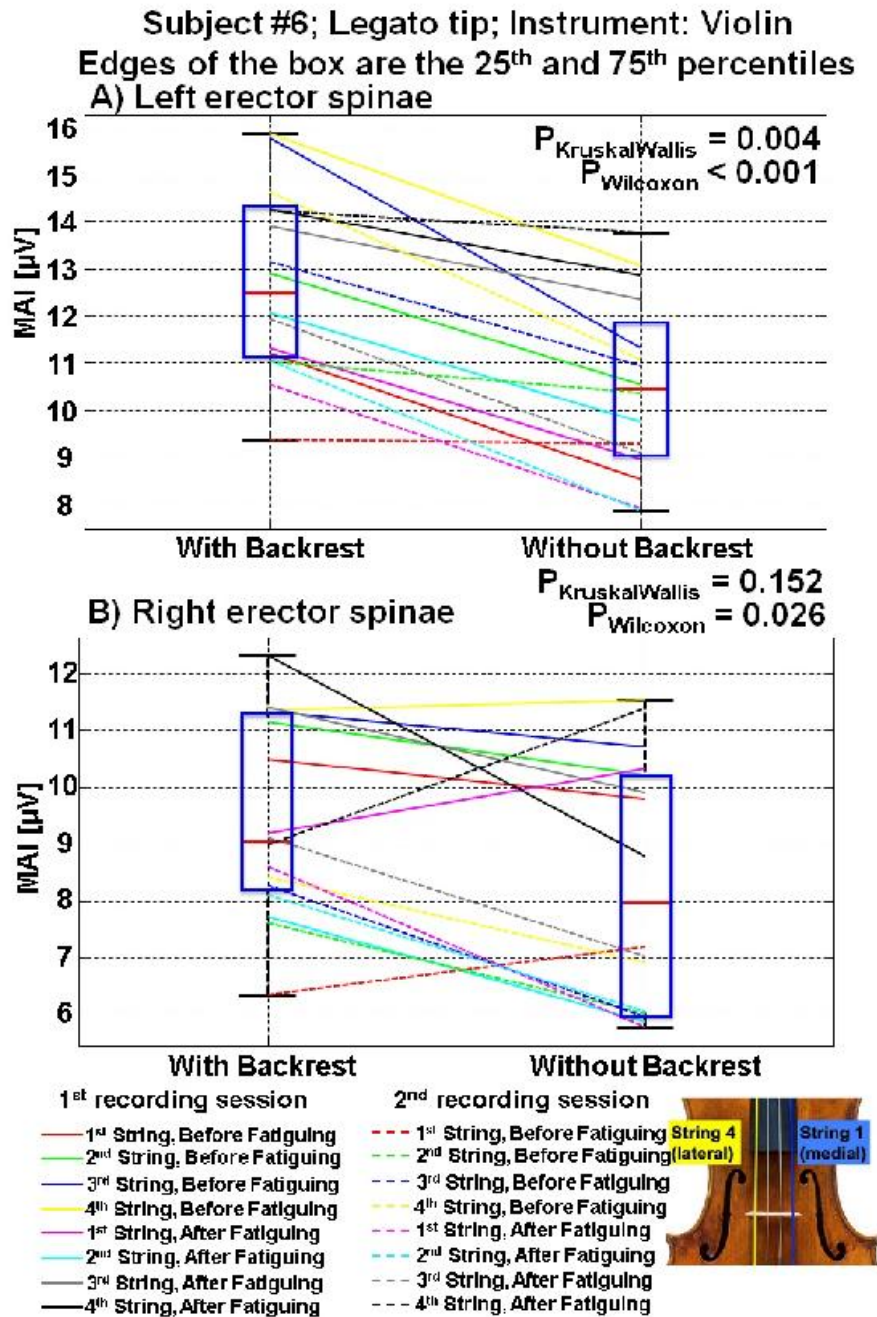
Figure 5.22: The boxplots represent the distribution of muscle activity index (MAI) of the subject 6 for A) left and B) right Erector Spinae muscles in legato tip bowing. KruskalWallis test shows significant difference in the MAI between the conditions of backrest and no backrest as $p = 0.004$ for "A" and $p = 0.152$ for "B". The MAI was defined as average of RMS values of the muscle active region detected by thresholding technique(channels with RMS>70% of max(RMS)). The RMS was computed in time, for each channel of the active region, over the total length of single differential signal (10s). Noise level(RMS) was computed (about 5 to 6μV) from recorded sEMGs in relaxed sitting position.

No backrest might imply recruiting more motor units of the left and right Erector Spinae during playing the notes. Since, the two subjects(5 and 6) are right handed and their bowing arm is right, during playing violin, the musicians might tend to turn or bend their torso to the left when they are playing with the tail of the bow. In legato tip, the bow length helps the subject not to turn toward left and having the same muscle activity index for both left and right Erector Spinae. This hypothesis can be validated in future studies using XSENS or other devices in order to track any turns of the torso toward the instrument (non-bowing arm) with more subjects. Meanwhile, leaning on a backrest support has no statistically significant effect on the activity of upper Trapezius of the bowing arm (please see table 5.3 on page 194). The effect of posture on the muscle activity index of the lower Trapezius muscle is not the same for the two subjects based on their bowing type. This difference might be because of the different strategies that musicians choose to play and might also be related to individual differences. Any inference for the lower Trapezius of the bowing arm can be misleading. More subjects and more recording sessions are needed to provide strong results. p-values concerning the effect of backrest support on the MAIs from the upper Trapezius of the non-bowing arm are also presented in table 5.3 as supplementary information.

According to the results related of subjects 5 and 6, it is concluded that the muscle activity index is significantly affected by the posture but it is not guaranteed that the backrest support cause smaller activity on the left and right Erector Spinae during playing strings. It should be noted that generalizing any conclusion based on two or three violin players can be misleading. More violin players and recording sessions are needed for stronger conclusions.

Violin players (subject 4):

Subject #4 was a student violin player. She performed only one session and since she reported some injuries and muscle pain before participating in the second recording session, her data was analyzed separately.

Significant effect ($p < 0.001$) of the played note (string number) in legato tip on the muscle's activity index (MAI) computed from the upper Trapezius (left and right side) was observed. The MAI increased as the increase of string number. The greatest MAI value was obtained, when the fourth string was played and the minimum activity was associated to the first string(see figures 5.23 and 5.24). Statistical difference ($p < 0.001$)

between the MAIs of the upper Trapezius of bowing arm, in large bowing of the string was observed. Regardless of the bowing type, no difference was observed between the MAIs of the Erector Spinae muscles, when different strings were played.

Leaning on a backrest support provided significant difference ($p < 0.001$) in all bowing types for both Erector Spinae muscles(left and right). No statistical differences between the MAIs of backrest and no backrest were observed for Trapezius muscles for this subject(subject #4).
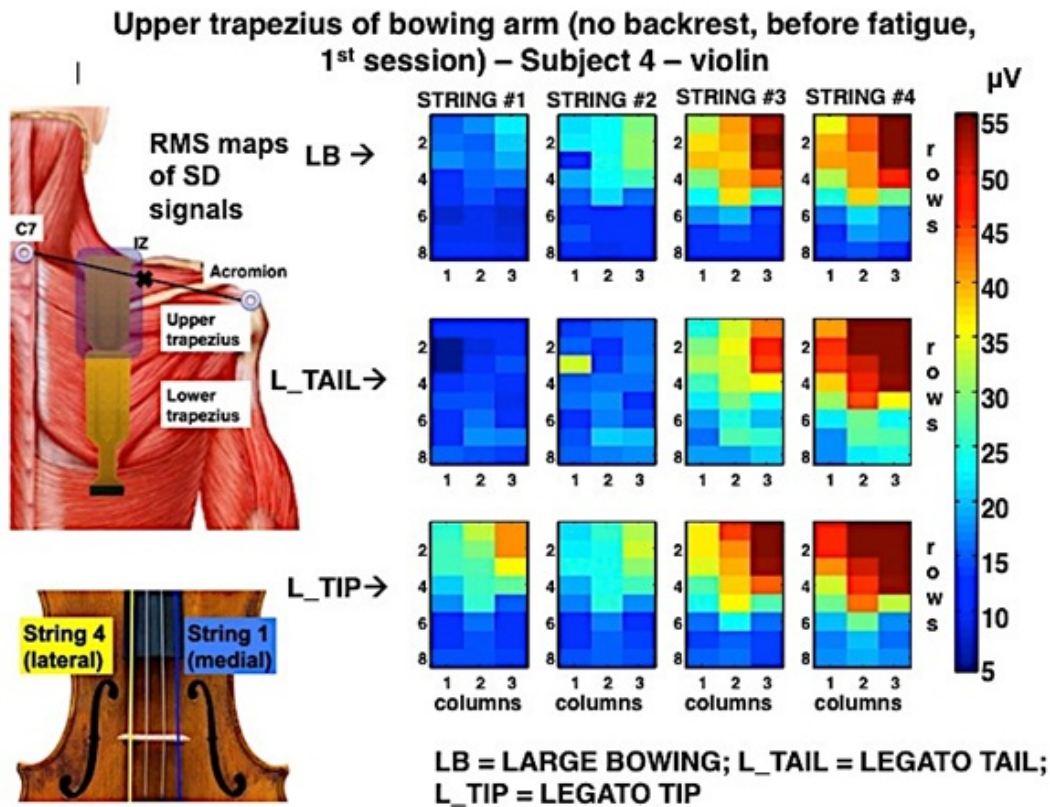
Figure 5.23: sEMG amplitude distributions obtained for the fourth subject playing four violin strings in different bowing types(large, legato tip and legato tail bowing movements). Each map (8 rows and 3 columns) represent the RMS values (calculated over 10s) of single differential signals(SD). sEMG signals were recorded from upper Trapezius (bowing arm). Signals were acquired in monopolar configuration using 8×4 electrode grid. SD signals were computed offline.
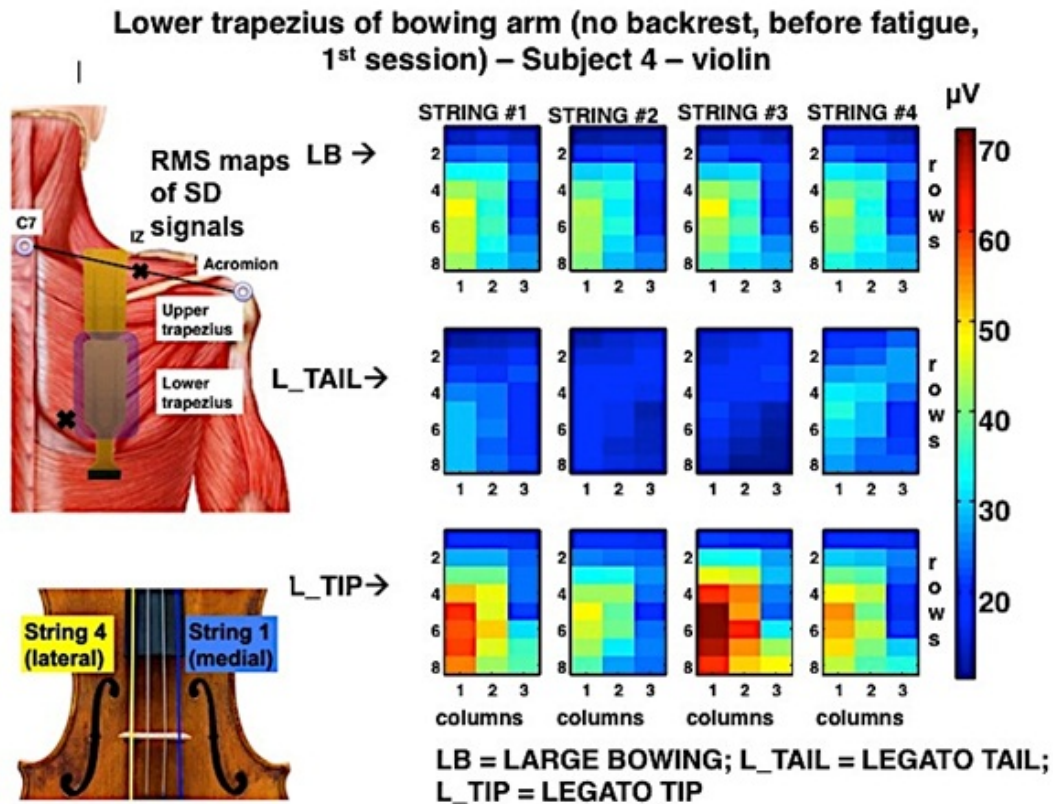
Figure 5.24: sEMG amplitude distributions obtained for subject #4 playing four violin strings in different bowing types(large, legato tip and legato tail bowing movements). Each map (8 rows and 3 columns) represent the RMS values (calculated over 10s) of single differential signals(SD). sEMG signals were recorded from lower Trapezius (bowing arm). Signals were acquired in monopolar configuration using 8×4 electrode grid. SD signals were computed offline.

In summary table 5.4 shows the results of statistical analysis in evaluation of the

effect of backrest support on violin players.

Table 5.4: Summary of the statistical test for evaluating the effect of backrest support on the violin players(subjects 4, 5 , and 6)

BOWING TYPES	MUSCLES	VIOLIN		
		#4	#5	#6
Large Bowing	L_ES	Y	Y	Y
	L_UT		Y	
	R_ES	Y	Y	Y
	R_LT			
	R_UT			
Legato tail	L_ES	Y	Y	Y
	L_UT			
	R_ES	Y	Y	Y
	R_LT			
	R_UT			
Legato tip	L_ES	Y	Y	Y
	L_UT			
	R_ES	Y		
	R_LT			
	R_UT			

L_ES = LEFT ERECTOR SPINAE
L_UT = LEFT UPPER TRAPEZIUS
R_ES = RIGHT ERECTOR SPINAE
R_LT = RIGHT LOWER TRAP.
R_UT = RIGHT UPPER TRAP.

"BACKREST EFFECT":
Y means $p<0.05$ of Kruskal_Wallis test between MAI calculated with and without backrest support (WB<WOB)

Effect of "fatigue session" on the muscle's activity index:

Statistical difference ($p < 0.05$) in the activity index (MAI) of the upper and lower Trapezius of the bowing arm for violin players, associated to the played strings in large bowing before and after fatiguing conditions(please see figure 5.25) was observed. Concerning subject #4, significant difference($p = 0.005$) between MAIs of before and after fatiguing performances in legato tail bowing was seen. The MAIs were greater when musicians played before fatiguing condition with respect to after fatiguing performances.

Concerning the lower Trapezius of the bowing arm of violin players, statistical effect of the fatigue session on the MAI was observed (please see table 5.5) in each type of bowing (except subject 6 performing a large bowing). Generally, the MAI value obtained

for before fatiguing, was greater than what observed after fatiguing.

The non-bowing arm was used for holding and supporting the instrument during play-ing. Statistical effect of the fatigue session on the MAIs of the left(non bowing arm) upper Trapezius(violin players), when the sixth subject played the strings in legato tail and legato tip ($p = 0.024$ and $p = 0.002$) were observed. This observation is also true, when subject #5 performed in legato tip bowing ($p = 0.022$).

Effect of fatiguing on the left and right Erector Spinae muscles

Table 5.6 shows the KruskalWallis p-values for three violin players (subjects 4, 5, and 6) in order to study the effect of fatigue on the muscle activity index. Subjects were student players. Concerning the fourth subject, significant difference ($p = 0.003$) on activity (MAI) of the right Erector Spinae in the legato tail bowing was observed. Considering subject #5, significant difference ($p = 0.007$) was seen in large bowing of strings before and after fatiguing condition from the right Erector Spinae muscle. The activity index (MAI) values were greater, when musicians played before fatiguing with respect to after fatiguing performances.
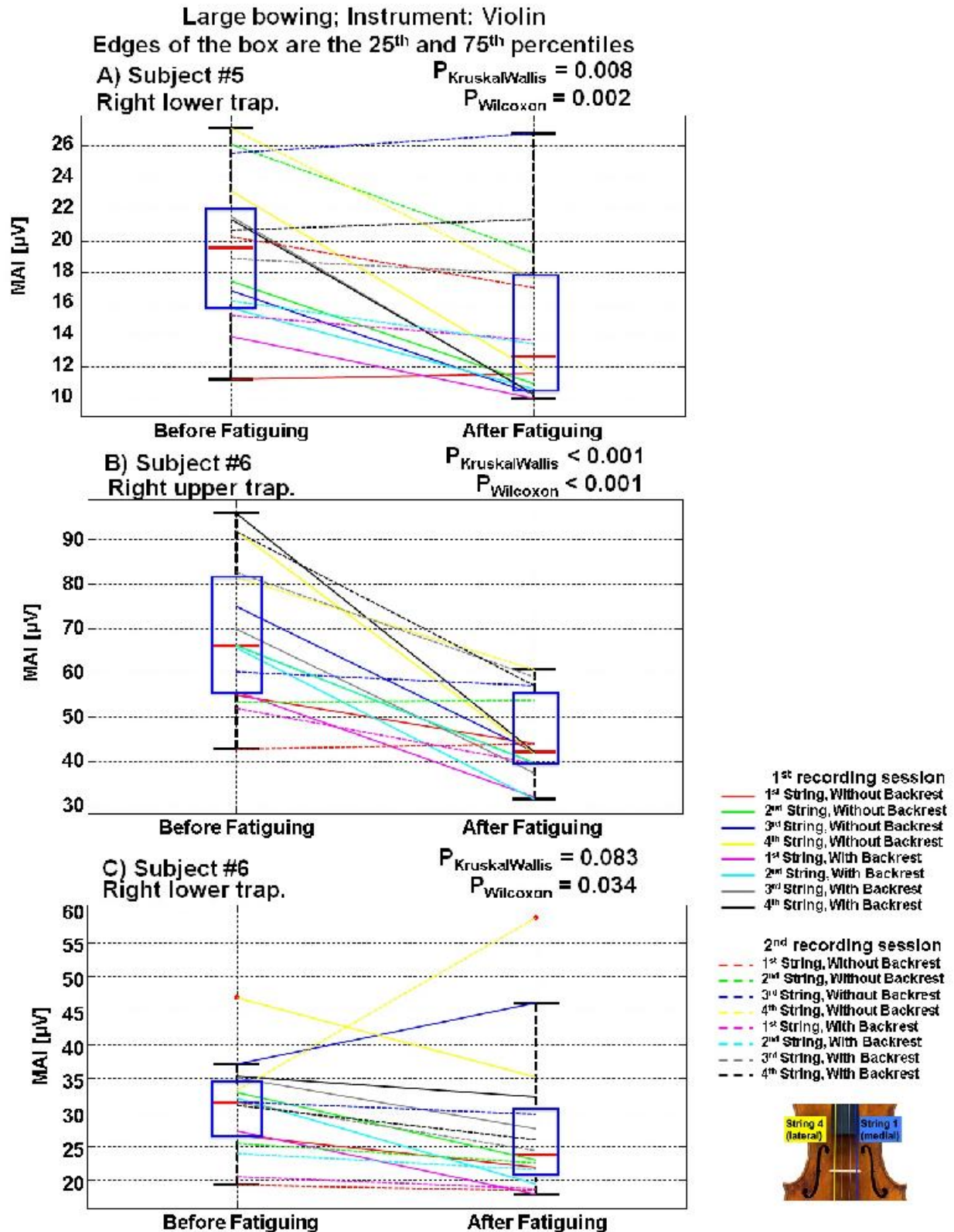
Figure 5.25: ...please see the caption on the next page ...

Figure 5.25: . . . from the previous page: The boxplots represent the distribution of the muscle's activity index(MAI) of A) subject 5, B) and C) subject 6 (violin players) in large bowing considering A) and B) upper Trapezius and C) lower Trapezius muscle of the bowing arm. The KruskalWallis test were applied to test the significance level of the effect of fatiguing condition (before and after fatiguing) on the MAI. Wilcoxon test is for the pair test(non-parametric). MAI was defined as the spatial average of RMS values of the muscle active region detected by modified watershed segmentation technique (watershed + equalization + 70% of the maximum value thresholding). The RMS was computed in time, for each channel of the active region, over the total length of single differential signal (10s). RMS of noise was about 5 to 6μV and was computed from a recording in relaxed sitting position.

## 5. A STUDY OF MUSCLE ACTIVITY IN MUSICIANS PLAYING STRING INSTRUMENTS

**Table 5.5: The *p*-values of the KruskalWallis test for violin players (subjects 4, 5 and 6) are exposed in order to study the effect of fatiguing condition on the muscle's activity index(MAI). For subjects 5 and 6, the *p*-values for each fatigue condition, were computed over 16 values (two sessions, backrest support(with/without), and four different strings were considered) and for subject 4 the *p*-values were computed over 8 values (one sessions, four strings, two backrest support conditions). The MAI was defined as average of RMS values of the muscle active region detected by modified watershed segmentation technique (watershed+equalization+70% of the maximum value thresholding). The RMS was computed in time, for each channel of the active region, over the total length of signal(10s). The fatigue session was defined as about 30 minutes playing a difficult piece of music. In all presented significant levels, the median value (over the 16 values for subjects 5 and 6; over 8 values for subject 4) of the MAIs associated to before fatiguing playing > the median of MAIs related to after fatiguing. The $p < 0.05$ values are highlighted.**

Subject No.	Muscle name	Bowing type	*p*-value
4	Right Upper Trapezius(bowing arm)	Large bowing	0,093
		Legato tail	0,005
		Legato tip	0,141
	Right Lower Trapezius(bowing arm)	Large bowing	0,027
		Legato tail	0,021
		Legato tip	0,021
	Left Upper Trapezius(non-bowing arm)	Large bowing	0,753
		Legato tail	0,753
		Legato tip	0,172
5	Right Upper Trapezius(bowing arm)	Large bowing	0,034
		Legato tail	0,274
		Legato tip	0,88
	Right Lower Trapezius(bowing arm)	Large bowing	0,008
		Legato tail	$< 0,001$
		Legato tip	$< 0,001$
	Left Upper Trapezius(non-bowing arm)	Large bowing	0,214
		Legato tail	0,214
		Legato tip	0,022
	please see the continue on the next page . . .		

Table 5.5: The *p*-values of the KruskalWallis test for violin players (subjects 4, 5 and 6) are exposed in order to study the effect of fatiguing condition on the muscle's activity index(MAI). For subjects 5 and 6, the *p*-values for each fatigue condition, were computed over 16 values (two sessions, backrest support(with/without), and four different strings were considered) and for subject 4 the *p*-values were computed over 8 values (one sessions, four strings, two backrest support conditions). The MAI was defined as average of RMS values of the muscle active region detected by modified watershed segmentation technique (watershed+equalization+70% of the maximum value thresholding). The RMS was computed in time, for each channel of the active region, over the total length of signal(10s). The fatigue session was defined as about 30 minutes playing a difficult piece of music. In all presented significant levels, the median value (over the 16 values for subjects 5 and 6; over 8 values for subject 4) of the MAIs associated to before fatiguing playing > the median of MAIs related to after fatiguing. The $p < 0.05$ values are highlighted.

Subject No.	Muscle name	Bowing type	*p*-value
		...from the previous page	
6	Right Upper Trapezius(bowing arm)	Large bowing	< 0,001
		Legato tail	< 0,001
		Legato tip	0,007
	Right Lower Trapezius(bowing arm)	Large bowing	0,083
		Legato tail	0,013
		Legato tip	0,024
	Left Upper Trapezius(non-bowing arm)	Large bowing	0,651
		Legato tail	0,024
		Legato tip	0,002

Table 5.6: The p-values of the KruskalWallis test for violin players (subjects 4, 5 and 6) are exposed in order to study the effect of fatiguing condition on the muscle's activity index(MAI). For subjects 5 and 6, the p-values were computed over 16 values (two sessions, in each session the presence of backrest support (with/without), and four different strings were considered) and for subject 4 the p-values were computed over 8 values (one sessions, four strings, two backrest support conditions). The MAI was defined as average of RMS values of the muscle active region detected by thresholding technique (70% of the maximum value). The RMS was computed in time, for each channel of the active region, over the total length of signal(10s). The fatigue session was defined as about 30 minutes playing a difficult piece of music. In all presented significant levels, the median value (over the 16 values for subjects 5 and 6; over 8 values for subject 4) of the MAIs associated to before fatiguing playing > the median of MAIs related to after fatiguing. The $p < 0.05$ values are highlighted.

Subject No.	Muscle name	Bowing type	p-value
4	Right Erector Spinae	Large bowing	0,115
		Legato tail	0,003
		Legato tip	0,208
	Left Erector Spinae	Large bowing	0,6
		Legato tail	0,141
		Legato tip	0,6
5	Right Erector Spinae	Large bowing	0,007
		Legato tail	0,105
		Legato tip	0,327
	Left Erector Spinae	Large bowing	0,214
		Legato tail	0,122
		Legato tip	0,97
6	Right Erector Spinae	Large bowing	0,152
		Legato tail	0,274
		Legato tip	0,851
	Left Erector Spinae	Large bowing	0,706
		Legato tail	0,274
		Legato tip	0,678

Another observation from the RMS plots (see figures 5.26 for instance) is that upper Trapezius of the bowing arm is more active at the time of changing the bow's direction.

At this time the subject is trying to control the bow to play the note as smooth as possible. In this situation the subject might provide a co-contraction among the shoulder muscles to produce a smooth movement. Future studies is needed to investigate this hypothesis (ex.: the Trapezius and Deltoid possible co-contraction). This trend has been observed in other subjects as well (Viola and Cello players).
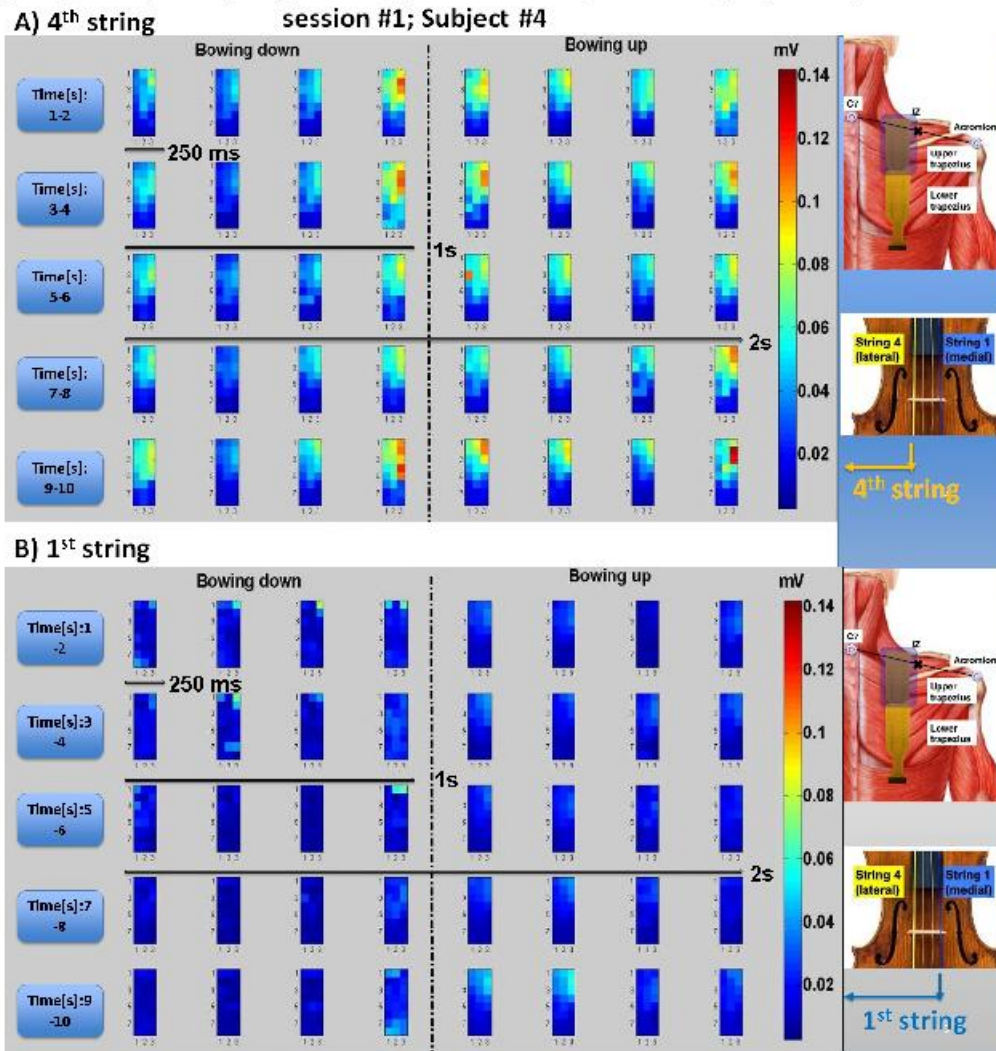
Figure 5.26: Sequence of single differential (along fiber direction, 8×3 channels) sEMG RMS maps, computed over a 250ms epochs from monopolar signals detected by 8×4 flexible detection grid (IED = 10mm) placed over the upper Trapezius (bowing arm side) are presented for 10s (each row in 2s, 1s bow up and 1s bow down). Dashed line represent the time when subject changed the bowing direction (from bowing down to bowing up). Each row of the RMS maps are parallel to the fiber direction. Subject (number 4) played (large bowing) the A) fourth and B) first string of Violin with backrest support before doing the fatiguing performance. Totally subject performed 5 bowing up and 5 bowing down movements during 10s.

5.6.2   Viola players (subject 1 and subject 7)

Effect of the string that was played on the muscle activity index

- **Upper and lower Trapezius muscle of the bowing arm:**

  Significant effect($p < 0.001$) of the played note (string) on the muscle's activity index (MAI) of the upper Trapezius of the bowing arm from viola players was observed, when subjects played the strings individually in large bowing (please see figure 5.27). The MAI increases as the string number increase (i.e. the highest activity was obtained when the fourth string was played and the minimum activity is when the first string was played, string 4 is the most lateral. This observation (increasing trend) is also true for the MAIs from the lower Trapezius muscle(please see figure 5.28 of as an instance) of both subjects. However, the p-value shows no significant effect($p = 0.294$) of the played strings(notes) in large bowing by the professional viola player (subject #1), on the MAIs of the right(the bowing arm) lower Trapezius and a significant effect ($p = 0.015$) for the seventh subject(student viola player). Viola is different in size (larger) with respect to violin, but both viola and violin are played similarly (not exactly) from the subject's posture point of view. Therefore, as violinists, similar reasoning can be provided for the increasing trend in the MAIs with respect to increasing the string number(from the most medial to the most lateral string with respect to the sagittal plane of the subject's body). This trend is due to the different posture of the arm that is needed for producing different notes. In fact, to play different notes, subjects change the position of the bowing arm and control their shoulder rotation. In particular, playing from string #1 to 4 needs an increased scapular protraction. To quantify the position of bowing arm and its angles with respect to a predefined body reference during playing different notes, further studies with applying the XSENS or motion analyzers for recording the arm's position, synchronized with sEMG recording is suggested and needed.

- **Left and Right Erector Spinae muscles:**

  Table 5.7 shows the KruskalWallis p-values computed for analyzing the effect the string number(note) that was played in different bowing types, on the muscle's activity index(MAI) of the lumbar muscles of the viola players. Subject #1 is

a professional player. For this subject, no significant difference was observed on the MAI, when different strings were played in different bowing types. For subject #7, our results (see figure 5.30) show that there is significant effect of the string played ($p < 0.001$) on the MAI for two different type of bowing (legato tip and large bowing). Figure 5.30 shows the boxplots concerning the two conditions where $p < 0.001$ were obtained for subject 7.

Subject #7 might turned the torso to the left during playing. Playing the notes in legatos, normally needs more control, because of the speed of bowing. Intrinsically, if the bowing arm is right, the player tends to turn its torso to the left. The other important issue that should be taken into account is the level of proficiency. Subject #1 is a professional player, whom might gained more experience in controlling his muscles during playing. Table 5.7 might implies that the professional viola player played the strings in large, legato tip and tail bowing types, without any turning of torso toward the instrument's side. To check this hypothesize and quantifying the amount of leaning or turning to the left, during playing the strings, in different bowing types, further studies using the XSENS is suggested.
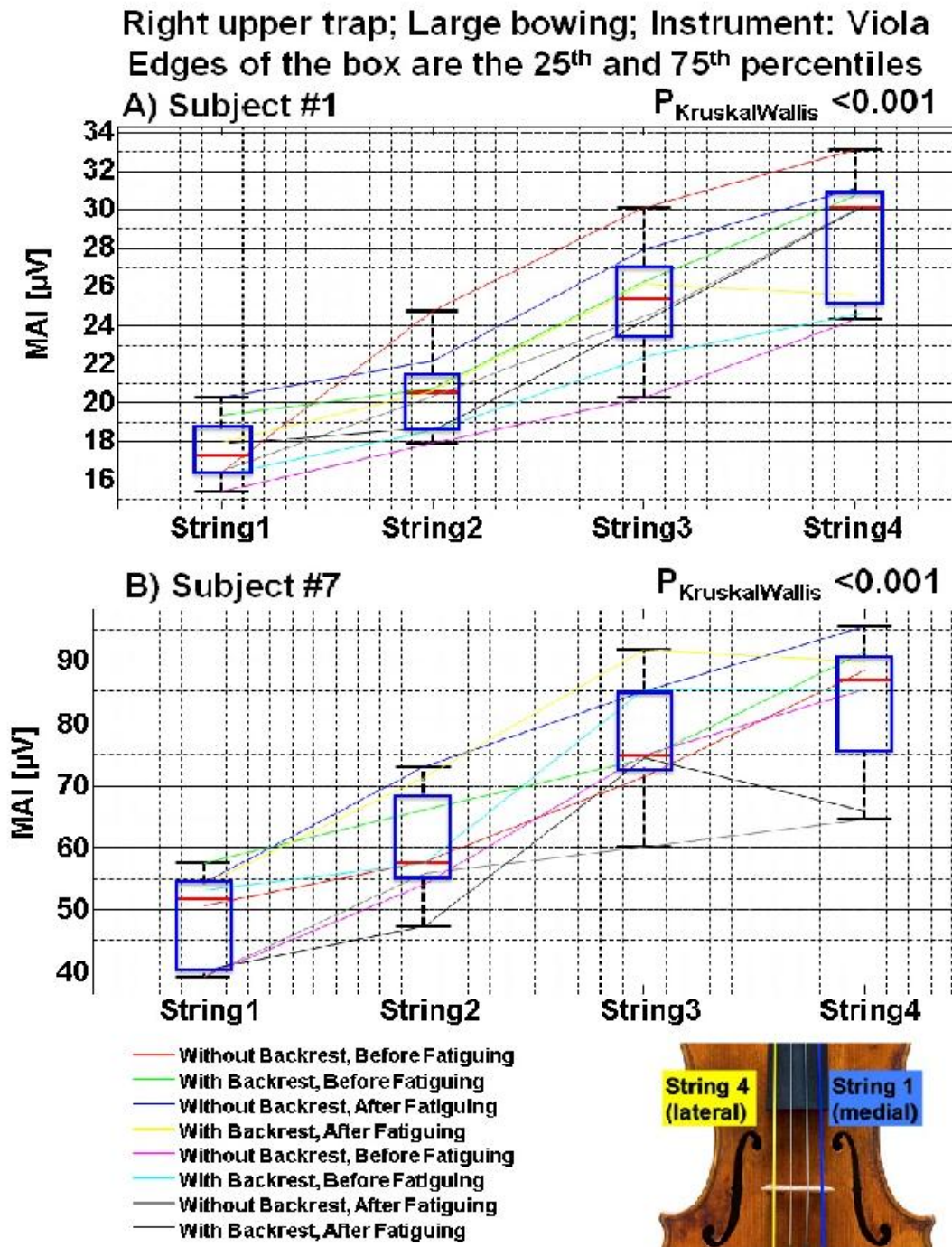
Figure 5.27: Boxplots represent the distribution of muscle activity index(MAI) of the A) first subject(professional viola player) and B) subject 7 (student viola player) from upper Trapezius muscle of the bowing arm in in large bowing versus the instrument's string number. The KruskalWallis test shows significant difference on the MAI, when subjects played different strings ($p < 0.001$). Please see the continue on the next page . . .

Figure 5.27: ... from the previous page: MAI was defined as the spatial average of RMS values of the muscle active region detected by modified watershed segmentation technique (watershed + equalization + 70% of the maximum value thresholding). The RMS was computed in time, for each channel of the active region, over the total length of single differential signal (10s). RMS of noise was about 5 to 6μV and was computed from recorded signals in relaxed sitting position.

Figure 5.28: Boxplots represent the distribution of muscle activity index(MAI) of the A) first subject(professional viola player) and B) subject 7 (student viola player) from lower Trapezius muscle of the bowing arm in in large bowing versus the instrument's string number. The KruskalWallis test shows significant difference on the MAI, when subjects played different strings (p < 0.001). Please see the continue on the next page . . .

217

Figure 5.28: ...from the previous page: MAI was defined as the spatial average of RMS values of the muscle active region detected by modified watershed segmentation technique (watershed + equalization + 70% of the maximum value thresholding). The RMS was computed in time, for each channel of the active region, over the total length of single differential signal (10s). RMS of noise was about 5 to 6μV and was computed from recorded signals in relaxed sitting position.

Table 5.7: The p-value corresponding to the KruskalWallis test for two Viola players (subjects 1=professional & 7=student player) for different bowing types for left and right Erector Spinae muscles in order to compare the muscle activity index(MAI), when different notes were played. For each subject, each bowing type and each muscle the p-values were computed over 8 values (two sessions, in each session before and after fatiguing, with and without backrest posture conditions were considered). MAI was defined as average of RMS values of the muscle active region detected by thresholding technique (70% of the maximum value). The RMS was computed in time, for each channel of the active region, over the total length of signal(10s).The $p < 0.05$ values are highlighted.

Subject No.	Muscle name	Bowing type	p-value
1	Left Erector Spinae	Legato tail	0.047
		Legato tip	0.124
		Large bowing	0.59
	Right Erector Spinae	Legato tail	0.73
		Legato tip	0.43
		Large bowing	0.97
7	Left Erector Spinae	Legato tail	0.871
		Legato tip	< 0.001
		Large bowing	< 0.001
	Right Erector Spinae	Legato tail	0.40
		Legato tip	0.67
		Large bowing	0.27
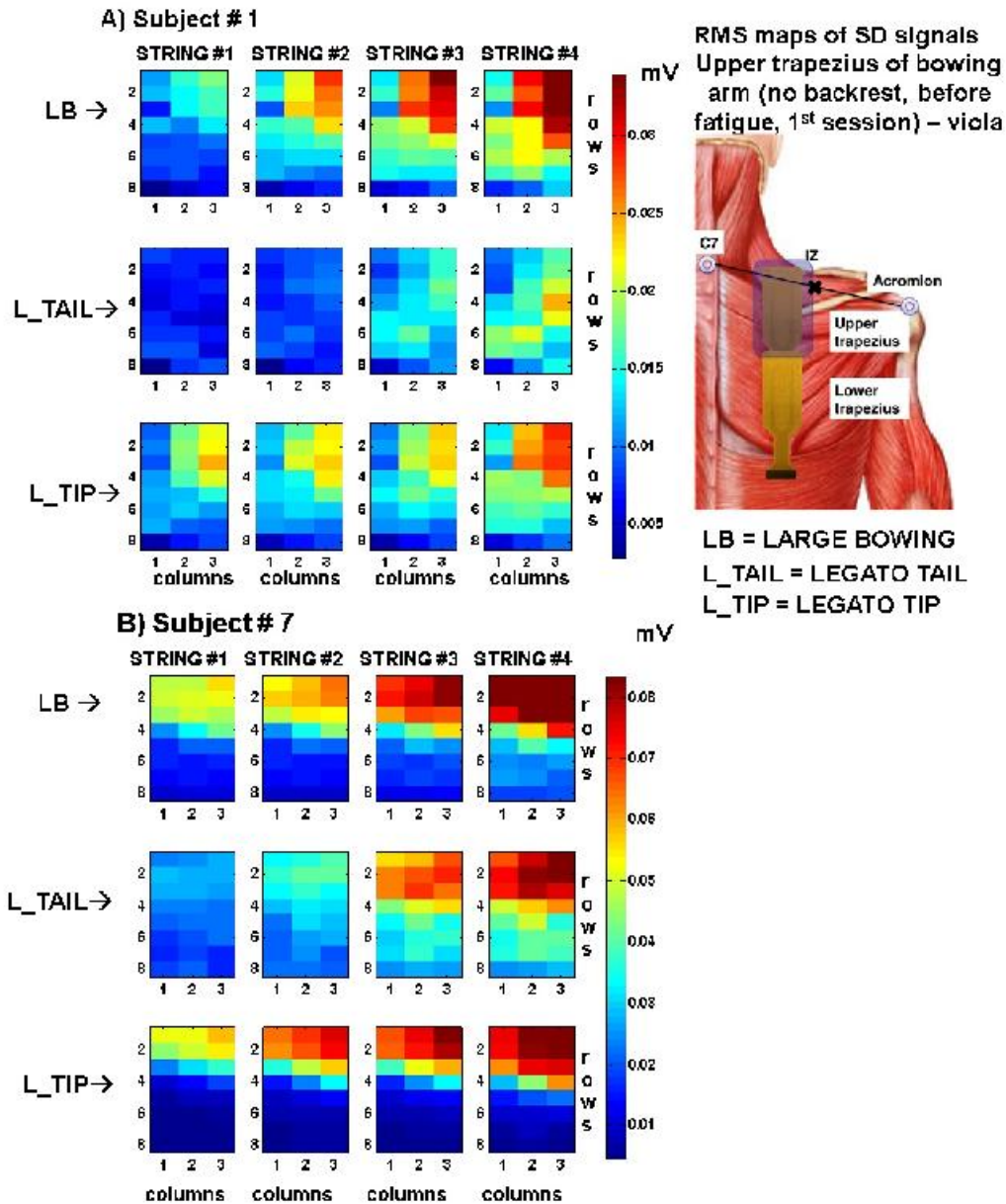
Figure 5.29: sEMG amplitude distributions obtained for A) subject 1 (professional viola player) and B) subject 7 (student viola player) playing four viola strings in different bowing types(large, legato tip and legato tail bowing movements). Each map (8 rows and 3 columns) represent the RMS values (calculated over 10s) of single differential signals(SD). sEMG signals were recorded from upper Trapezius (bowing arm). Signals were acquired in monopolar configuration using 8×4 electrode grid. SD signals were computed offline along fiber direction.
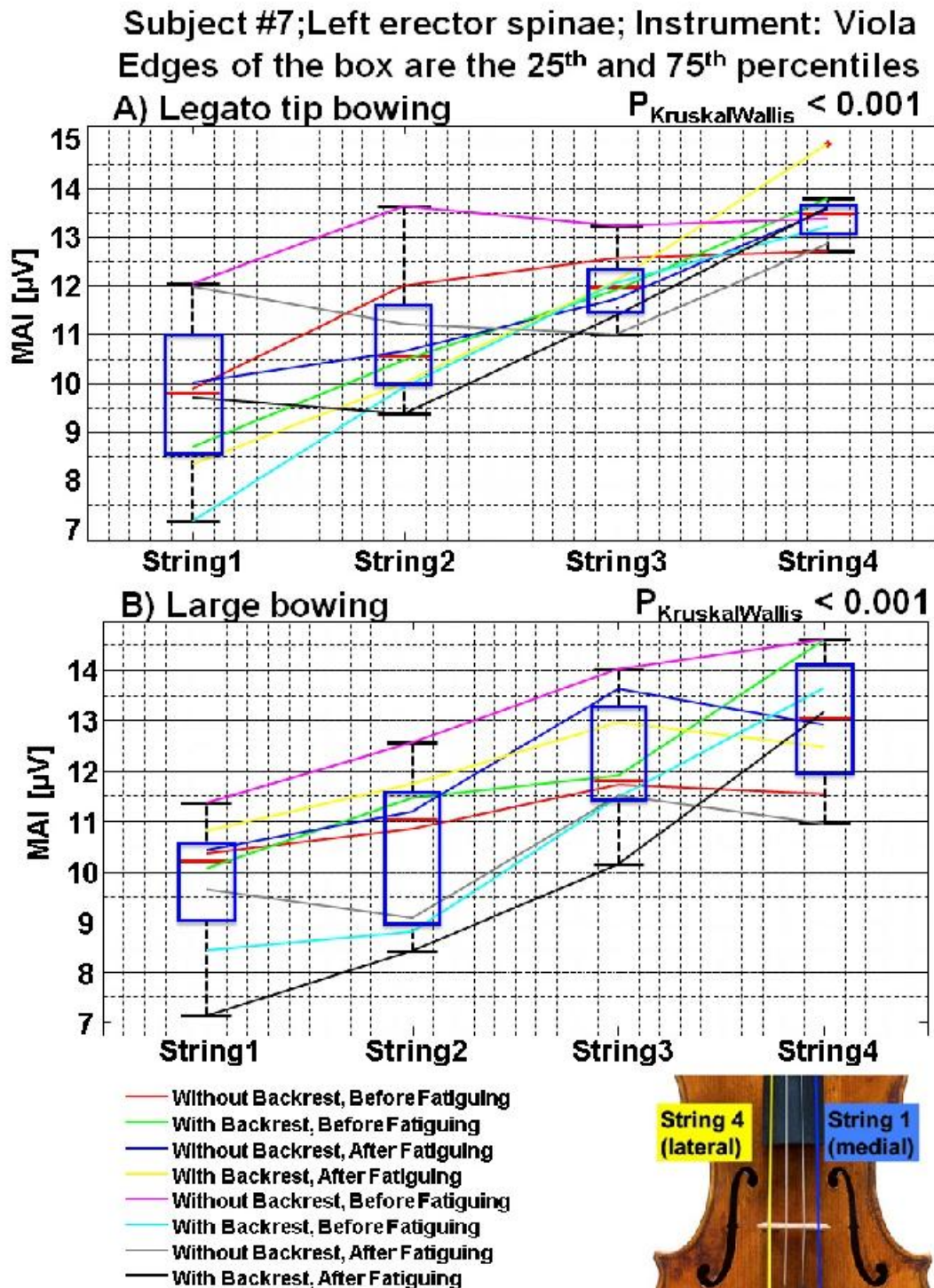
Figure 5.30: Boxplots represent the distribution of muscle activity index(MAI) of subject 7(student viola player) in A) legato tip bowing and B) large bowing from the left Erector Spinae muscle (see also table 5.7). Please see the continue on the next page ...

Figure 5.30: ...from the previous page: The KruskalWallis test shows significant difference on the MAI, when subjects played different strings (p < 0.001). MAI was defined as the spatial average of RMS values of the muscle active region detected by thresholding technique (70% of the maximum value). The RMS was computed in time, for each channel of the active region, over the total length of single differential signal (10s). RMS of noise was about 5 to 6μV and was computed from recorded signals in relaxed sitting position.

Effect of backrest on muscle activity:

Table 5.8 shows the p-value corresponding to different muscles and different bowing types for analyzing the effect of posture (playing with and without back rest support) on the muscles' activity index. The effect of posture is not the same for the two viola players (subject 1 is a professional and subject 7 is a student player). Results (table 5.8) show no significant difference for Trapezius muscle (upper and lower compartments) activity of the bowing arm in the presence of back rest support. This is true for both subjects. Posture's condition affects significantly ($p < 0.001$) the muscle activity of left and right Erector Spinae in large bowing of the first subject and of the right Erector Spinae of the seventh subject, when strings were played in legato tip bowing ($p = 0.019$). Figure 5.31 shows (for instance) the boxplots concerning the left Erector Spinae of the seventh subjects in legato tail bowing. This figure shows that no significant effect of the presence of backrest support can be observed($p = 0.429$).

Table 5.8: The p-values of the KruskalWallis test for the two viola players (subjects 1=professional & 7=student) are exposed in order to study the effect of backrest support on the the muscle activity index(MAI). For each subject, each bowing type and each muscle, the p-values were computed over 16 values (two sessions, in each session before and after fatiguing, and four different strings were considered). In all cases the MAI with no backrest support > MAI with backrest. The $p < 0.05$ values are highlighted.

Subject No.	Muscle name	Bowing type	p-value
1	Left Erector Spinae	Legato tail	0.132
		Legato tip	0.565
		Large bowing	**0.008**
	Right Erector Spinae	Legato tail	0.851
		Legato tip	0.336
		Large bowing	**0.018**
	Upper Trapezius of the bowing arm	Legato tail	0.474
		Legato tip	0.44
		Large bowing	0.792
	Lower Trapezius of the bowing arm	Legato tail	0.346
		Legato tip	0.127
		Large bowing	0.451
	Upper Trapezius of the non-bowing arm	Legato tail	**0.007**
		Legato tip	0.534
		Large bowing	0.346
7	Left Erector Spinae	Legato tail	0.429
		Legato tip	0.163
		Large bowing	0.546
	Right Erector Spinae	Legato tail	0.291
		Legato tip	**0.019**
		Large bowing	0.706
	Upper Trapezius of the bowing arm	Legato tail	0.97
		Legato tip	0.851
		Large bowing	0.598
	Lower Trapezius of the bowing arm	Legato tail	0.851
		Legato tip	0.451
		Large bowing	0.309
	Upper Trapezius of the non-bowing arm	Legato tail	0.97
		Legato tip	0.99
		Large bowing	0.821
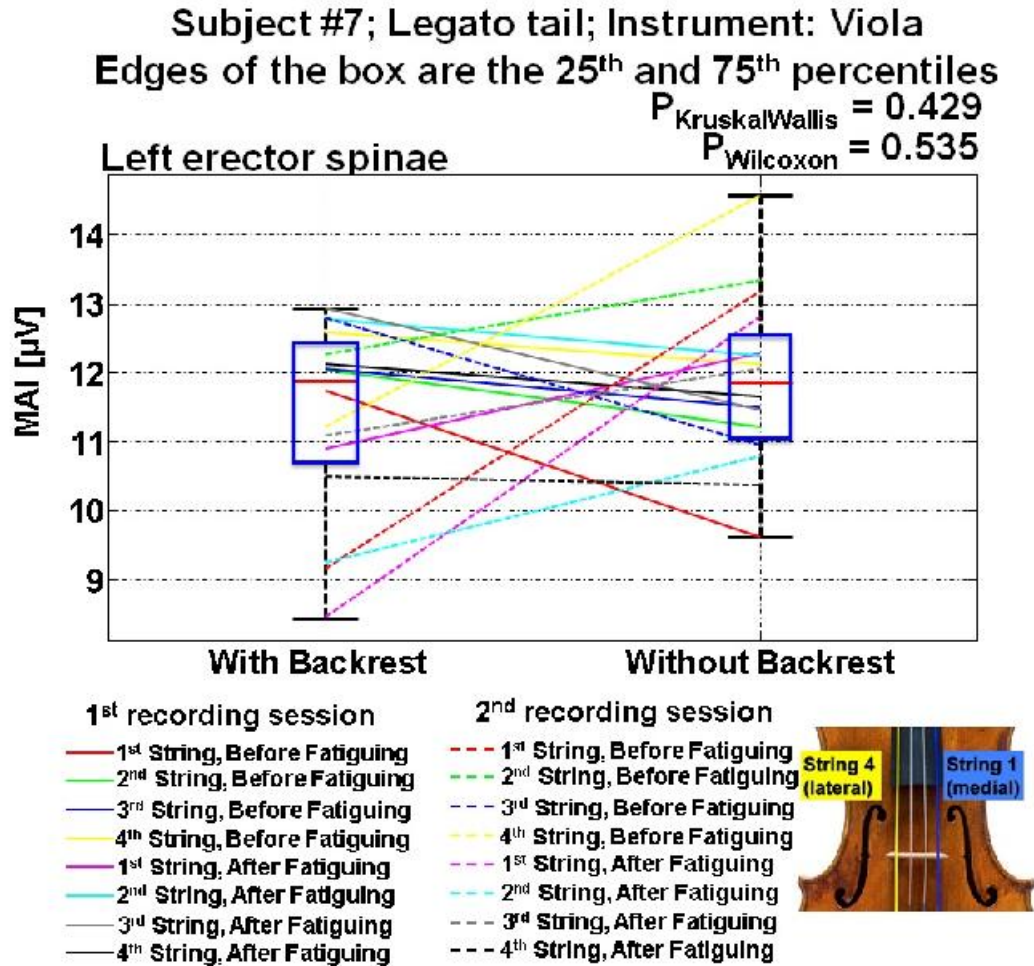
Figure 5.31: The boxplots represent the distribution of muscle activity index (MAI) of the seventh subject (professional viola player) for left Erector Spinae muscle in legato tail bowing. KruskalWallis test shows no significant difference in the MAI between the conditions of backrest and no backrest as $p = 0.429$. The MAI was defined as average of RMS values of the muscle active region detected by thresholding (channels with RMS>70% of max(RMS)). The RMS was computed in time, for each channel of the active region, over the total length of single differential signal (10s). Noise level(RMS) was computed (about 5 to 6μV) from recorded sEMGs in relaxed sitting position.

5. A STUDY OF MUSCLE ACTIVITY IN MUSICIANS PLAYING STRING INSTRUMENTS

Effect of fatiguing on muscle activity:

Table 5.9 and table 5.10 show the p-values of the KruskalWallis test for viola players (subjects 1 and 7). The p-values for each fatigue condition, were computed over 16 values (two sessions, backrest support(with/without), and four different strings were considered). The fatigue session was defined as about 30 minutes playing a difficult piece of music. In all presented significant levels, the median value (over the 16 values for both subjects) of the MAIs associated to the before fatiguing playings > the median of MAIs related to after fatiguing.

- **Upper and lower Trapezius muscle of the bowing arm:**

  Statistical difference ($p < 0.05$) between the activity index computed for before and after fatigue condition from the upper Trapezius of the bowing arm of viola player (subject 7) was observed (please see figure 5.32-panel "A") during legato tail bowing. In general, greater activity (MAI)was obtained for the playing before fatiguing with respect to playing after fatiguing.

  The lower Trapezius muscle of the bowing arm (right hand) is less active in comparison to the right upper Trapezius, and this has been observed for all subjects. Statistical effect of the fatigue session ($p < 0.05$) on the muscle's activity index of the lower Trapezius of the bowing arm was observed (please see figure 5.32-panel "B") in legato tip bowing for the seventh subject. Greater MAI values was obtained for playing before fatiguing in comparison with playing after fatiguing.

- **Upper Trapezius muscle of the non-bowing arm:**

  The non-bowing arm (left hand) was used for holding and supporting the instrument during playing. The p-values (KruskalWallis test) computed for the first subject(left upper Trapezius) are $p = 0.002$ and $p = 0.044$, when he played the notes applying legato tail and legato tip bowing movements respectively. Significant difference between the muscle activity index of signals recorded before and after fatiguing can be observed in the seventh subject's results concerning legato tail bowing ($p = 0.007$).

- **Left and right Erector Spinae:**

  Significant difference ($p < 0.05$) for right Erector Spinae muscle activity can be observed in each type of bowing (please see figure5.33 and table 5.10). Greater muscle activity index was obtained for signals recorded before fatiguing with

respect to after fatiguing.

Our data(see table 5.10) shows no significant difference in the MAI of the left Erector Spinae considering the MAIs of before and after fatiguing.

Table 5.9: The *p*-values of the KruskalWallis test for viola players (subjects 1 and 7) are exposed in order to study the effect of fatiguing condition on the muscles activity index(MAI). The *p*-values for each fatigue condition, were computed over 16 values (two sessions, backrest support(with/without), and four different strings were considered). The MAI was defined as average of RMS values of the muscle active region detected by modified watershed segmentation technique (watershed+equalization+70%of the maximum value thresholding). The RMS was computed in time, for each channel of the active region, over the total length of signal(10s). The fatigue session was defined as about 30 minutes playing a difficult piece of music. In all presented significant levels, the median value (over the 16 values for both subjects) of the MAIs at before fatiguing condition > the median of MAIs at after fatiguing condition. The $p < 0.05$ values are highlighted.

Subject No.	Muscle name	Bowing type	*p*-value
1	Right Upper Trapezius(bowing arm)	Large bowing	0,496
		Legato tail	0,366
		Legato tip	0,418
	Right Lower Trapezius(bowing arm)	Large bowing	0,291
		Legato tail	0,175
		Legato tip	0,093
	Left Upper Trapezius(non-bowing arm)	Large bowing	0,474
		Legato tail	0,002
		Legato tip	0,044
7	Right Upper Trapezius(bowing arm)	Large bowing	0,763
		Legato tail	0,003
		Legato tip	0,88
	Right Lower Trapezius(bowing arm)	Large bowing	0,105
		Legato tail	0,09
		Legato tip	0,038
	Left Upper Trapezius(non-bowing arm)	Large bowing	0,327
		Legato tail	0,007
		Legato tip	0,113

Table 5.10: The p-values of the KruskalWallis test for two viola players (subject 1 = professional and subject 7 = student) are presented in order to study the effect of fatiguing condition on the muscle's activity index(MAI). The p-values were computed over 16 values (two sessions, in each session presence of backrest support (with/without), and four different strings were considered). The MAI was defined as average of RMS values of the muscle active region detected by thresholding technique (70%of the maximum value). The RMS was computed in time, for each channel of the active region, over the total length of signal(10s). The fatigue session was defined as about 30 minutes playing a difficult piece of music. In all presented significant levels, the median value (over the 16 values) of the MAIs at before fatiguing condition > the median of MAIs at after fatiguing condition. The $p < 0.05$ values are highlighted.

Subject No.	Muscle name	Bowing type	p-value
1	Right Erector Spinae	Large bowing	0,706
		Legato tail	0,105
		Legato tip	0,72
	Left Erector Spinae	Large bowing	0,163
		Legato tail	0,94
		Legato tip	0,486
7	Right Erector Spinae	Large bowing	0,004
		Legato tail	0,001
		Legato tip	0,001
	Left Erector Spinae	Large bowing	0,327
		Legato tail	0,309
		Legato tip	0,451
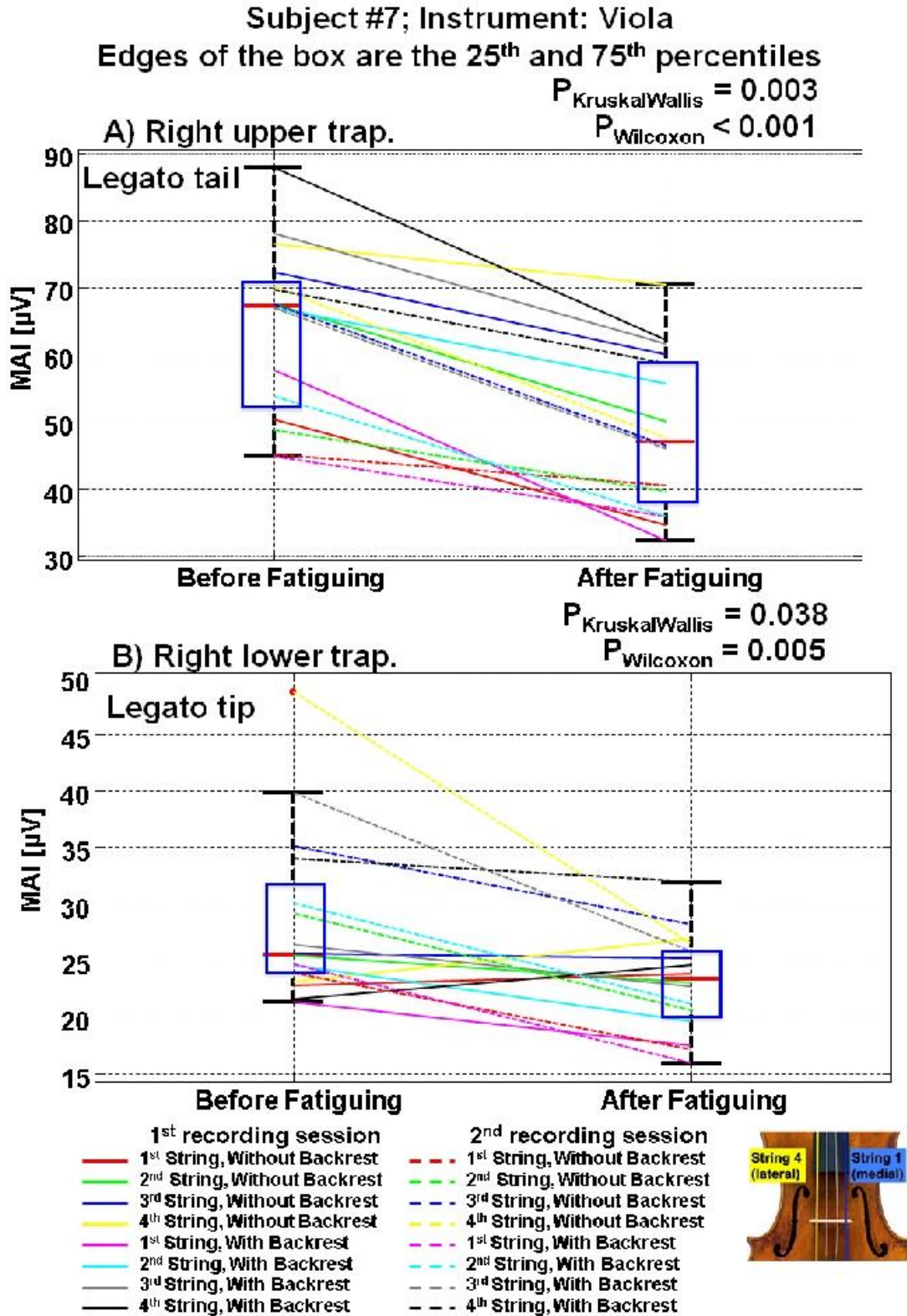
Figure 5.32: Boxplots represent the distribution of the muscle's activity index(MAI) from ... please see the continue on the next page ...

Figure 5.32: ... from the previous page: A) upper Trapezius and B) lower Trapezius of the bowing arm of the seventh subject (student viola player), when he played the notes (strings) in A) legato tail and B) legato tip. The KruskalWallis test were applied to test the significance level of the effect of fatiguing condition (before and after fatiguing) on the MAI. Wilcoxon test is for the pair test(non-parametric). MAI was defined as the spatial average of RMS values of the muscle active region detected by modified watershed segmentation technique (watershed + equalization + 70% of the maximum value thresholding). The RMS was computed in time, for each channel of the active region, over the total length of single differential signal (10s). RMS of noise level was about 5 to $6\mu V$ and was recorded in relaxed sitting position.
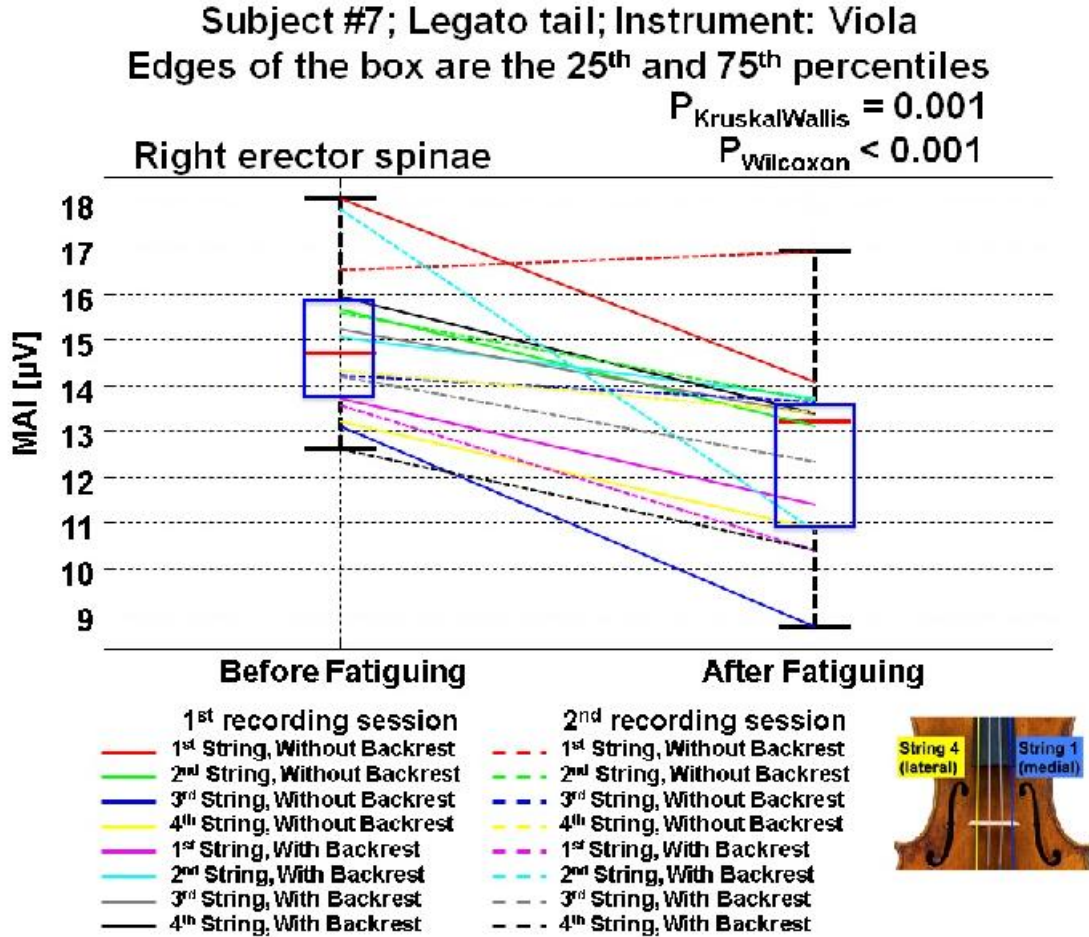
Figure 5.33: Boxplots represent the distribution of the muscle's activity index(MAI) from the right Erector Spinae muscle of the seventh subject (student viola player), when he played the notes (strings) in legato tail. The KruskalWallis test were applied to test the significance level of the effect of fatiguing condition (before and after fatiguing) on the MAI. Wilcoxon test is for the pair test(non-parametric). MAI was defined as the spatial average of RMS values of the muscle active region detected by thresholding technique (70% of the maximum value). The RMS was computed in time, for each channel of the active region, over the total length of single differential signal (10s). RMS of noise level was about 5 to 6μV and was recorded in relaxed sitting position.

5.6.3 Cello players (subject 2 and subject 3)

Subject 2 was a professional and subject 3 was a student cello player. Two sEMG
recording sessions conducted for subject 2 and three recording session were carried out
for subject 3.

Effect of the string that was played on the muscle activity index

- **Upper and lower Trapezius muscle of the bowing arm:**

  The muscle's activity index (MAI) was defined as the average of RMS values be-
  longing to the active region detected by modified watershed segmentation algo-
  rithm (watershed+equalization+70%of the maximum thresholding). By applying
  the Kruskal-Wallis test, significant effect of the string number (played note) on
  MAI of the uppert Trapezius of bowing arm was observed for subject #2, when he
  played different strings in large bowing ($p = 0.01$)(see panel "A" of figure 5.34).
  Concerning the third subject, by comparing the MAI versus string number, a
  positive (increasing) trend from the first to the fourth string, but non-significant
  ($p = 0.1$) on the MAI, was seen.

  Similar to the upper Trapezius of the bowing arm, the lower Trapezius muscle
  was seen more active (greater MAI) when the fourth string was played in large
  bowing (please see panels "B" and "C" of figure 5.34). There is a significant
  difference between the MAIs corresponding to the string numbers for both large
  and legato tail bowing (Figure 5.34, panels "B" and "C", and figure 5.35 panels
  "A" and "C").

  Considering the third subject in large bowing, the p-value was computed $p =
  0.005$, which implies significant difference in the MAI of the lower Trapezius of
  the bowing arm with respect to the string number. For this subject, in legato tip
  bowing ($p = 0.13$) and legato tail bowing ($p = 0.89$) no significant difference was
  observed (see panels "B" and "D" of figure 5.35).

- **Upper Trapezius muscle of the non-bowing arm :**

  During playing the strings, subjects used the non-bowing arm as a support for
  controlling and holding the instrument. No significant difference ($p > 0.05$) on the
  muscle's activity index of the upper Trapezius (non-bowing arm) was observed
  for legato tip, legato tail, and large bowing movements corresponding the string
  number that was played by the subjects.

- **Left and Right Erector Spinae muscles:**

  Table 5.11 shows the Kruskall-Wallis p-values for the two cello players (subject 2=professional and subject 3=student). No significant effect of the string number on the MAI was observed for left and right Erector Spinae muscles, in all bowing types (large, legato tail and tip bowing).
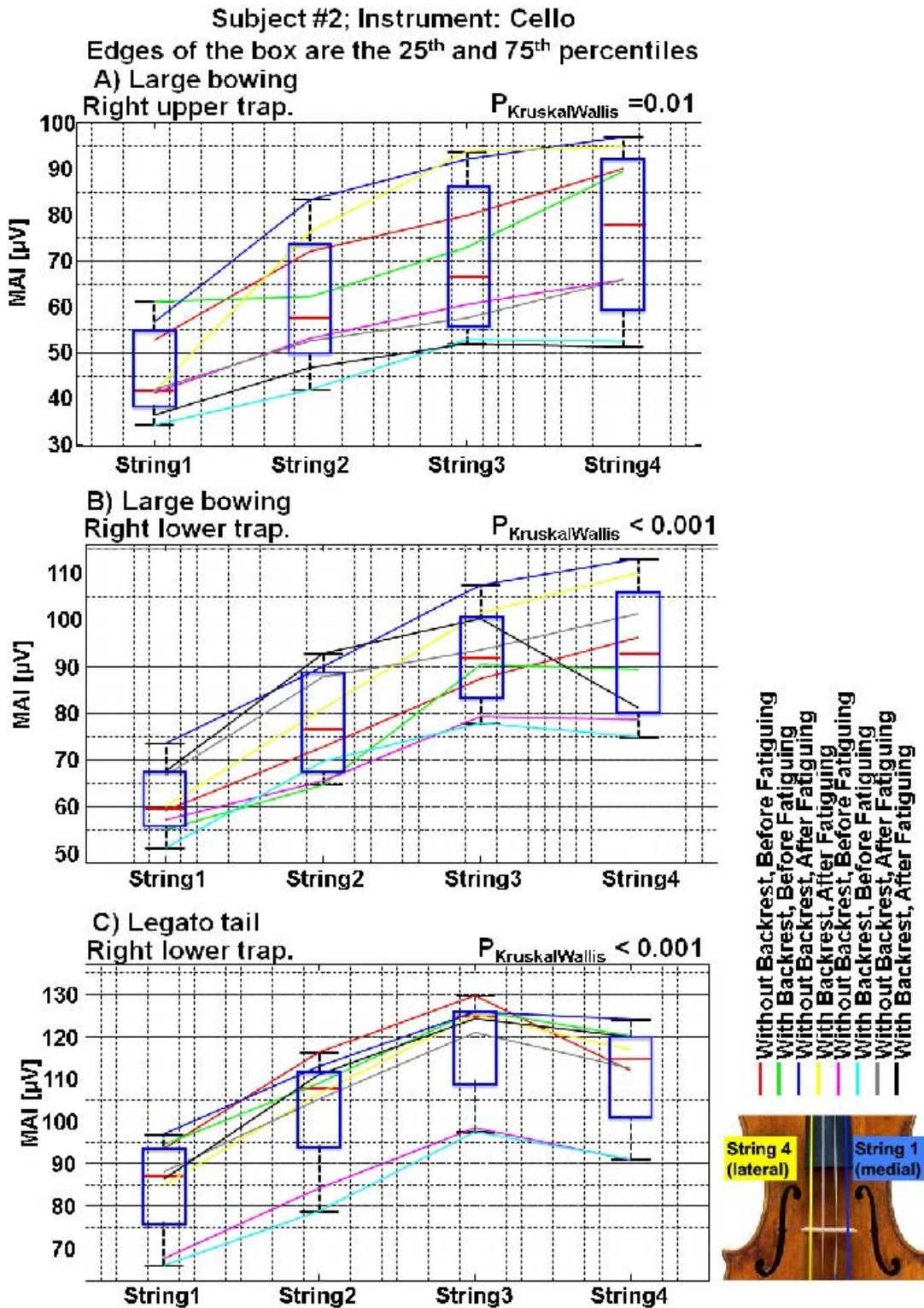
Figure 5.34: Please see the caption on the next page ...

Figure 5.34: ...from the previous page: Boxplots represent the distribution of muscle activity index(MAI) of the second subject (professional cello player) from A) upper Trapezius of the bowing arm in large bowing; B) lower Trapezius in large bowing; C) lower Trapezius in legato tail bowing versus the instrument's string number. The KruskalWallis test shows significant difference $p = 0.01$ for "A" and $p < 0.001$ for "B" and "C" on the MAI, when subjects played different strings. MAI was defined as the spatial average of RMS values of the muscle active region detected by modified watershed segmentation technique (watershed + equalization + 70% of the maximum value thresholding). The RMS was computed in time, for each channel of the active region, over the total length of single differential signal (10s). RMS of noise was about 5 to 6μV and was computed from recorded signals in relaxed sitting position.
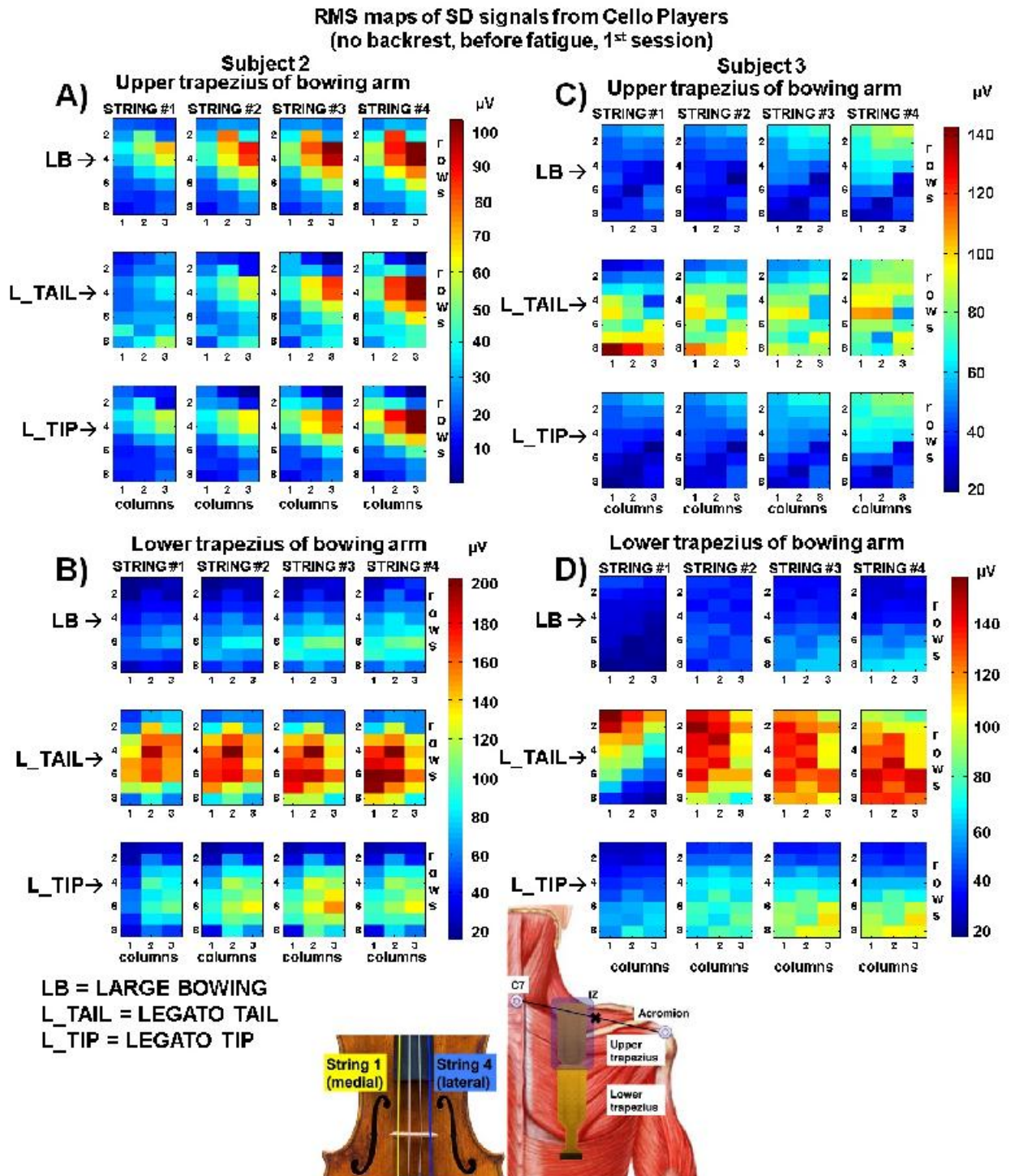
Figure 5.35: sEMG amplitude distributions obtained for A), B) subject 2 (professional cello player) and C), D) subject 3 (student cello player) playing four cello strings in different bowing types(large, legato tip and legato tail bowing movements) from A), C) upper Trapezius and B), D) lower Trapezius muscles. Please see the continue on the next page . . .

Figure 5.35: ...from the previous page: Each map (8 rows and 3 columns) represent the RMS values (calculated over 10s) of single differential signals(SD). sEMG signals were recorded from upper Trapezius (bowing arm). Signals were acquired in monopolar configuration using 8×4 electrode grid. SD signals were computed offline along fiber direction.

Table 5.11: The p-value corresponding to the KruskalWallis test for two cello players (subjects 2=professional & 3=student player) for different bowing types for left and right Erector Spinae muscles in order to compare the muscle activity index(MAI), when different notes were played. For each subject, each bowing type and each muscle the p-values were computed over 8 values (two sessions, in each session before and after fatiguing, with and without backrest posture conditions were considered). MAI was defined as average of RMS values of the muscle active region detected by thresholding technique (70% of the maximum value). The RMS was computed in time, for each channel of the active region, over the total length of signal(10s). The $p < 0.05$ values are highlighted.

Subject No.	Muscle name	Bowing type	p-value
2	Left Erector Spinae	Legato tail	0.334
		Legato tip	0.377
		Large bowing	0.053
	Right Erector Spinae	Legato tail	0.073
		Legato tip	0.849
		Large bowing	0.04
3	Left Erector Spinae	Legato tail	0.736
		Legato tip	0.513
		Large bowing	0.812
	Right Erector Spinae	Legato tail	0.491
		Legato tip	0.599
		Large bowing	0.200

Effect of backrest on muscle activity:

Posture condition has a significant effect ($p < 0.01$) on the muscle's activity index of the left Erector Spinae of the third subject (student cello player) in all bowing types. The boxplots corresponding to these conditions are shown in figure 5.36 for the second and in figure 5.37 for the third subject. In legato tip bowing, the backrest support

provides smaller MAI ($p = 0.002$) for the right Erector Spinae of the third subject(see figure 5.38). Statistical results of the Kruskal-Wallis test for analyzing the effect of backrest support (with and without backrest) on the MAI, for different muscles and different bowing types, concerning both cello players, are presented in table 5.12.
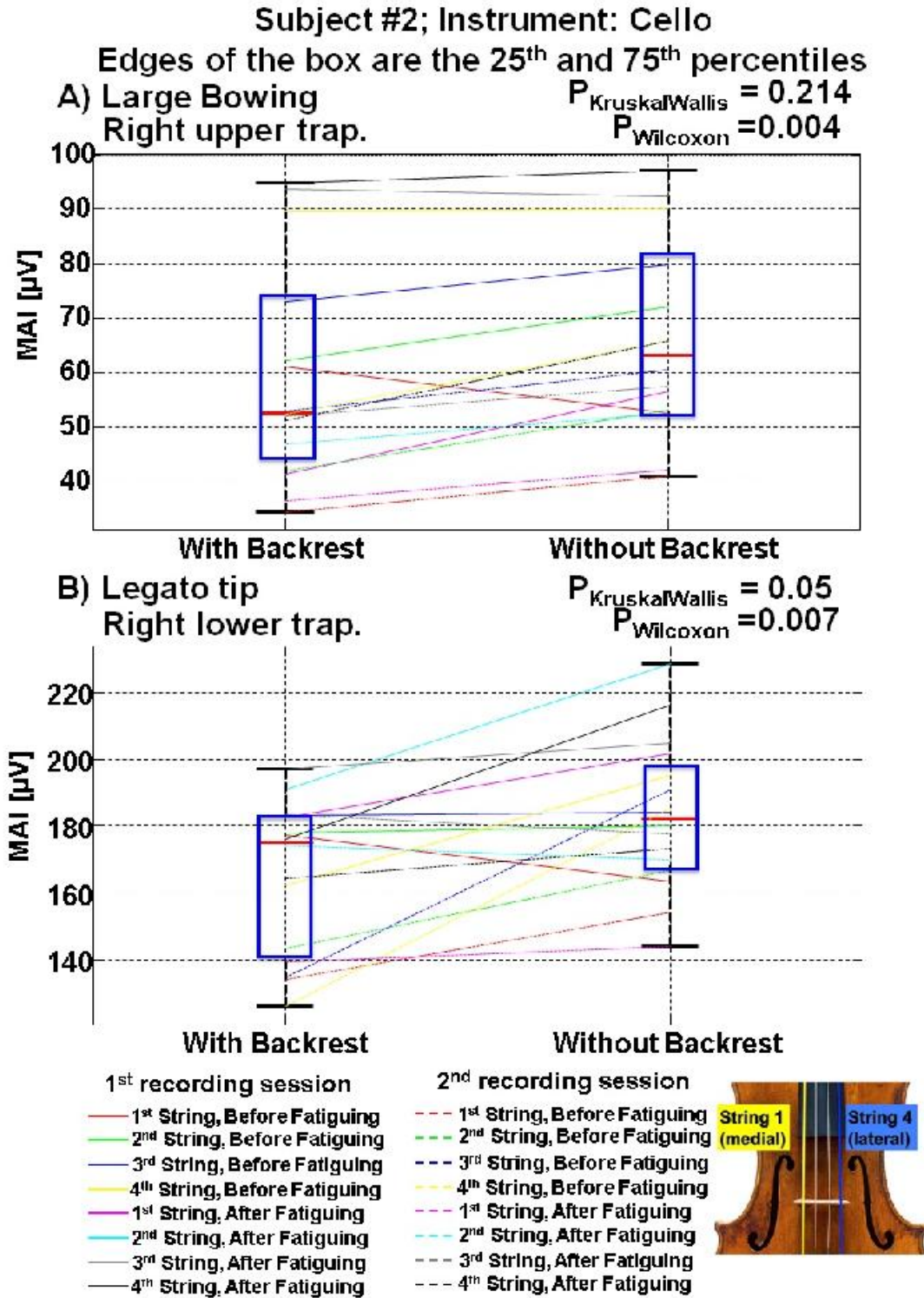
Figure 5.36: Boxplots represent the distribution of muscle activity index(MAI) of the second subject(professional cello player) in A) large bowing from the upper Trapezius and B) legato tip from the lower Trapezius muscles (see also table 5.12) of the bowing arm. Please see the continue on the next page . . .

237

Figure 5.36: . . . from the previous page: The KruskalWallis test shows no significant difference of the presence of backrest support on the MAIs. MAI was defined as the spatial average of RMS values of the muscle active region detected by modified watershed segmentation technique (watershed + equalization + 70% of the maximum value thresholding). The RMS was computed in time, for each channel of the active region, over the total length of single differential signal (10s). RMS of noise was about 5 to 6μV and was computed from the recorded signals in relaxed sitting position.

Figure 5.37: Please see the cation on the next page ...

Figure 5.37: ... from the previous page: Boxplots represent the distribution of muscle activity index(MAI) of the third subject (student cello player) from left erector muscle, when the stings were played in A) in large bowing; B) legato tail bowing; and C) legato tip bowing versus the backrest support conditions (with and without). The computed p-value for the KruskalWallis test are $p = 0.005$ for "A", $p = 0.002$, for "B", and $p < 0.001$ for "C". MAI was defined as the spatial average of RMS values of the muscle active region detected by thresholding technique (**70% of the maximum value**). The RMS was computed in time, for each channel of the active region, over the total length of single differential signal (10s). RMS of noise was about 5 to 6μV and was computed from the recorded signals in relaxed sitting position.

Figure 5.38: Boxplots represent the distribution of muscle activity index(MAI) of the third subject (student cello player) from right erector muscle, when the stings were played in legato tip bowing versus the backrest support conditions (with and without). The KruskalWallis test shows significant difference $p = 0.002$. MAI was defined as the spatial average of RMS values of the muscle active region detected by thresholding technique (70% of the maximum value). The RMS was computed in time, for each channel of the active region, over the total length of single differential signal (10s). RMS of noise was about 5 to $6\mu V$ and was computed from the recorded signals in relaxed sitting position.

Table 5.12: The p-values of the KruskalWallis test for the two cello players (subjects 2=professional & 3=student) are exposed in order to study the effect of backrest support on the the muscle activity index(MAI). For each subject, each bowing type and each muscle, the p-values were computed over 16 values (two sessions, in each session before and after fatiguing, and four different strings were considered). In all cases the MAI with no backrest support > MAI with backrest. The $p < 0.05$ values are highlighted.

Subject No.	Muscle name	Bowing type	p-value
2	Left Erector Spinae	Legato tail	0.113
		Legato tip	0.055
		Large bowing	1
	Right Erector Spinae	Legato tail	0.065
		Legato tip	0.624
		Large bowing	0.346
	Upper Trapezius of the bowing arm	Legato tail	0.651
		Legato tip	0.309
		Large bowing	0.214
	Lower Trapezius of the bowing arm	Legato tail	0.851
		Legato tip	0.05
		Large bowing	0.572
	Upper Trapezius of the non-bowing arm	Legato tail	0.366
		Legato tip	0.88
		Large bowing	0.474
3	Left Erector Spinae	Legato tail	0.002
		Legato tip	< 0.001
		Large bowing	0.005
	Right Erector Spinae	Legato tail	0.592
		Legato tip	0.002
		Large bowing	0.122
	Upper Trapezius of the bowing arm	Legato tail	0.951
		Legato tip	0.433
		Large bowing	0.161
	Lower Trapezius of the bowing arm	Legato tail	0.918
		Legato tip	0.805
		Large bowing	0.967
	Upper Trapezius of the non-bowing arm	Legato tail	0.312
		Legato tip	0.026
		Large bowing	0.55

Effect of the fatigue condition on the muscle activity index

Table 5.13 and table 5.14 show the p-values of the KruskalWallis test for cello players (subjects 2 and 3). The p-values for each fatigue condition, were computed over 16 values (two sessions, backrest support(with/without), and four different strings were considered). The fatigue session was defined as about 30 minutes playing a difficult piece of music.

- **Upper Trapezius muscle of the bowing arm:**

  Fatiguing condition (playing after and before fatiguing) provides statistical difference ($p = 0.016$ for the second subject and $p < 0.001$ for the third subject) on the muscle's activity index (MAI) of the upper Trapezius of the bowing arm in legato tail. There is an opposite trend for the MAIs in fatiguing conditions comparing the two subjects. In fact, playing before the fatigue session provides smaller muscle activity index than playing after the fatigue session for the second subject, while an opposite trend has been observed for the third subject (see panels "A" of figure 5.39 and figure 5.40).

- **Lower Trapezius muscle of the bowing arm :**

  Statistical difference, $p = 0.006$ for the professional cello player (second subject) and $p < 0.001$ for the student cello player (subject 3), was observer between the muscle's activity index of the lower Trapezius of the bowing arm in large bowing, when the effect of fatiguing condition were studied. Two different trends were seen for the second and third subjects. In fact, playing before the fatigue session provides smaller MAI comparing with the after fatiguing for the professional player in large bowing, while an opposite trend was seen for the student player.(see panels "B" of figure 5.39 and figure 5.40)

- **Upper Trapezius muscle of the non-bowing arm :**

  The non-bowing arm (left hand) was used for holding and supporting the instrument during playing. The muscle's activity index of the left upper Trapezius was not significantly different considering before and after fatiguing, except when subject #2 played the noted in legato tail bowing ($p = 0.038$). The status of being active (upper Trapezius of the non-bwing arm) might be due to the fact that during rapid movements especially legato tail, more effort is needed for holding and controlling the cello.

243

- **Left and Right Erector Spinae muscles:**

  Table 5.14 shows the KruskalWallis p-values for two cello players (subjects 2 and 3). There is a significant difference ($p < 0.05$) between the activity index associated to before with the MAI related to after fatiguing session for the right Erector Spinae muscles, of the student cello player (the third subject) in all types of bowing (see figure 5.42 as an example). This is true also for the MAIs of the left Erector Spinae, except for playing in legato tip($p = 0.24$, see table 5.14). Playing after the fatigue session provides smaller muscle activity index than playing before the fatigue session for the student cello player.
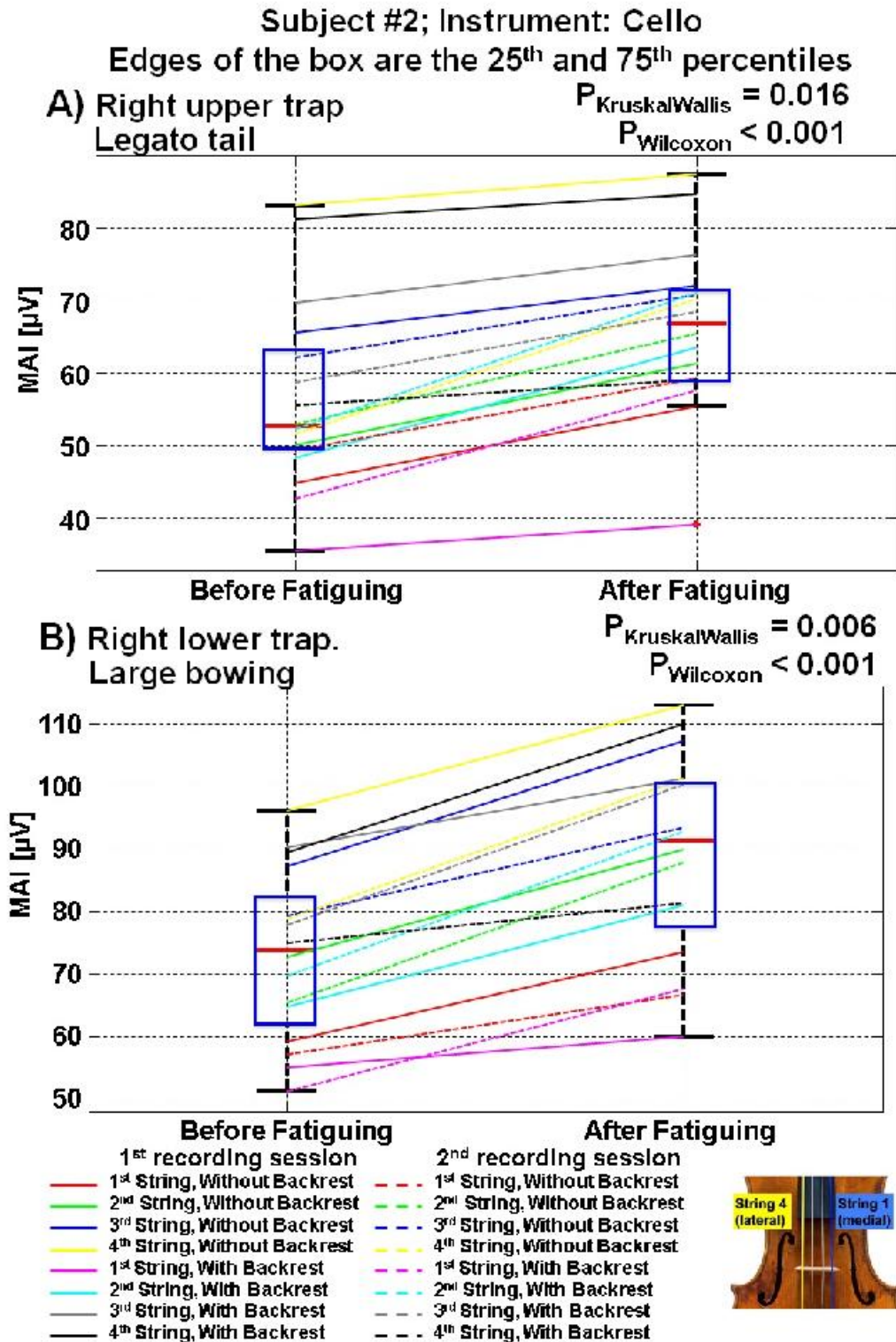
Figure 5.39: **Boxplots represent the distribution of the muscle's activity index(MAI) from A) upper Trapezius and B) lower Trapezius muscles of the bowing arm from subject 2(professional cello player) ...please see the continue on the next page ...**

245

Figure 5.39: . . . from the previous page: , when he played the notes (strings) in A) legato tail bowing and B) large bowing. The KruskalWallis test were applied to analyze the significance level of the effect of fatiguing condition (before and after fatiguing) on the MAI. Wilcoxon test is for the pair test(non-parametric). MAI was defined as the spatial average of RMS values of the muscle active region detected by modified watershed segmentation technique (watershed + equalization + 70% of the maximum value thresholding). The RMS was computed in time, for each channel of the active region, over the total length of single differential signal (10s). RMS of noise level was about 5 to 6μV and was recorded in relaxed sitting position.

Figure 5.40: Boxplots represent the distribution of the muscle's activity index(MAI) from the A) upper Trapezius and B) lower Trapezius muscles of the bowing arm from the third subject(student cello player), when he played the notes (strings) in A) legato tail bowing and B) large bowing. See the continue on the next page ...

Figure 5.41: . . . from the previous page: The KruskalWallis test were applied to analyze the significance level of the effect of fatiguing condition (before and after fatiguing) on the MAI. Wilcoxon test is for the pair test(non-parametric). MAI was defined as the spatial average of RMS values of the muscle active region detected by modified watershed segmentation technique (watershed + equalization + 70% of the maximum value thresholding). The RMS was computed in time, for each channel of the active region, over the total length of single differential signal (10s). RMS of noise level was about 5 to 6μV and was recorded in relaxed sitting position.

Table 5.13: The *p*-values of the KruskalWallis test for the cello players (subjects 2=professional and 3=student) are exposed in order to study the effect of fatiguing condition on the muscles activity index(MAI). The *p*-values for each fatigue condition, were computed over 16 values (two sessions, backrest support(with/without), and four different strings were considered). The MAI was defined as average of RMS values of the muscle active region detected by modified watershed segmentation technique (watershed+equalization+70% of the maximum value thresholding). The RMS was computed in time, for each channel of the active region, over the total length of signal(10s). The fatigue session was defined as about 30 minutes playing a difficult piece of music. In all presented significant levels except those *p*-values were specified with *, the median value (over the 16 values for both subjects) of the MAIs at before fatiguing condition > the median of MAIs at after fatiguing condition. * is for the median value of the MAIs before fatiguing condition < the median of MAIs at after fatiguing condition. The $p < 0.05$ values are highlighted.

Subject No.	Muscle name	Bowing type	*p*-value
2	Right Upper Trapezius(bowing arm)	Large bowing	0,792
		Legato tail	0,016 *
		Legato tip	0,407
	Right Lower Trapezius(bowing arm)	Large bowing	0,006
		Legato tail	0,105
		Legato tip	0,097
	Left Upper Trapezius(non-bowing arm)	Large bowing	0,624
		Legato tail	0,038 *
		Legato tip	0,083
3	Right Upper Trapezius(bowing arm)	Large bowing	< 0,001
		Legato tail	< 0,001
		Legato tip	0,122
	Right Lower Trapezius(bowing arm)	Large bowing	0,016
		Legato tail	0,122
		Legato tip	0,058
	Left Upper Trapezius(non-bowing arm)	Large bowing	0,177
		Legato tail	0,398
		Legato tip	0,695

Table 5.14: The p-values of the KruskalWallis test for two cello players (subject 2 = professional and subject 3 = student) are presented in order to study the effect of fatiguing condition on the muscle's activity index(MAI) of left and right Erector Spinae muscles. The p-values were computed over 16 values (two sessions, in each session presence of backrest support (with/without), and four different strings were considered). The MAI was defined as average of RMS values of the muscle active region detected by thresholding technique (70% of the maximum value). The RMS was computed in time, for each channel of the active region, over the total length of signal(10s). The fatigue session was defined as about 30 minutes playing a difficult piece of music. In all presented significant levels, the median value (over the 16 values) of the MAIs at before fatiguing condition > the median of MAIs at after fatiguing condition. The $p < 0.05$ values are highlighted.

Subject No.	Muscle name	Bowing type	p-value
2	Right Erector Spinae	Large bowing	0,105
		Legato tail	0,214
		Legato tip	0,94
	Left Erector Spinae	Large bowing	0,175
		Legato tail	0,214
		Legato tip	0,572
3	Right Erector Spinae	Large bowing	0,011
		Legato tail	0,001
		Legato tip	0,001
	Left Erector Spinae	Large bowing	< 0.001
		Legato tail	0,005
		Legato tip	0,24
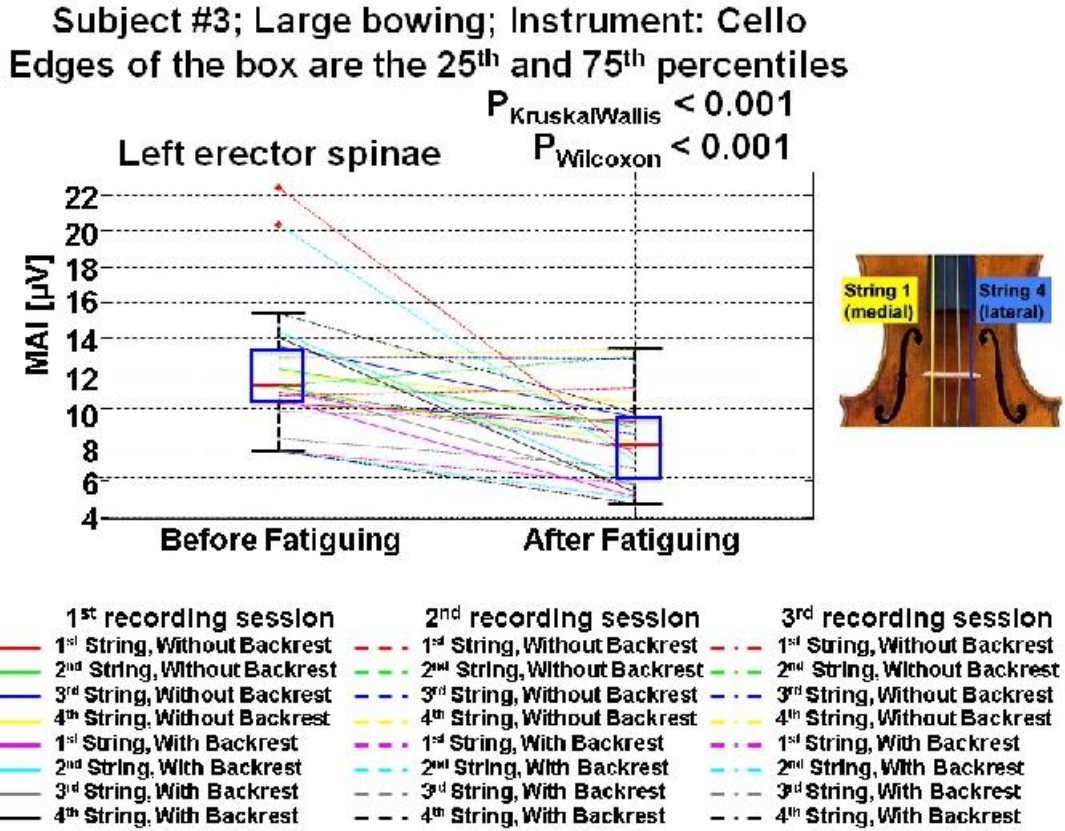
Figure 5.42: **Boxplots represent the distribution of the muscle's activity index(MAI) from the left Erector Spinae muscle of the third subject (student cello player), when he played the notes (strings) in large bowing. The KruskalWallis test were applied to test the significance level of the effect of fatiguing condition (before and after fatiguing) on the MAI. Wilcoxon test is for the pair test(non-parametric). MAI was defined as the spatial average of RMS values of the muscle active region detected by thresholding technique (70% of the maximum value). The RMS was computed in time, for each channel of the active region, over the total length of single differential signal (10s). RMS of noise level was about 5μV and was recorded in relaxed sitting position.**
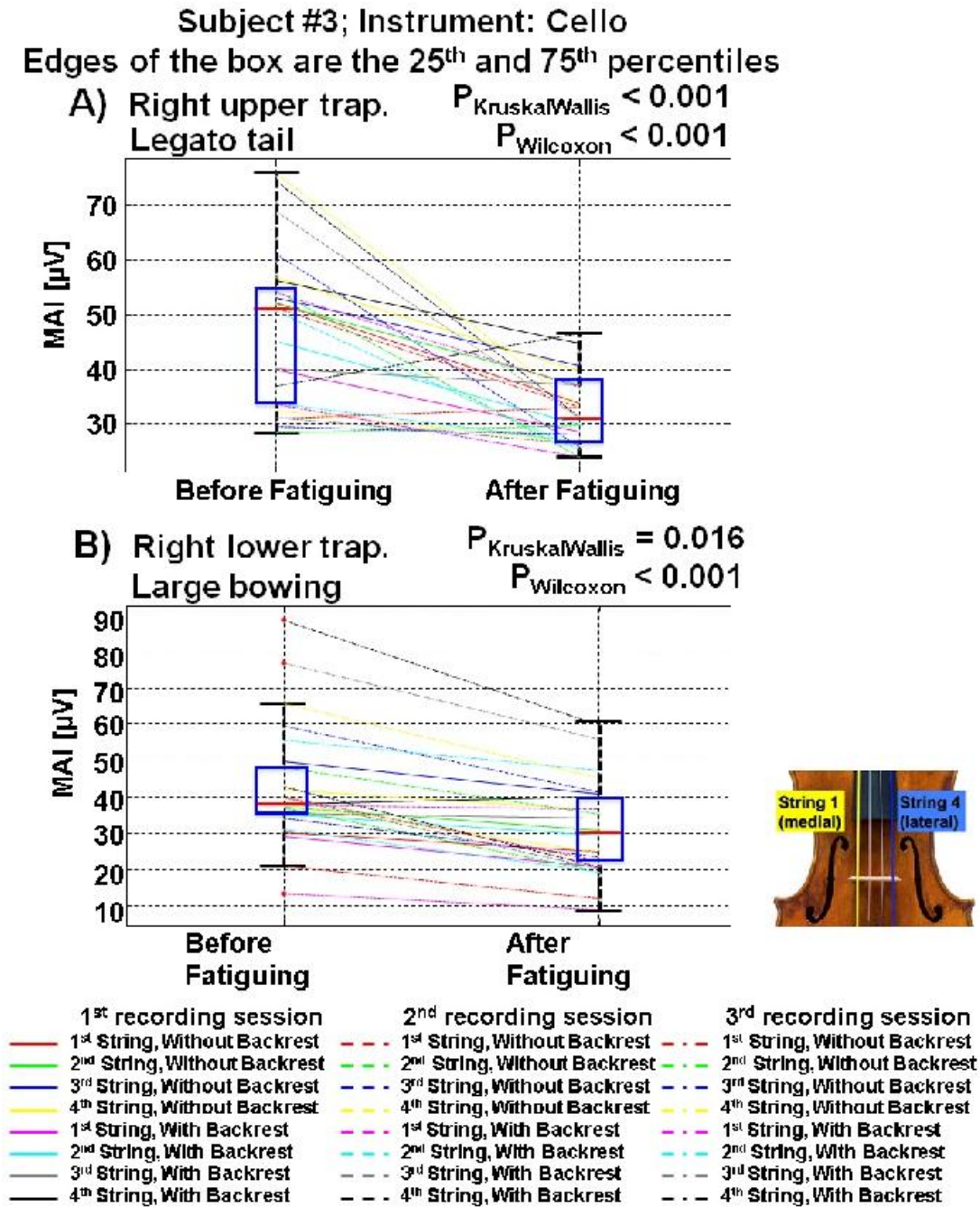
5.6.4   Summary

In summary for the musicians whom participated in this study (i.e. subjects 1 to 7), statistical analysis can be summarized as table 5.15.

Table 5.15: pannels A), B) and C) show the summary results of the effect of A) the strings that was played, B) presence of backrest support (with and without), and C) fatiguing condition (playing before and after fatiguing) on the muscle's activity index (MAI) of upper and lower Trapezius of the bowing arm, upper Trapezius of the non-bowing arm, left and right Erector Spinae muscles in three different bowing types(large, legato tail a legato tip). MAI was defined as the spatial average of RMS values of the muscle active region detected by thresholding technique (70% of the maximum value) for left and right Erector Spinae muscles and by modified watershed segmentation technique (watershed+equalization+70%of the maximum value thresholding) for Trapezius muscles. The RMS was computed in time, for each channel of the active region, over the total length of single differential signal (10s). Significant level ($p < 0.05$) was checked by Kruskal Wallis test

A) Bowing Types

Bowing Types	Muscle	Violin #4	Violin #5	Violin #6	Viola #1	Viola #7	Cello #2	Cello #3
Large Bowing	L_ES		Y	Y		Y	Y	
Large Bowing	L_UT			Y				
Large Bowing	R_ES							
Large Bowing	R_LT			Y		Y	Y	Y
Large Bowing	R_UT	Y	Y		Y	Y	Y	
Legato tail	L_ES			Y	Y			
Legato tail	L_UT	Y						
Legato tail	R_ES							
Legato tail	R_LT			Y		Y	Y	
Legato tail	R_UT		Y		Y	Y	Y	
Legato tip	L_ES		Y	Y		Y		
Legato tip	L_UT	Y						
Legato tip	R_ES		Y					
Legato tip	R_LT			Y	Y	Y		
Legato tip	R_UT	Y	Y	Y	Y	Y		

B) Bowing Types

Bowing Types	Muscle	Violin #4	Violin #5	Violin #6	Viola #1	Viola #7	Cello #2	Cello #3
Large Bowing	L_ES	Y	Y	Y	Y			Y
Large Bowing	L_UT		Y					
Large Bowing	R_ES	Y	Y	Y	Y			
Large Bowing	R_LT							
Large Bowing	R_UT							
Legato tail	L_ES	Y	Y	Y				Y
Legato tail	L_UT					Y		
Legato tail	R_ES	Y	Y	Y		Y		
Legato tail	R_LT							
Legato tail	R_UT							
Legato tip	L_ES	Y	Y	Y				Y
Legato tip	L_UT							
Legato tip	R_ES	Y						Y
Legato tip	R_LT						Y	
Legato tip	R_UT							

C) Bowing Types

Bowing Types	Muscle	Violin #4	Violin #5	Violin #6	Viola #1	Viola #7	Cello #2	Cello #3
Large Bowing	L_ES							Y
Large Bowing	L_UT							
Large Bowing	R_ES		Y			Y		Y
Large Bowing	R_LT	Y	Y				Y	Y
Large Bowing	R_UT		Y	Y				Y
Legato tail	L_ES							Y
Legato tail	L_UT			Y	Y	Y	Y	
Legato tail	R_ES	Y				Y		Y
Legato tail	R_LT	Y	Y	Y				
Legato tail	R_UT	Y		Y				Y
Legato tip	L_ES				Y			
Legato tip	L_UT		Y	Y				
Legato tip	R_ES					Y		Y
Legato tip	R_LT	Y	Y	Y		Y		
Legato tip	R_UT		Y					

A) String Played Effect
Y means $P<0.05$ (Kruskal Wallis test) between MAIs of different strings(notes)

B) Posture Effect
Y means $P<0.05$ (Kruskal Wallis test) between MAIs of different posture condition (with or without back rest)
$MAI_{WithoutBackrest} > MAI_{withBackrest}$

C) Fatigue Effect
Y means $P<0.05$ (Kruskal Wallis test) between MAIs of different fatigue condition (before or after fatiguing)
$MAI_{BeforeFatiguing} > MAI_{AfterFatiguing}$

L_ES = Left Erector Spinae Muscle
L_UT = Left (non-bowing arm) Upper Trapezius Muscle
R_ES = Right Erector Spinae Muscle
R_LT = Right (bowing arm) Lower Trapezius Muscle
R_UT = Right (bowing arm) Upper Trapezius Muscle

5.6.5 Conclusions

Recalling that the muscle activity index (MAI) was defined as the spatial average of RMS values (computed over 10s) of the muscle active region detected by thresholding technique (70% of the maximum value) for left and right Erector Spinae muscles (those muscles that were recorded using electrode arrays) and by modified watershed segmentation technique (watershed+equalization+70% of the maximum value thresholding) for Trapezius muscles (those muscles that were recorded using electrode grids), we can conclude from this study as follows:

- The upper and lower Trapezius of the bowing arm, upper Trapezius of the non-bowing arm, left and right Erector Spinae muscles were activated to a different extent depending on the note (string) being played. There is significant difference between the MAIs considering the string number. The MAI of the upper Trapezius of the bowing arm is statistically ($p < 0.001$) affected by the note (string number). The greatest MAI of both upper and lower Trapezius muscles were obtained when the fourth string (the most lateral string with respect to the sagittal plane of body's subject) was played and the minimum activity was observed when the first string (the most medial string with respect to the sagittal plane of the body's subject) was played. Generally, an increasing trend of EMG RMS based on the string number from the first to the fourth can be seen for both upper and lower Trapezius muscles, but not always implying a statistically significant difference for the lower Trapezius.

- Trapezius muscles of bowing arm were more active (produced higher activity index) when the direction of bowing was inverted in large bowing performance. Change of direction implies higher accelerations and greater muscle forces to counteract inertia. This trend (higher RMS value) at the time of change of bow direction was observed for all subjects.

- Differences between results (statistical test) were observed when student and professional players were compared. The MAIs of student players affected more by posture (playing with or without backrest support) than professional players. Since professionals might provide more control on muscles with less muscle activity, because of their experience in playing, it is reasonable to obtain higher *p-value*

253

(less significance difference among the muscle activity for playing different strings and with different postures) for professional players in comparison to the student players. To reach a stronger inference more subjects are needed.

- Statistically significant difference (Kruskal-Wallies $p < 0.05$) between the MAIs of left Erector Spinae muscle during playing with and without backrest support was observed in 4 (out of 5) student players (violin and cello student players). Only exception was the seventh subject (student viola player). The musicians might tend to turn or bend their torso to the left and this might causes a difference between the MAIs of left and right Erector Spinae muscles (the turn of torso on the left hypothesis can be validated in future studies using inertial systems and gyroscopes in order to track any movement of the torso toward the instrument). The MAI was greater when subjects played without backrest support with respect to when they played with backrest support.

- Generally, no significant differences were observed in our study between the MAIs of Trapezius muscles in the presence of a backrest (playing with and without backrest support), when the strings were played in different types of bowing (large bowing, legato tip and legato tail). In fact, some differences, which are reported in panel "B" of table 5.15 (summary of Results) were observed only for a limited number of cases and it is therefore impossible to infer strong conclusions. The presence and the size of the effect of backrest may be an individual issue.

- Statistically significant differences (Kruskal-Wallies $p < 0.05$) between the MAIs of right Erector Spinae muscle playing with and without backrest support was observed for violin student players (subject 5 and 6), when they played in large bowing and in legato tail. The MAIs were greater when they played without backrest support with respect to when they played with backrest support.

- Statistically significant differences (Kruskal-Wallies $p < 0.05$) between the MAIs of playing before and after the fatigue session (defined as about 30 minutes playing a difficult piece of music) was observed for all players. The activity index was greater when subjects played before with respect to after fatigue session. This is contrary to expectation and may mean that half our of playing is more like a "warm up" session rather than a fatiguing performance.

References

[1] A. Fjellman-Wiklund, Andersson H. Grip, H., K. J. Stefan, and G. Sundelin. **EMG trapezius muscle activity pattern in string players:: Part Iis there variability in the playing technique?** *International Journal of Industrial Ergonomics*, **33**(4):347–356, 2004. 157, 163

[2] Eckart Altenmüller, Wilfried Gruhn, Dietrich Parlitz, and Gundhild Liebert. **The impact of music education on brain networks: evidence from EEG-studies.** *International Journal of Music Education*, **os-35**(1):47–53, 2000. 157

[3] Ralph A. Manchester. **Toward better prevention of injuries among performing artists.** *Medical Problems of Performing Artists*, **21**(1):1, 2006. 157, 158

[4] B. Ackermann, R. Adams, and E. Marshall. **The effect of scapula taping on electromyographic activity and musical performance in professional violinists.** *Aust J Physiother*, **48**(3):197–203, 2002. 158, 166

[5] J. Lledó, S. Llana, P. Pérez, and E. Lledó. **Injuries prevention in string players.** *Journal of Sport and Health Research*, **4**(1):23–34, 2012. 158, 159

[6] Richard Lederman. **Neuromuscular and musculoskeletal problems in instrumental musicians.** *Muscle and nerve*, **27**(5):549–561, 2003. 159

[7] Dianna T. Kenny and Bronwen Ackermann. *Optimising physical and psychological health in performing musicians*, pages 390–400. Oxford University Press, Oxford, UK, 2008. 159

[8] A. B. M. Rietveld. **Dancers' and musicians' injuries.** *Clinical Rheumatology*, **32**(4):425–434, 2013. 159

[9] Stephan Schuele and Richard J. Lederman. **Long-term outcome of focal dystonia in string instrumentalists.** *Movement Disorders*, **19**(1):43–48, 2004. 161

[10] A. B. M. Rietveld and J. N. A. L. Leijnse. **Focal hand dystonia in musicians: a synopsis.** *Clinical Rheumatology*, **32**(4):481–486, 2013. 161

[11] Jennifer. Wales. *3D movement and muscle activity patterns in a violin bowing task.* M.sc. applied health sciences, 2007. xxiii, 161, 162, 163

[12] Otto Szende. *The physiology of violin playing.* Collet's, London, 1971. 161, 162

[13] G. Shan, P. Visentin, and A. Schultz. **Multidimensional signal analysis as a means of better understanding factors associated with repetitive use in violin performance.** *Medical Problems of Performing Artists*, **19**(3):129, 2004. 161, 162

[14] Gray H. Berque, P. **The influence of neck-shoulder pain on trapezius muscle activity among professional violin and viola players: an electromyographic study.** *Medical Problems of Performing Arts*, **17**(2):68–75, 2002. xxiii, 161, 164, 165

[15] Charles E. Levy, Wynne A. Lee, Alice G. Brandfonbrener, Joel Press, and Alexis Engel Levy. **Electromyographic analysis of muscular activity in the upper extremity generated by supporting a violin with and without a shoulder rest.** *Medical Problems of Performing Artists*, **7**(4):103, 1992. 161, 164, 166

[16] Hunter J.H. Fry. **Incidence of overuse syndrome in the symphony orchestra.** *Medical Problems of Performing Artists*, **1**(2):51, 1986. 161

[17] A. Fjellman-Wiklund, Andersson H. Grip, H., K. J. Stefan, and G. Sundelin. **EMG trapezius muscle activity pattern in string players: Part IIInfluences of basic body awareness therapy on the violin playing technique.** *International Journal of Industrial Ergonomics*, **33**(4):357–367, 2004. 162, 163

[18] Lennart Philipson, Rolf Sorbye, Pal Larsson, and Stojan Kaladjev. **Muscular load levels in performing musicians as monitored by quantitative electromyography.** *Medical Problems of Performing Artists*, **5**(2):79, 1990. 164

[19] K. Guettler, H. Jahren, and K. Hartviksen. **On the muscular activity of the performing violinist.** In *Conf. Proceeding; British Performing Arts Medicine Trust: Health and the Musician*, 1997. 166

[20] Carolyn Yarbrough. *Electromyography (EMG) Biofeedback Training in Music Performance: Preventing and Reducing Musculoskeletal Pain in Musicians.* Thesis, 2012. 167

[21] R. Merletti, M. Aventaggiato, A. Botter, A. Holobar, H. Marateb, and T. M. Vieira. **Advances in surface EMG: recent progress in detection and processing techniques.** *Crit Rev Biomed Eng*, **38**(4):305–345, 2010. 167

[22] Kenneth S. Saladin. *Anatomy & Physiology: The Unity of Form and Function, 3/e.* New York, NY : McGraw-Hill, 2003. xxiv, 169, 170, 171

[23] Hamid Marateb, Monica Rojas-Martínez, Marjan Mansourian, Roberto Merletti, and Miguel Mañanas Villanueva. **Outlier detection in high-density surface electromyographic signals.** *Medical and Biological Engineering and Computing*, **50**(1):79–89, 2012. 178

6

General conclusions, limitations of the studies and future perspectives

6.1 Conclusions

The following conclusions, provided in this work, represent a step ahead in the field of surface EMG technology:

- The RMS (either of a map in space or of a signal sampled in time) is preferable to ARV.

- Spatial sampling with interelectrode distances greater than 10 mm introduces aliasing and affects the estimates of EMG features in space.

- The watershed segmentation algorithm is preferable to the k-means and the h-dome algorithm for the identification of regions of interest of EMG maps.

- The force/torque contributed by individual muscles to the total force/torque acting on a joint can be estimated using an Analytical-Graphycal Algorithm (based on a particular model) or by an Optimization Algorithm (Particle Swarm Optimization). Both algorithms provide more than one solution to the problem and the solutions provided by the two methods coincide.

- Yoga relaxation affects myoelectric manifestations of muscle fatigue.

257

- The activation of the Trapzius muscle of the bowing arm in musicians playing string instruments (violin, viola and cello) depends on the string played (is higher for more lateral strings).

- The activation of the Erector Spinae muscles depends on the presence or absence of backrest.

6.2   Limitations of the studies

No gold standard exists for verifying the correctness of the solutions of the load sharing problem. Therefore, there is no way of knowing if the solutions obtained by means of the proposed algorithms are correct. Only one experimental application of the algorithms has been implemented.

The studies on Yoga relaxations (one subject) justifies further work but has no statistical value.

The study on musicians have statistical significance for individual subjects but further measurements should be performed to investigate repeatability and general (across subjects) conclusions.

6.3   Future perspectives

Additional experiments should be carried out to verify the applicability and sensitivity (to noise and model parameters or starting point) of the load sharing algorithms. Research should be focused on the identification of a gold standard to validate the solutions identified by the algorithms.

Testing of more musicians is required to statistically validate and to generalize the observations presented in this work. The results presented in this work have applications in many different fields, specifically in sports, in rehabilitation and in preventive medicine.

7

Papers (Presentations to congresses)

List of papers (Presentations to congresses):

- Botter, A., H. R. Marateb, Afsharipour,B, Merletti, R. (2011). "Solving EMG-force relationship using Particle Swarm Optimization." Conference proceedings : ... Annual International Conference of the IEEE Engineering in Medicine and Biology Society. IEEE Engineering in Medicine and Biology Society. Conference 2011: 3861-3864.

- Merletti, R., Afsharipour, B., Piervirgili, G., (2012). High Density Surface EMG Technology. ICNR 2012, Toledo (Spain) High Density Surface EMG Technology, Toledo, 2012

- Merletti, R. and Afsharipour, B. (2012). Variability of Electromyographic (EMG) Signals and Their Features. ICB 2012, Warsaw (Poland), International Center of Biocybernetics Polish Academy of Sciences.

- Gallina, A., Vieira, T. M. M. , Afsharipour,B.,Camarota,G., Merletti, R. (2012). Surface EMG amplitude distribution over the trapezius muscle during cello playing: a single case report. XIII Conference-Societ Italiana di Analisi del Movimento in Clinica. Bellaria, Italy, October 3-6 [Poster].

- Ullah, K., Afsharipour,B., Merletti, R. (2013). EMG Topographic Image Enhancement Using Multi Scale Filtering. XIII Mediterranean Conference on Med-

ical and Biological Engineering and Computing 2013. Heidelberg, Springer. 41: 674-677.

- Afsharipour, B., Ullah, K., Merletti, R. (2013). Spatial Aliasing and EMG Amplitude in Time and Space: Simulated Action Potential Maps. XIII Mediterranean Conference on Medical and Biological Engineering and Computing 2013. Heidelberg, Springer. 41: 293-296.